University of Cincinnati

Date: 11/1/2017

I, Alexander J. Brath, hereby submit this original work as part of the requirements for the degree of Doctor of Philosophy in Aerospace Engineering.

It is entitled:

Advanced techniques for ultrasonic imaging in the presence of material and geometrical complexity

Student's name: **Alexander J. Brath**

This work and its defense approved by:

Committee chair: Francesco Simonetti, Ph.D.

Committee member: Gui-Rong Liu, Ph.D.

Committee member: Peter Nagy, Ph.D.

28005

ADVANCED TECHNIQUES FOR ULTRASONIC IMAGING IN THE PRESENCE OF MATERIAL AND GEOMETRICAL COMPLEXITY

A dissertation submitted to The Graduate School of the University of Cincinnati

in partial fulfillment of the requirements for the degree of

Doctor of Philosophy

in the Department of Aerospace Engineering and Engineering Mechanics of the College of Engineering

2017

by Alexander Joseph Brath

B.S., University of Cincinnati, 2014

Committee Chair: Professor Francesco Simonetti

Abstract

The complexity of modern engineering systems is increasing in several ways: advances in materials science are leading to the design of materials which are optimized for material strength, conductivity, temperature resistance etc., leading to complex material microstructure; the combination of additive manufacturing and shape optimization algorithms are leading to components with incredibly intricate geometrical complexity; and engineering systems are being designed to operate at larger scales in ever harsher environments. As a result, at the same time that there is an increasing need for reliable and accurate defect detection and monitoring capabilities, many of the currently available non-destructive evaluation techniques are rendered ineffective by this increasing material and geometrical complexity.

This thesis addresses the challenges posed by inspection and monitoring problems in complex engineering systems with a three-part approach. In order to address material complexities, a model of wavefront propagation in anisotropic materials is developed, along with efficient numerical techniques to solve for the wavefront propagation in inhomogeneous, anisotropic material. Since material and geometrical complexities significantly affect the ability of ultrasonic energy to penetrate into the specimen, measurement configurations are tailored to specific applications which utilize arrays of either piezoelectric (PZT) or electromagnetic acoustic transducers (EMAT). These measurement configurations include novel array architectures as well as the exploration of ice as an acoustic coupling medium. Imaging algorithms which were previously developed for isotropic materials with simple geometry are adapted to utilize the more powerful wavefront propagation model and novel measurement configurations.

Acknowledgments

Working at the Ultrasonic Imaging Lab (USIL) has been a stimulating and rewarding experience from beginning to end. I am very thankful to my adviser Dr. Francesco Simonetti for his support, guidance and patience. My colleagues at USIL have also been a joy to work with, and have been the source of many fruitful discussions and collaborations.

I would also like to thank the staff members of the Department of Aerospace Engineering and Engineering Mechanics and Graduate Student Office for always being helpful with every technical, administrative and clerical difficulty that I have encountered during my time here.

Finally, my thanks goes to Stephanie and my family for their unwavering encouragement and enthusiasm.

Contents

List of Figures

List of Tables

Nomenclature

$\mathbb{R}$	Set of real numbers
$\mathbb{R}^n$	Real coordinate space of n dimensions (n-D)
$\mathbf{e}_1, \mathbf{e}_2, \mathbf{e}_3$	Orthonormal basis vectors for $\mathbb{R}^3$
$\mathbf{v}, v_i$	Where $\mathbf{v}$ is a n-D vector, v_i is the i$^{\text{th}}$ component of $\mathbf{v}$
$\frac{\partial}{\partial x_i}$	Partial derivative taken with respect to direction $\mathbf{e}_i$
$\frac{\partial}{\partial t}$	Partial derivative taken with respect to time
$\mathbf{u}$	Particle displacement vector
ρ	Material density
σ_{ij}	Component of stress tensor, equal to stress acting in direction $\mathbf{e}_i$ on a surface with surface normal pointing in direction $\mathbf{e}_j$
C_{ijhk}	Component of elastic stiffness tensor
ε_{hk}	Component of strain tensor, equal to $\frac{1}{2}\left(\frac{\partial u_h}{\partial x_k} + \frac{\partial u_k}{\partial x_h}\right)$
δ_{ik}	Kronecker delta
F_t	Wavefront at time t
τ	Function of space which returns the time that the wavefront passes through a point, F_t is equivalent to the surface defined by $\tau - t = 0$
τ_j	Derivative of τ with respect to $\mathbf{e}_j$, equal to $\frac{\partial \tau}{\partial x_j}$
K_{ijhk}	Component of stiffness tensor divided by material density, equal to C_{ijhk}/ρ
$\mathbf{V}, V$	Phase velocity vector, magnitude of phase velocity
θ	Angle between phase velocity vector and x_3 axis
θ_g	Group propagation angle measured from x_3 axis
$\mathbf{V}_g, V_g$	Group velocity vector, magnitude of group velocity
c	Speed of compressional waves in isotropic media
c_w	Speed of sound in water
p	Acoustic pressure

$\mathcal{M}$	Function mapping points in 3-D euclidean space to 3×3 matrices, used to construct metric
$\mathcal{R}$	3×3 rotation matrix
Z	Acoustic impedance, in isotropic material $Z = \rho c$
α_{cr}	Critical angle of reflection
f	Frequency
d	Wall thickness
Σ	3-D surface representing surface of pipe
Ω	2-D acoustic domain
$\mathbf{r}$	Parametric function mapping $\Omega \to \Sigma$
Γ	Path contained in Σ
Γ'	Path contained in Ω
Chapter 3	
α	Angle measuring orientation of anisotropy in composite material
Chapters 5, 6, 7	
α	Measure of anisotropy caused by parametric stretching

Chapter 1

Introduction

1.1 Motivation

Technological advances which are occurring in parallel across many disciplines are having compounding effects on industrial manufacturing capabilities and practices. In particular, there is a trend toward increased complexity in both material design and component geometry which is being driven by advances in several key fields. Progress in material science is enabling the design and manufacture of materials with complicated microstructure which can be optimized for specific engineering applications in terms of the material strength, temperature resistance, conductivity and more. An example is provided by the GE Aviation Leap which is the first commercial jet engine featuring ceramic matrix composite (CMC) components. This engine contains CMC turbine shrouds which are both lighter weight and more temperature resistant than a comparable part made from high grade metal alloys [1]. Additional research is exploring the possibility of making critical engine components from composite materials, such as the prototype CMC blade shown in Figure 1-1 (a). Advances in manufacturing processes, particularly in additive manufacturing (AM), are beginning to allow complex components to be fabricated at much lower cost than traditional machining methods. Another Leap component, the fuel injection nozzle shown in Figure 1-1 (b), is the first AM component used in a commercial jet engine [2], and very recently the Federal Aviation Administration (FAA) approved the first AM airframe component

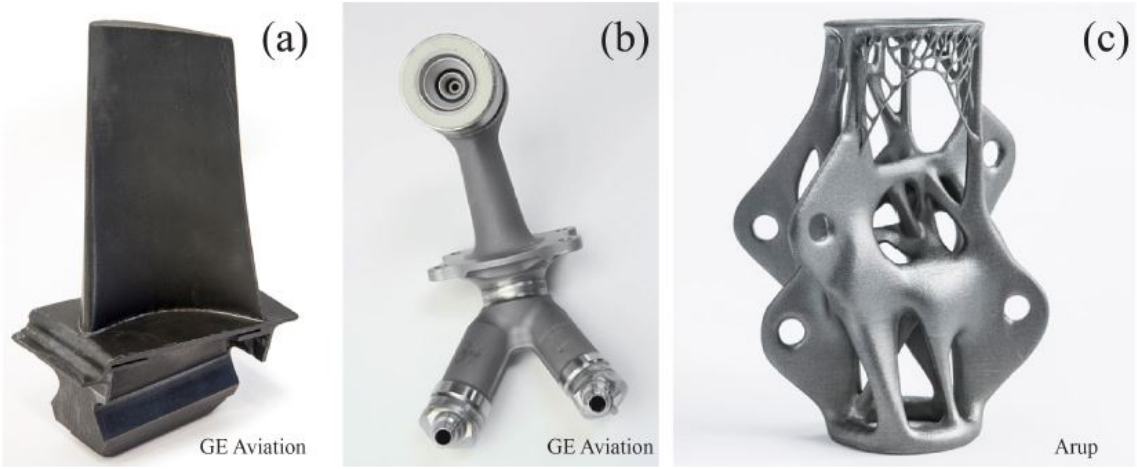

Figure 1-1: Examples of increasing complexity in engineering systems. (a) prototype jet engine turbine blade made from CMC, (b) fuel injection nozzle and first AM component used in commercial jet engine, (c) AM structural node designed via a topology optimization algorithm.

for commercial use [3]. With AM removing the cost barrier associated with high-complexity parts, engineers are beginning to use advanced optimization routines to explore the space of potential geometries [4]. The additively manufactured structural node shown in Figure 1-1 (c) was designed with topology optimization [5].

There is also a growing need for engineering systems to operate in extreme conditions. The global market's increasing energy demand is out-pacing the production capability of conventional, relatively easy to reach oil fields. This demand must be met in part by increased extraction from more difficult to reach locations such as oil deposits under the sea bed and natural gas trapped in shale. The amount of oil coming from deep-sea drilling operations, which stagnated when oil prices fell in 2014, is beginning to rise again [6], and will include exploration further north into the Arctic Ocean, for example into the Barents Sea [7]. The challenges of deep-sea drilling extend beyond the extreme pressures and relative inaccessibility of the sea bed and potentially extreme weather conditions at the surface. The sea floor can also be composed of highly permeable rocks where the bore pressure is close to the fracture pressure of the surrounding material [8]. Extraction of natural gas from shale via horizontal drilling and hydraulic fracturing [9] has exploded in the United States,

which began producing more natural than crude oil in 1995 and became a net exporter of refined petroleum products in 2010 as a result [10]. In addition to extreme operating pressures and temperatures, the extracted product is highly corrosive to the carbon steel pipelines used for its transportation. Failure of such systems can be catastrophic, as evidenced by the 2010 off-shore oil spill in the Gulf of Mexico which incurred an estimated cost of tens of billions USD [11]. Therefore, effective life-cycle management strategies are vital to ensure the safe and cost-effective operation of these complex systems.

The fundamental problem which must be solved in order to facilitate safe and efficient life-cycle management of engineering systems is to establish sufficient capabilities to detect and monitor damage. The scheduling of inspections is typically guided by the principle of damage tolerance [12], in which engineers assume the existence of flaws which are just below the detection threshold of the relevant inspection technique, calculate the time that the component can be safely used before such flaws could cause failure, and schedule inspections at intervals shorter than the calculated time to failure. In principle this will allow damaged or fatigued components to be replaced well before they pose a significant risk of causing catastrophic failure. The accuracy and coverage of the inspection techniques used is therefore vital to safe operation by ensuring that dangerous defects are not left undiscovered, and the sensitivity of the inspection is crucial in the efficient operation of the system, as sensitivity to more subtle damage increases the projected time to failure and therefore reduces the required inspection frequency.

In situations where accuracy of defect characterization is critical and/or accessibility for inspection is limited then NDT monitoring techniques using permanently installed sensors may be more suitable than inspection. Permanent installation of sensors can remove some of the obstacles associated with accessibility, for example when sensors are mounted underneath insulation thereby alleviating the need to remove it before an inspection. Another benefit is the removal of uncertainty in sensor position, orientation and contact, leading to more stable and repeatable measurements that allow greater accuracy in measuring the rate at which defects are developing.

This integration of NDT technology within a structure is known as structural health monitoring (SHM) [13]. A significant challenge for SHM is to decouple changes in the measurement caused by defects in the material from changes in the measurement caused by environmental changes such as temperature fluctuations and degradation of the sensor. Currently used industrial applications of SHM include attached optical fibers which measure strain in aircraft [14, 15] and civil engineering structures [16], and permanently installed ultrasonic sensors which continuously measure the pipe wall thickness of oil pipelines directly under the transducer [17].

There are a great variety of non-destructive testing (NDT) techniques currently in use in industry. This variety has arisen at least in part due to the huge diversity in the defects which must be detected and monitored, including mechanical flaws such as porosity, cracks, and disbondments, as well as degradation of material properties such creep and fatigue damage. Furthermore the location of the defect, whether it penetrates or is close to the specimen surface, how large the defect is, all must be considered when determining if a given NDE technique is suitable for a given application. The most commonly used methods in industry can be broadly grouped into five categories according to their underlying physical principals: liquid penetrant, eddy current, magnetic particles, radiographic, and ultrasonic. Newer applications such as thermo-graphic, laser, and electric potential drop techniques are also starting to see use [18]. The increasing need to inspect complex components and provide SHM solutions significantly constrains the field of potential techniques for new applications, as only liquid penetrant and radiographic techniques can handle geometrical complexity with relative ease, while ultrasound is best suited to permanent installation in SHM applications. As liquid penetrants are limited to surface breaking flaws, we will now shift our focus to radiographic and ultrasonic techniques.

Radiography consists of passing high energy photons through the component to a detector which measures the location and energy density of the radiation. While passing through the material the radiation attenuates at a rate which is dependent on the material's atomic properties and density, therefore changes in density throughout the specimen will produce contrast in the image [18]. Traditional radiography is

performed with a film placed behind the specimen which is then developed in much the same way as a photograph. Detectors which acquire a digital measurement of the transmitted radiation amplitude are gaining in popularity, but much industrial inspection is still performed with film. More advanced radiographic techniques such as X-Ray computer aided tomography (CT) [19] combine radiographic projections from multiple angles into a volumetric map of material density. The radiation used does not experience significant refraction or diffraction in typical engineering materials, therefore parts with complicated geometry can be inspected with little difficulty. While radiographic testing is incredibly effective at detecting changes in material density throughout the thickness of complex specimen, defects which do not introduce changes in density such as closed cracks remain elusive. Materials which have a high average atomic number such as nickel-based alloys can be highly attenuative, requiring higher energy levels for inspection. Furthermore, the inherent costs and dangers of working with radiation limit the extent to which these inspections are available.

Ultrasonic inspection consists of the creation of elastic waves which propagate on the surface and/or in the interior of a specimen and recording either the reflected or transmitted waves. Information about the presence and characteristics of flaws, or the degradation of the material properties, can then the gained through interpretation of the recorded signals. Due to the numerous types of waves that can be excited across a wide range of frequencies, there are a tremendous variety of ultrasonic inspection techniques [20]. The hardware required to transmit and record ultrasonic signals can be relatively light-weight, compact, and does not pose any overt safety hazards which makes ultrasound attractive for SHM applications. In contrast with radiography, ultrasonic techniques are more strongly affected by material and geometric complexity. Refraction and diffraction effects occur at material inhomogeneities, multiple reflections can occur at the interfaces between materials, and anisotropy caused by, for example, preferential grain orientations in austenitic welds or fibers in fiber reinforced composite materials, can affect the energy propagation within the specimen. Because of this, adapting existing ultrasonic inspection techniques to specimens with complex geometry remains an open challenge. However, if this complexity can be ad-

dressed then the strong interaction of ultrasonic waves with the specimen can allow for measurements which are sensitive to subtle defects such as closed cracks which remain elusive to radiographic techniques.

1.2 Objective

The fundamental hypothesis of this thesis is that many of the challenges in inspection and SHM which are being brought about by the need for increased system complexity and better life cycle management tools can be addressed by combining ultrasonics with array technology and advanced modeling and imaging techniques.

The array technology which will be employed in this thesis is a continuation of decades worth of research which includes the use of antennae arrays to increase the gain of radio signals [21], arrangement of seismometers in geophysical exploration [22] and ultrasonic phased array probes which have long been used in medical imaging [23]. The use of array measurements allows for directional information to be encoded in the recorded wave field and allows greater control over the shape of transmitted energy. Unlike radar or medical applications where strong refraction effects are not encountered, geophysical exploration and industrial NDE must deal with large velocity contrasts. Extensive research has been conducted in the context of geophysics into imaging techniques which can account for such effects, and the application of these techniques to industrial inspections is justified as the problem domains are very similar, differing mainly in the scale of the inspection area and the frequency of the elastic waves used for inspection. At the core of these imaging techniques is a sophisticated understanding of the manner in which ultrasonic energy interacts with matter. This understanding is encoded in a simplified model of elastic wavefront propagation developed in the context of geophysics and utilized here in this work in the context of industrial NDE inspections. This marriage of array technology with advanced imaging techniques will be used to address the issue of specimen complexity while bringing the versatility and sensitivity of ultrasonic measurement to bear on relevant inspection and monitoring applications.

This thesis will address a range of applications which include inspection with portable phased array systems and monitoring with permanently installed sensors. The applications considered will span various industries, including aerospace component inspection and oil and gas structural health monitoring. Various array configurations will be utilized for the different applications, including configurations which utilize reflected signals and signals which have been transmitted through the test piece. The inspection of various materials will also be considered, including polymer matrix composites and metals. Finally, the detection of various types of defects will be studied.

1.3 Outline

This thesis is divided into chapters which will be for the most part self-contained discussions of each application considered.

Chapter 2 develops the theoretical background for the wave propagation model used in this thesis. The numerical methods used to efficiently implement this model will also be described.

Chapter 3 introduces a phased array measurement technique designed to detect ply waviness and other defects in composite laminate specimens. The technique utilizes two linear arrays in a yoke configuration which allows for reflection and transmission measurements. The setup is submerged in water to provide coupling, and focal laws which correct for refraction at the specimen boundary as well as anisotropy within the specimen are developed. Experimental results from a variety of samples demonstrate the technique's sensitivity to porosity and ply waviness.

Chapter 4 investigates the challenges associated with ultrasonically inspecting parts with high shape complexity and multiple interfaces, specifically in samples with rich internal structure such as impellers which have an internal network of vanes. A technique for encasing the specimen in ice in order to reduce the impedance mismatch between the coupling medium and the sample, thereby allowing more energy to penetrate the specimen, is introduced. Focal laws are applied which account for multiple

interfaces by utilizing a known model of the sample geometry and using the methods described in chapter 2 to numerically model wave propagation in the sample. The technique is experimentally verified on an aluminum fixture with multiple interfaces and side-drilled hole (SDH) defects, and additively manufactured Ti64 samples.

Chapter 5 performs an initial investigation into the use of matrix arrays to account for 3-D curvature in specimen geometry. Various measurements are taken on a cylindrical sample with a conical inner surface. Fully 3-D focal laws are developed to account for the distortion that the out of plane curvature causes to the wavefront. The results obtained with a matrix array are compared to those obtained with a linear array to demonstrate the effectiveness of matrix arrays to account for fully 3-D specimen geometry.

Chapter 6 presents a novel forward model which efficiently describes key aspects of the propagation of guided waves through curved pipes. This model is intended to facilitate tomographic wall-thickness mapping through a region of pipeline bordered by two ring-arrays of transducers, where the region of pipe in question may contain curvature. The model is numerically verified with finite element simulation, and initial experimental verification is performed on a stainless steel pipe which contains a 90° bend, but which does not contain a defect.

Chapter 7 focuses on further experimental validation of the forward model introduced in Chapter 5 through the introduction of realistic corrosion defects. The method of impressed currents is explained and used to introduce areas of accelerated corrosion into key locations on the pipe. A laser scanning system is then used to map the depth profile of the defects, and the forward model introduced in Chapter 5 is used to predict how guided waves will interact with the defects. These predictions are compared to measurement showing good agreement.

Chapter 8 introduces a tomography algorithm which utilizes the forward model introduced in Chapter 5 and experimentally verified in Chapter 6. The sensitivity of the algorithm to defect growth is evaluated numerically and experimentally for several locations around the bend, revealing that the pair of ring-arrays achieve poor sensitivity to defects on the outside of the bend. An alternative array configuration is

introduced and evaluated and is shown to have more uniform sensitivity with respect to defect location.

Chapter 9 will summarize the main results of this thesis and discuss the potential for future research.

Chapter 2

Theoretical background: Elliptically anisotropic wavefronts

Throughout this thesis a simplified elliptical model of anisotropy will be employed. This chapter will provide the theoretical background for generally anisotropic elastic wavefront propagation, describe the theoretical motivation for and derivation of elliptical anisotropy, and finally discuss the numerical methods used to model the elliptically anisotropic wavefronts. The derivations presented here largely follow the work of Gassmann et al. in [24]. Let $\mathbf{e}_1, \mathbf{e}_2$ and $\mathbf{e}_3$ denote an orthogonal basis for $\mathbb{R}^3$, and let t denote time. We begin with the equations of motion for particle displacement,

$$\rho \frac{\partial^2 u_i}{\partial t^2} = \sum_j \frac{\partial \sigma_{ij}}{\partial x_j}, \tag{2.1}$$

where $i, j = 1..3$, ρ is material density, u_i is the value of particle displacement along axis $\mathbf{e}_i$, and σ is the second-order stress tensor, where σ_{ij} denotes the component of stress acting along axis $\mathbf{e}_i$ on a surface whose normal points in the $\mathbf{e}_j$ direction. We assume that the particle displacements are small, and therefore the constitutive

equation can be expressed as

$$\sigma_{ij} = \sum_{j,h} C_{ijhk}\varepsilon_{hk}, \tag{2.2}$$

where $\varepsilon_{hk} = \frac{1}{2}\left(\frac{\partial u_h}{\partial x_k} + \frac{\partial u_k}{\partial x_h}\right)$ are the components of the second-order strain tensor, and C is a fourth-order tensor containing the material stiffness constants. Combining Equation 2.1 and Equation 2.2 yields the elasto-dynamic equation which describes elastic wave propagation

$$\sum_k \left(\sum_{j,h} C_{ijhk}\frac{\partial^2}{\partial x_j \partial x_h} - \delta_{ik}\rho\frac{\partial^2}{\partial t^2}\right) u_k + \sum_{k,h}\left(\sum_j \frac{\partial C_{ijhk}}{\partial x_j}\right)\frac{\partial u_k}{\partial x_h} = 0. \tag{2.3}$$

2.1 Wavefronts

The majority of imaging methods discussed in this thesis are based on the propagation of wavefronts, or the manner in which a perturbation in the displacement spreads out in time from some source. Assume that such a perturbation has occurred in some domain, and that there are perturbed and unperturbed displacement solutions, $\tilde{\mathbf{u}}$ and $\bar{\mathbf{u}}$, which are valid on sub-domains $\tilde{B}_t$ and $\bar{B}_t$ at any given time t, as shown in Figure 2-1 (a). Further assume that the intersection of these domains forms a surface in $\mathbb{R}^3$, $F_t = \tilde{B}_t \cap \bar{B}_t$, that F_t is continuous and differentiable, and that the two displacement solutions satisfy the following conditions on F_t for $j, k = 1, 2$ or 3:

$$\begin{aligned} \tilde{u}_k &= \bar{u}_k, \\ \frac{\partial \tilde{u}_k}{\partial x_j} &= \frac{\partial \bar{u}_k}{\partial x_j} \quad \text{and} \\ \frac{\partial \tilde{u}_k}{\partial t} &= \frac{\partial \bar{u}_k}{\partial t}. \end{aligned} \tag{2.4}$$

The surface F_t is the wavefront at time t, alternatively referred to as the front hereafter.

To determine how the front evolves with time we define the wavefront traveltime function $\tau : \mathbb{R}^3 \to \mathbb{R}$ such that the front at time t is given by the level set $\tau =$

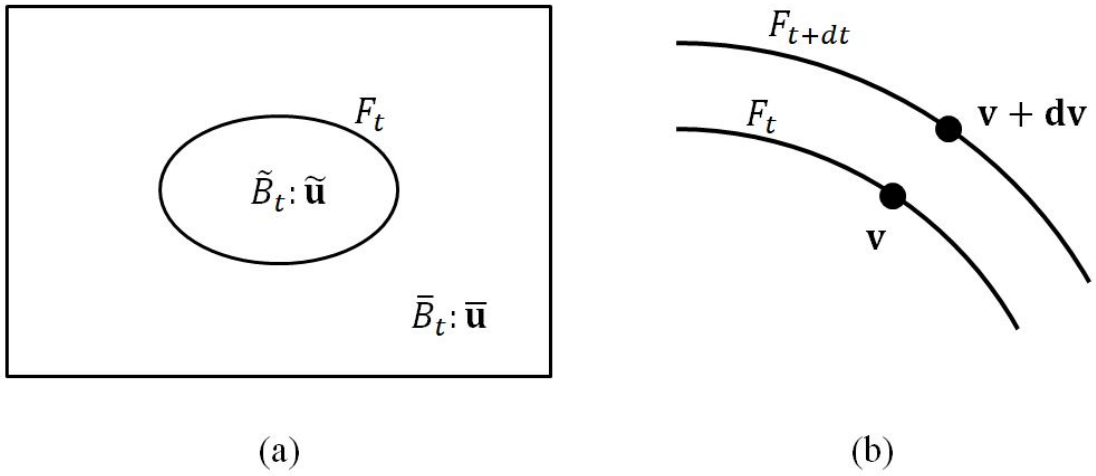

Figure 2-1: (a) Diagram of evolving wavefront. At time t, perturbed $\tilde{\mathbf{u}}$ and unperturbed $\bar{\mathbf{u}}$ displacement solutions are valid on domains $\tilde{B}_t$ and $\bar{B}_t$, respectively. The intersection of the two domains forms a surface F_t along which the displacement solutions are continuous and their first derivatives are equal. (b) Schematic showing a point $\mathbf{v}$ on the wavefront at time t and a point $\mathbf{v} + \mathbf{dv}$ which is along the wavefront a short time later at $t + dt$.

t. We will now derive the eikonal equations which are first-order non-linear partial differential equations for τ, and which describe the propagation of fronts in an elastic material. We begin by plugging the two displacement solutions into Equation 2.3 and subtracting, which leads to

$$\sum_k \left(\sum_{j,h} K_{ijhk} \Delta^k_{jh} - \delta_{ik} \Delta^k_{tt} \right) = 0 \tag{2.5}$$

where $K_{ijhk} = C_{ijhk}/\rho$, and

$$\begin{aligned} \Delta^k_{jh} &= \frac{\partial^2 \tilde{u}_k}{\partial x_j \partial x_h} - \frac{\partial^2 \bar{u}_k}{\partial x_j \partial x_h} \\ \Delta^k_{tt} &= \frac{\partial^2 \tilde{u}_k}{\partial t^2} - \frac{\partial^2 \bar{u}_k}{\partial t^2}. \end{aligned} \tag{2.6}$$

Note that we have not assumed that the material is homogeneous; the terms involving the spatial derivatives of the stiffness constants cancel during subtraction. A relationship between the discontinuities in the spatial and temporal second derivatives of

displacement, Δ^k_{jh} and Δ^k_{tt}, can be derived by considering that the first derivatives of the two displacement solutions with respect to space and time must remain equal as the wavefront evolves. For a given point $\mathbf{v} \in \mathbb{R}^3$ the front passes through $\mathbf{v}$ at time $\tau(\mathbf{v})$. Consider a small change in time dt and a point $\mathbf{v} + \mathbf{dv}$ which belongs to the evolved front F_{t+dt}, as shown in Figure 2-1 (b). The front passes through $\mathbf{v} + \mathbf{dv}$ at time $\tau(\mathbf{v} + \mathbf{dv}) = \tau(\mathbf{v}) + dt$. The change in time can be linearized as $dt \approx \sum_h \frac{\partial \tau}{\partial x_h} dv_h$. For the points $\mathbf{v} + \mathbf{dv}$ on the front F_{t+dt} which are close to $\mathbf{v}$, the change in the first derivatives of displacement can be linearized as

$$\begin{aligned} \left.\frac{\partial u_k}{\partial x_j}\right|_{\mathbf{v}+\mathbf{dv}} &\approx \left.\frac{\partial u_k}{\partial x_j}\right|_{\mathbf{v}} + \sum_h \frac{\partial^2 u_k}{\partial x_j \partial x_h} dv_h + \frac{\partial^2 u_k}{\partial x_j \partial t} dt \\ \left.\frac{\partial u_k}{\partial t}\right|_{\mathbf{v}+\mathbf{dv}} &\approx \left.\frac{\partial u_k}{\partial t}\right|_{\mathbf{v}} + \sum_h \frac{\partial^2 u_k}{\partial x_h \partial t} dv_h + \frac{\partial^2 u_k}{\partial t^2} dt. \end{aligned} \tag{2.7}$$

Requiring that $\partial \tilde{u}_k / \partial x_j|_{\mathbf{v}+\mathbf{dv}} = \partial \bar{u}_k / \partial x_j|_{\mathbf{v}+\mathbf{dv}}$, $\partial \tilde{u}_k / \partial t|_{\mathbf{v}+\mathbf{dv}} = \partial \bar{u}_k / \partial t|_{\mathbf{v}+\mathbf{dv}}$ and performing some manipulation leads to the desired relation $\Delta^k_{jh} = \Delta^k_{tt} \tau_j \tau_h$, where $\tau_i = \partial \tau / \partial x_i$. Upon substitution into Equation 2.5 this relation yields

$$\sum_k \left(\sum_{j,h} K_{ijhk} \tau_j \tau_h - \delta_{ik} \right) \Delta^k_{tt} = 0, \tag{2.8}$$

which can be expressed in matrix form by utilizing symmetries in the stiffness tensor (i.e. $C_{ijhk} = C_{hkij}$) as

$$\begin{bmatrix} Q_{11} - 1 & Q_{12} & Q_{13} \\ Q_{12} & Q_{22} - 1 & Q_{23} \\ Q_{13} & Q_{23} & Q_{33} - 1 \end{bmatrix} \begin{bmatrix} \Delta^1_{tt} \\ \Delta^2_{tt} \\ \Delta^3_{tt} \end{bmatrix} = 0, \quad Q_{ik} = \sum_{j,h} K_{ijhk} \tau_j \tau_h. \tag{2.9}$$

When the particle acceleration is not continuous along the front, Equation 2.9 will only have a solution when the determinant of the left-hand side (LHS) matrix is zero. This will in general lead to three first-order, non-linear partial differential equations for τ corresponding to the three types of wavefronts that may propagate in anisotropic elastic material: quasi pressure (qP), quasi shear-vertical (qSV) and

quasi shear-horizontal (qSH), where here the quasi qualifier indicates that the polarization direction is not necessarily parallel or orthogonal to the wave vectors, see for example [25].

2.2 Elliptical anisotropy

Two types of anisotropy that are commonly encountered [26] are orthotropy, as in the case of shale with vertical fractures and the effective properties of composite laminate materials; and transverse isotropy, which is encountered in horizontal layers of sediment and composite laminate materials with uniaxial fiber orientation. Elliptical anisotropy is a special case of transverse isotropy which is commonly used as an approximation to more complex forms of anisotropy. Orthotropy occurs when the material stiffness tensor exhibits mirror symmetry along three orthogonal planes, which reduces the number of independent stiffness constants to eight. The eikonal equations under orthotropy are up to sixth degree polynomial functions of the first derivatives of τ. In the case of transverse isotropy (TI), the stiffness tensor exhibits mirror symmetry about one plane and rotational symmetry about the axis orthogonal to that plane, reducing the number of independent stiffness constants to five. TI eikonal equations can be up to fourth degree polynomial functions of the first derivatives of τ. Elliptical anisotropy occurs when an additional constraint is placed on transversely isotropic material which results in the eikonal equations being reduced to second degree polynomial functions of the first derivatives of τ.

Consider a homogeneous, transversely isotropic material in which the axis of rotational symmetry is in the $\mathbf{e}_3$ direction; a condition referred to as vertical transverse isotropy (VTI). The constitutive equations in VTI material can be expressed in sim-

plified matrix form as

$$\begin{bmatrix} \sigma_1 \\ \sigma_2 \\ \sigma_3 \\ \sigma_4 \\ \sigma_5 \\ \sigma_6 \end{bmatrix} = \begin{bmatrix} C_{11} & C_{12} & C_{13} & 0 & 0 & 0 \\ C_{12} & C_{11} & C_{13} & 0 & 0 & 0 \\ C_{13} & C_{13} & C_{33} & 0 & 0 & 0 \\ 0 & 0 & 0 & C_{55} & 0 & 0 \\ 0 & 0 & 0 & 0 & C_{55} & 0 \\ 0 & 0 & 0 & 0 & 0 & C_{66} \end{bmatrix} \begin{bmatrix} \varepsilon_1 \\ \varepsilon_2 \\ \varepsilon_3 \\ \varepsilon_4 \\ \varepsilon_5 \\ \varepsilon_6 \end{bmatrix}, \tag{2.10}$$

using the familiar Voigt notation and engineering strain and with $C_{66} = \frac{1}{2}(C_{11} - C_{12})$. From Equation 2.9 we obtain

$$\begin{aligned} Q_{11} &= K_{11}\tau_1^2 + K_{66}\tau_2^2 + K_{55}\tau_3^2 \\ Q_{22} &= K_{66}\tau_1^2 + K_{11}\tau_2^2 + K_{55}\tau_3^2 \\ Q_{33} &= K_{55}\left(\tau_1^2 + \tau_2^2\right) + K_{33}\tau_3^2 \\ Q_{12} &= \left(K_{11} - K_{66}\right)\tau_1\tau_2 \\ Q_{13} &= \left(K_{13} + K_{55}\right)\tau_1\tau_3 \\ Q_{23} &= \left(K_{13} + K_{55}\right)\tau_2\tau_3 \end{aligned}$$

where $K_{ij} = C_{ij}/\rho$. The determinant of the matrix in the LHS of Equation 2.9 then vanishes when one of the following three conditions are met, where each condition corresponds to a wave type:

$$\begin{aligned} 1 &= \frac{Q_S + Q_D}{2}, \quad \text{(qP)} \\ 1 &= \frac{Q_S - Q_D}{2}, \quad \text{(qSV)} \\ 1 &= K_{66}\tau_r^2 + K_{55}\tau_z^2, \quad \text{(qSH)} \end{aligned} \tag{2.11}$$

where

$$\begin{aligned}
\tau_r &= \sqrt{\tau_1^2 + \tau_2^2}, \\
\tau_z &= \tau_3, \\
Q_S &= (K_{11} + K_{55})\,\tau_r^2 + (K_{33} + K_{55})\,\tau_z^2 \quad \text{and} \\
Q_D &= \sqrt{\left[(K_{11} - K_{55})\,\tau_r^2 - (K_{33} - K_{55})\,\tau_z^2\right]^2 + 4\,(K_{13} + K_{55})^2\,\tau_r^2\tau_z^2}.
\end{aligned}$$

One can see that the equations for the qP and qSV fronts are indeed fourth-degree polynomials of the first derivatives of τ, and second-degree in the case of qSH waves. Elliptical anisotropy is the result of applying the additional constraint

$$(C_{13} + C_{55})^2 = (C_{11} - C_{55})\,(C_{33} - C_{55}) \tag{2.12}$$

which simplifies the expression for Q_D and reduces the qP and qSV eikonal equations to second-degree polynomial functions, with the elliptically anisotropic eikonal equations for qP and qSV wavefront propagation given as

$$\begin{aligned}
K_{11}\left(\left(\frac{\partial\tau}{\partial x_1}\right)^2 + \left(\frac{\partial\tau}{\partial x_2}\right)^2\right) + K_{33}\left(\frac{\partial\tau}{\partial x_3}\right)^2 &= 1 \quad \text{(qP)} \\
K_{55}\left(\left(\frac{\partial\tau}{\partial x_1}\right)^2 + \left(\frac{\partial\tau}{\partial x_2}\right)^2 + \left(\frac{\partial\tau}{\partial x_3}\right)^2\right) &= 1 \quad \text{(qSV)}
\end{aligned} \tag{2.13}$$

with no change in the qSH eikonal equation given in Equation 2.11. This reduction in polynomial degree significantly simplifies the task of numerically computing wavefront traveltimes in elliptically anisotropic media. The name elliptical anisotropy comes from the fact that the qP group velocity as a function of propagation direction forms an ellipsoid of revolution in such materials.

The concepts of phase velocity and group velocity can be defined by considering the propagation of the front in two directions; normal to the front in the case of phase velocity, and along the direction of energy propagation in the case of group velocity. For elliptical anisotropy specifically, qSV and qSH propagation is not direction dependent

so the focus will now shift exclusively to qP wavefront propagation. The wavefront traveltime function τ will be assumed to refer exclusively to the qP wavefront from this point. The phase velocity vector $\mathbf{V}$ is given simply as

$$\mathbf{V} = \frac{\nabla\tau}{||\nabla\tau||^2}. \tag{2.14}$$

We may define θ as the angle between the phase velocity vector and the x_3 axis, as shown in Figure 2-2, which allows Equation 2.13 to be expressed in terms of phase velocity magnitude V, which is now a function of θ, as

$$V(\theta)^2 = K_{11}\sin^2\theta + K_{33}\cos^2\theta. \tag{2.15}$$

The direction of energy propagation corresponds to the characteristic curves of the eikonal equations, which are often referred to as the rays. The characteristics for a fully non-linear, first-order partial differential equation can be obtained from the Charpit equations [27], which, when applied to Equation 2.13, yield expressions for the group propagation angle θ_g and velocity V_g

$$\begin{aligned} \tan^2\theta_g &= \frac{K_{11}}{K_{33}}\tan^2\theta \\ V_g(\theta_g)^2 &= \frac{K_{11}K_{33}}{K_{11}\cos^2\theta_g + K_{33}\sin^2\theta_g}. \end{aligned} \tag{2.16}$$

The expression for V_g in Equation 2.16 is the equation of an ellipse in polar coordinates with radii $\sqrt{K_{11}}$ and $\sqrt{K_{33}}$. It is also worth noting that in the isotropic case the characteristic curves are normal to the fronts, therefore the phase and group velocities are equivalent in isotropic materials.

2.3 Numerical solutions

A considerable amount of research into numerical solutions of the eikonal equation has been conducted, with a particular focus on the isotropic version of Equation 2.13,

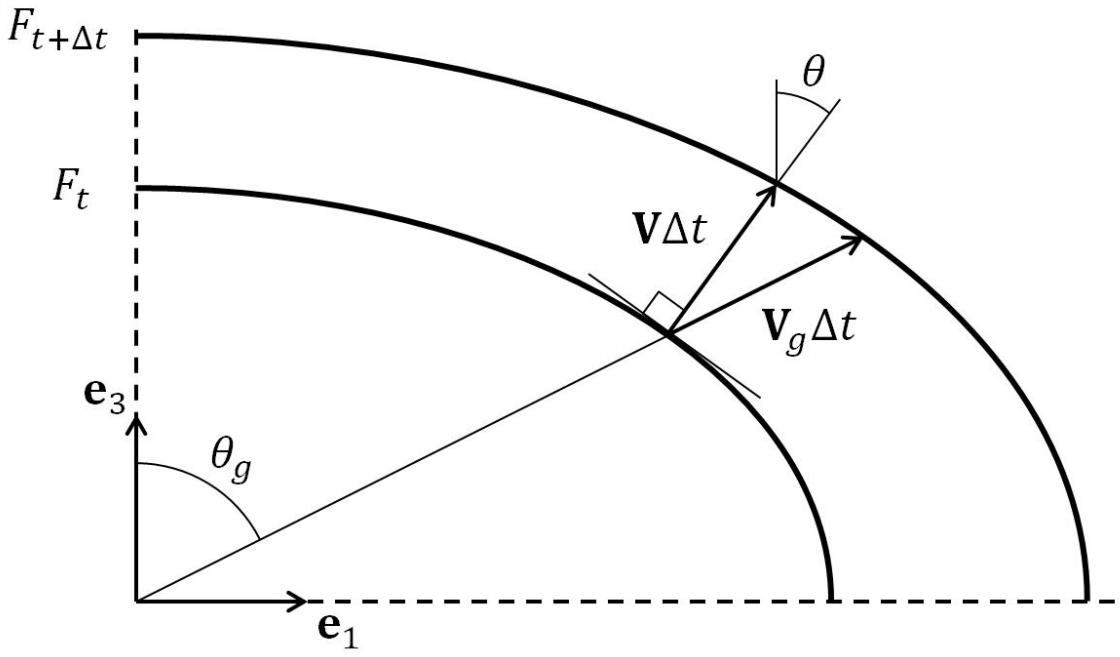

Figure 2-2: Example of relationship between phase and group velocity vectors. A homogeneous, elliptically anisotropic medium is considered. The location of an elastic qP wavefront spreading from a point source at the origin is shown at times t and $t + \Delta t$. The phase velocity vector $\mathbf{V}$ is normal to the front while the group velocity vector $\mathbf{V}_g$ is in the direction of energy propagation, which in this example is in straight lines from the origin. When the velocity vectors are scaled by a factor of Δt, the vector $\mathbf{V}_g\Delta t$ exactly spans the distance between the two wavefronts, while $\mathbf{V}\Delta t$ approximately spans this distance given that Δt is small. The angles that the phase and group velocity vectors make with the $\mathbf{e}_3$ axes are shown as θ and θ_g, respectively.

here given as

$$\left(\frac{\partial\tau}{\partial x_1}\right)^2 + \left(\frac{\partial\tau}{\partial x_2}\right)^2 + \left(\frac{\partial\tau}{\partial x_3}\right)^2 = \frac{1}{c^2} \tag{2.17}$$

with c being the isotropic wave velocity. The two main approaches are based on the application of Fermat's and Huygen's principles to network and graph theory according to the shortest-path ray (SPR) method [28] or by solving the eikonal equation directly over a regular grid of points using the finite difference method [29] or the fast marching method (FMM) [30]; the FMM is preferred to the finite difference method because the latter can violate causality [31]. SPR and FMM both begin with a start location and incrementally expand the solution in order of increasing travel-

time, or expanding wavefront making use of efficient heap sorting algorithms to attain $O(n \log n)$ complexity, where n is the number of unknowns. Because FMM attempts to solve the eikonal equation, implementation of anisotropy requires modifying the differential equation and the finite difference scheme. On the other hand, SPR directly operates on the rays, which makes implementation of the angular dependence of the velocity straightforward [32]. The drawback of SPR compared to FMM however is that additional nodes are required to allow for a sufficient angular diversity in the rays, as in [33], whereas FMM can operate over a regular grid with similar accuracy. Both SPR and FMM are utilized at various points in this thesis.

2.3.1 Shortest path method

The key idea behind the SPR method is that the propagation medium can be represented by a network of nodes which are connected based on a graph template. The domain is first divided in regular, discrete grid of rectangular elements each containing a fixed number of nodes around their boundary. In general, a single edge can span nodes across multiple elements; however, in this work the nodes are defined such that all edges are contained inside a single element according to [33]. An example of the node placement with five nodes per edge can be seen in Figure 2-3 (a). The edges of the graph are then defined as the straight lines connecting any two nodes which border a single element without being on the same side of the element. The edges adjacent to a single node can be seen in Figure 2-3 (b), and the complete set of edges contained inside a single element can be seen in Figure 2-3 (c). Additionally, nodes may be inserted anywhere inside the element to more accurately represent the locations of the source and receivers. The edges connecting these nodes would then be the straight line paths to the nodes bordering the element which the source / receiver node is placed inside.

Connected sequences of edges running from a node placed at the source location to a node placed at the receiver location lead to multiple geometrical paths. To determine the geometrical path that most closely approximates the true ray, a cost function is defined for each edge of the graph, such that summing the costs along the edges of

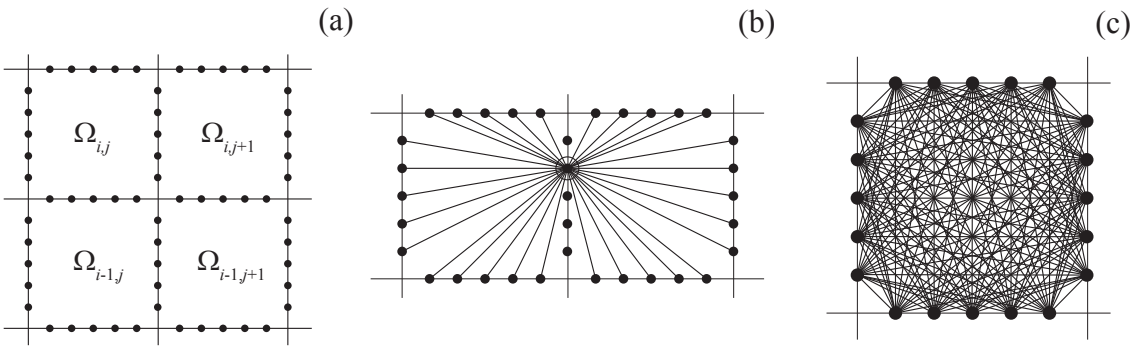

Figure 2-3: Graph templates used in this this to implement the shortest path ray method. (a) Discretization with eight nodes per element side; (b) allowed edges from a source node; (c) all the possible edges inside one element.

each geometrical path will produce a traveltime estimate. The path that leads to the least traveltime is then chosen to be the physical ray. A distinct advantage of SPR is that defining the edge costs to account for anisotropy is relatively simple. For an edge of the graph E which has length $|E|$ and makes an angle θ_E with the x_3 axis, the cost function, $C(E)$, associated with the edge is obtained directly from Equation 2.16, i. e.

$$C(E) = \frac{|E|}{V_g\left(\theta_E\right)}, \tag{2.18}$$

where the relevant material constants associated with the element containing E are used in the calculation of V_g. The minimization of the cost function is achieved using Dijkstra's shortest path algorithm [34] which is an established graph algorithm for complex networks. Dijkstra's algorithm was implemented in C++ using a Fibonacci heap for optimal computational efficiency [35].

2.3.2 Fast marching method

The fast marching method presented by Sethian et al. in [30] divides the domain into three sets as shown in Figure 2-4 (a): one which contains nodes on which a traveltime solution has been finalized, and which must be initialized to contain one or more nodes; one for nodes which have been visited but which have not been finalized, and which can be visualized as points on an advancing front; and one for nodes which

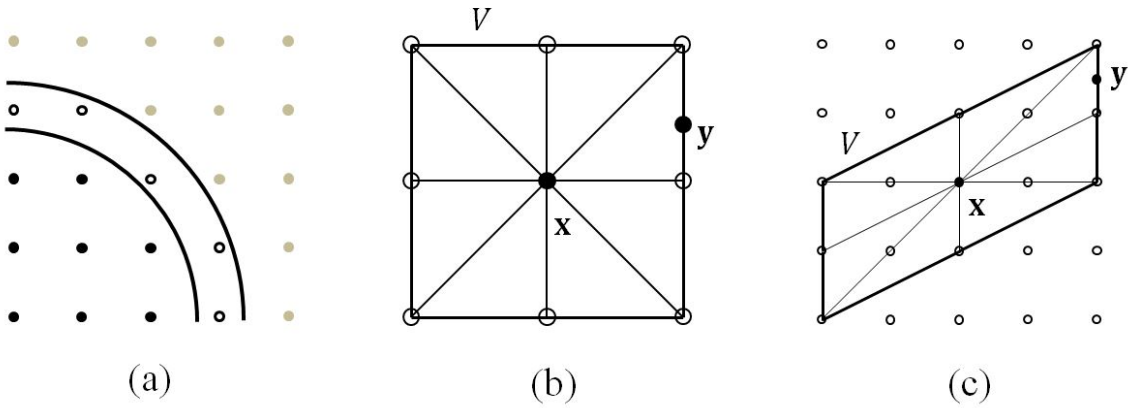

Figure 2-4: (a) Separation of domain containing regular grid points into three sets. Solid black circles signify locations where traveltime solution is finalized. Circles with black outline show locations which have been visited. Light gray circles denote locations which have not been visited yet. (b) Schematic of Cartesian grid point $\mathbf{x}$ and a small mesh V containing $\mathbf{x}$. The point $\mathbf{x}$ and a point $\mathbf{y}$ along the boundary of V serve as inputs to the Hopf-Lax operator described in Equation 2.21. (c) Example of how mesh may deform in order to satisfy the causality condition expressed in Equation 2.22.

have not been touched. The set of nodes which have been visited are stored in a heap, which efficiently keeps track of the node with the smallest traveltime solution as nodes are added and removed. The algorithm operates by repeatedly removing the node with the smallest traveltime solution from the set of visited nodes, placing that node in the finalized set, and visiting (updating the traveltime of and placing in the visited set) any nodes adjacent to that node.

The anisotropic FMM solution used in this thesis is the fast marching method with lattice basis reduction (FMM-LBR) presented in [36]. This method is similar to that described in [30] except that the calculation of traveltimes at each node is based on the Hopf-Lax operator rather than finite difference operators (and is described below), and the set of neighbors for each node are not simply the adjacent grid-points, but are carefully chosen to satisfy a causality condition. In order to more concisely express this solution we will introduce some notation for formulating the problem in terms of Riemannian metrics [37]. Let $\mathcal{M} : \mathbb{R}^3 \to \mathrm{M}^{3\times 3}$ be a continuous function which maps every point of 3-D space to a 3×3 matrix. Furthermore, let $\langle \mathbf{x}, \mathbf{y} \rangle_M = \mathbf{x}^T M \mathbf{y}$ and

$||\mathbf{x}||_M = \sqrt{\langle \mathbf{x}, \mathbf{x} \rangle_M}$ for any two vectors $\mathbf{x}$ and $\mathbf{y}$ in $\mathbb{R}^3$ and any 3×3 matrix M. Then we can say $\langle \cdot, \cdot \rangle_{\mathcal{M}(\mathbf{x})}$ is the metric associated with $\mathcal{M}$, which is Riemannian when the matrix $\mathcal{M}(\mathbf{x})$ is symmetric positive definite for any $\mathbf{x}$. In the case of elliptical anisotropy we can define a suitable metric such that the traveltime along a path $p : [0, 1] \to \mathbb{R}^3$ can be expressed as $\int_0^1 ||p'(s)||_{\mathcal{M}(p(s))} \, ds$. In the case of elliptically anisotropic media where the axis of rotational symmetry is in the $\mathbf{e}_3$ direction and the material stiffness constants are continuous functions of position that metric can be constructed from the function $\mathcal{M}_{\text{vert}}$ given by

$$\mathcal{M}_{\text{vert}}(\mathbf{x}) = \begin{bmatrix} 1/K_{11}(\mathbf{x}) & 0 & 0 \\ 0 & 1/K_{11}(\mathbf{x}) & 0 \\ 0 & 0 & 1/K_{33}(\mathbf{x}) \end{bmatrix}. \tag{2.19}$$

When the direction of the axis of anisotropy is allowed to vary from the $\mathbf{e}_3$ direction, such that the material is rotated according to the 3-D rotation matrix $\mathcal{R}(\mathbf{x})$ at each location $\mathbf{x}$ and the function $\mathcal{R}$ is also continuous, then the metric for the rotated material is given by

$$\mathcal{M}(\mathbf{x}) = \mathcal{R}(\mathbf{x})^T \mathcal{M}_{\text{vert}}(\mathbf{x}) \mathcal{R}(\mathbf{x}). \tag{2.20}$$

The elliptically anisotropic eikonal equation for qP wave propagation can now be expressed equivalently as $||\nabla \tau(\mathbf{x})||_{\mathcal{M}(\mathbf{x})^{-1}} = 1$. The FMM-LBR begins with an initial condition of $\tau = 0$ on some boundary, and expands the solution along a regular grid in order of increasing traveltime. A first-order solution to the eikonal equation can be obtained by utilizing the Hopf-Lax operator $\Lambda(\mathbf{x}, \mathbf{y})$, which is a function of two locations: one being a grid point $\mathbf{x}$, and another being a point $\mathbf{y}$ on the boundary of a mesh $V(\mathbf{x})$ which covers a small neighborhood of $\mathbf{x}$, and which has points in the cartesian grid as vertices, as shown in Figure 2-4 (b). The Hopf-Lax operator is then given as

$$\Lambda(\mathbf{x}, \mathbf{y}) = ||\mathbf{x} - \mathbf{y}||_{\mathcal{M}(\mathbf{x})} + I_V[\tau(\mathbf{y})], \tag{2.21}$$

where $I_V[\tau(\cdot)]$ denotes linear interpolation of the values of τ at neighboring grid points. Setting the values of $\tau(\mathbf{x})$ to minimize $\Lambda(\mathbf{x}, \mathbf{y})$ for all points $\mathbf{y}$ on the boundary of $V(\mathbf{x})$, and updating each grid location in order of increasing travel-time guarantees convergence to a unique and first-order accurate solution for τ on the entire domain [38], given that each mesh $V(\mathbf{x})$ satisfies a causality condition. This condition is that for any two vertices $\mathbf{v}_1$, $\mathbf{v}_2$ of $V(\mathbf{x})$ which share an edge,

$$\langle \mathbf{v}_1 - \mathbf{x}, \mathbf{v}_2 - \mathbf{x} \rangle_{\mathcal{M}(\mathbf{x})} \geq 0. \tag{2.22}$$

A mesh is said to be causality preserving if all vertices satisfy this condition. The FMM-LBR presented in [36] proposes an efficient scheme based on lattice basis reduction for defining a causality preserving mesh for each location $\mathbf{x}$, where each mesh may deform in a manner similar to that shown in Figure 2-4 (c) in order to satisfy the causality condition.

2.4 Conclusions

This chapter has reviewed the theoretical foundations of elastic wavefront propagation in generally anisotropic material, with the wavefront being defined as a discontinuity in material acceleration. The wavefront traveltime function τ has been introduced, along with the eikonal equations which are partial differential equations describing τ. A full derivation of the eikonal equations for VTI media was given, and elliptical anisotropy was defined as a special case of VTI. The concepts of phase velocity and group velocity were explored specifically in the context of elliptically anisotropic material, where the group velocity profile forms an ellipsoid.

Two methods of numerically calculating wavefront traveltimes in elliptically anisotropic media have been discussed. Of the two methods, both have similar (first-order) accuracy. The SPR method has the advantage of being easier to implement; however, the additional nodes included on the edges of each element increase the memory requirements and computation time significantly. The FMM-LBR achieves similar accuracy

with only one node for each element in the SPR calculation, although the implementation is significantly more complex. As a result the SPR was used during the initial stages of this work, and was phased out in favor of FMM-LBR at the later stages.

Chapter 3

Phased array imaging of complex geometry composite components

3.1 Introduction

An interesting example of the necessity for NDT inspection of complex parts is provided by the polymer matrix composite (PMC) fan blades which are beginning to see use in modern turbofan engines. These blades have complex curvature optimized for aerodynamic efficiency and exhibit an intricate microstructure that leads to strongly anisotropic properties. X-ray CT is currently used to detect porosity damage; however, it has poor sensitivity to defects such as waviness in the plies due to their much lower density contrast. Therefore, X-ray CT is complemented by ultrasonic spot through-transmission measurements which can detect wrinkles in the lamina since the wrinkles cause a loss of transmission amplitude. However, the X-ray CT inspection is expensive and time-consuming, and the ultrasonic spot measurements have poor coverage and are highly dependent on operator skill.

Inspection with linear arrays of ultrasonic transducers is an attractive alternative which can potentially provide good sensitivity to delaminations and porosity as well as lamina waviness in components with complex geometry. Linear arrays have long been used in medical imaging [39], and have been extensively studied for use in NDE applications, where parallel transmission allows for the transmitted wave to be focused

or steered without the need for replacing probes. Over the last decade, the increasing speed of computers and electronic systems has made the acquisition of full matrix capture (FMC) datasets and the real-time implementation of beamforming methods such as the Total Focusing Method possible [40]. More recently, the formation of phased array images through complex interfaces is a subject that has attracted significant attention. For instances in which the interface geometry and position relative to the probe is known, and in which the material is homogeneous, ray-shooting methods can be used to efficiently develop appropriate delay laws for focusing inside the material [41]. Where the interface geometry and position is not known beforehand, adaptive techniques have been developed to allow for reconstruction of the interface using ultrasonic data [41, 42, 43, 44]. Furthermore, some novel techniques have been developed which do not require explicitly accounting for refraction [43], [45]. Techniques for developing delay laws which account for anisotropy have been previously developed in applications such as phased array imaging of austenitic welds [46, 47] and for composite laminates [48, 49]. In the case where the anisotropic material is homogeneous, if the probe is in contact then a measured velocity profile within the material can be used to directly calculate the delay laws, or if there is liquid coupling between the probe and the specimen, then ray-shooting methods which satisfy Fermat's principle can be used to account for refraction. Work has also been done on detecting waviness in composite laminate materials using contact phased array reflection measurements [50]. Curvature in the laminate further complicates the problem, as the anisotropic properties are no longer homogeneous since the orientation of the material is changing throughout the specimen. Such inhomogeneity can be handled by approaches which operate over discretized domains such as the SPR and FMM discussed in Section 2.3.

All of the work previously mentioned regarding the use of phased array imaging for NDE applications has considered the use of linear arrays in reflection. Due to the low contrast nature of waviness defects, the backscattered information from these defects is quite weak. In this work, we explore the use of phased array imaging in transmission, where changes in traveltime and attenuation caused by the waviness can

be detected with higher sensitivity than with conventional backscattering imaging. We propose an inspection configuration consisting of two linear arrays situated on either side of a specimen and coupled via a liquid medium. The arrays simultaneously obtain reflection and transmission data, where the back-scattered data provides good sensitivity to delaminations and porosity in the material and the transmitted signals provide sensitivity to ply waviness.

Section 3.2 will justify use of the elliptically anisotropic model of wavefront propagation for the calculation of focal laws in the anisotropic material. This simplification will reduce the need for detailed knowledge of the material properties and to allow for efficient calculation. This section will also describe the interface reconstruction and imaging algorithms. Section 3.3 will describe the experimental setup and introduces a range of Plexiglas and polymer matrix composite specimens used to experimentally validate the imaging technique. The imaging algorithm will be applied to experimental data to demonstrate sensitivity on samples with known porosity and waviness defects in Section 3.4. Conclusions will be given in Section 3.5.

3.2 Methods

Let us consider a two dimensional (2-D) global coordinate system with axes x_1 and x_3. Two linear arrays, A_1 and A_2, are positioned parallel to the x_3 axis as shown in Figure 3-1 (a). A composite laminate specimen is placed between the transducer arrays and the setup is submerged to provide liquid coupling. The specimen is assumed to partition the image domain into three regions, W_1 and W_2 containing liquid, and S consisting of the specimen. The liquid-specimen interfaces are denoted as Γ_1 and Γ_2. Each array contains N_1 and N_2 transducer elements, respectively, with each element capable of performing both transmission and reception. The transducer elements are labeled $1, ..., N$ with $N = N_1 + N_2$, where the $i^{\mathtt{th}}$ element belongs to array A_1 if $i \leq N_1$, and belongs to A_2 otherwise. Figure 3-1 (a) illustrates examples of back-scattering and through-transmission ray-paths through a point $\mathbf{z}$ inside the specimen. Both paths begin at the position of the $i^{\mathtt{th}}$ element, $\mathbf{r}_i$, and travel to the position $\mathbf{z}$. From

there one path follows the scattered energy to the position of the j^{th} element, $\mathbf{r}_j$, and the other path transmits through the material to the position of the k^{th} element, $\mathbf{r}_k$. Data acquisition is performed by exciting each transducer in turn and receiving with all N transducers in parallel. The resulting dataset contains all transmit-receive combinations for each element in the two arrays, and can be represented as a $N \times N$ matrix of measurements where the rows and columns correspond to elements used in transmission and reception, respectively. This measurement matrix can be subdivided into four sub-matrices as shown in Figure 3-2 (b), where the diagonal sub-matrices M_{11} and M_{22} correspond to the sets of reflection measurements from each array, and the off-diagonal sub-matrices M_{12} and M_{21} correspond to transmission measurements. According to reciprocity, the signal obtained from the (i, j) transmit-receive pair is the same as that obtained from the (j, i) pair, therefore the measurement matrix is expected to be symmetric, though the presence of electronic noise and the use of different hardware channels in transmission and reception can cause some asymmetry in practice.

The propagation of waves in the liquid regions W_1 and W_2 is governed by the acoustic wave equation

$$\frac{\partial^2 p}{\partial x_1^2} + \frac{\partial^2 p}{\partial x_3^2} = \frac{1}{c^2}\frac{\partial^2 p}{\partial t^2}, \tag{3.1}$$

where p is acoustic pressure and c is the velocity of sound in the liquid. The propagation of waves within the specimen S, which here is assumed to consist of composite laminate material, is significantly more complicated due to elastic effects and anisotropy. Let y_1, y_2, and y_3 denote a set of local material coordinates with the y_1 and y_2 axes tangent to the plies and pointing in the 0° and 90° ply orientation directions, respectively, and the y_3 coordinate normal to the plies, as shown in Figure 3-2. By assuming that the fibers are small compared to the wavelength the individual plies can be modeled as homogeneous and transversely isotropic. Further assuming that the ply thickness is small compared to the wavelength and that the ply orientations are balanced to avoid coupling between in-plane normal and shear stresses allows the

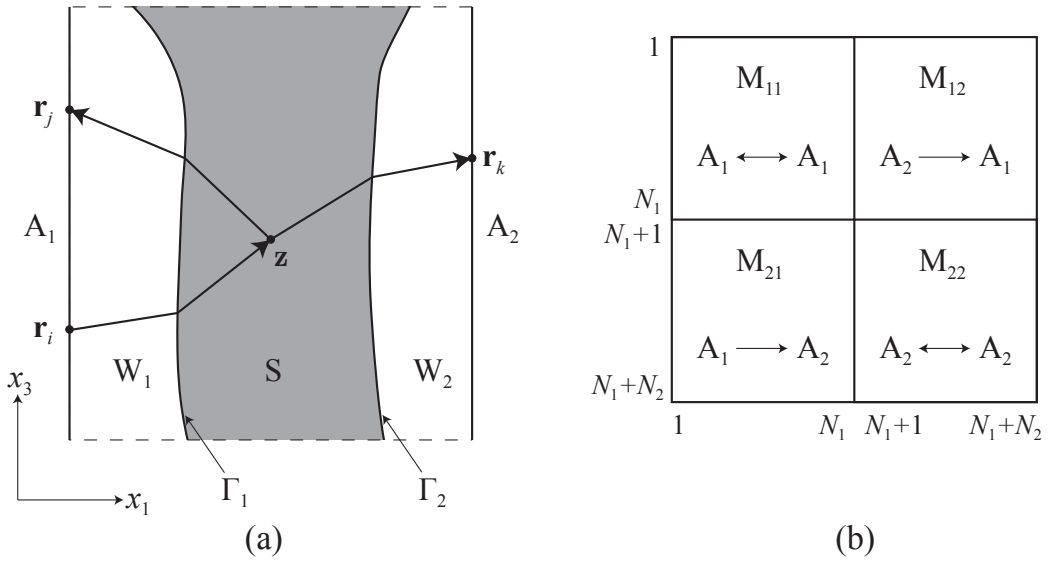

Figure 3-1: (a) Schematic of measurement setup consisting of two parallel linear arrays A_1 and A_2 containing N_1 and N_2 elements, respectively. The image domain includes three separate regions, W_1 and W_2 consisting of coupling liquid and S containing the specimen. The liquid-specimen interfaces are denoted Γ_1 and Γ_2. Examples of reflection and through-transmission ray paths through an image point $\mathbf{z}$ are shown. (b) Depiction of complete dataset obtained by transmitting with each element in turn while receiving with all $N_1 + N_2$ elements in parallel. Measurements are arranged in a matrix where the rows correspond to elements used in transmission and columns correspond to elements used in reception. Diagonal sub-matrices contain reflection measurements while off-diagonal sub-matrices contain transmission measurements.

material to be modeled as locally homogeneous and orthotropic. Orthotropic materials have three planes of mirror symmetry, namely the y_1y_2, y_1y_3, and y_2y_3 planes as expressed in material coordinates. Although the effective material properties are assumed to be homogeneous, gradual variations in material orientation will be allowed in the model in order to account for curvature of the plies, as will be explained further below. Acoustic waves impinging on the specimen will excite qP, qSV and qSH waves; in this work the qSV and qSH waves are neglected and image formation is performed by focusing on the expected arrival times of qP waves which have been scattered in or transmitted through the material. The complexity of this problem can be reduced to two dimensions by assuming that the plane of the image contains one of the material planes of symmetry, here we assume that the x_1x_3 image plane

is co-planar with the y_1y_3 material symmetry plane; that the material is extending uniformly in the direction orthogonal to the image plane, which is similar to a plane strain constraint; and that the array elements are sufficiently long in the y_3 direction to be considered as cylindrical sources. It should be noted that this assumption is violated when the array is tilted about the x_1 or x_3 axis, or when the specimen contains out of plane curvature; in practice the method is observed to be robust under mild tilt (5°) and mild out of plane curvature such as that seen in the fan blade. Under these assumptions the phase velocity of qP and qSV waves in the orthotropic material can be calculated according to the reduced Christoffel equation [51]

$$\begin{bmatrix} K_{11}\sin^2(\theta) + K_{55}\cos^2(\theta) - V^2 & (K_{13}+K_{55})\sin(\theta)\cos(\theta) \\ (K_{13}+K_{55})\sin(\theta)\cos(\theta) & K_{55}\sin^2(\theta) + K_{33}\cos^2(\theta) - V^2 \end{bmatrix} \begin{bmatrix} U_1 \\ U_2 \end{bmatrix} = 0, \quad (3.2)$$

where here θ is the angle that the phase velocity vector makes with the y_3 axis, U_1 and U_2 are components of the displacement vector expressed in the material coordinate system. The in-plane orthotropic group velocity, V_g, and angle that the group velocity vector makes with the y_3 axis, θ_g, can then be obtained as [51]

$$\begin{aligned} V_g &= V\sqrt{1+\left(\frac{1}{V}\frac{dV}{d\theta}\right)^2} \\ \tan\theta_g &= \frac{\tan\theta + \frac{1}{V}\frac{dV}{d\theta}}{1 - \frac{\tan\theta}{V}\frac{dV}{d\theta}}. \end{aligned} \quad (3.3)$$

Equation 3.2 and Equation 3.3 sufficiently describe orthotropic qP propagation through the symmetry plane of the material; however, in practice the relevant values of the stiffness tensor are not likely to be known at the time of inspection. Furthermore, even if those values are known, there may be viscoelastic effects at the inspection frequency which must be accounted for. Therefore the simplified model of elliptical anisotropy is utilized here which is described by only two velocities, $v_1 = \sqrt{K_{11}}$ and $v_3 = \sqrt{K_{33}}$, defined as the velocities within the image plane that are parallel and normal to the ply, respectively. At their respective orientations, the magnitudes of v_1 and v_3 are equivalent to both the phase and group velocity magnitudes. The

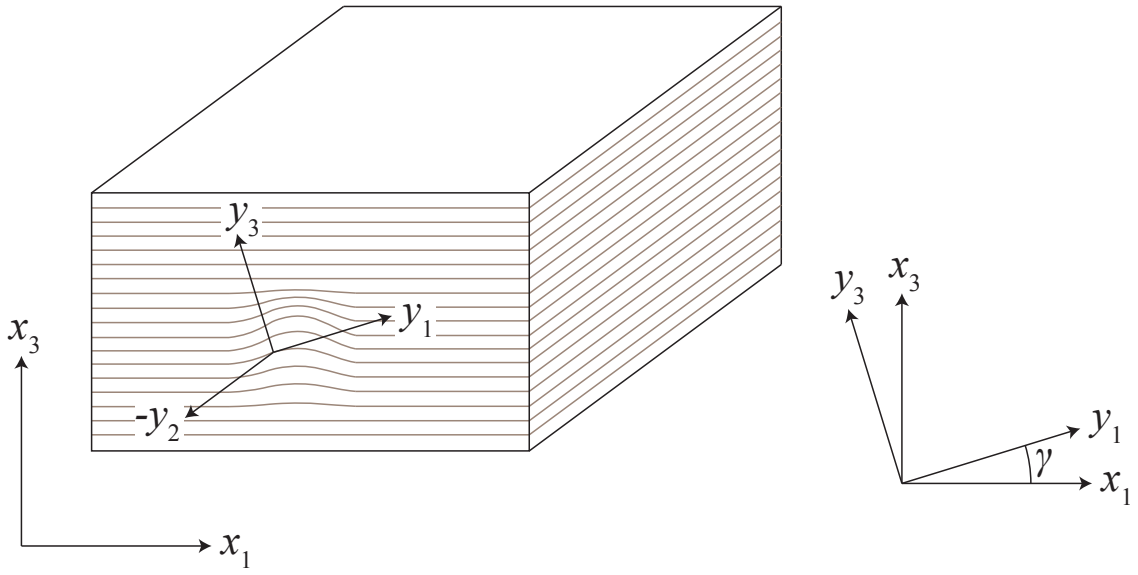

Figure 3-2: Relationship between 2-D global coordinates x_1, x_2 and 3-D material coordinates y_1, y_2, y_3. The y_1 and y_2 axes lie tangent to the ply orientation at a given point. The material is assumed to extend uniformly in the y_3 direction which is orthogonal to the global coordinate plane. The angle between the x_1 and y_1 axes, γ, defines the local orientation of the plies.

magnitude of the acoustic phase and group velocities in this simplified model are then given by Equation 2.15 and Equation 2.16, respectively, and are here equivalently expressed in terms of v_1 and v_3 as

$$\begin{aligned} V(\theta)^2 &= v_1^2 \sin^2\theta + v_3^2 \cos^2\theta \\ \tan\theta_g &= \frac{v_1^2}{v_3^2}\tan\theta \\ V_g(\theta_g)^2 &= \frac{v_1^2 v_3^2}{v_1^2\cos^2\theta_g + v_3^2\sin^2\theta_g}. \end{aligned} \tag{3.4}$$

If we let γ denote the angle between the x_1 and y_1 axes at any given location (Figure 3-2) and assume that variations in γ are also locally smooth, then as in Section 2.3 we can construct a suitable metric which describes traveltimes along paths from the function

$$\mathcal{M}(\mathbf{x}) = R(\mathbf{x})^T \mathcal{M}_{vert}(\mathbf{x}) R(\mathbf{x}), \tag{3.5}$$

with

$$\mathcal{M}_{vert} = \begin{bmatrix} 1/v_1^2 & 0 \\ 0 & 1/v_3^2 \end{bmatrix}$$

$$R(\mathbf{x}) = \begin{bmatrix} \cos(\gamma(\mathbf{x})) & -\sin(\gamma(\mathbf{x})) \\ \sin(\gamma(\mathbf{x})) & \cos(\gamma(\mathbf{x})) \end{bmatrix}$$

The dependence of Equation 3.5 on the ply orientation γ is the mechanism that is used in this model to describe how ply waviness defects affect wave propagation.

Figure 3-3 (a) shows a plot of phase velocity as a function of θ, the angle the phase velocity vector makes with the y_2 axis, for a polymer matrix composite material S2/3501-6 with $[0, 90, \pm 45]_s$ stacking sequence and with the effective material properties listed in [52]. Similarly, Figure 3-3 (b) shows a plot of group velocity as a function of θ_g, the angle the group velocity vector makes with the y_3 axis. For comparison, the velocity curves associated with an elliptically anisotropic model and with an isotropic model for the same material are also shown. Here, the elliptical model is obtained by setting v_1 and v_3 to the group velocities in the material when the group velocity vector is oriented parallel to the y_1 and y_3 axis, respectively, and the velocity curves are calculated according to Equation 3.2, Equation 3.3), and Equation 3.4. Although the elliptically anisotropic model deviates from the orthotropic model, it clearly represents a significant improvement over the isotropic model and requires much less detailed knowledge of the material properties than the orthotropic model.

3.2.1 Imaging

Let the wavefront traveltime τ be defined as in Section 2.1 but in 2 dimensions now. The traveltime between a source location $\mathbf{r}_i$ and a point $\boldsymbol{z}$ in the image domain is then given by $\tau(\mathbf{r}_i, \boldsymbol{z})$, and the traveltime between $\boldsymbol{z}$ and a receiver location $\mathbf{r}_j$ as $\tau(\boldsymbol{z}, \mathbf{r}_j)$. The Total Focusing Method [40] is a well established processing method

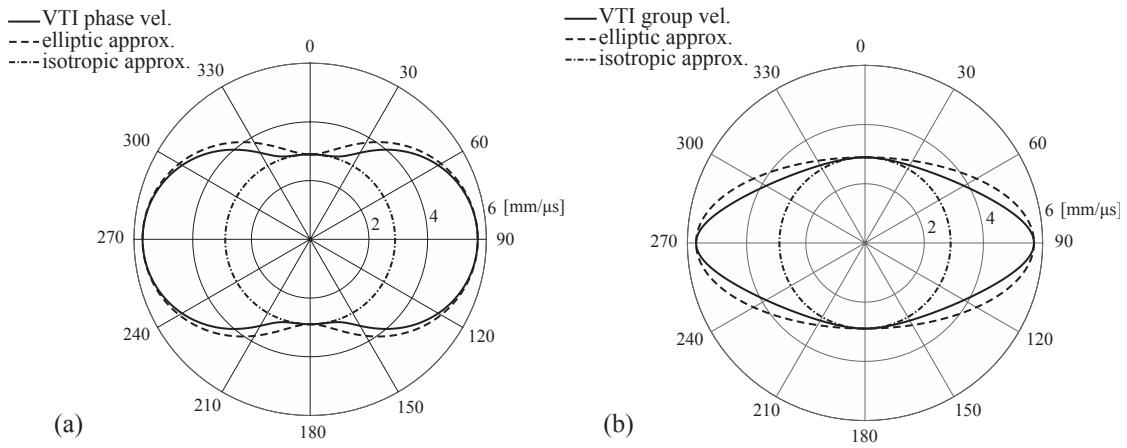

Figure 3-3: Example of transverse isotropic (TI) phase and group velocities compared to elliptically anisotropic and isotropic models for a composite material S2/3501-6 with the properties given in [52]. (a) Phase velocities as a function of the angle that the phase velocity vector makes with the y_3 axis. (b) Group velocities as a function of the angle formed by the group velocity vector and the y_3 axis. Though the TI velocity profile can be highly anelliptic, the elliptical anisotropy approximation is clearly a more accurate representation of wave velocity with respect to angle than the isotropic approximation.

which defines the image value at a point $\mathbf{z}$ as

$$I(\mathbf{z}) \quad = \quad \left| \sum_i \sum_j a_{ij} \left[\tau(\mathbf{r}_i, \mathbf{z}) + \tau(\mathbf{z}, \mathbf{r}_j) \right] \right|, \tag{3.6}$$

where $|\cdot|$ is the modulus and $a_{i,j}(t)$ is the analytic signal obtained as

$$a_{ij}(t) \quad = \quad s_{ij}(t) + i\mathtt{H}[s_{ij}(t)], \tag{3.7}$$

with $s_{i,j}(t)$ being the time domain signal obtained when transducer i transmits and j receives and evaluated at time t, and $\mathtt{H}$ is the Hilbert transform. The range of the indices being summed over in Equation 3.6 is dependent on the sub-aperture of the array that is sensitive to the signals scattered and transmitted through $\mathbf{z}$ as explained in Section 3.3. Due to reciprocity of traveltimes $\tau(\mathbf{z}, \mathbf{r}_j) = \tau(\mathbf{r}_j, \mathbf{z})$, and therefore all relevant traveltime information is contained in the N traveltime fields $\tau(\mathbf{r}_i, \cdot)$. Obtaining $\tau(\mathbf{r}_i, \cdot)$ for a given transducer i is complicated by refraction effects that

occur at the boundaries Γ_1 and Γ_2 as well as the anisotropy and inhomogeneity of the specimen, and therefore is obtained by numerically solving the elliptically anisotropic eikonal equation for qP wavefront traveltimes Equation 2.13, here expressed in two dimensions, in material coordinates and referencing the two velocities as

$$v_1^2 \left(\frac{\partial \tau}{\partial y_1} \right)^2 + v_3^2 \left(\frac{\partial \tau}{\partial y_3} \right)^2 \tag{3.8}$$

This equation can be expressed in image coordinates by applying a coordinate transformation, leading to

$$\begin{aligned} \left(\frac{\partial \tau}{\partial x_1} \right)^2 \left(v_1^2 \cos^2 \gamma + v_3^2 \sin^2 \gamma \right) \quad &+ \quad \left(\frac{\partial \tau}{\partial x_3} \right)^2 \left(v_1^2 \sin^2 \gamma + v_3^2 \cos^2 \gamma \right) \\ &+ \quad 2 \frac{\partial \tau}{\partial x_1} \frac{\partial \tau}{\partial x_3} \cos \gamma \sin \gamma \left(v_1^2 - v_3^2 \right) = 1. \end{aligned} \tag{3.9}$$

This equation can also be used to determine the traveltimes in the isotropic liquid regions W_1 and W_2 by setting $v_1 = v_3 = c$. Before the eikonal equation can be solved, a model of the specimen-liquid interfaces Γ_1 and Γ_2, and ply orientations γ, must be formed; the next section will describe how these can be modeled by utilizing two initial reflection images where $v_1 = v_3 = c$ is assumed throughout the image domain.

3.2.2 Interface Reconstruction and Ply Orientation Model

Techniques for reconstructing an arbitrary material interface using ultrasonic pitch-catch and pulse-echo measurements have been studied in [44]. The principle behind these methods is to use the arrival times of the first reflections to triangulate the position of several reflection points along the interface. A model of the interface can then be constructed by interpolating along these points, or as in the case of [45], these points can be used to determine the location of virtual source and receiver elements along the interface. Such methods are very efficient and have good potential for automation in the context of repetitive inspections of multiple parts with complex but consistent geometry. The present work utilizes a method which is less computationally efficient but allows for visual verification and manual adjustment

of the detection algorithm. Two initial reflection images are formed by assuming $v_1 = v_3 = c$ throughout the image domain, and by restricting the transmit-receive pairs used to the sub-matrices M_{11} and M_{22} (Figure 3-2 (b)) for the first and second image, respectively. Ideally, since the assumption placed on the velocities is only valid in the liquid regions W_1 and W_2, then only the reflections from the interface will be correctly focused in these initial images. For each x_1 grid location, the x_3 location of maximal image amplitude is collected to form an approximation of the interface geometry. The discretization of the image domain is expected to introduce digitization noise, therefore a smoothing spline, as implemented in MATLAB [53], is built with the x_1 image grid locations and x_3 locations of maximal image amplitude as the independent and dependent variables, respectively. This spline is then used as a model of the interface. In practice, the curvature of the specimen can lead to strong artifacts in the image, and multiple reverberations from reflectors close to the surface can lead to image amplitudes greater than that from the front wall, therefore the interface models are visually evaluated in comparison to the initial image and such artifacts are manually removed from the image where necessary.

In order to solve Equation 3.9 the spatial distribution of γ throughout the material must be known in addition to the velocities v_1 and v_3. For this work a model of ply orientations within the specimen is not available a priori, thus a model is built on the assumptions that the plies close to an interface Γ_i are oriented parallel to Γ_i and that the ply orientations vary smoothly between the two interfaces. The interfaces can be expressed as functions of x_3, i.e. $\Gamma_1(x_3)$ and $\Gamma_2(x_3)$, and the orientation of the plies at a position $x_1 = d$ is interpolated as

$$\begin{aligned}\gamma\left(d, x_3\right) = & \frac{d - \Gamma_1\left(x_3\right)}{\Gamma_2\left(x_3\right) - \Gamma_1\left(x_3\right)} \gamma_2\left(x_3\right) \\ & + \frac{\Gamma_2\left(x_3\right) - d}{\Gamma_2\left(x_3\right) - \Gamma_1\left(x_3\right)} \gamma_1\left(x_3\right)\end{aligned} \tag{3.10}$$

where $\gamma_1\left(x_3\right)$ and $\gamma_2\left(x_3\right)$ are the orientations of Γ_1 and Γ_2 at x_3 and measured clockwise from the x_1 axis.

3.2.3 Fast Marching Method

In applications where sections of homogeneous material are separated by sharp interfaces, ray-shooting methods can be utilized to efficiently determine traveltimes. Such methods only require discretization along the interface to find the ray-intersection point which satisfies Fermat's principle. The calculation of traveltimes in this work is complicated by the inhomogeneity in the material orientation, which can vary gradually throughout the material, and which would therefore require discretization along the length of the rays as well. Instead, the numerical solution to Equation 3.9 is obtained using the FMM-LBR method discussed in Section 2.3. The implementation of the algorithm used in this work takes as input the location of the source transducer $\mathbf{r}_i$, and point-by-point maps of the velocities v_1 and v_2, and the angle between the global and local coordinate systems γ, and outputs the point-by-point map of first arrival traveltimes for an acoustic wave emanating from a given source. This algorithm is run once per transducer to obtain the traveltime maps $\tau(\mathbf{r}_i, \cdot)$ used for imaging in Equation 3.6. The choice of FMM-LBR over the other method discussed in Section 2.3, SPR, is here motivated by the large number of traveltime simulations which must be run for each image which led to prohibitively long processing times when employing SPR.

3.3 Experimental Methods

Experimental measurements are performed using two identical Imasonic linear arrays having center frequency 2 MHz, $N_1 = N_2 = 128$ elements, pitch 0.8 mm, and element width 10 mm in the x_3 direction. The choice of 2 MHz center frequency is motivated by the high attenuation that PMC materials exhibit at higher frequencies. The arrays are held parallel to each other using the stainless steel yoke shown in Figure 3-4. Each element is excited in turn with a negative square pulse of width 250 ns. The signals received by all transducers are recorded in parallel using a Lecoeur custom-built acquisition system that consists of 32 $\times$ 8-channel, 12-bit analog-to-digital converters (ADC). The ADCs are set to operate at a sampling rate of 40 MHz and record for

125 µs, and the data is streamed to disk and transferred to a separate computer for off-line processing. In order to increase the amplitude resolution available to image the inner structure, two datasets are used in the formation of each image. The first dataset is gain-adjusted such that the reflection from the first interface is not saturated, and this data is used to form the interface model. The second dataset is taken with a 20 dB gain increase, which saturates the front surface but more clearly resolves sub-surface features. The process of recording and transferring the data takes approximately 6 minutes with the experimental setup used; though the acquisition time could potentially be reduced to a few seconds with a specialized acquisition system. The fixture and arrays are submersed in a water bath to provide coupling between the arrays and the sample. This section will discuss the digital preprocessing, calibration, choice of elliptical anisotropy parameters, and selection of aperture used during image formation.

3.3.1 Preprocessing and calibration

Before the imaging algorithm is run, some pre-processing procedures are performed to limit noise, and to calibrate the system to address timing of the signals and temperature dependence of water, which can negatively affect image quality if not accounted for. To reduce noise the signals are individually band-pass filtered using a Hann window with cut-off frequencies of 0.5 MHz and 3.5 MHz. To address timing issues, the signals are time shifted such that the maximum envelope of the transmitted signal occurs at time $t = 0$. This time shifting must account for electronic delay and satisfies the implicit assumption in Equation 3.6 that the position of a scatterer corresponds to the time at which the peak modulus of the scattered analytic signal arrives. Calibration of ultrasonic transducers used in through-transmission is a complex issue which has been addressed, for example, in ultrasonic tomography with ring arrays [54]. In this thesis a simple approach is favored. Pulse-echo measurements are made in contact with a flat specimen, and the time-shift is determined from the train of reverberations produced within the specimen. Temperature dependence of water velocity is accounted for by taking an incident measurement immediately before acquiring data

with the sample present. Pulse-echo and transmission time of flight measurements in the incident data are used to calculate water velocity from the measured distance between arrays.

3.3.2 Samples

Experimental validation of the imaging method is performed on a selection of two Plexiglas and four PMC specimens shown in Figure 3-4. Plexiglass is chosen as a sample material because the density in Plexiglas and the PMC samples are very similar, and also the P-wave velocity in Plexiglas is very close to the qP-wave velocity normal to the plies in the PMC samples. The two Plexiglas samples, labeled Plex1 and Plex2, both have side-drilled hole (SDH) defects, but differ in the complexity of their geometry; Plex1 has been machined to mimic the curvature of the PMC blade, while Plex2 has flat sides and a thickness of 15 mm. The four PMC samples are: Pmc1, a flat coupon of 15 mm thickness with side drilled holes (SDH) that has very similar geometry to Plex2; Pmc2, a coupon with one flat and one slightly curved surface with thickness ranging from 13 mm to 16 mm and which contains a waviness defect; Pmc3, a flat 17 mm thick coupon with a porosity defect; and Pmc4 which is a cut-out section of a representative fan blade. The laminate properties and stacking sequences are consistent across the three PMC coupons, and are chosen to be representative of the material properties in the fan blade.

3.3.3 Anisotropy model definition

Suitable velocity parameters must be chosen to define the model of elliptical anisotropy within the samples. The Plexiglas samples are isotropic, thus there is only one velocity, $v_1 = v_3 = 2673.5\,\mathrm{m/s}$, which can be measured directly via time-of-flight measurements. Obtaining the velocities in the PMC samples is more challenging, especially the velocity parallel to the plies, v_1, as the high attenuation in the material and large transverse sizes make direct measurement difficult. In this work the method presented in [48] is used to measure the velocity profile. One array is placed in contact

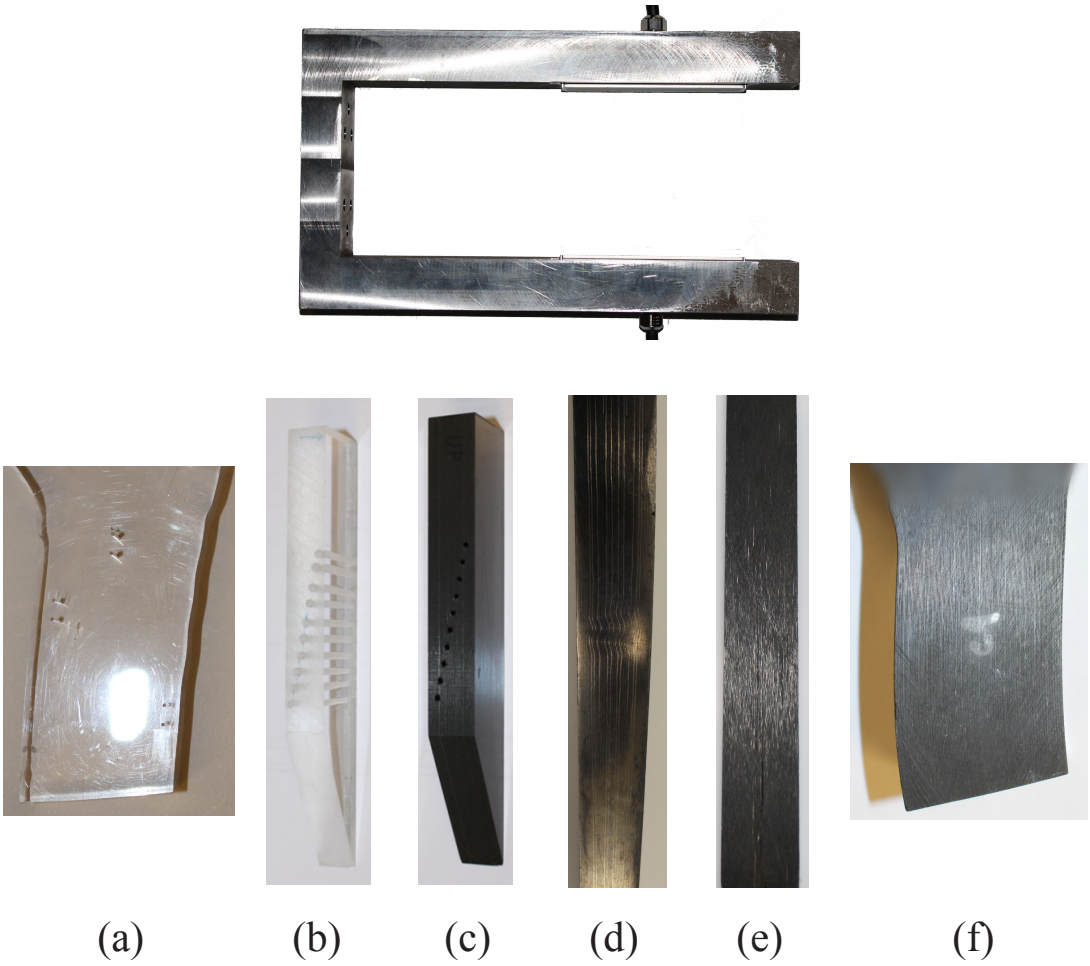

Figure 3-4: Top: stainless steel yoke used to hold two linear arrays for use in transmission and reflection. Bottom: samples used in experimental validation. (a) Plex1: Plexiglass sample machined to mimic fan blade dovetail section geometry. Includes 0.5 mm SDH. (b) Plex2: Flat Plexiglas specimen with 1.5 mm SDH. (c) Pmc1: Flat PMC coupon with 1.5 mm SDH; has very similar geometry to Plex2. (d) Pmc2: Nearly flat PMC coupon with waviness defect. (e) Pmc3: Flat PMC coupon with porosity damage. (e) Pmc4: Sample cut out of a representative PMC fan blade.

with a PMC sample which has parallel surfaces and the pitch-catch measurements between one transmitter and 36 receivers are used to measure the velocity profile at various group propagation angles ranging from 0° to 44°. From the measured profile, v_1 and v_2 are chosen such that the mean squared error between the measured velocity profile and that given by the elliptically anisotropic model is minimized. Figure 3-5 shows the measured velocity profile in comparison with the optimized elliptically anisotropic model, where $v_1 = 4850\,\mathrm{m/s}$ and $v_3 = 2950\,\mathrm{m/s}$. Measurements at greater

than 44° were not possible using this method due to increased attenuation observed in the measurements. To measure the velocity in the transversal, or v_1 direction, a pair of 2.25 MHz spot transducers was used in a pitch-catch configuration. Exact measurement of the velocity was complicated by the extreme dispersion experienced by the signal in the transversal direction, though by picking the first arrival a maximum velocity of 3900 m/s is observed. The large discrepancy between the measured transversal velocity and that predicted by the elliptically anisotropic model, as well as the strong dispersion in the transversal direction further motivate the use of the adaptive aperture.

3.3.4 Adaptive aperture

During image formation according to Equation 3.6, a subset of transmit-receive pairs is summed over to form the image value at a given location. Here, the method of determining which transmit-receive pairs to include for a given image location is discussed. The first restriction is made based on the type of image being formed. In most of the results shown below, the reflection images from array A1 and A2, and the transmission image from A1 to A2 are formed separately. During the formation of the transmission image the transmit indices are restricted to $i = 1, ..., 128$ while the receivers are restricted to $j = 129, ..., 256$, with similarly obvious restrictions for the two reflection images. Still further restrictions are made based on propagation direction. Very strong attenuation is observed when the group propagation angle is greater than 44 deg from the ply normal, and including wider ranges of propagation angle is observed to increase the level of noise present in the reconstructed image when imaging the PMC specimens. Since a level-set method is being used to calculate traveltimes the ray directions are not directly available, but can be recovered by observing that, for a given location $\mathbf{z}$, the phase velocity vector at $\mathbf{z}$ is collinear to the gradient of the traveltimes $\nabla\tau(\mathbf{r}_i, \cdot)$ evaluated at $\mathbf{z}$. The relationship between phase and group velocity vectors expressed in Equation 3.4 can then be used to determine the ray direction. Therefore, in the results shown below the image formed at each location includes only transducers for which the phase velocity vector at that location

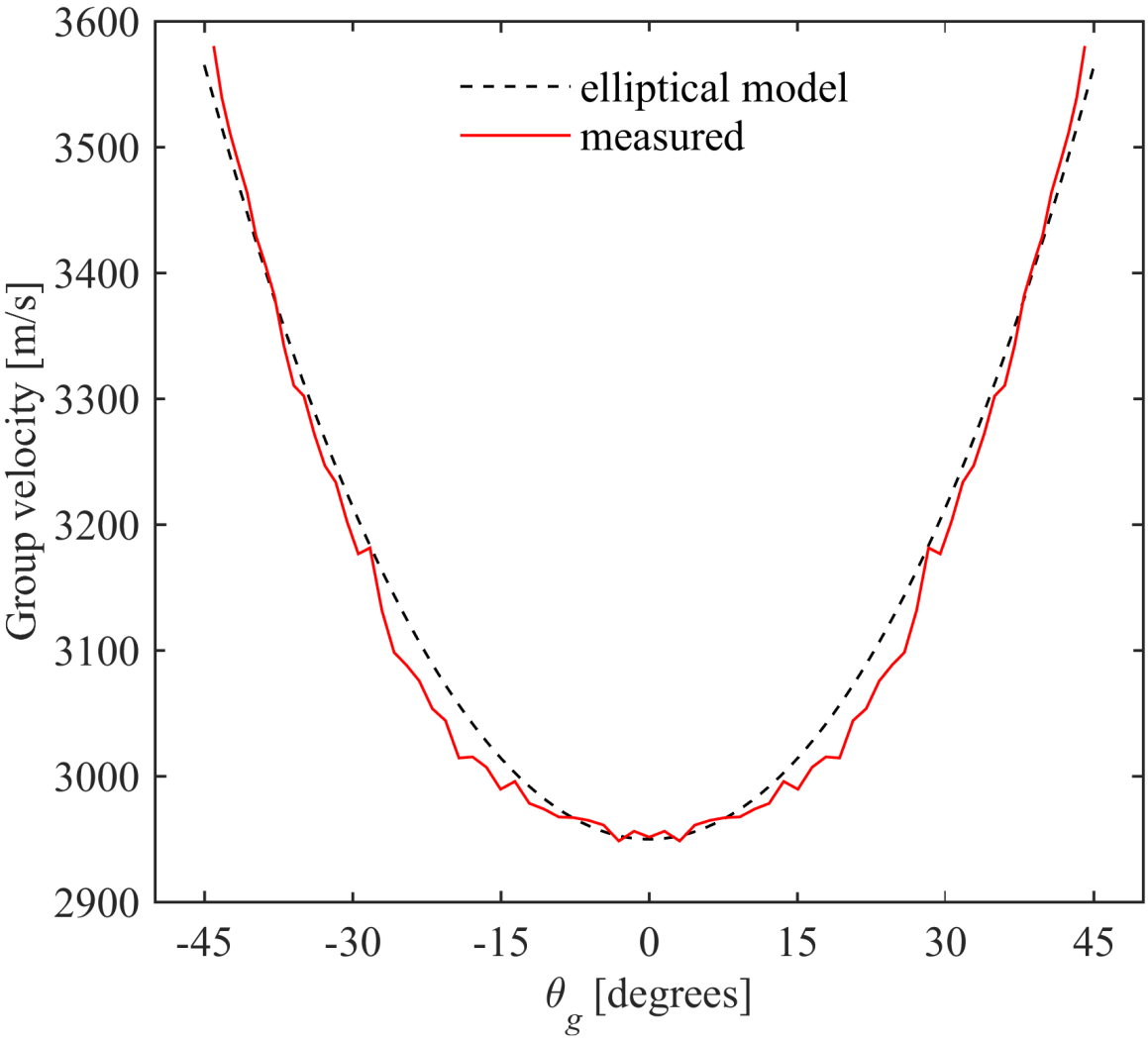

Figure 3-5: Measured group velocity curve in PMC sample. The measured group velocity is plotted as a function of the angle θ_g that the group velocity vector makes with a vector normal to the plies. The group velocities in the elliptically anisotropic model are shown for comparison.

falls within 20 deg of the ply normal, which corresponds to the group propagation direction of 44 deg from the ply normal. A diagram of the aperture selection process is shown in Figure 3-6. A wider cut-off of 50° is specified while forming images of the Plexiglas specimens.

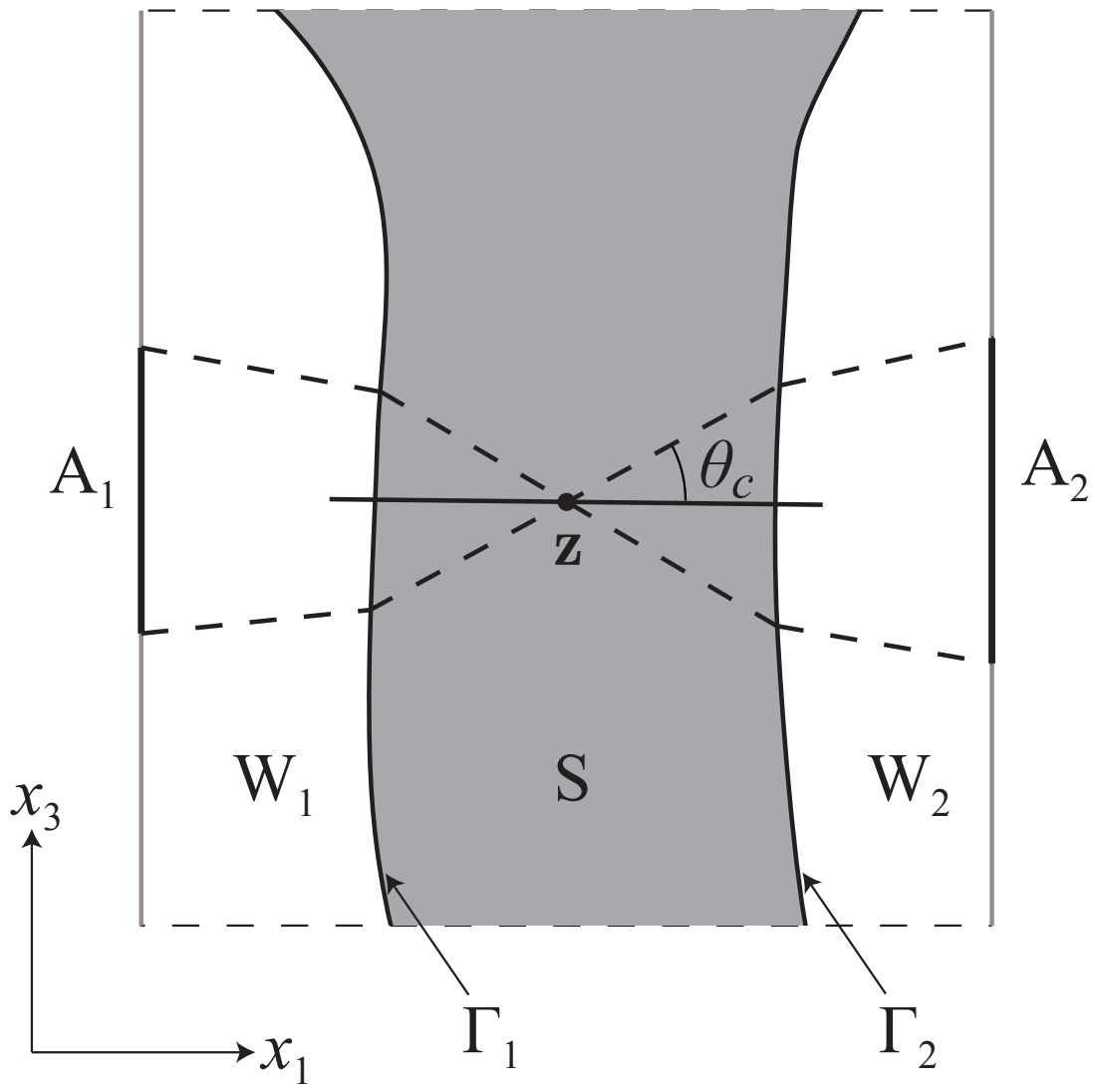

Figure 3-6: Illustration of how the aperture is defined for a given image location. Array faces for arrays A_1 and A_2 are represented by vertical lines. Direction of ply normal at $\mathbf{z}$ is marked by a solid line. A cut-off angle, θ_c, is defined which denotes the maximum angle that the group velocity vector may make with the ply normal, and is determined from the observed attenuation in the material. When forming the image at $\mathbf{z}$, the active elements on each array are those for which the group velocity vector at $\mathbf{z}$ is oriented within θ_c of the ply normal, as shown by the darker lines on the array faces.

3.4 Results

This section will first present results in the Plexiglas samples, as they provide an opportunity to validate the described methods for interface reconstruction, accounting

of refraction effects, and calibration of signal timing, without the added complication of anisotropy. All images are processed on a laptop with an Intel® Core™ Due i7-4810MQ processor and 16 GB RAM, and the formation of each image takes approximately 5-6 minutes processing time. This time includes the initial image formation, approx. 30 seconds for user input to adjust/verify the initial image reconstruction, calculation of traveltime maps for each transducer, and formation of final images using the adaptive aperture. In the context of an industrial inspection, further optimizations such as GPU implementation and automation of front surface detection for a particular specimen shape could significantly reduce the required processing time. The images formed from Plex1, the Plexiglas sample which mimics the blade geometry, are shown in Figure 3-7. These images are in dB scale, normalized to the maximum image amplitude. The elements of the array A_1 are marked as white circles along the line $x_1 = 0\,\text{mm}$ and those of A_2 along the line $x_1 = 105\,\text{mm}$. The three pairs of SDH in the lower section of the sample are clearly visible, and appear correctly focused in both reflection and transmission. In reflection the holes have upwards of 55 dB signal to noise ratio, while in transmission the holes cause a 35 dB loss of image amplitude. In the combined reflection image (left + right) the scattering from the SDH and from the interfaces in each direction line up well, indicating that the calibration is successful. Further up, the specimen widens to mimic the beginning of the dovetail. In this region the angle of the interface relative to the array exceeds the directivity of the array elements, which is approximately 30°. This causes a decrease in the strength of reflections received to the point that the interface reconstruction algorithm fails.

To illustrate the effect of anisotropy on image quality, reflection images formed from samples Plex2 and Pmc1 are shown in Figure 3-8. The images shown here are formed without anisotropy correction, meaning the PMC is treated as an isotropic material with $v_1 = v_3 = 2950\,\text{m/s}$, and are displayed in linear scale to give greater visual contrast between the hole reflections and background noise in the Pmc1 image. The Plexiglas sample Plex2 has been machined to mimic the geometry of the Pmc1, with the same number of SDH placed with the same spacing and variation in depth.

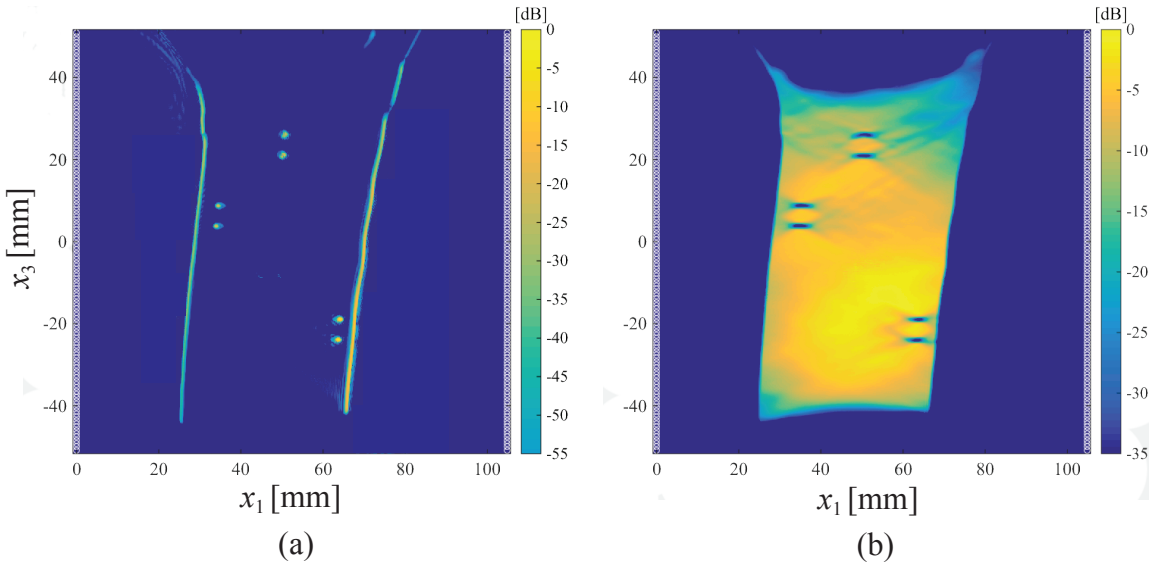

Figure 3-7: Phased array images formed of Plexiglas sample Plex1. (a) Combined reflection image using backscattered data from both arrays. The SDH are focused correctly through the complex interface. (b) Transmission image of the same sample. The SDH are clearly visible as regions of lower image amplitude.

The image of the Plexiglas specimen shows very clearly resolved reflections from each hole with a minimum SNR of 30 dB. By contrast, the image of the PMC specimen has reflections from the holes which, where they are visible above the significantly increased noise floor, are not clearly individually resolved, and which display a SNR ranging from 0 dB to 20 dB. To demonstrate that this loss of image quality is largely due to the unaccounted for presence of anisotropy, Figure 3-9 shows the A_1 and A_2 reflection, as well as transmission images formed from the same PMC sample with correction for anisotropy applied. Each hole is now clearly resolved in reflection at SNR ranging from 20 dB to 30 dB. The transmission image also shows the presence of the holes as a loss in image amplitude of 25 dB, though the hole depths are not as clearly indicated due to the lower resolution in transmission caused by the limited range of propagation angles included in the image formation. To demonstrate the robustness of the imaging algorithm, the sample is rotated at 7.5° and 15°, and the corresponding images are the second and third rows in Figure 3-9. Minimal loss of image quality is observed under rotation, while the indications of the holes in reflection and transmission remain consistent. The reflection images formed from

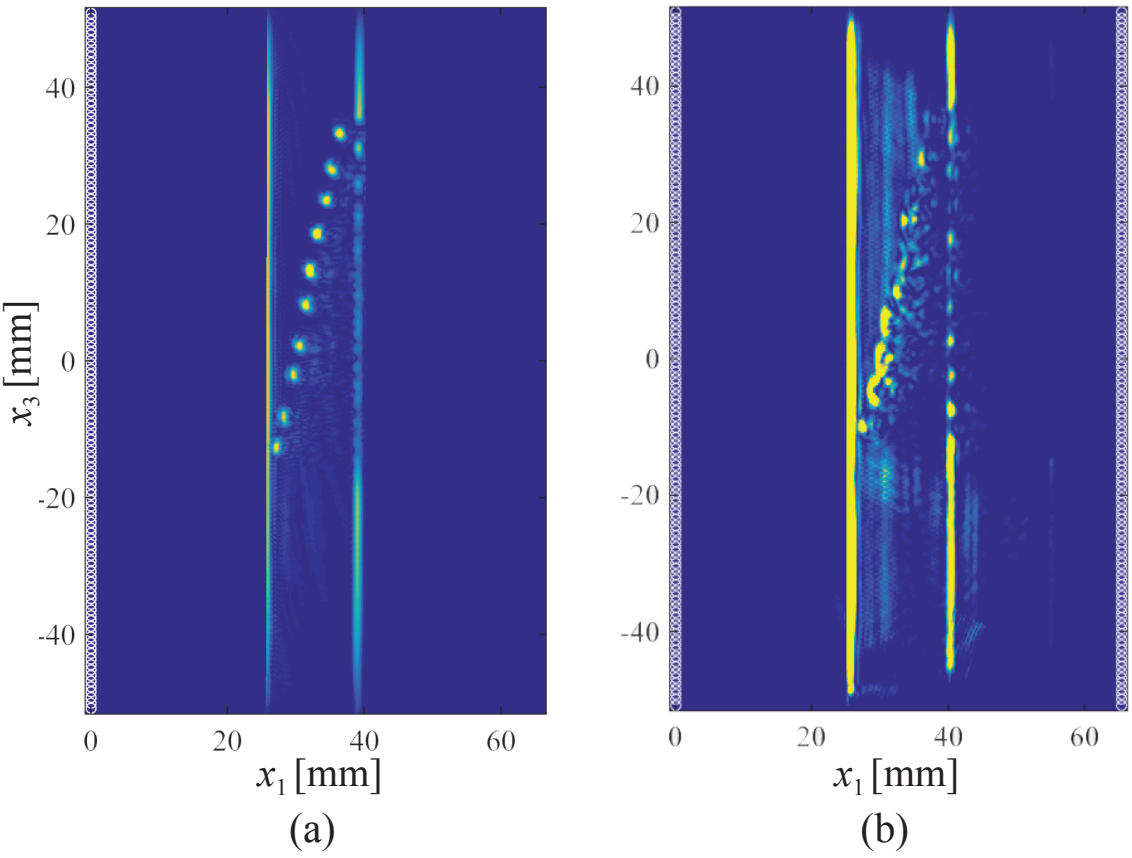

Figure 3-8: Reflection images formed with the array on the left and without correction for anisotropy in two geometrically similar specimens (a) Plexiglas specimen, Plex2, and (b) flat PMC coupon, Pmc1. The image quality is significantly degraded in the anisotropic material.

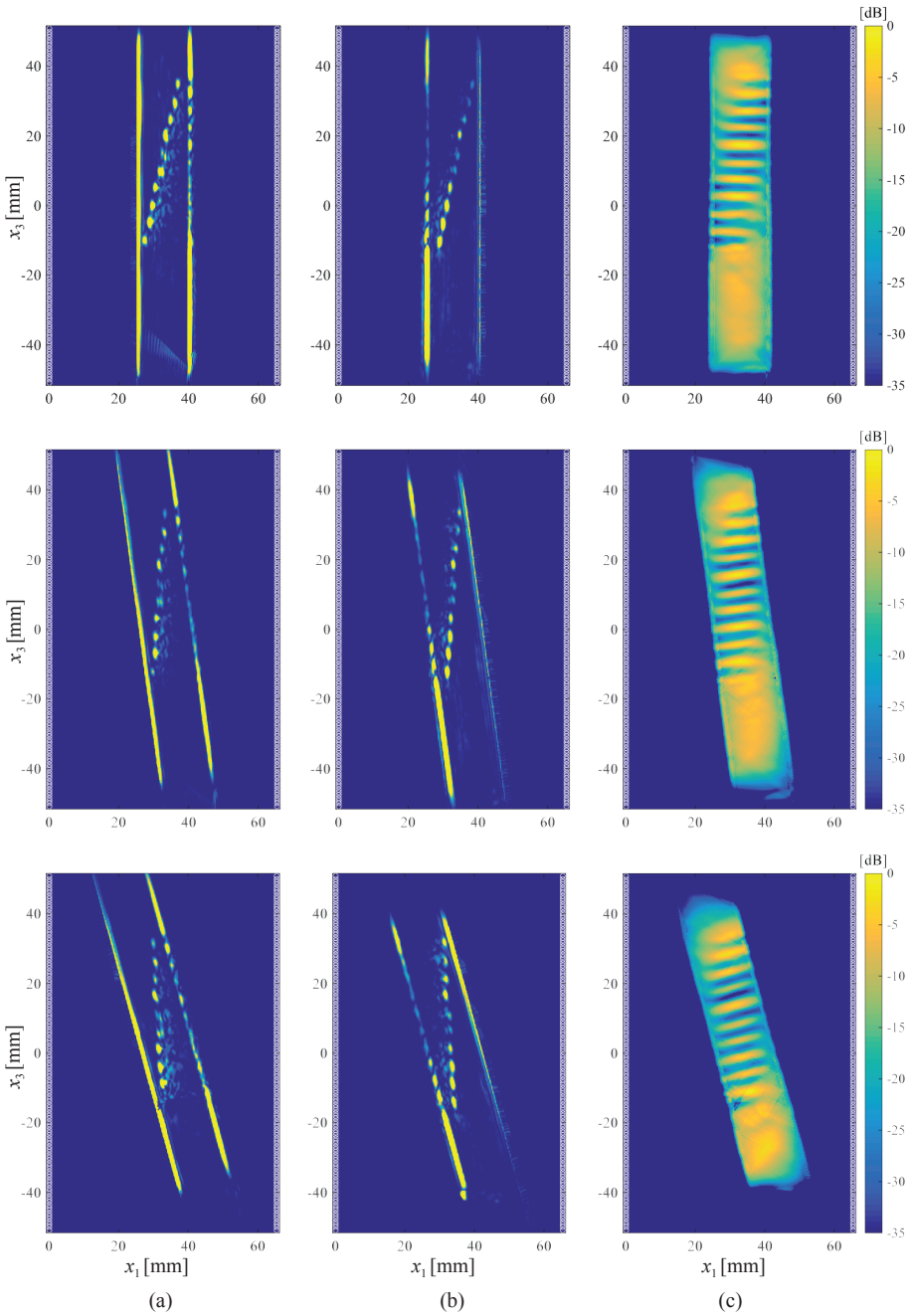

Figure 3-9: Images formed from flat PMC coupon with SDH, Pmc1. Anisotropy correction is performed. Significant improvement from the image without anisotropy correction (Figure 3-8 (b)) is observed. Each row corresponds to a different sample orientation, with the top row being parallel to the arrays, the second row rotated 7.5°, and the third row rotated 15°. The images are formed from the (a) array A_1 reflection, (b) A_2 reflection, and (c) A_1 to A_2 transmission data.

array A_1 show very similar amplitude between the front and back interfaces. This is due in part to the use of a high-gain dataset in which the front interface echo is saturated, as explained above, and is also due to the definition of the adaptive aperture, which includes more transmit-receive pairs in the formation of the back interface. These effects, combined with a slight misalignment between the interface model and the actual specimen location, explain why the image of the front interface in the A_2 reflection images is actually dimmer than the back interface, and also affects the amplitudes of the closest SDH's. Two of the middle SDH show lower amplitude in reflection, and this is due to the drill having walked significantly off course in the y_3 direction, resulting in lower amplitude reflections from these two holes.

Images formed from Pmc2, the PMC coupon with a waviness defect, are shown in Figure 3-10. The layout of these images is similar to that of Figure 3-9, as this sample has also been placed at orientations of 0°, 7.5°, and 15° relative to the array. The reflection images show inconsistent sensitivity to the waviness defect, as there is a bright spot at 15 dB SNR in each A_1 reflection image corresponds to the defect, while the A_2 image has no indication in that region. This difference may be due to a focusing effect caused by the shape of the wrinkle, which is most prominently concave in the direction of array A_1. The key result is the transmission image, which shows a sharp and severe loss of image brightness in the location of the waviness defect. Furthermore, this indication is consistent under rotation of the sample. Two mechanisms which may be causing the sensitivity in transmission are as follows: one is that the waves passing through the defect may be experiencing higher attenuation due to the direction dependent attenuation characteristics of the material; another is that the varying orientation of the plies in the region of the defect is violating the model's assumptions about ply orientation, causing the transmitted energy to arrive at a different time than that predicted by the focal laws.

Figure 3-11 shows images formed from the PMC coupon with porosity damage. The sample contains some rather severe porosity damage that is visible on the side of the specimen, and corresponds to the bottom portion of the images. This severe damage is sufficient to completely suppress the back-wall echo in the reflection images

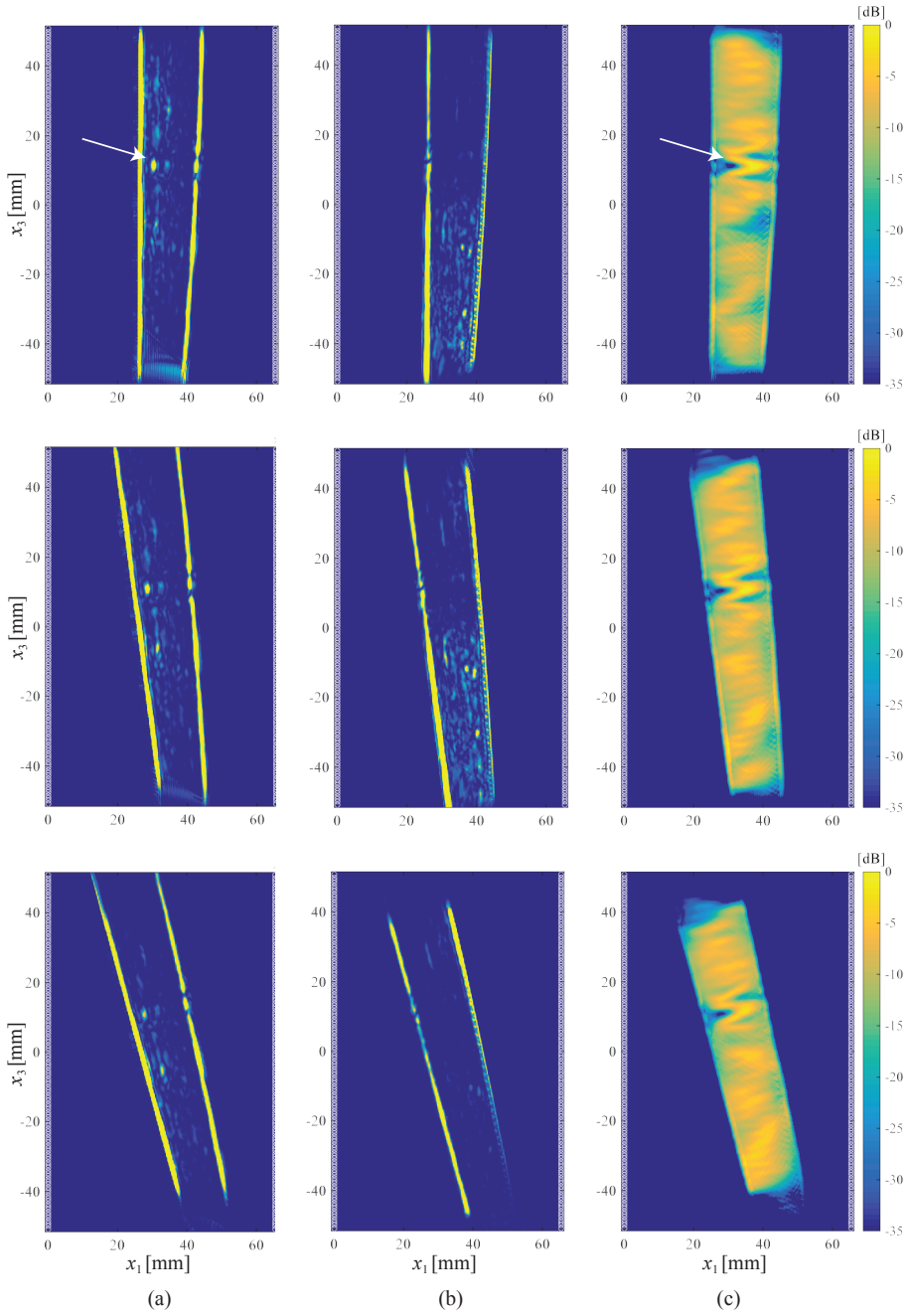

Figure 3-10: Images formed from flat PMC coupon with waviness defect, Plex2. Anisotropy correction is performed. Each row corresponds to a different sample orientation, with the top row being parallel to the arrays, the second rotated 7.5°, and the third rotated 15°. The images are formed from the (a) array A_1 reflection, (b) array A_2 reflection, and (c) A_1 to A_2 transmission data. Arrows indicate the position of the wrinkle defect.

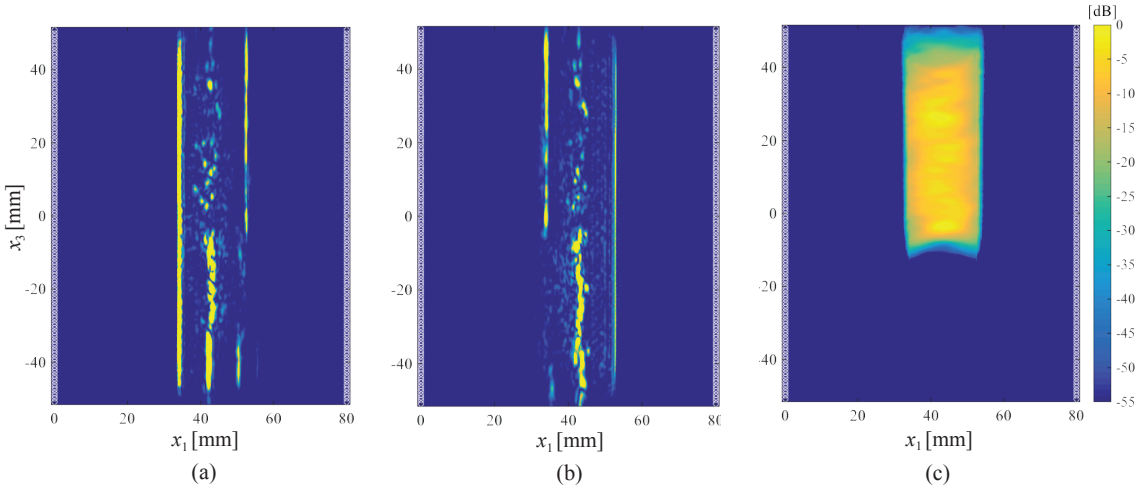

Figure 3-11: Images formed from the PMC coupon with porosity damage. Severe porosity damage is present in the lower half of the specimen, more subtle damage is present in the remaining area. The images are formed from the (a) A_1 reflection, (b) A_2 reflection, and (c) A_1 to A_2 transmission data. Consistent damage indications are present in reflection.

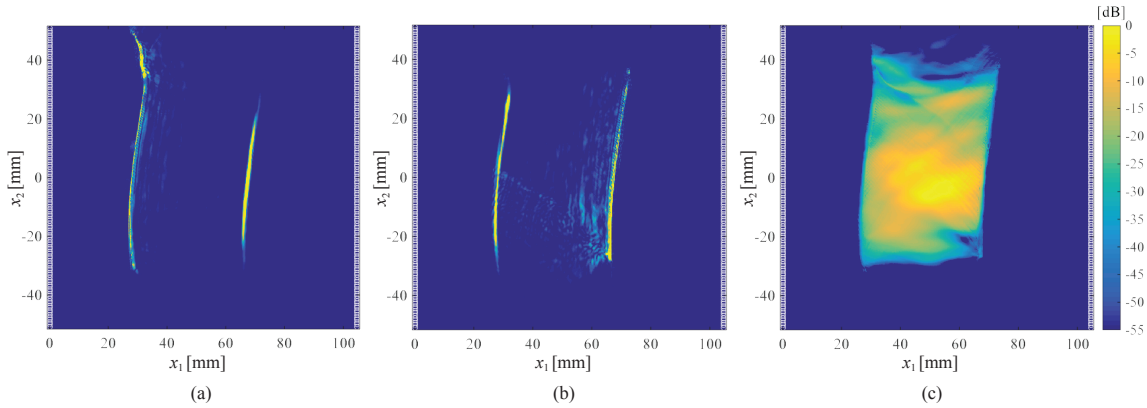

Figure 3-12: Images formed from the section of a representative PMC fan blade. The specimen does not contain a defect. The images are formed from the (a) array A_1 reflection, (b) A_2 reflection, and (c) A_1 to A_2 transmission data.

and block the transmission signal, leading to an area of sharp contrast in Figure 3-11 (c). The more subtle porosity damage through the rest of the specimen is visible in the reflection images, which give consistent indications of damage in that region. The transmission image however does not seem to be sensitive to the more subtle porosity damage, which is not surprising due to the decreased resolution in transmission.

Finally, a sample cut from a fan blade is imaged to demonstrate viability of the

measurement on the blade (Figure 3-12). This specimen does not contain any known defects. The reflection measurements from each direction clearly reconstruct the back-wall through the thickness of the blade, and the transmission image is relatively consistent through the shank of the blade, which is the targeted area for inspection. Some artifacts, which can be seen in the lower region of the transmission image and the A_2 reflection image, are caused by the sharp corners where the sample has been cut.

3.5 Conclusions

This chapter has introduced a linear array beamforming technique which, in addition to the conventional backscattered data, utilizes through-transmission signals to detect damage in components with complex geometry and with anisotropic material properties.

A measurement configuration consisting of two linear arrays held on either side of a component within a liquid bath is presented. A method of obtaining cross-sectional images by synthetically focusing the ultrasonic beam over a grid of points inside the specimen is described. The focal laws are obtained by accounting for refraction occurring at the liquid-specimen interface and, for composite laminate components specifically, accounting for anisotropic effects caused by the fiber orientation in the specimen.

Experiments performed on polymer matrix composite (PMC) material similar to that used for fan blades in modern turbofan engines demonstrate that the anisotropy within the material, if not accounted for, will significantly degrade image quality. We show that a simplified elliptically anisotropic model (EAM) provides a practical method of addressing the anisotropy and allows for the focal laws to be efficiently calculated via the Fast Marching Method. Implementation of EAM significantly improves image quality, with SNR increases of up to 30 dB. Testing on a range of PMC samples shows that transmission images are effective at detecting subtle forms of damage, such as ply waviness, which tend to produce lower contrast in the back-

scattered images. However, the reflection images tend to have higher resolution and therefore are better suited to detect smaller, higher contrast damage such as porosity. As a result the two imaging modalities complement each other.

Chapter 4

Cryoultrasonic NDE

4.1 Introduction

As discussed in Chapter 1, ultrasonic testing may provide an attractive alternative to X-ray CT; however, in order for UT to provide an effective solution, its limitations in the presence of complex geometries must be overcome. To illustrate the difficulties faced by UT let us consider the example shown in Figure 4-1 which begins with the ideal scenario of a simple-shape cylindrical solid with the cross section given in Figure 4-1 (a). A conventional UT inspection is typically conducted with a single element transducer in direct contact with the part or at a standoff distance through a water column. The transducer excites an ultrasonic wave that propagates inside the part and is then reflected by geometrical and material discontinuities, such as defects. The reflected wavefield is received by the same transducer under the so-called pulse-echo inspection mode and is used to detect the presence of damage. For the example in Figure 4-1 (a), a full volume inspection can be achieved by raster scanning the transducer along the top surface of the specimen or using a transducer array, as shown for defect B in Figure 4-1 (a). Whether a single element probe or an array are used, the UT inspection of the solid in Figure 4-1 (a) can be achieved with high sensitivity in most metals.

Let us now assume that some of the material from the cylinder is removed to form a complex shape part such as that shown in the cross section of Figure 4-1

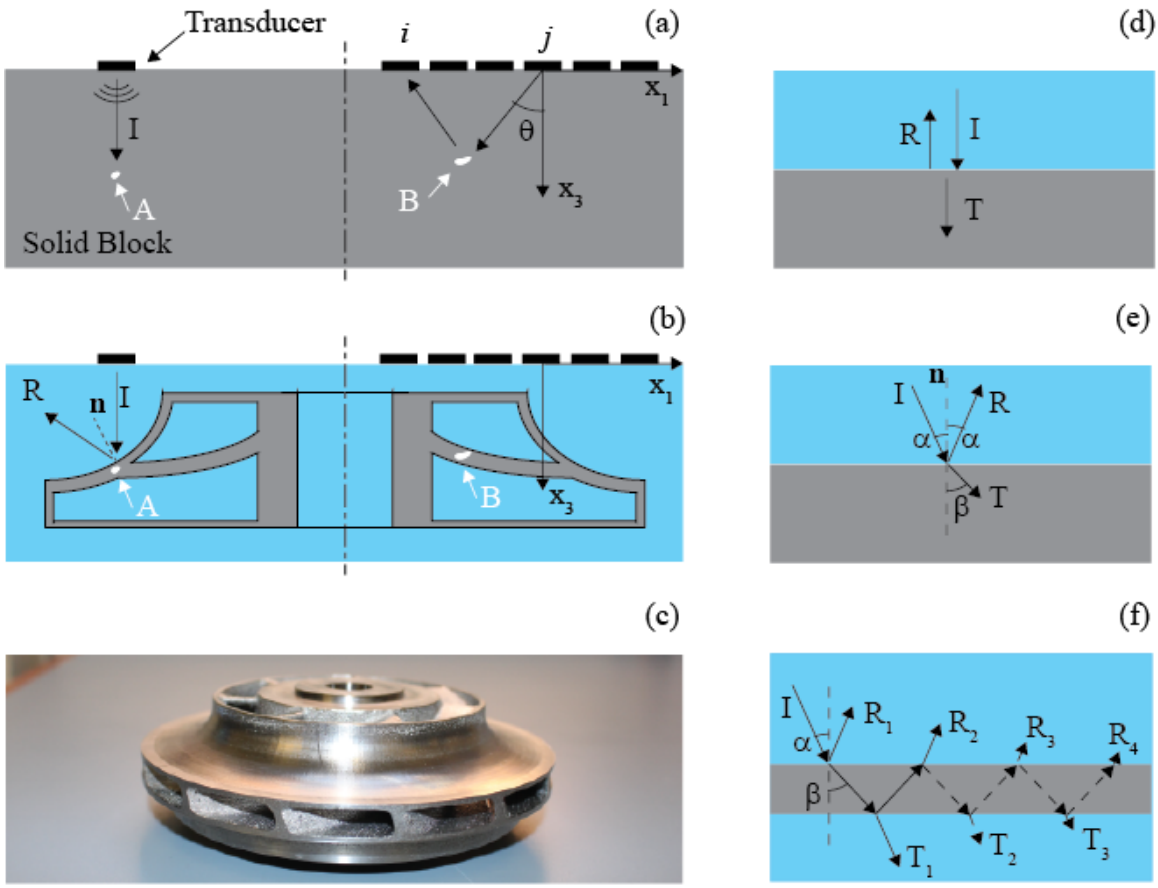

Figure 4-1: (a) Ideal conditions for ultrasonic testing (UT) with a single element probe or an array - the part is a solid cylinder containing two defects labeled A and B; (b) Schematic of a shrouded impeller *carved out* from the cylinder in (a); (c) Prototype 3-D printed impeller; (d) Reflection and transmission at normal incidence; (e) Refraction; (f) Scattering by a layer, the solid arrows are the primary reflected and transmitted waves while the dashed arrows are the internal multiples.

(b). Besides having curved interfaces, the part contains internal vanes which could be similar to those found in many engine components such as the shrouded impeller shown in Figure 4-1 (c) - this is a titanium alloy (Ti-6Al-4V) prototype obtained through the AM process. In order to inspect such a part with a conventional single element probe, the probe would need to be kept in contact with the part and scanned over its entire surface including the internal vanes. This is not practical because: (a) reliable contact is not possible in the presence of highly curved surfaces; (b) vanes and cavities may be too narrow to position the probe; (c) the scan would be highly

time consuming and operator dependent. A more attractive solution is to perform the inspection in immersion with linear arrays and using advanced imaging algorithms applied to FMC data to focus through complex interfaces. Here, it is important to note that internal vanes are typically open to the exterior either because they need to ensure the passage of fluid flow during operation or simply because of the need for removing material during the manufacturing process, e.g. unmelted powder in AM. As a result, it is always possible to flood the internal spaces with liquid. In spite of this, current applications of ultrasonic array imaging have been limited to solid components with no cavities or vanes and with relatively low surface curvature [55, 42, 45]. This is due to the large contrast between the acoustic properties of water and those of metals which affects the transmission of ultrasound at the water-part interfaces and amplifies the effects of reflection and refraction phenomena. In fact, when considering a planar interface between two media and a plane wave of intensity I impinging on the interface at normal incidence, Figure 4-1 (d), transmitted and reflected waves of intensity I_T and I_R, respectively emerge from the interface such that

$$\frac{I_T}{I} = \frac{4B}{(B+1)^2}, \quad \frac{I_R}{I} = \frac{(B-1)^2}{(B+1)^2}, \tag{4.1}$$

where, B, is the ratio between the acoustic impedance, Z, of the two media [56]. For each medium Z is defined as the product between mass density, ρ, and wave speed, c, i. e. $Z = \rho c$. Table 4.1 shows indicative values of compressional wave speed and density for various materials and the corresponding transmission and reflection coefficients under water immersion (c=1480 m s^{-1} and ρ=1000 kg m^{-3}). It can be seen that while it is possible to transmit 86% of energy through a single water-Plexiglas interface, this value can drop to 12% for metals like Inconel. It should be noted that the expressions in Equation 4.1 are valid for a smooth interface between the media. The presence of surface roughness on a scale comparable to the ultrasonic wavelength can also significantly contribute to signal loss as the coherence of the incident wave front is partially destroyed by the profile of the interface [57] - this is particularly

Table 4.1: Transmission, I_T/I, and reflection, I_R/I, coefficients at normal incidence between liquid water or ice and various engineering materials and corresponding critical angles, α_{cr}.

			Water immersion			Ice encapsulation		
Material	c [m s^{-1}]	ρ [kg m^{-3}]	I_T/I	I_R/I	α_{cr}	I_T/I	I_R/I	α_{cr}
Plexiglas	2730	1180	0.86	0.14	32.8°	1.00	0.00	N/A
Aluminum	6320	2700	0.29	0.71	13.5°	0.57	0.43	37.5°
CMC	6850	2800	0.27	0.73	12.5°	0.53	0.47	34.2°
Ti-6Al-4V	6170	4430	0.19	0.81	13.9°	0.41	0.59	38.6°
Steel	5890	7800	0.12	0.88	14.6°	0.27	0.73	40.8°
Inconel	5720	8250	0.12	0.88	15.0°	0.26	0.74	42.3°

important for as-built AM parts that tend to have high surface roughness. Therefore, the sensitivity of UT to defect B in Figure 4-1 (b) would be very low since very little energy is able to penetrate through the three interfaces.

In addition to the impedance mismatch, the angle, α, formed by the incident wave with the normal to the surface, $\mathbf{n}$, can cause additional signal losses. As illustrated in Figure 4-1 (e), while the reflected wave emerges at the same angle as the incident one, the transmitted wave is refracted at an angle β that satisfies Snell's law, $\sin\beta = (c/c_w)\sin\alpha$, where c_w is the speed of sound in water and c is the velocity of compressional waves in the material of the part. Oblique incidence arises due to the shape of the ultrasonic beam excited by the transducers and the geometry of the part as depicted in the case of defect A in Figure 4-1 (b). With a wide transducer active area, the beam is narrow with most of the energy leaving the transducer in the direction normal to its active surface - the wavefield can be represented by a single ray orthogonal to the transducer as shown in Figure 4-1 (b). As the transducer diameter decreases, the beam widens and more energy begins to propagate at oblique angles [58]. Importantly, the principle of reciprocity ensures that the same dependence is observed when the transducer is used as a receiver. As a result, if the transducer above defect A of Figure 4-1 (b) is highly directional (wide), it will not be able to detect the surface of the component due to the specular reflection effect. On the other hand, the surface can be detected by using the narrower elements of a linear array that can insonify the surface from a broader range of angles and which

are more sensitive to waves reflected at oblique angles.

Oblique incidence also has an effect on the transmitted energy as now the reflection and transmission coefficients are no longer given by Equation 4.1. Typically, the transmission coefficient will decrease with α until the angle reaches a critical value $\alpha_{cr} = \arcsin(c_w/c)$ beyond which total reflection occurs and the transmitted wave becomes evanescent [59]. As shown in Table 4.1, α_{cr} is typically less than 15° for most metals. Therefore, in order to transmit ultrasonic energy inside the part the angle of incidence must be lower than 15° which is seldom the case in the presence of complex parts. Strictly, the previous analysis should also include a refracted shear vertical wave that is mode converted from the incident compressional wave since solids support the propagation of both compressional and shear waves. This chapter focuses on compressional waves because the mode converted shear waves are typically weak and are usually neglected in phased array inspections.

Finally, reverberation of ultrasonic waves between multiple interfaces pose a further challenge to UT. Figure 4-1 (f) illustrates this phenomenon for the simple case of a layer immersed in a liquid, which could represent a wall in a complex component. Due to multiple scattering the primary reflections from the top and bottom surface of the layer (R_1 and R_2) are followed by a train of reflections, R_3, R_4, ..., which in the seismic literature are referred to as internal multiples. Similarly, internal multiples, T_2, T_3, ..., follow the primary transmitted wave T_1. For the multilayered structure shown in Figure 4-1 (b), the elements of the array would record highly complex waveforms since the multiples from the shallower layers interfere with the primaries and multiples from the deeper layers - examples of such waveforms will be later given in Section 4.3. Internal multiples are not accounted for by conventional ultrasonic array imaging methods and therefore are a source of image artifacts.

From the example in Figure 4-1 it is clear that the physical phenomena that prevent the use of current ultrasonic techniques for the inspection of complex-shape parts can be seen as a consequence of the removal of material required to transform a simple shape solid, e.g. the cylinder in Figure 4-1 (a), into a complex geometry part, such as the impeller in Figure 4-1 (b). If the material could be temporarily

restored to transform the impeller back into a solid cylinder, standard ultrasonic inspections could be performed with high sensitivity. The central idea of this chapter is that this ideal condition could be approximated by encapsulating the component in ice. In fact, thanks to the higher ultrasonic velocity of ice relative to liquid water (c_{ice} =3850 m s^{-1} [60, 61]) transmission coefficients through ice-metal interfaces are more than double those between water and metal and most importantly the critical angle increases from around 15° to about 40° as shown in Table 4.1. Moreover, ice encapsulation is a practical and reversible process. Since the internal channels of complex shape parts are typically connected to the exterior, ice encapsulation can be obtained by immersing the part in water and subsequently freezing it. Thanks to the good adhesion properties of ice to non hydrophobic surfaces [62, 63, 64] or surfaces with some degree of roughness [65], freezing water in contact with the part prevents the loss of ultrasonic transmission that is observed at the interface between two solids in dry contact. Moreover, the process is reversible because ice can be simply melted away at the end of the inspection without leaving residuals on the component.

The fundamental hypothesis of this chapter is that detection of defects in a complex-shape component can be achieved in a nondestructive fashion by applying imaging methods to the ultrasonic signals measured by a transducer array that probes the component after it has been encapsulated in ice. Here, this approach is referred to as Cryoultrasonic NDE.

This chapter provides an initial assessment of the feasibility of Cryoultrasonic NDE through a series of model experiments that simulate parts of increasing geometrical complexity. We begin with a description of the experimental setup and imaging methods in Section 4.2, which is followed by experimental results in Section 4.3. The results are further discussed in Section 4.4 were future research avenues for Cryoultrasonic NDE are outlined. Concluding remarks are given in Section 4.5.

4.2 Methods

4.2.1 Experimental setup

To simulate components with internal vanes, two different sets of 50.8×152.4 mm^2 plates, referred to as Set #1 and Set #2, were arranged to form specimens containing a gap whose geometry could be adjusted using a system of spacers and screws as shown in Figure 4-2 (a). Set #1 consisted of one thick (25.4 mm) and one thin (12.7 mm) aluminum plates, with the thin plate containing three groups of holes introduced through electrical discharged machining (EDM) and with diameters ranging from 1.5 to 2.5 mm according to the diagram in Figure 4-2 (a). Set #2 was formed with the same thick plate as in Set #1 and a Ti-6Al-4V (Ti64) thin plate (12.7 mm) produced with the AM process (selective laser melting). The Ti64 plate did not contain defects and its surface was as built exhibiting a high roughness level, R_z >250 μm.

The specimens were ice encapsulated by immersing them in a distilled water bath which was first degassed at room temperature in a vacuum chamber and subsequently placed in a freezer at -17 C°. Figure 4-2 (b) is an example of the ice layer formed in the gap between the two plates of Set #1 when they are held parallel to each other. Thanks to vacuum degassing, the ice is free from bubbles; however, some transversal cracks caused by the expansion of freezing water are visible as indicated by the arrow.

Ultrasonic waveforms were acquired using a 10 MHz, 128-element linear array manufactured by Imasonic and impedance matched for water coupling. The array was either placed in contact with the thick aluminum plate or with the ice volume encapsulating the specimen. In both cases, salt water was used as ultrasonic couplant to avoid freezing at the transducer active surface. The elements of the array were 0.25×5 mm^2 in size resulting in an array aperture of 32 mm.

The array was driven by an AOS controller model OEM-PA 256/256. The system is based on a 256-channel, 14 bit, parallel architecture, operates over a 0.1 to 15 MHz bandwidth, and can perform the acquisition of all the 128×128 transmit-receive pairs that can be formed with the 128 elements of the array (FMC dataset) in under one

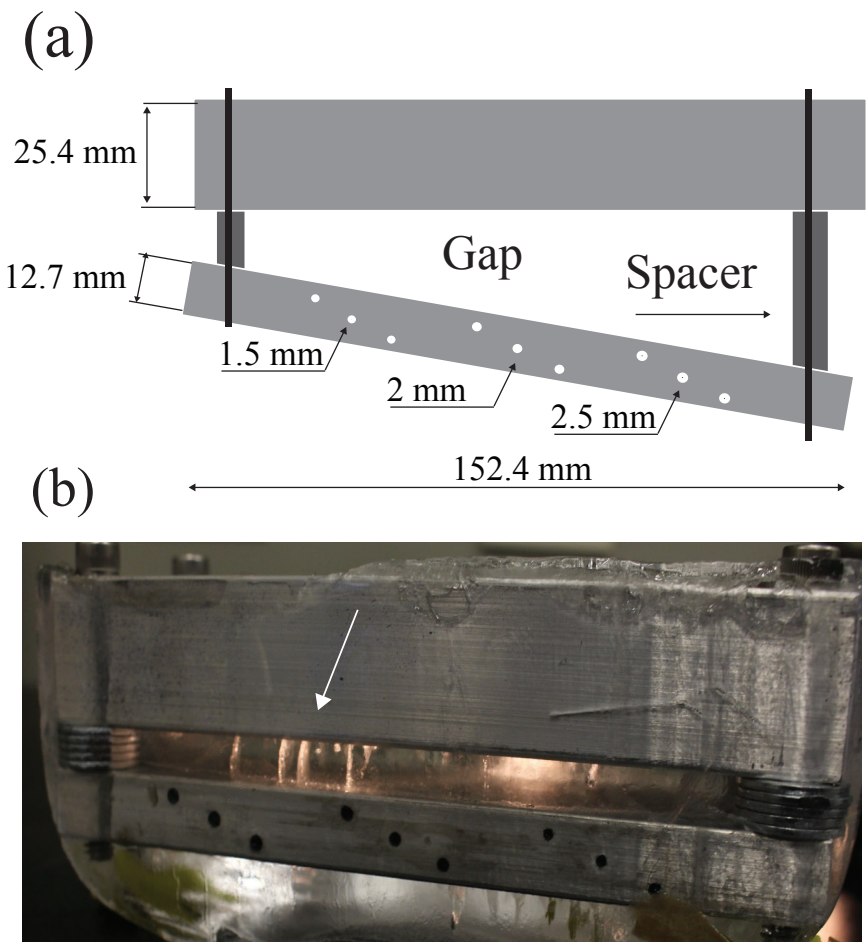

Figure 4-2: (a) Geometry of the Set #1 specimens; (b) Example of ice-encapsulated specimen - the arrow points at a region with cracks in the ice layer.

second. In these experiments the controller was driven from a PC using the AOS Matlab interface and fast data transfer between the controller and PC was achieved using 2 LAN ports with 1 GB capacity each.

4.2.2 Migration Imaging

Since the cross sections of an ice encapsulated part can exhibit a complex layered structure similar to that of the earth, migration algorithms developed for seismic imaging are best suited to image the interior of an ice encapsulated part. The principle behind migration imaging is that each point along an interface within an object acts

as a secondary source that launches a pulse at the exact time when the wave from the actual source reaches that point. To form the image two wavefields are considered. These are the incident wavefield generated by the source and the field that results from the extrapolation in space of the field received along the array aperture. The points in space where the two wavefields arrive simultaneously correspond to reflectors. Various migration methods have been proposed based on how the wavefield extrapolation is performed and how the condition of simultaneous arrival is imposed - most common migration techniques include Kirchhoff [66], Frequency-Wavenumber [67], Reverse-Time [68], Downward-Continuation [69], and Wave Equation [70]. In this study we use a form of Kirchhoff migration known as Diffraction migration [71] (DM). With reference to the diagram in Figure 4-1 (a), let $s_{ij}(t)$ be the waveform recorded by the i-th element of the array when the j-th element transmits, and $a_{ij}(t) = s_{ij}(t) + i\mathtt{H}[s_{ij}(t)]$ the complex analytical signal derived from $s_{ij}(t)$ in which $\mathtt{H}$ represents the Hilbert transform. Moreover, let $\{O, x_1, x_2, x_3\}$ be a system of Cartesian coordinates with the origin O coincident with the center of the array active surface, the x_1 axis passing through the centers of all the array elements, and the x_3 axis orthogonal to the array active surface so that the $x_2 = 0$ plane is coincident with the so-called azimuth plane according to the diagram in Figure 4-1 (a). The position of a point P in the azimuth plane is determined by a vector $\mathbf{x} \in \mathbb{R}^3$ of coordinates $(x_1, 0, x_3)$. An image of the component in the azimuth plane is obtained by discretizing the plane into a regular grid of points and evaluating at each node, $\mathbf{x}$, the image value, $I(\mathbf{x})$, through

$$I(\mathbf{x}) = \left| \sum_{i=1}^{N} \sum_{j=1}^{N} a_{ij}[\tau(\mathbf{x}, \mathbf{e}_j) + \tau(\mathbf{e}_i, \mathbf{x})] \right|, \tag{4.2}$$

where N is the number of array elements, $|\cdot|$ denotes the modulus, and the function $\tau(\mathbf{r}, \mathbf{s})$ is the least traveltime from a source at $\mathbf{s}$ to a receiver at $\mathbf{r}$ according to Fermat's principle. Moreover, $\tau(\mathbf{r}, \mathbf{s}) = \tau(\mathbf{s}, \mathbf{r})$ by reciprocity. Therefore, in Equation 4.2 the analytical signal is evaluated at the time corresponding to the total traveltime from the source array element centered at $\mathbf{e}_j$ to pixel $\mathbf{x}$ and from pixel $\mathbf{x}$ to the receiver element at $\mathbf{e}_i$. This imaging method is in fact equivalent to that described

in Section 3.2.1; however, the redundancy is justified as establishing this connection to migration methods suggests avenues for potential improvement in NDE imaging algorithms parallel to recent advancements in migration imaging.

4.2.3 Travel time Computation

The traveltime functions in Equation 4.2 are computed as in Chapter 3 using a FMM method discussed in Section 2.3. In order to employ this method one must first assign a sound speed (SS) map that describes how $c(\mathbf{x})$ varies in space and then solve the eikonal equation. In principle, the SS map could be built by using the CAD model of the part to extract the geometrical characteristics of the section beneath the array. The known ultrasonic velocity of the material of the part and the velocity of ice would then be assigned to the corresponding layers. However, this approach poses two challenges. First, due to manufacturing tolerances the CAD model may not provide a sufficiently accurate representation of the geometry of the part. Secondly, for imaging purposes the position of the array relative to the part must be known. A more robust approach is to form the SS map by extracting the geometry of the different part-ice interfaces from the CAD model and then using the ultrasonic signals to correctly position the interfaces relative to the array. For the specimens considered in this study the interfaces are straight lines which are positioned one at the time starting from the one closest to the array. To position the first interface the SS map is set to be uniform and equal to the velocity of the first layer beneath the array. From this map the traveltime functions are estimated and used together with the FMC data in Equation 4.2 to reconstruct the initial outline of the first interface. The nominal geometry of the first interface (straight line in this study) is then best fitted to the ultrasonic outline to provide an updated SS map consisting of the geometry of the first layer bounding a half space with the same velocity as the second layer. The updated model is then used to calculate the traveltimes inside the second layer and hence form the ultrasonic outline of the second interface. From this the SS map is again updated using the CAD model. This process is repeated until all the interfaces are positioned.

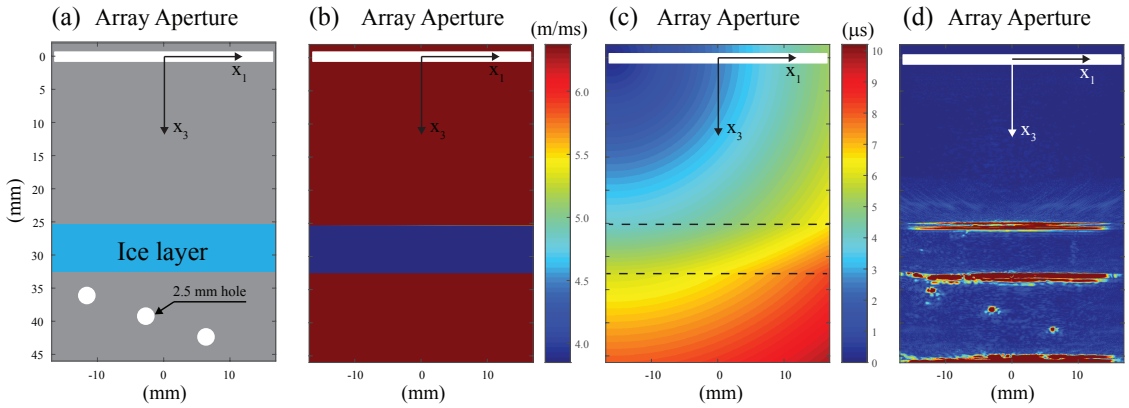

Figure 4-3: Migration imaging of an ice-encapsulated specimen. (a) Geometry of the specimen section below the array aperture; (b) Sound speed map used to compute traveltimes; (c) Example of traveltime map when the element at $x_1 = -16$ mm transmits; (d) Diffraction migration image.

4.3 Results

Figure 4-3 summarizes the image formation process for the data recorded with the specimen shown in Figure 4-2 (b) when the array aperture is in contact with the thick plate and over the 2.5 mm diameter set of holes (left side of the photograph). Figure 4-3 (a) is a diagram of the area directly beneath the array aperture. The corresponding SS map obtained at the end of the iterative scheme described in Section 4.2.3 is shown in Figure 4-3 (b) - note that the map does not include the holes. Figure 4-3 (c) provides an example of traveltime map $\tau(\mathbf{x}, \mathbf{e}_1)$ corresponding to the SS map in Figure 4-3 (b) for any point $\mathbf{x}$ in the azimuth plane when the first element of the array, $\mathbf{e}_1 \equiv (-16, 0, 0)$, transmits. To compute the expression in Equation 4.2 128 traveltime maps need to be computed - one for each source in the array. Figure 4-2 (d) shows the reconstructed cross section of the ice-encapsulated specimen along the azimuth plane obtained through Equation 4.2. The image correctly reconstructs the interfaces of the ice layer, the backwall of the thin plate, and most importantly it provides a clear indication of the presence of the three holes. Moreover, the presence of cracks in the ice layer above the defects does not appear to cause image degradation. Indeed, the fact that the cracks are detectable under visible light does not necessarily mean that they can be detected by ultrasonic waves given that the wavelength of

ultrasound in ice (λ 400 μm at 10 MHz) is some three orders of magnitude larger that the wavelength of light.

To illustrate the benefit of ice encapsulation, Figure 4-4 (a) shows the DM image obtained when the gap between the plates in Figure 4-3 (a) is filled with liquid water - the SS map is now updated to account for the correct speed of sound in the gap (1480 m s^{-1} versus 3850 m s^{-1}). Compared to the image obtained under ice encapsulation, Figure 4-4 (b), the image in immersion shows a higher level of noise and the appearance of three line artifacts pointed by the arrows. The artifacts are caused by surface waves traveling at the metal-water interfaces and by strong multiples inside the thick aluminum plate. The multiples produce the artifact that interferes with the central hole and which significantly degrades the quality of the image inside the thin plate. Such an effect is not present with ice encapsulation because the primary reflections from inside the thin plate arrive before any multiples inside the thick plate. The presence of internal multiples is apparent when considering the ultrasonic waveforms. As an example, Figure 4-4 (c) and (d) show the 128 signals received when the first array element transmits and the gap is filled with liquid water and ice, respectively. For each receiver, more pulses are present when the gap is filled with liquid water due to the water-aluminum impedance contrast being about 2.5 times higher than that between ice and aluminum. Therefore, energy tends to be trapped between the thick plate and the liquid layer resulting in a long train of reverberations. Instead, the ice layer is more effective in radiating the energy in the downward direction resulting in weaker reverberations.

Figure 4-5 shows the results of DM for the ultrasonic data measured when the array was placed in contact with the thick plate over the central set of holes (2.0 mm diameter) and the thin plate was rotated by 15° according to the diagram in Figure 4-5 (a). The reconstructions obtained when the gap is filled with ice and liquid water are shown in Figure 4-5 (b) and (c), respectively. Ice encapsulation leads to the detection of the three central holes (2.0 mm diameter) as well as the smallest set (1.5 mm diameter) on the left side of the array thanks to the remarkably wide field of view produced by ray bending. Because of refraction, the aluminum-ice interfaces of the

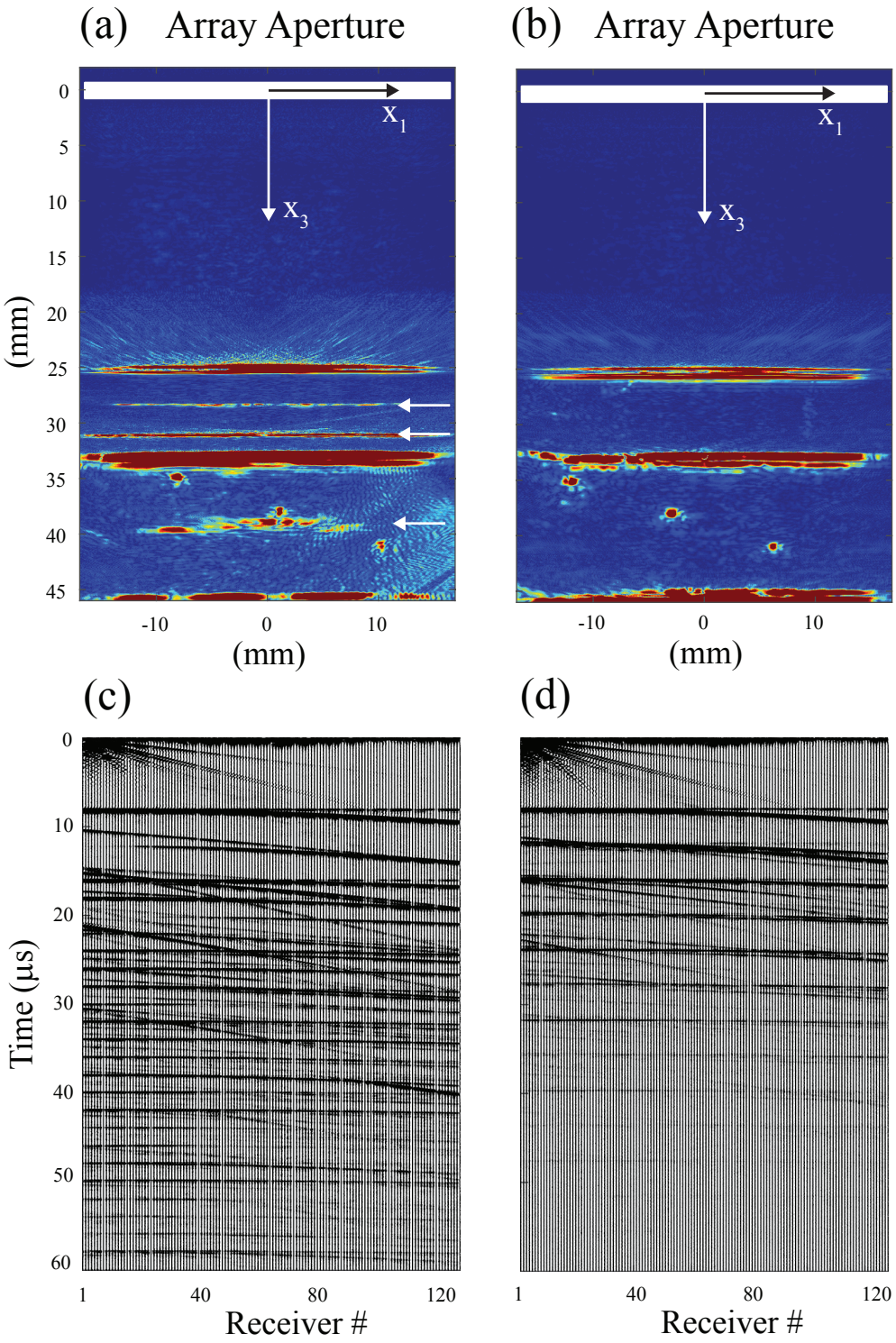

Figure 4-4: Water immersion, (a) and (c), versus ice encapsulation, (b) and (d). (a) and (b) Diffraction migration images - arrows in (a) indicate artifacts; (c) and (d) 128 waveforms recorder across the array aperture when the element at $x_1 = -16$ mm transmits.

thin plate are not reconstructed directly beneath the array aperture but are instead skewed to the left - the 25° angle in Figure 4-5 (a) is obtained by applying Snell's law and imposing normal incidence on the thin plate. This effect however does not prevent the detection of the central set of holes since they scatter the incident field

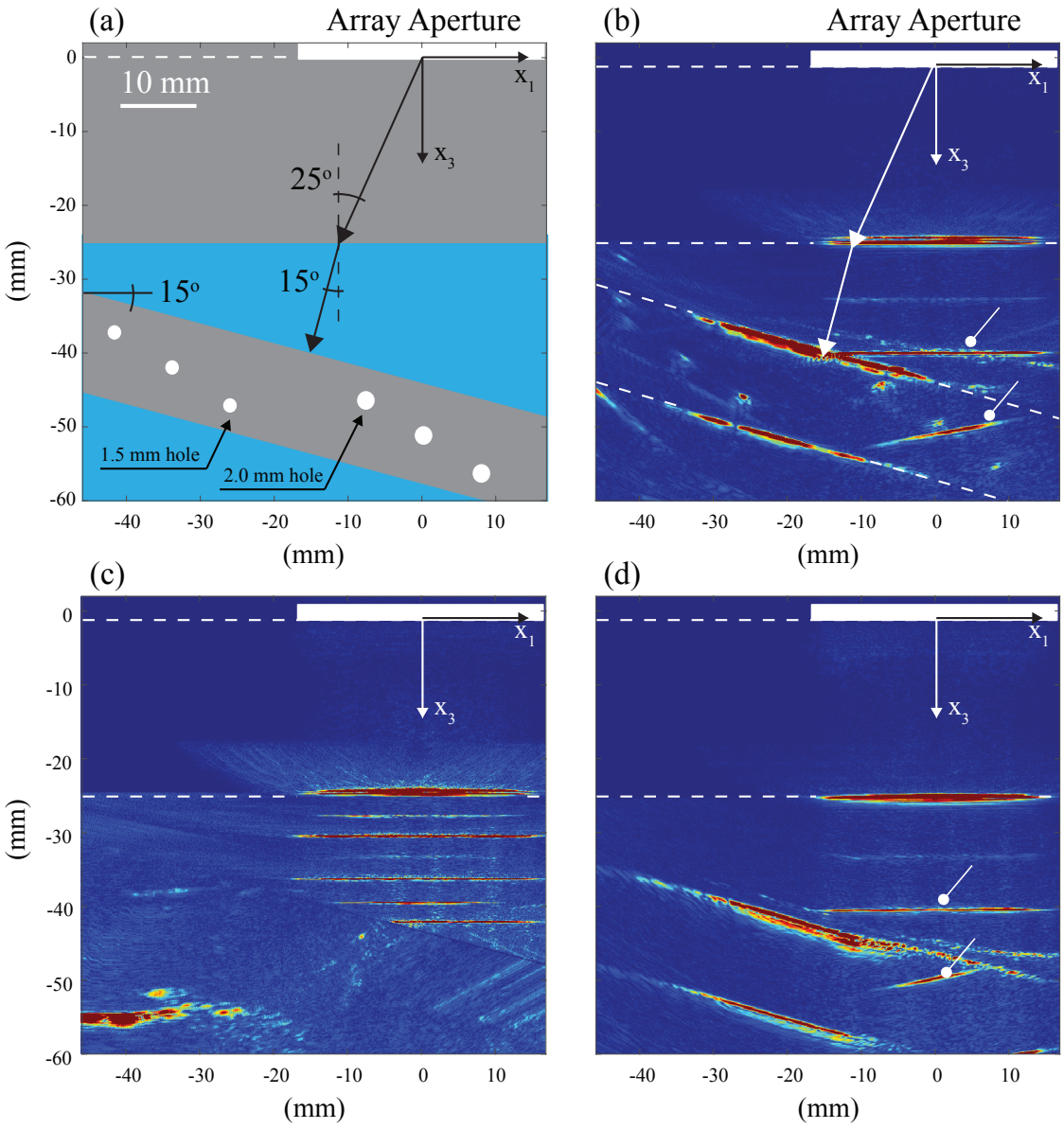

Figure 4-5: (a) Specimen geometry relative to the array aperture - the arrows show the path of one of the most energized rays; (b) DM under ice encapsulation - round ended arrows indicate artifacts; (c) DM under water immersion; (d) Same as (b) but with the thin aluminum plate replaced by a 3-D printed Ti64 plate of the same thickness with as-built surface roughness - the Ti64 plate does not contain defects.

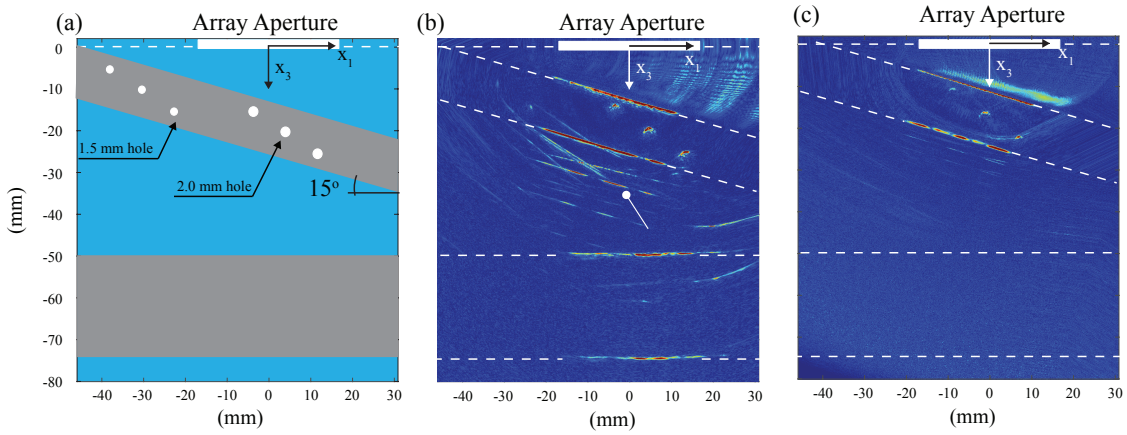

Figure 4-6: Effect of array probe coupling. (a) Experimental configuration showing the probe at a standoff distance in ice or water from the thin plate; (b) DM image obtained under ice encapsulation; (c) DM image obtained in water immersion.

over a broader range of angles. The artifacts indicated by the round ended arrows in Figure 4-5(b) are due to the relatively large thickness of the ice wedge on the right side of the array which causes the multiples inside the thick aluminum plate to arrive before the primary reflections from the thin plate. As in the case of the image in Figure 4-4 (a) DM is only able to interpret the information contained in the primary waves while the internal multiples appear as artifacts. Nevertheless, the DM image obtained under ice encapsulation provides a dramatic improvement compared to the image formed in immersion, Figure 4-5 (c). Here, neither the front surface of the thin plate nor the internal holes are reconstructed due to extreme ray bending and the fact that many rays experience total internal reflection as the inclination of the plate is beyond the 13.5° critical angle. Finally, Figure 4-5 (d) shows the DM reconstruction obtained when the thin aluminum plate is replaced with the 3-D printed Ti64 plate of the same thickness and the specimen is ice encapsulated - note that the Ti64 plate does not contain holes. In spite of the impedance of Ti64 being about 1.6 times larger than that of aluminum and the high surface roughness of the Ti64 plate ($R_z > 250$ μm), DM is able to reconstruct both the front and back surfaces of the thin plate with the same contrast obtained with the thin aluminum plate - note that the position of the array relative to the specimen in Figure 4-5 (d) is slightly different from that in Figure 4-5 (b).

Figure 4-6 shows the DM images obtained when the specimen in Figure 4-3 was flipped upside down and tested after ice encapsulation, Figure 4-6 (b), and water immersion, Figure 4-6 (c). In the former configuration the probe was placed in contact with the ice volume above the thin plate while in the latter water coupling was used. Ice encapsulation leads to a clear reconstruction of the three 2 mm diameter holes inside the thin plate and provides an indication of two of the three 1.5 mm diameter holes to left. Importantly, the ultrasonic signal is able to penetrate through three ice-aluminum interfaces to reconstruct the front and back interfaces of the thick plate at the bottom. As in previous cases, internal multiples lead to line artifacts that partially degrade the image. On the other hand, under water immersion no signal is detected beyond the arrivals corresponding to the backwall of the thin plate and the thick plate is not reconstructed, Figure 4-6 (c). Additionally, a strong artifact is observed in close proximity to the front surface of the thin plate which is due to large amplitude surface waves traveling at the aluminum-water interface. It should be stressed that the electronic gain settings between the ice encapsulation and water immersion measurements were kept the same. Moreover, the array probe is matched for water coupling which means that the signals excited by the array in water have larger amplitude than those excited in ice and that the array has greater sensitivity to signals reflected in water than in ice. Therefore, the poor image quality obtained in immersion despite the ideal probe coupling conditions further demonstrates the benefit of ice encapsulation.

4.4 Discussion

From the initial investigation presented in this chapter, the freezing process for ice encapsulation and the removal of image artifacts caused by internal multiples have emerged as two areas that require further development as discussed next.

When a water volume is placed inside a conventional freezer, it starts to freeze from its external surface forming a solid shell that tends to trap any residual gas phase in a cloud of bubbles around the core of the ice block. In addition, when

the liquid core solidifies it expands against the shell causing the build up of stresses and possibly leading to cracking. To avoid the formation of the shell, a planar ice front propagating in a single direction is desirable. This can be achieved by placing the liquid water in insulated chambers in which only the top [72] or bottom [73] is cooled. Moreover, controlling the cooling rate determines the speed of propagation of the ice front which is critical to the clarity of the ice volume. In fact, the front speed determines whether particles and other impurities present in the liquid phase are encapsulated in the ice or simply pushed away by the front [74]. Additionally, a front propagating at a sufficiently slow speed allows stresses resulting from the expansion of freezing water to be released thus preventing the formation of cracks in the ice volume. In this context, it should be noted that while the contact pressure that results from the expansion of water inside the vanes of a component improves the transfer of ultrasonic energy through the part-ice interfaces [75], it also generates a state of stress inside the material of the part which, if excessive, may cause its plastic deformation or even fracture in the case of low strength brittle materials. The pressure level is typically insufficient to cause damage when the liquid water stays at atmospheric pressure during freezing; indeed under these conditions the compressive strength of ice is relatively low, 5 MPa at -10 °C [76]. However, if the liquid water pressure can increase and equal the ice pressure during freezing, compressive stresses in the order of 100 MPa or more can be observed [77]. For the high liquid pressure condition to occur, it is necessary that first ice plugs form at the ends of vanes or channels so as to seal a liquid water volume inside them. Then as water freezes within such confined volumes pressure can increase as described in Ref. [78]. To prevent the formation of ice plugs it is sufficient to limit the cooling rate so as to slow down the freezing process. As a result, specialized freezers that can achieve unidirectional ice front propagation and can regulate its speed are desirable to achieve optimal ice encapsulation.

The artifacts in the cryoultrosonic image caused by internal multiples can be addressed with a combination of improved ice properties and more advanced imaging methods. If the ultrasonic impedance of ice could be increased to better match that

of typical metals, the internal multiple would weaken significantly and with them the image artifacts. One possibility is to freeze colloidal particle suspensions instead of pure water. The use of high density small diameter particles (micrometer scale or less) could greatly increase the effective mass density of the resulting ice composite and to a smaller extent its ultrasonic velocity. This would be similar to the effect that tungsten powder has on the properties of the backing material used in conventional ultrasonic transducers. Clearly, it is essential to formulate the suspension so that the overall attenuation of the ice composite is limited. Increasing the impedance of ice would also make linear arrays more effective in imaging through highly curved 3-D surfaces since scattering off the azimuth plane of the array would be reduced.

The DM method used in this study is one of the first migration techniques introduced in seismic imaging. Indeed, there are many similarities between the imaging problem considered in this chapter and seismic imaging due to the marked layered structure of the earth. As a result, internal multiples have long been studied by the seismic imaging community. While several signal processing techniques have been proposed to remove the multiples from the waveforms before forming the images [79, 80, 81, 82, 83], their effectiveness is somewhat limited and today's trend in seismic imaging is to use more advanced imaging methods that include multiples in the inversion since it has been recognized that they encode additional information that can improve image quality [84, 85, 86, 87]. These results are remarkable because multiples cover larger distances than primary waves and therefore are more susceptible to errors in the *long scale* macromodel used to approximate the earth SS map. This suggests that the benefit of multiples in Cryoultrasonic NDE may be even greater since the SS map of an ice-encapsulated part is known with higher accuracy than the macromodel of the earth.

4.5 Conclusions

The inspection of complex-shape components, which may include the presence of internal vanes and channels, represents an open challenge for existing NDE techniques.

This chapter has proposed a new inspection principle whereby the component is encapsulated in ice to form a simple shape solid that can be inspected with ultrasonic waves. The idea of adding material (ice) to the component deviates from conventional NDE methods that do not modify the physical characteristics of the object under inspection. Once the part has been encapsulated, defect detection is achieved by analyzing cross-sectional images, similar to those obtained with x-ray CT, and formed from the signals measured by an array of ultrasonic transducers. The process, which here has been referred to as Cryoultrasonic NDE, is entirely reversible and nondestructive as the ice can be melted away at the end of the inspection without causing damage or leaving residuals on the part.

Model experiments performed with specimens simulating parts containing internal vanes have shown the potential of Cryoultrasonic NDE for the detection of damage inside the internal walls of a complex component. Thanks to the good adhesion properties of ice to metals, ultrasonic penetration through multiple ice-metal interfaces, including slanted surfaces, was achieved that enabled the reconstruction of the internal features of the specimens including defects. Ice coupling also limited the effect of surface roughness as demonstrated in the case of the as-built surface of an additively manufactured Ti64 specimen.

For each specimen, experiments were performed under both ice encapsulation and water immersion. The former consistently outperformed the latter since immersion testing suffers from limitations dictated by the large impedance mismatch between water and typical metals. Because the speed of compressional waves in ice is more than 2.5 times higher than the speed in water, the transmission coefficient through an ice-metal interface is typically more than twice that observed for a water-metal interface. Most importantly, the critical angle of incidence beyond which no transmission occurs in the metal increases from around 15° in immersion to about 40° under ice encapsulation. Here lies the main advantage of cryoultrasonics since the slanted interfaces of complex parts can lead to very large angles of incidence.

From this study it has also emerged that the presence of internal ultrasonic reverberations in the ice-encapsulated part leads to image artifacts that may affect defect

detectability. A strategy to minimize these artifacts has been proposed as the future development of Cryoultrasonic NDE. Specifically, it has been suggested that the reverberations could be weakened by increasing the impedance of ice. Additionally, any residual reverberation could be treated using new migration techniques that have been developed in seismic imaging to address the very same challenge.

Chapter 5

Matrix phased arrays for image formation through out of plane curvature

5.1 Introduction

In Chapters 3 and 4 the problem of forming an image from phased array measurements is reduced to two dimensions by the assumption that curvature in the direction orthogonal to the image plane, what is here referred to as out of plane curvature, can be neglected. This assumption is valid where it is previously made; however, there are regions of the PMC turbine blades mentioned in Chapter 3 where the surfaces of the blade are not approximately parallel along any direction, and the additively manufactured impellers referred to in Chapter 4 exhibit complicated 3-D curvature in their internal structure. Therefore, overcoming the limitation that the inability to account for out of plane curvature places on the applicability of these methods is important if UT is to become a viable alternative to X-Ray CT for the inspection of complex geometries. In this chapter we will perform an initial study using matrix arrays to account for out of plane curvature, and will compare the performance to linear arrays in similar measurement configurations.

Matrix arrays differ from linear arrays in that their elements are arranged in a 2-D rather than a linear aperture. This gives matrix arrays an extra degree of freedom which allows them to focus on locations within a 3-D volume beneath the array, and allows them to implement focal laws which account for fully 3-D curvature at the interface between the coupling medium and the specimen. Matrix arrays have long been studied in the context of medical imaging [88], and have been used in specific clinical applications such as imaging of the heart [89]. In medical ultrasound applications the velocity of sound in the coupling medium is nearly identical to that in tissue; therefore, there is no need to account for refraction when programming the individual delays applied to each element in transmission and reception. The advantage that matrix arrays have in this context is that they have the ability to image volumes of tissue without mechanical scanning of the probe. This differs from the application being studied in this chapter as here we are specifically studying the ability to form a 2-D cross sectional image while accounting for the 3-D refraction occurring at the interface between the coupling medium and the specimen.

Section 5.2 will describe the specimen and measurement setup used in the study. The imaging algorithm and the additional complexities encountered when considering 3-D curvature are discussed in Section 5.3. Some images formed with linear and matrix arrays are compared in Section 5.4 and the results will be discussed in Section 5.5.

5.2 Experimental setup

All experiments are performed on a cylindrical aluminum specimen which has been bisected along the azimuthal axis. The inner surface of the specimen consists of two inner diameters joined by a conical section, as shown in Figure 5-1. The diffraction migration imaging algorithm used in Chapter 4 is used here without alteration, along with the coordinate system $\{O, x_1, x_2, x_3\}$. The coordinate x_1 is measured along the azimuthal axis of the cylinder, x_3 is orthogonal to the surface along which the cylinder has been bisected, and the image planes are defined orthogonally to the x_2 axis. The

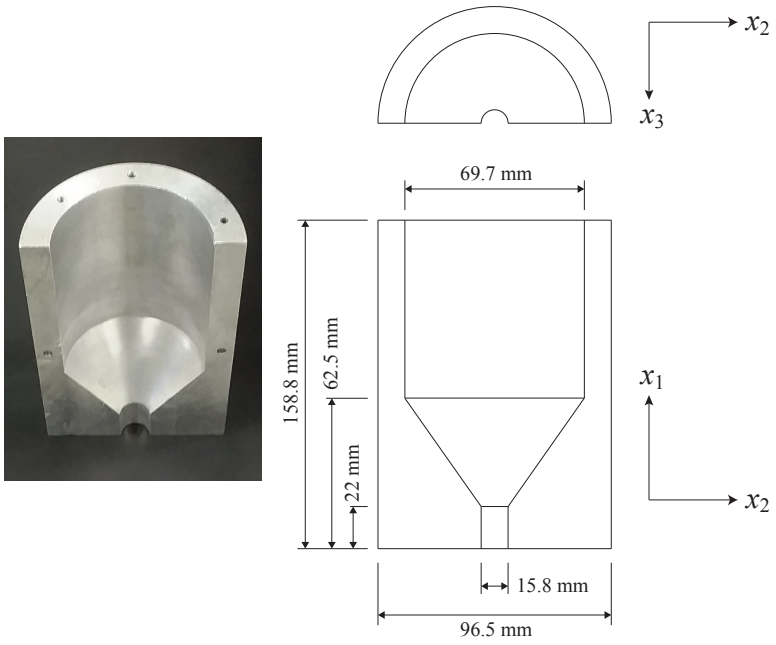

Figure 5-1: Schematic showing geometry of aluminum test piece.

effect that different levels of out of plane curvature have on the imaging algorithm's ability to reconstruct the specimen's inner surface are evaluated by forming images in the x_1x_3 plane while the arrays are held at various positions in the x_2 direction.

The specimen is immersed in water to provide coupling and two arrays are used to perform measurements; one linear and one matrix. The linear array is an Olympus 5 MHz probe with 128 elements separated at 0.31 mm pitch in the x_1 direction and a width of 5 mm in the x_2 direction. The matrix array is an Imasonic 5 MHz probe with 256 elements which are separated at 0.6 mm pitch in both the x_1 and x_2 directions, with the elements arranged in the pattern shown in Figure 5-2 (a). The arrays are mounted to a two-axis traverse and measurements are obtained at the locations shown in Figure 5-2 (b) and (c) for the matrix and linear arrays, respectively. Here the internal geometry of the specimen relative to the measurement locations is sketched for reference. The five measurement locations taken in the x_1 direction with the linear array provide a similar area of coverage in that direction to the one measurement taken by the linear array due to the smaller size of the active length of the matrix array in the x_1 direction. The arrays are driven using the same 256 channel AOS controller

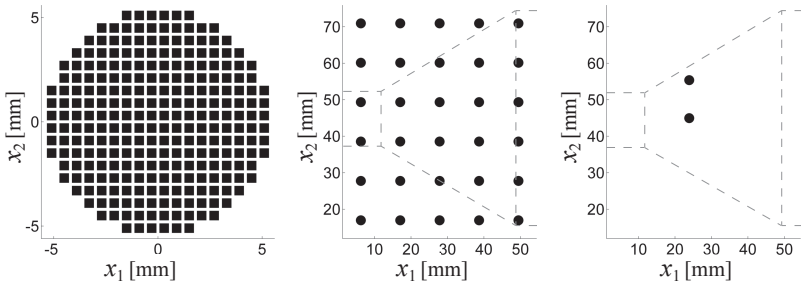

(a) (b) (c)

Figure 5-2: Diagrams of transducer element arrangement and measurement positions. (a) Arrangement of 256 elements in matrix array. (b) Positions at which measurements were taken with matrix array. Relative position of interior geometry of specimen is sketched for reference. (c) Positions at which measurements were taken with linear array.

described in Section 4.2.1.

5.3 Methods

All images are formed using the Diffraction Migration algorithm expressed in Equation 4.2. The key difference when forming matrix array images here is that the travel-time fields τ are calculated in a 3-D domain containing the array positions and the specimen. The sound speed model is constructed by taking initial images which assume that the domain contains only water ($c = 1480\,\mathrm{m/s}$). The reflections from the cylindrical interface allow for the location of the specimen to be determined, and the speed of sound within the area defined by the outer diameter of the specimen is assumed to be $6300\,\mathrm{m/s}$. The travel-time fields describing the wavefront propagation from each element location at each scan position are then calculated using the Fast Marching Method described in Section 2.3. When forming images from data taken with the matrix probe, multiple scan positions are included in the image formation; this is done by simply adding the image contribution from each scan position before taking the modulus in Equation 4.2.

5.3.1 Complexity

The computational complexity and memory requirements associated with the work done in this chapter are dramatically higher than those of the work performed in Chapter 4. Due to the double summation in Equation 4.2, the computational complexity of the imaging algorithm grows with the square of the number of elements. Therefore, going from 128 to 256 transducers and including five positions leads to a factor of 20 slow-down in image formation. Calculation of the focal laws is now being done in 3-D, which does incur a cost in computational speed, as the traveltime field for each element takes approximately 2.5 s to compute, but more importantly leads to enormous memory requirements. At a simulation resolution of 0.25 mm, the full travel-time fields for 256 transducers at 10 scan locations occupy over 60 GB of memory, which is more than most desktop computers can hold in random access memory at the time of this publication. These issues of increased computational complexity and memory requirements led to processing times of over one hour for each matrix-array image shown in Section 5.4.

This processing time is quite long. However, it may not be prohibitive in some contexts, for example in the cryoultrasonic inspection proposed in Chapter 4 which already involves a freezing and thawing process which could require an amount of time which is on the same order as the processing time. There are also many optimizations which could be investigated to reduce the processing time, including GPU computing techniques for the travel-time calculation [90] and image formation [91].

5.4 Results

Figure 5-3 shows two images formed using the linear array. The image in Figure 5-3 (a) is formed with the array aligned with the azimuthal axis of the specimen, as marked by the circle in the diagram in the left column of the figure. The image is formed in the plane indicated by the red dotted line in the left diagram, and the dotted rectangle shown in the central diagram which is drawn relative to the cross-section of the specimen taken in the image plane. This cross-sectional geometry is overlaid in

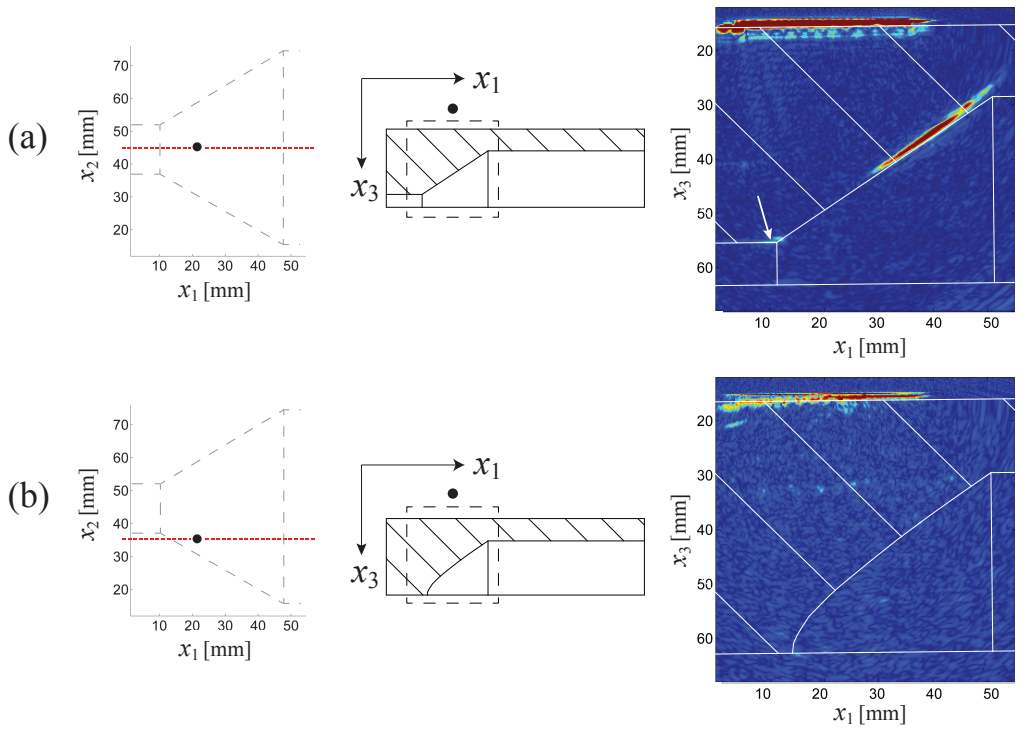

Figure 5-3: Images formed from linear array. Left diagrams shows x_2 location of image plane relative to specimen geometry. Central diagrams show cross section of cylinder in the image plane, with the dashed rectangles marking the image bounds. Circles mark measurement locations used in image formation. (a) Image formed along central plane of the specimen. Arrow indicates weak reflection at small inner diameter of specimen. (b) Image formed in a plane shifted by 10 mm from central plane. The internal geometry of the specimen is no longer visible.

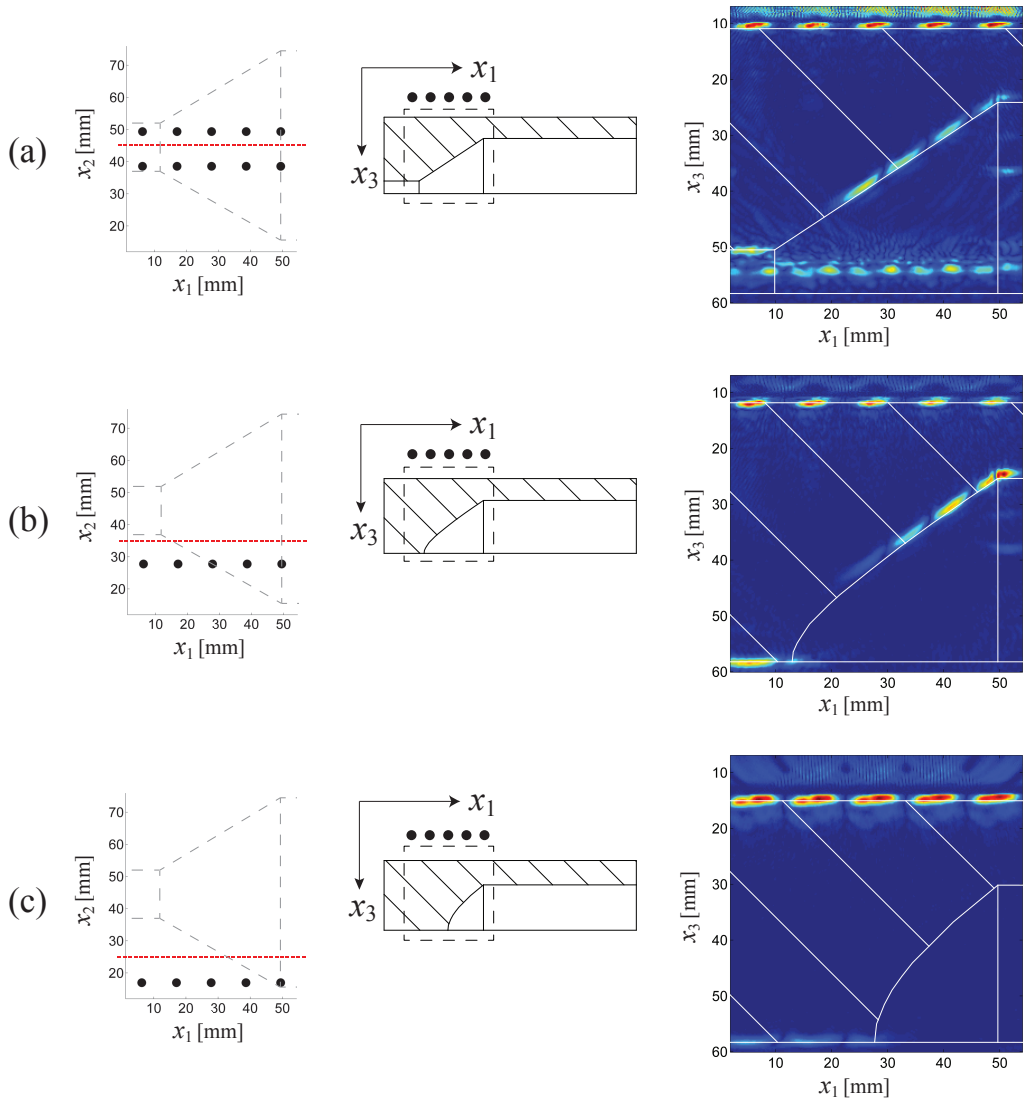

Figure 5-4: Images formed from matrix array. Left diagrams shows x_2 location of image plane relative to specimen geometry. Central diagrams show cross section of cylinder in the image plane, with the dashed rectangles marking the image bounds. Circles mark measurement locations used in image formation. (a) Image formed along central plane of the specimen. The noise at $x_3 = 55\,\text{mm}$ is caused by the second reflection from the top of the specimen in water. (b) Image formed in a plane shifted by 10 mm from central plane. (c) Image formed in a plane shifted by 20 mm from central plane.

white across the image, which shows strong reflections at the water-specimen interface at $x_3 = 17\,\text{mm}$ and at the conical inner geometry of the specimen. The reflection from the small inner diameter of the specimen at $x_3 = 55\,\text{mm}$ (see arrow in Figure 5-3 (a)) is very weak due to the divergence of the ultrasonic beam in the x_2 direction caused by the out of plane curvature of the cylinder. The effect of the increased out of plane curvature encountered by moving the probe by 10 mm in the x_2 direction is illustrated in Figure 5-3 (b), where the reflection from the interface is still clearly visible, but no reflections from the internal geometry can be resolved.

The images formed using the matrix-array are shown in Figure 5-4. Here a pattern of five bright and dark region along the reflectors corresponds to the five scan positions of the probe. Multiple scan positions are used with the matrix array in order to obtain a similar area of coverage with the two methods, as the aperture of the linear array is approximately 40 mm in the x_1 direction while the corresponding aperture of the matrix array is approximately 10 mm. Since only one measurement from the linear array is used to form each image this effect is not present in Figure 5-3. The image formed central to the azimuthal axis in Figure 5-4 (a) again shows strong reflections from the water specimen interface at $x_3 = 11\,\text{mm}$ and the conical inner surface; however, the reflection from the small inner diameter at $x_3 = 50\,\text{mm}$ is now much stronger as the focused beam is no longer diverging at the cylindrical interface. Also visible at $x_3 = 55\,\text{mm}$ is an artifact caused by the second reflection between the probe face and the specimen, which is not visible in the linear images due to the 5 mm difference in vertical positioning between the two measurements. The image formed at $x_2 = 10\,\text{mm}$ now clearly shows reflections from the conical inner surface and the larger and smaller inner diameters, which is a marked difference from Figure 5-3 (b). A further offset of $x_2 = 20\,\text{mm}$ is shown in Figure 5-4 (c), where a weak reflection from the bottom of the specimen can be seen at $x_3 = 58\,\text{mm}$, but the reflection from the conical inner surface is not recovered due to the orientation of the surface directing most of the reflected energy in the $-x_2$ direction away from the probe.

5.5 Conclusions

Ultrasonic testing of complex geometries remains an open challenge. Many initial efforts to develop ultrasonic imaging methods for complex geometries assume that the curvature of the specimen in the direction orthogonal to the image plane can be neglected. While this is a useful and a necessary first step, many real world applications involve complex 3-D geometries which cannot be sufficiently described by a 2-D model, and therefore the problem of out of plane curvature must be addressed. This work has investigated the use of matrix phased arrays to incorporate information about out of plane curvature into the focal laws used to form cross-sectional images of the interior of a specimen.

Experiments are performed on a cylindrical specimen in order to allow for the amount of out of plane curvature encountered in water-specimen interface beneath the probe to be controlled by changing the position of the probe. Images formed using linear arrays with a 2-D wavefront traveltime model are compared to those formed using matrix arrays with a 3-D model. The images formed using the matrix array clearly exhibit a superior ability to resolve the inner structure of the specimen when out of plane curvature is present.

Chapter 6

Acoustic formulation of elastic guided wave propagation and scattering in curved tubular structures

6.1 Introduction

Life management of complex industrial assets often requires continuous monitoring of corrosion and erosion damage. For instance, in the oil and gas industry, estimating the corrosion rates of pipe networks is essential to ensure the cost-effective operation of both the upstream exploration and production, and the downstream refining [92, 93]. Due to the large extent of typical pipe networks, a now widely used inspection method employs guided ultrasonic waves which travel within the wall of a pipe and can propagate over a large distance from a single transducer position [56]. While commercially available guided wave systems provide effective, long-range screening tools for defect detection [94, 95, 96], characterization of damage extent, particularly depth, remains an open challenge especially with irregularly shaped defects [97]. The problem is even more acute when considering defects in complex sections of pipelines such as joints and bends which are also the most susceptible to developing damage.

Guided wave tomography (GWT) has attracted renewed interest as a potential

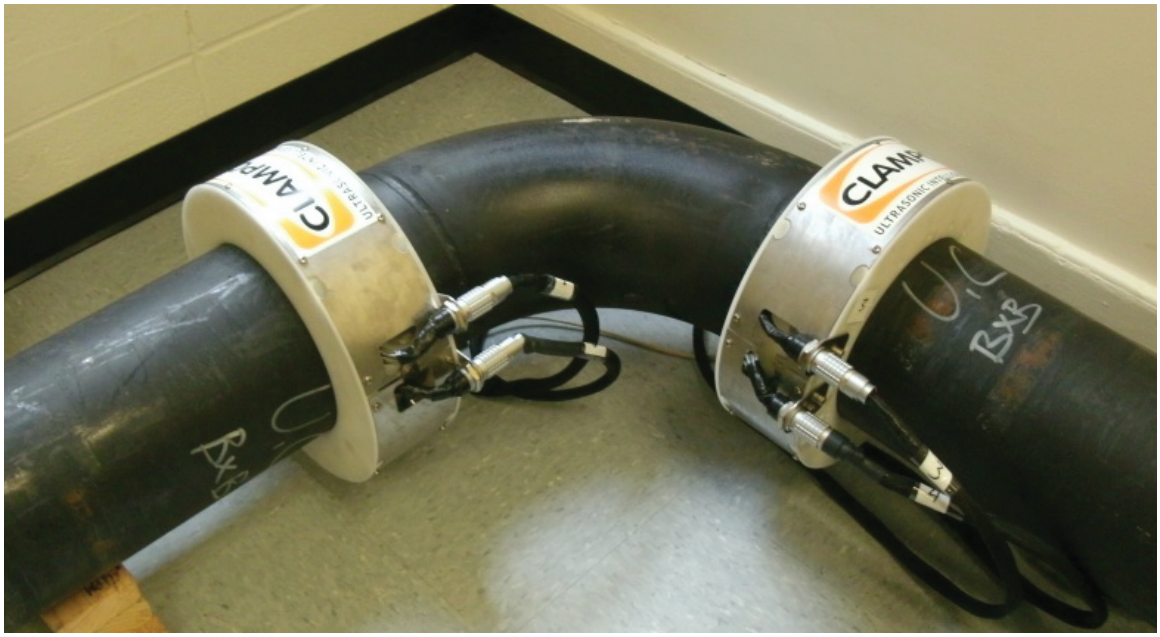

Figure 6-1: Example of inspection configuration for guided wave tomography of pipe bends. Two ring arrays of ultrasonic transducers are mounted at the ends of the bend along the straight sections of the pipeline. Transmit-receive pairs are then formed with the transducers of the two arrays to propagate guided wave signals inside the thickness of the pipe wall and across the bend.

approach to ameliorate the depth estimation of guided wave inspections in targeted locations [98, 99, 100, 101]. In a possible GWT test configuration, a pair of transmit- and receive-ring arrays of ultrasonic transducers encircle the pipe and delimit the section to be monitored as shown in Figure 6-1. The arrays are used to transmit guided wave signals from any transducer of the transmit array to any transducer of the receive array, thus insonifying potential defects from multiple angles. Each transmitted signal encodes information about the defect geometrical characteristics which are then decoded exploiting the complementary information carried by multiple transmission signals, hereafter referred to as the angular diversity of the measurements.

The depth profile of the defect can be reconstructed by solving an inverse problem which takes as an input the transmission measurements and returns a point-by-point map of wall thickness loss. The inverse problem is typically solved using iterative schemes based on a forward solver and a backprojection algorithm. The forward solver is a numerical implementation of the set of differential equations governing the

interaction of guided waves with defects and allows synthetic transmission measurements to be predicted for a known defect geometry. The objective of the iteration is then to adjust the shape of the defect until the residual between the true and synthetic measurements is minimized. The backprojection algorithm uses the current residual to update the defect shape between iterations and is itself based on the forward solver, see, for instance, the seminal paper by Pratt [102].

The accuracy of depth profile reconstructions is dependent on the accuracy of the forward solver and the availability of a set of transmission measurements with sufficient angular diversity. The Lamè-Navier equations of elasticity provide an exact description of guided wave scattering from defects and are successfully implemented in numerical techniques such as the finite element method. However, the computational burden associated with modeling the fully three-dimensional (3-D) elastic problem leads to prohibitively time consuming calculations which are not feasible within the context of an iterative inversion. For this reason, one of the key challenges in GWT is to define approximate forward models which are computationally efficient and consistent with the measurements. The latter condition is more important than absolute accuracy from the perspective of the inverse problem and arises from the fact that measurements contain noise and are subject to a variety of experimental uncertainties. As an example, in some circumstances amplitude data extracted from the measurements may be far less accurate than the traveltime data obtained from the same measurements, thus meaning that only the latter contains information accessible to inversion schemes. In this case, it would be sufficient to base the forward model on the Eikonal equation of ray theory which can be implemented with greater computational efficiency than the Lamè-Navier equations and yields accurate traveltime estimations. Therefore, the level of approximation which can be introduced in the forward model without having a detrimental effect on the accuracy of the inversion is dependent upon the quality and completeness of the measurements; approximations can be introduced to the extent that the model predictions can be reconciled with the information-bearing data available from the measurements.

Due to the challenges posed by 3-D elastic forward models, the vast majority of re-

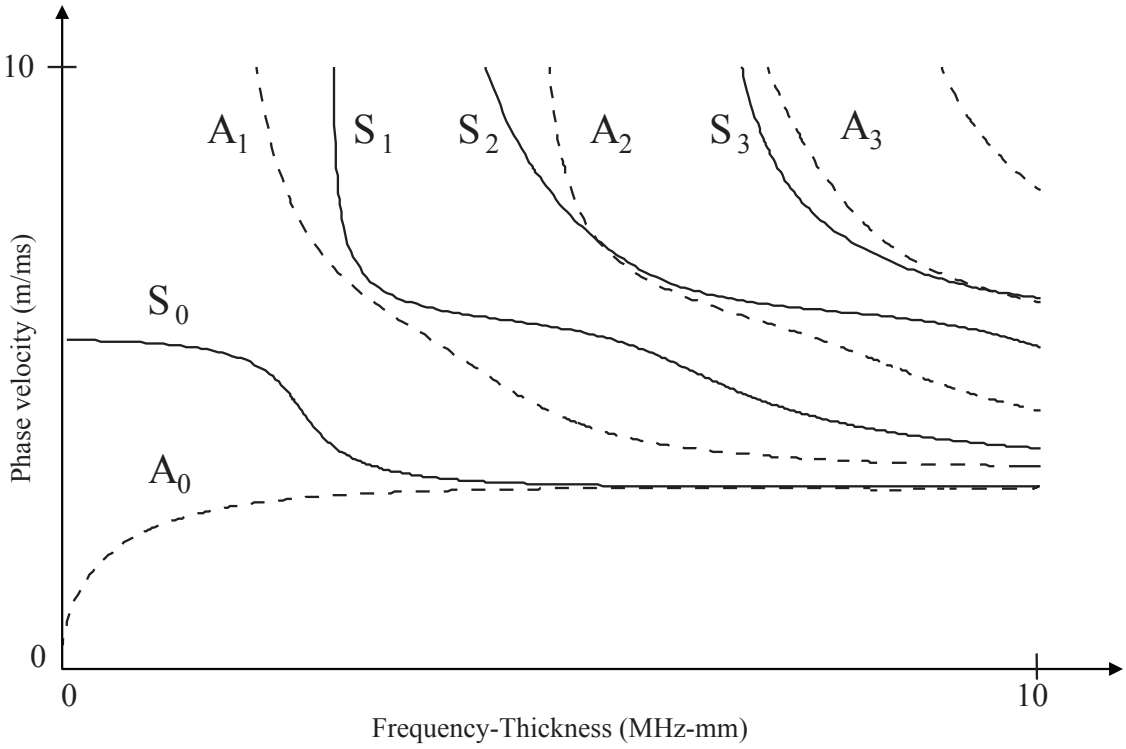

Figure 6-2: Lamb wave dispersion curves in steel plates showing phase velocity as a function of the frequency-thickness ($f \cdot d$) product for all the propagating modes up to 10 MHz-mm. Solid and dashes curves refer to the so-called symmetric and antisymmetric modes, respectively.

search on GWT has considered flat plates [103, 104, 105, 106, 101] and more recently sections of straight pipes [107, 100, 108], which are treated as flat plates under the assumption that the wall thickness is much smaller than the pipe radius. In plates, the full 3-D solution to the wave propagation problem can be obtained directly from the Rayleigh-Lamb secular equation [109, 110] which provides a modal solution to the Lamè-Navier equations. The Rayleigh-Lamb equation can therefore be used to determine the phase velocity dispersion characteristics of different modes and their mode shapes, however it does not describe guided wave scattering. To overcome this limitation, two-dimensional (2-D) approximate scattering models based on the fourth order differential equation obtained from Mindlin plate theory [111, 112], or the Helmholtz equation of acoustics [103, 104, 105, 106, 101] have been introduced. The former, is limited to the low-frequency propagation and scattering of the fundamental flexural mode, A_0, while the latter can be applied to higher order modes and frequencies.

In contrast with the Mindlin formulation, the 2-D acoustic model is derived from a heuristic argument. Central to the approach is the dependence of the phase velocity dispersion curves of Lamb waves on the frequency-thickness, $f \cdot d$, product rather than f and d separately as shown in Figure 6-2. In particular, it is postulated that the perturbation induced by the presence of a defect to the free propagation of a guided mode is equivalent to the perturbation experienced by an acoustic pressure wave traveling in a region of non-uniform sound speed. The phase velocity dispersion curve of a selected mode then provides the one-to-one mapping linking the wall thickness at a particular point in the plate to the sound speed at the corresponding point in the acoustic model. For instance, the sound speed of the A_0 mode in a corroded region will be lower than in the intact plate due to the wall thinning that causes the $f \cdot d$ product to decrease. Like the Mindlin formulation, the acoustic model does not take into account mode conversion phenomena. However, it is better suited than the former to capture refraction and diffraction effects since the phase velocity is obtained from the exact Rayleigh-Lamb secular equation. The validity of the acoustic model has been confirmed by comparisons with 3-D elastic simulations and experiments [106, 101].

The objective of this chapter is to introduce a generalized 2-D acoustic model that can be used to describe guided wave propagation and scattering in arbitrary tubular structures with wall thickness small compared to the local radius of curvature. The velocity field of the acoustic model is made artificially inhomogeneous and anisotropic to take into account the stretching and compression required to unwrap a complex 3-D surface.

Based on the preservation of traveltime, Section 6.2 introduces the mathematical formulation required to map a complex 3-D surface onto the inhomogeneous and anisotropic acoustic model, with an explicit solution being provided for the case of a bend. The numerical implementation of the generalized acoustic model is discussed in Section 6.3 where both the shortest path ray (SPR) tracing method and the finite element method (FEM) are considered. Section 6.4 compares SPR and FEM, and presents typical wave paths for modes wrapping around a bend joining two straight

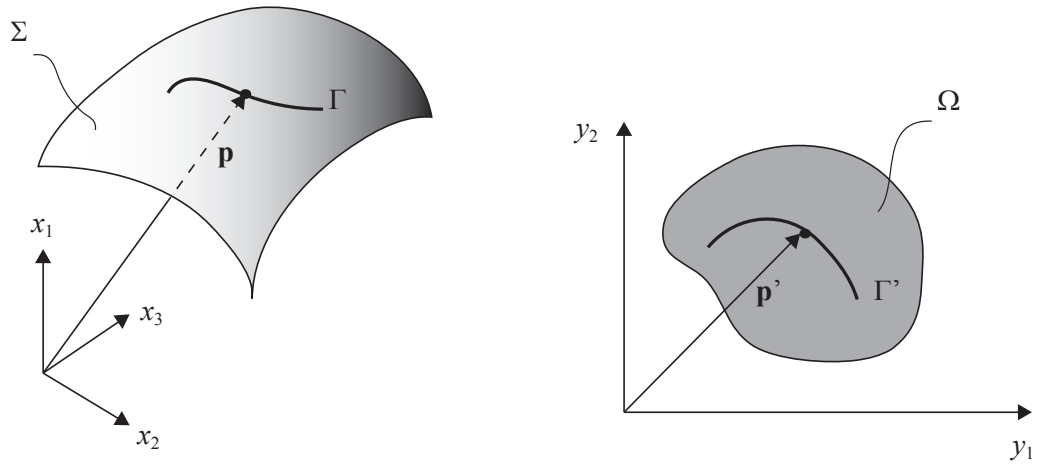

Figure 6-3: A 3-D surface Σ is mapped onto a domain Ω in the 2-D space.

pipe sections. Here, a lensing effect occurring on the outer side of the bend and leading to a strong focusing effect is examined. The numerical predictions of Section 6.4 are then validated against experimental results in Section 6.5 which is followed by concluding remarks in Section 6.6.

6.2 Theoretical formulation

This section builds on some fundamental results from differential geometry with the goal of providing a 2-D representation of guided wave propagation in a complex 3-D structure. For this purpose, a structure is reduced to a 3-D surface, Σ, and a function $d(\mathbf{p})$ providing the wall thickness, d, at any point, $\mathbf{p}$, on Σ. In the 3-D Euclidean coordinate system $\{O, x_1, x_2, x_3\}$, the position of $\mathbf{p}$ can be specified by a vector of coordinates (p_1, p_2, p_3) as shown in Figure 6-3. Similarly, the position of a point $\mathbf{p}'$ in the 2-D acoustic domain, relative to the Cartesian coordinate system $\{O', y_1, y_2\}$, is uniquely determined by the vector having coordinates (p'_1, p'_2). Note that throughout this section the prime sign is used to refer to quantities in the 2-D domain.

Central to the 2-D acoustic model is the definition of a suitable parametric rep-

resentation $\mathbf{r} : \Omega \to \Sigma$ providing a one-to-one mapping between a subset, Ω, of $\mathbb{R}^2$ and the 2-D manifold surface Σ embedded in $\mathbb{R}^3$. So long as $\mathbf{r}$ is one-to-one then any curve $\Gamma' : [0,1] \to \Omega$ is mapped onto one and only one curve $\Gamma : [0,1] \to \Sigma$, i. e.

$$\Gamma(s) = \mathbf{r}(\Gamma'(s)). \tag{6.1}$$

Moreover, from the first fundamental form of differential geometry [113], the length of the element arc of Γ is

$$d\Gamma = \sqrt{\left|\frac{\partial \mathbf{r}}{\partial y_1}\right|^2 (dy_1)^2 + 2\frac{\partial \mathbf{r}}{\partial y_1} \cdot \frac{\partial \mathbf{r}}{\partial y_2} dy_1 dy_2 + \left|\frac{\partial \mathbf{r}}{\partial y_2}\right|^2 (dy_2)^2}, \tag{6.2}$$

where $\partial \mathbf{r}/\partial y_1$ and $\partial \mathbf{r}/\partial y_2$ are vectors tangent to Σ and dy_1, dy_2 are the component lengths of $d\Gamma'$; that is, $d\Gamma' = \sqrt{(dy_1)^2 + (dy_2)^2}$. If the velocity of the ultrasonic perturbation at a position $\mathbf{p}$ is given by $c(\mathbf{p})$, then the traveltime along the path is given by

$$\tau(\Gamma) = \int_0^1 \frac{d\Gamma(s)}{c(\Gamma(s))} ds. \tag{6.3}$$

In this definition c can refer to either the phase or group velocity at a selected frequency depending on whether the propagation of phase or energy is to be considered. Strictly, the velocity field $c(\mathbf{p})$ is anisotropic since for an arbitrary 3-D surface the radius of curvature varies depending on the propagation direction. However, when the thickness is small relative to the minimum radius of curvature (5-10%) the velocity dependence on curvature can be neglected [114] and $c(\mathbf{p})$ can be treated as isotropic - this case will be considered throughout the following chapters.

In the 2-D acoustic domain the time to travel along the path Γ' is given by

$$\tau'(\Gamma') = \int_0^1 \frac{\sqrt{(dy_1)^2 + (dy_2)^2}}{c'(\Gamma'(s))} ds, \tag{6.4}$$

where $c'(\mathbf{p}')$ is acoustic velocity field of the 2-D model. The central idea of this section is to define the field $c'(\mathbf{p}')$ and a parametric representation $\mathbf{r}$ so that traveltime is

preserved, i. e.

$$\Gamma = \mathbf{r}(\Gamma') \implies \tau(\Gamma) = \tau'(\Gamma'). \tag{6.5}$$

Equation 6.5 ensures that the solution to the wave equation in the 2-D domain is consistent with the physical propagation in the 3-D space. This can be demonstrated by considering any two points A and B on Σ and their corresponding image points A' and B' in the 2-D domain. According to Fermat's principle the wave path from A to B is the curve of Σ, Γ_{min}^{AB}, that results in the shortest group traveltime, $\Delta\tau_{min}$. Similarly, the wave path from A' to B' in the 2-D domain is the curve, $\Gamma_{min}^{\prime A'B'}$ which leads to the shortest traveltime $\Delta\tau'_{min}$. Moreover, from Equation 6.5 the traveltime $\Delta\tau'$ along any arbitrary path joining A' to B', $\Gamma^{\prime A'B'}$, is the same as the traveltime $\Delta\tau$ along the 3-D path $\mathbf{r}(\Gamma^{\prime A'B'})$. As a result, if $\Delta\tau'_{min}$ is the shortest traveltime for all the possible paths $\Gamma^{\prime A'B'}$ in the 2-D domain it will also be the shortest traveltime for all the possible paths Γ^{AB} that can join A to B on Σ. Therefore, the 2-D solution is physically consistent with the 3-D wave propagation which can be obtained from the former using the parametric mapping.

Next we discuss two general approaches to define parametric representations and acoustic velocity fields that satisfy Equation 6.5.

6.2.1 Isometric parameterization

An isometric mapping is characterized by preservation of length, i. e.

$$d\Gamma = d\Gamma'. \tag{6.6}$$

In order for the mapping to be isometric it has to satisfy the so called arc-length condition

$$\left|\frac{\partial \mathbf{r}}{\partial y_1}\right| = \left|\frac{\partial \mathbf{r}}{\partial y_2}\right| = 1, \tag{6.7}$$

and the orthogonality condition

$$\frac{\partial \mathbf{r}}{\partial y_1} \cdot \frac{\partial \mathbf{r}}{\partial y_2} = 0. \tag{6.8}$$

Substitution of Equation 6.7 and Equation 6.8 into Equation 6.2 leads to the identity

$$d\Gamma = \sqrt{(dy_1)^2 + (dy_2)^2} = d\Gamma', \tag{6.9}$$

which expresses length preservation. Since $d\Gamma = d\Gamma'$ condition Equation 6.5 is satisfied if

$$c'(\mathbf{p}) = c(\mathbf{p}), \quad \forall \mathbf{p}' \in \Omega, \quad \& \quad \forall \mathbf{p} \in \Sigma. \tag{6.10}$$

Equation 6.10 is very desirable in GWT applications because it enables the use of the standard acoustic model to describe guided wave scattering. The acoustic model is built starting from the dispersion curve, $c(fd)$, of a selected Lamb mode and the thickness distribution along the structure, d. Using Equation 6.10 the wall thickness loss is transformed into an isotropic inhomogeneous 2-D sound-speed field through

$$c'(\mathbf{p}', f) = c(fd) = c\{fd[\mathbf{r}(\mathbf{p}')]\}. \tag{6.11}$$

Guided wave scattering is then described by a scalar potential $\phi(y_1, y_2, f)$ solution to the inhomogeneous Helmholtz equation [115]

$$\nabla^2 \phi(y_1, y_2, f) + k_0^2 \phi(y_1, y_2, f) = -4\pi O_H(y_1, y_2, f)\phi(y_1, y_2, f), \tag{6.12}$$

where $k_0 = 2\pi f / c_0'$ is the background wavenumber dependent on the background velocity $c_0'(f) = c(fd_0)$, with d_0 being a reference thickness, e.g. the thickness of the undamaged structure. $O_H(y_1, y_2, f)$, is the object function given by

$$O_H(y_1, y_2, f) = \frac{k_0^2}{4\pi}\left[\left(\frac{c_0'(f)}{c'(y_1, y_2, f)}\right)^2 - 1\right], \tag{6.13}$$

and is the acoustic representation of the wall thickness loss; $O_H(y_1, y_2, f)$ vanishes outside the damage area. The high-frequency asymptotic form of Equation 6.12 leads to the ray theory of geometrical acoustics described by the Eikonal equation

$$\left(\frac{\partial \tau}{\partial y_1}\right)^2 + \left(\frac{\partial \tau}{\partial y_2}\right)^2 = O_e(y_1, y_2), \tag{6.14}$$

where the function $\tau(y_1, y_2)$ is the traveltime of the acoustic wave to point (y_1, y_2) and the object function $O_e(y_1, y_2)$ is now defined as

$$O_e(y_1, y_2) = \frac{1}{c'(y_1, y_2)^2} \tag{6.15}$$

where $c'(y_1, y_2)$ can refer to the phase velocity at the center frequency of the wave pulse or its group velocity at the same frequency depending on whether the propagation of the signal phase or energy is to be represented. Although ray theory fails to account for diffraction effects it provides the basis for widely used methods such as seismic traveltime tomography [116].

Isometric parameterizations are known for circular cylinders and lead to the familiar concept of unwrapping. For instance, for a cylinder of radius r and height H the parameterization

$$x_1 = r \sin \frac{y_1}{r},\ x_2 = r \cos \frac{y_1}{r},\ x_3 = y_2, \quad \forall (y_1, y_2) \in [0 \quad 2\pi r] \times [0 \quad H], \tag{6.16}$$

satisfies properties Equation 6.7 and Equation 6.8. Importantly, for an undamaged cylinder the sound-speed field is homogeneous and equal to $c(fd_0)$.

6.2.2 Orthogonal parameterization

While the isometric parameterization leads to a straightforward formulation of the 2-D acoustic model, finding a parametrization that satisfies conditions Equation 6.7 and Equation 6.8 for a shape different from a circular cylinder is often not possible. The purpose of this section is therefore to develop the acoustic formulation for a broader class of parameterizations which satisfy orthogonality but relax the requirement on the

arc-length condition Equation 6.7. In particular, orthogonal parameterizations can be found for a subset of the so-called generalized cylinders. A generalized cylinder is obtained by sweeping an arbitrarily shaped planar curve C along a 3-D, curved spine, S. With reference to Figure 6-4, we consider the subset in which C is rigid and its plane is always maintained normal to the spine, this being representative of a number of important engineering geometries such as extrusions and tubing. A parameterization that uses y_1 defined as the arc-length along C and y_2 as the arc-length along the spine satisfies the orthogonality condition, Equation 6.8, for any point along the surface. Moreover, the support of the 2-D acoustic domain is the rectangular set $\Omega = [0 \quad L] \times [0 \quad D]$ where L and D are the lengths of curves C and S, respectively.

To formulate the acoustic model it is observed that Equation 6.2 under the orthogonality condition can be rearranged to give

$$\frac{d\Gamma^2}{c(\mathbf{p})^2} = \frac{(dy_1)^2}{c_1'(\mathbf{p}')^2} + \frac{(dy_2)^2}{c_2'(\mathbf{p}')^2}, \tag{6.17}$$

with the introduction of two velocities

$$\frac{1}{c_1'(\mathbf{p}')} = \frac{1}{c(\mathbf{p})}\left|\frac{\partial \mathbf{r}}{\partial y_1}\right|, \quad \& \quad \frac{1}{c_2'(\mathbf{p}')} = \frac{1}{c(\mathbf{p})}\left|\frac{\partial \mathbf{r}}{\partial y_2}\right| \tag{6.18}$$

which depend only on position. Here it is understood that $\mathbf{p} = \Gamma(s)$ and the dependence of $d\Gamma$ and $d\Gamma'$ on s are left implicit. Let $c'(\mathbf{p}, \theta_g)$ be an inhomogeneous and anisotropic velocity field which is dependent both on position $\mathbf{p}$ and the angle of propagation θ_g measured counter clockwise from the y_1 axis. An arc element $d\Gamma'$ parallel to the propagation direction has components of length $dy_1 = d\Gamma' \cos\theta_g$ and $dy_2 = d\Gamma' \sin\theta_g$ that by substitution into Equation 6.17 yield

$$\frac{d\Gamma^2}{c(\mathbf{p})^2} = \frac{(d\Gamma' \cos\theta_g)^2}{c_1'(\mathbf{p}')^2} + \frac{(d\Gamma' \sin\theta_g)^2}{c_2'(\mathbf{p}')^2} = \frac{(d\Gamma')^2}{c'(\mathbf{p}', \theta_g)^2}, \tag{6.19}$$

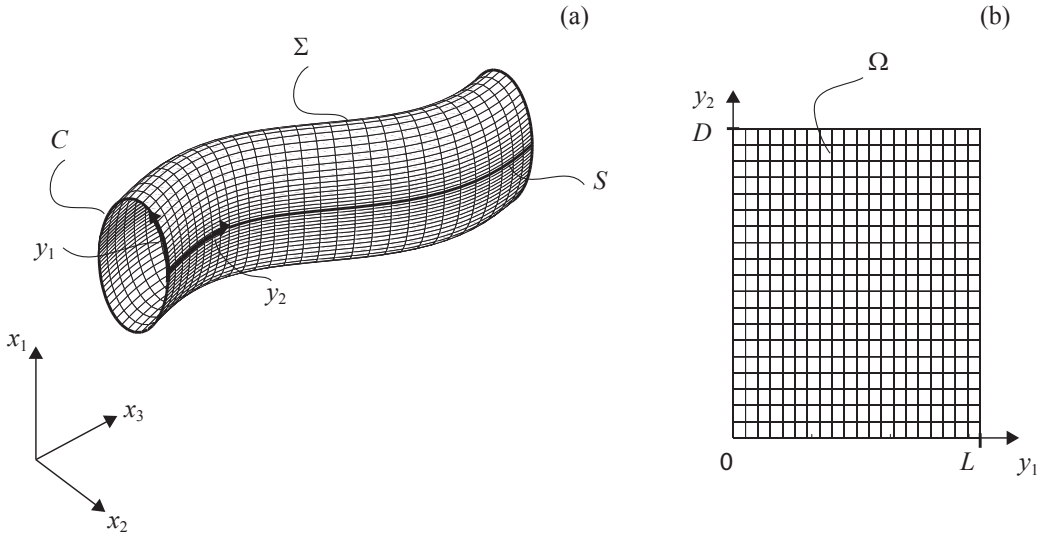

Figure 6-4: Coordinate systems used to form the parameterization of a generalized cylinder. The closed curve C is rigidly swept along the 3-D spine curve S and is maintained normal to it. (a) representation of the parameters x' and y' that result in orthogonal parameterization; (b) 2-D acoustic domain.

which solving with respect to $c'(\mathbf{p}', \theta_g)$ gives

$$c'(\mathbf{p}', \theta_g) = \frac{c'_1(\mathbf{p}')c'_2(\mathbf{p}')}{\sqrt{c'_1(\mathbf{p}')^2 \sin^2\theta_g + c'_2(\mathbf{p}')^2 \cos^2\theta_g}}. \tag{6.20}$$

Equation 6.20 is the polar representation of an ellipse with semi-diameters $c'_1(\mathbf{p}')$ and $c'_2(\mathbf{p}')$ and is formally equivalent to the expression of group velocity in an elliptically anisotropic as given in Equation 2.16. Therefore, from Equation 6.20 it can be concluded that for any orthogonal parameterization, the sound-speed field associated with the 2-D acoustic model is inhomogeneous, elliptically anisotropic, and it is completely characterized by Equation 6.20 and Equation 6.18. The corresponding eikonal

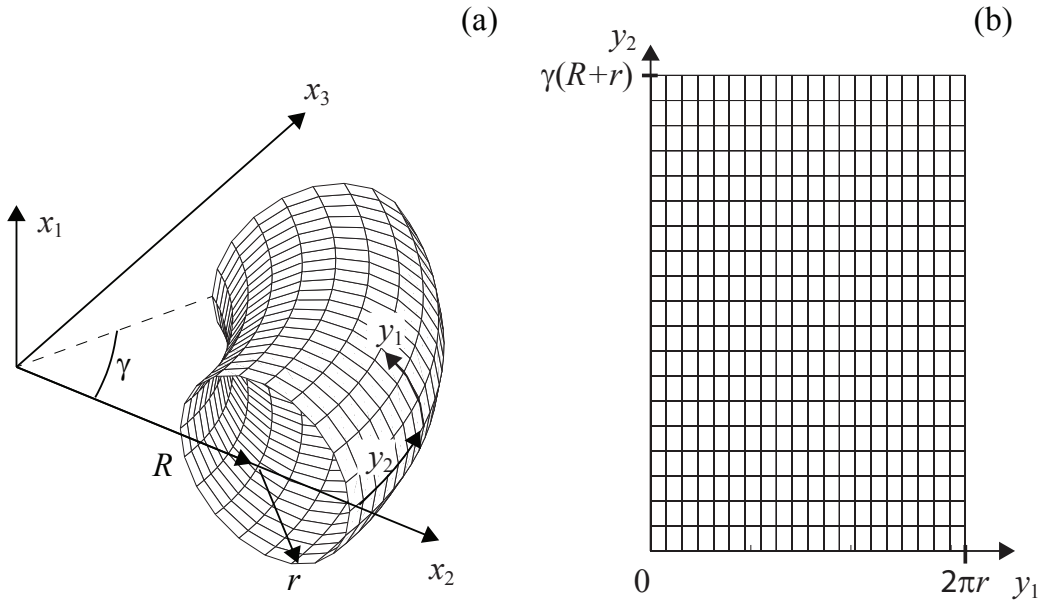

Figure 6-5: Coordinate systems used to form the parameterization of a torus section. (a) 3-D physical space; (b) 2-D acoustic domain.

equation is adopted from Equation 2.13 and is given as

$$c_1'(\mathbf{p}')^2 \left(\frac{\partial \tau}{\partial y_1}\right)^2 + c_2'(\mathbf{p}')^2 \left(\frac{\partial \tau}{\partial y_2}\right)^2 = 1. \tag{6.21}$$

In geophysics the acoustic wave equation for an elliptically anisotropic medium has been extensively studied to represent transversely isotropic media with a vertical symmetry axis. According to Alkhalifah [117] the frequency domain wave equation $\phi(y_1, y_2, \omega)$ is described by

$$\phi + \frac{c_1'(\mathbf{p}')^2}{\omega^2}\frac{\partial^2 \phi}{\partial y_1'^2} + \frac{c_2'(\mathbf{p}')^2}{\omega^2}\frac{\partial^2 \phi}{\partial y_2^2} = 0, \tag{6.22}$$

which reduces to the standard acoustic wave equation when $c_1'(\mathbf{p}') = c_2'(\mathbf{p}')$.

An explicit expression for the elliptically anisotropic sound-speed field is now derived for a section of a torus, this being representative of a pipe bend. Let the radius of the torus tube be denoted by r, the distance from the center of the torus to the center

of the tube by R, and the angular aperture by γ as shown in Figure 6-5. A possible orthogonal parameterization is

$$\begin{aligned} x_1 &= r \sin \frac{y_1}{r}, \\ x_2 &= \left(R + r \cos \frac{y_1}{r} \right) \cos \frac{y_2}{R+r}, \\ x_3 &= \left(R + r \cos \frac{y_1}{r} \right) \sin \frac{y_2}{R+r}, \quad \forall (y_1, y_2) \in [0 \; 2\pi r] \times [0 \; \gamma(R+r)]. \end{aligned} \tag{6.23}$$

from which the moduli of the tangent vectors are

$$\left| \frac{\partial \mathbf{r}}{\partial y_1} \right| = 1 \quad \& \quad \left| \frac{\partial \mathbf{r}}{\partial y_2} \right| = \frac{R + r \cos(y_1/r)}{R+r}. \tag{6.24}$$

By substituting the expressions in Equation 6.24 into Equation 6.18 and Equation 6.20 the anisotropic and inhomogeneous sound-speed field is

$$c'(\mathbf{p}', \theta_g) = \frac{c[\mathbf{r}(\mathbf{p}')]}{\sqrt{\cos^2 \theta_g + \alpha^2(\mathbf{p}') \sin^2 \theta_g}}, \quad \text{with} \quad \alpha(\mathbf{p}') = \frac{R + r \cos(y_1/r)}{R+r}. \tag{6.25}$$

The non-dimensional parameter α characterizes both the inhomogeneity and anisotropy of the sound-speed field $c'(\mathbf{p}', \theta_g)$. The spatial modulation induced by α is readily apparent when considering a bend with uniform thickness; in this case $c[\mathbf{r}(\mathbf{p}')] = c(fd) = const.$ However, $c'(\mathbf{p}', \theta_g)$ is still inhomogeneous due to the dependence of α on y_1. From Figure 6-6 (a) it can be observed that α oscillates between 1 and $(R-r)/(R+r)$ as y_1 spans the circumference of the tube. The condition $\alpha = 1$ occurs on the outer radius of the torus [pointed by the circle in Figure 6-6 (b)] where the velocity is isotropic and equal to $c[\mathbf{r}(\mathbf{p}')]$. On the other hand, α has its minimum value along the inner radius of the torus (indicated by the square) where the sound speed reaches its maximum value and the velocity field becomes highly anisotropic. Finally, it can be observed that as the R/r ratio tends to infinity, $\alpha \to 1$ for any y_1/r, this is consistent with the fact that for large R the torus tends to a straight tube which is described by an isotropic acoustic model.

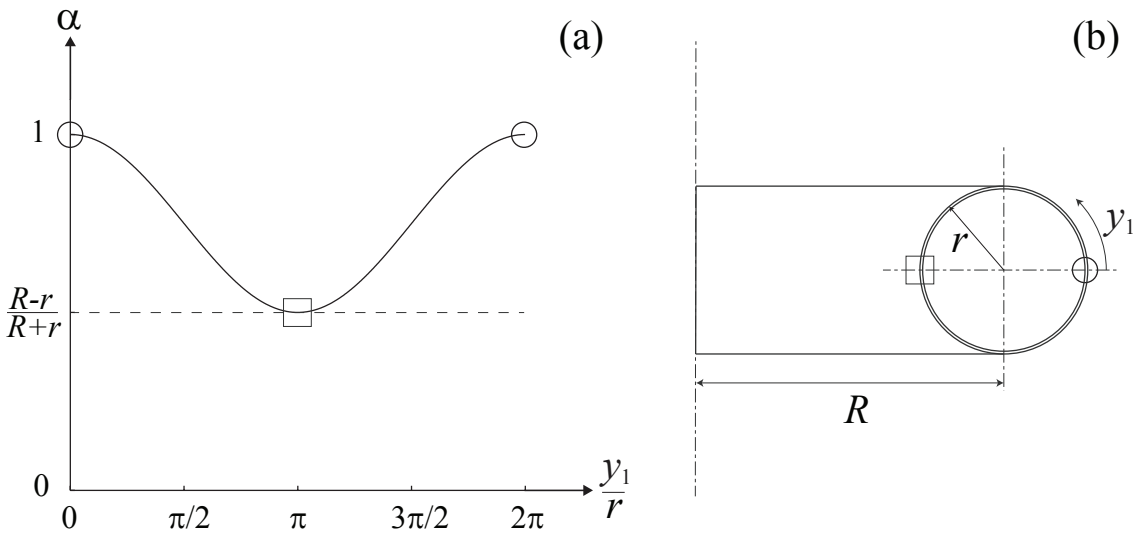

Figure 6-6: (a) Dependence of the α parameter on the arc length x' relative to the radius of the torus tube; (b) torus cross-section showing the origin of the x' arc, the square and circle denote the inner and outer radii of the torus. Small α values lead to high sound speed and anisotropy.

6.2.3 Phase versus group velocity

It is important to notice that the anisotropy of the 2-D acoustic model causes a difference between the phase and group velocities even for non-dispersive guided modes. Equation 6.20, which can also be re-written in the form

$$\frac{1}{c'(\mathbf{p}', \theta_g)^2} = \frac{\cos^2 \theta_g}{c_1'(\mathbf{p}')^2} + \frac{\sin^2 \theta_g}{c_2'(\mathbf{p}')^2}, \tag{6.26}$$

describes the angular dependence of the group velocity. The angular dependence of the corresponding phase velocity, $V'(\mathbf{p}', \theta)$, is given by Equation 2.15, here re-expressed as

$$V'(\mathbf{p}', \theta)^2 = c_1'(\mathbf{p}')^2 \cos^2 \theta + c_2'(\mathbf{p}')^2 \sin^2 \theta, \tag{6.27}$$

where θ is the phase angle related to the group angle θ_g according to Equation 2.16 as

$$\tan\theta = \frac{(c_1')^2}{(c_2')^2}\tan\theta_g. \tag{6.28}$$

Importantly, the anisotropic phase velocity $V'(\mathbf{p}', \theta)^2$ does not directly correspond to the phase or the group velocity of the physical guided mode. In fact the traveltime preservation expressed by Equation 6.5 leads to Equation 6.20 which describes the angular dependence of the group velocity. As result, anisotropic group propagation in the 2-D acoustic domain is used to describe both phase and group propagation in the 3-D physical space. These two types of propagation are modeled by using different definitions of the anisotropic group velocity Equation 6.20. In particular, to model the propagation of phase, the velocities c_1' and c_2' are obtained from Equation 6.18 by defining $c(\mathbf{p})$ as the mode phase velocity. On the other hand, group propagation is modeled by letting $c(\mathbf{p})$ equal to the mode group velocity.

6.2.4 Wave-paths wrapping around Σ

In the presence of closed surfaces such as pipes and tubes there exist infinite wave paths that can join any two points on the surface. Here, the approach introduced in Ref. [108] for straight cylinders is extended to a generalized cylinder. With reference to Figure 6-7 (a) let us considered two closed curves Γ_T and Γ_R representing the transmit and receive arrays, respectively. Each curve has length L, and they both delimit a section of a tubular structure with lateral surface σ. Using the coordinate system (x', y') shown in Figure 6-7 (a) σ maps onto the 2-D domain $\Omega = [0 \quad L] \times [0 \quad D]$, where D is the distance between Γ_T and Γ_R measured along the spine, Figure 6-7 (b).

It is now observed that the domain Ω can be extended to infinity by connecting replicas of Ω as illustrated in Figure 6-7 (b). As a result, for any point $P' \in \Omega$ with position vector $\mathbf{r}'$ there exist infinite points in the the extended domain Ω_∞, with the

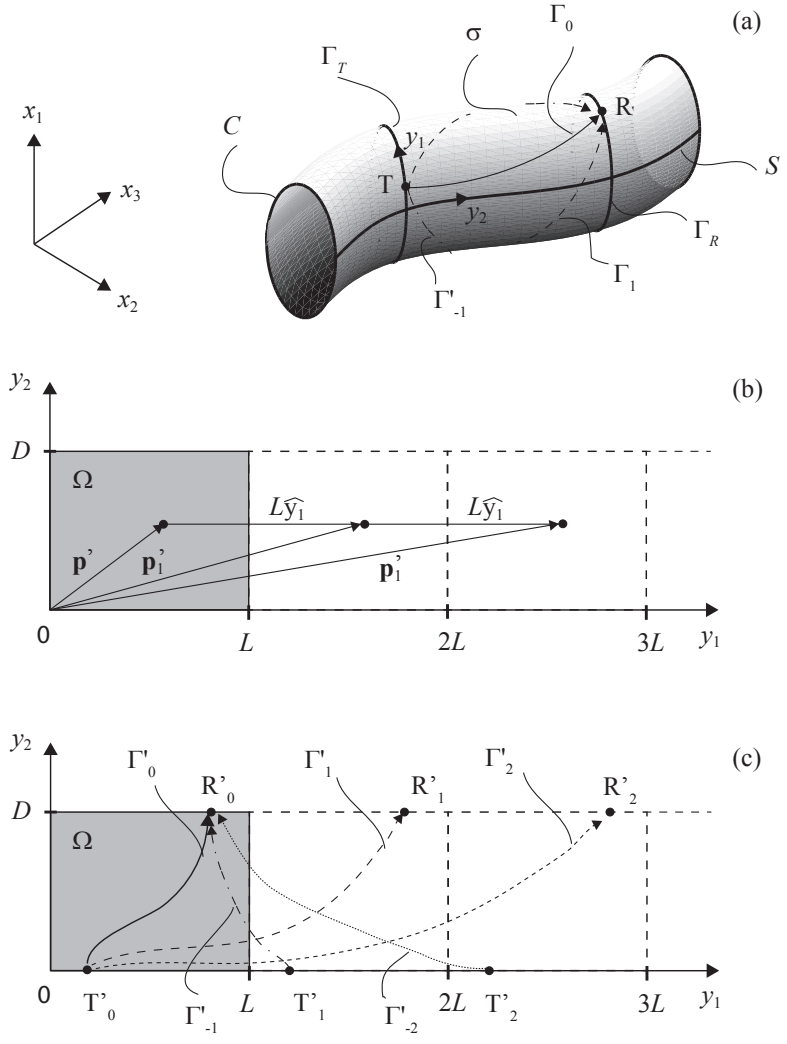

Figure 6-7: Replication method used to describe wave-paths wrapping around a tubular structure. (a) 3-D physical model showing the position of a point source (T) and receiver (R) and the corresponding first three wave-paths Γ_0, Γ_1, and Γ_{-1}; (b) Extended acoustic domain Ω_∞ showing the dependence of $\mathbf{r}'_n$ on $\mathbf{r}'$ for the first two replicas; (c) acoustic wave-paths corresponding to the guided wave-path on the surface σ.

point P'_n belonging to the n-th replica being defined by the position vector

$$\mathbf{p}'_n = \mathbf{p}' + nL\mathbf{e}'_1, \tag{6.29}$$

where $\mathbf{e}_1'$ is the unit vector parallel to the y_1-axis. In a similar fashion, the object function can be extended to the Ω_∞ domain through

$$\tilde{O}(\mathbf{p}_n') = O(\mathbf{p}'). \tag{6.30}$$

To map Ω_∞ onto the surface of the cylinder a new parametric representation $\tilde{\mathbf{r}}$: $\Omega_\infty \to \sigma$ is defined as

$$\tilde{\mathbf{r}}(\mathbf{p}_n') = \mathbf{r}(\mathbf{p}), \tag{6.31}$$

By definition, the mapping $\tilde{\mathbf{r}}(\mathbf{p}_n')$ is not one-to-one as infinite points in the Ω_∞ domain correspond to the same point on the surface σ.

Let us now consider a point source T and a point receiver R and their corresponding points T_0' and R_0' in the Ω domain. Direct guided wave propagation from T to R can be represented in the Ω domain by computing the solution to Equation 6.12 at point R_0' for a point source in T_0'. Therefore, the direct wave-path from T to R, Γ_0, is obtained by applying $\mathbf{r}$ to wave-path Γ_0' which in the Ω domain joins T_0' and R_0'. In order to describe wave-paths that wrap around the tube multiple times, it is sufficient to consider the infinite replicas of T_0', T_n', and R_0', R_n', that can be generated from T_0' and R_0' with Equation 6.29. As a result, the wavefield at R due to a point source in T and corresponding to a guided wave that has wrapped around the tube n times is given by the solution to Equation 6.12 computed at point R_n' for a point source in T_0'. The wave-path joining T to R after performing n full turns is then obtained by applying mapping Equation 6.31 to the wave path, Γ_n', that in the Ω_∞ domain joins T_0' to R_n'. Similarly, the wave path Γ_{-n}' joining T_n' to R_1' maps onto wave-path Γ_{-n} that wraps n-times around the cylinder but in the opposite direction of Γ_n.

6.3 Numerical implementation

To describe the numerical implementation of the theory introduced in Section 6.2 the propagation of guided wave signals in the structure shown in Figure 6-1 is modeled.

The structure consists of two straight, 8" nominal diameter (220 mm measured), 7.5 mm wall thickness, carbon steel pipe sections joined by a 90° bend with the geometrical characteristics shown in Figure 6-8 (a). The goal of the forward model is to simulate the propagation of the fundamental A_0 mode from 16 point sources along section A-A to 16 point receivers along section C-C. The selected center frequency is 0.175 MHz, or 1.31 MHz-mm which corresponds to 2539 m/s phase velocity and 3276 m/s group velocity.

The surface σ consists of two sections of circular cylinders of radius $r = 110$ mm and length $\delta = 100$ mm, labeled A and B, and a $\gamma = \pi/2$ section of torus of radius $R = 3r$ and tube radius r, labeled B. The group of three sections forms a generalized cylinder with the spine curve S shown in Figure 6-8 (a). Using the set of parametric equations given in Equation 6.23 for section B and unwrapping sections A and C, the 2-D acoustic domain is $\Omega = [-\pi r \quad \pi r] \times [0 \quad 2\delta + \pi(R+r)/2]$ as shown in Figure 6-8 (b). The sound-speed field is calculated using Equation 6.20 with the spatial distribution of the α-parameter being illustrated by the color map in Figure 6-8 (b). In sections A' and B' $\alpha = 1$ since straight pipe sections do not require anisotropy. In order to model guided waves that perform up to two full turns around the structures, the Ω domain is extended by adding two replicas as shown in Figure 6-8 (b).

The extended geometrical domain $\Omega_e = [-\pi r \quad 5\pi r] \times [0 \quad 2\delta + \pi(R+r)/2]$ and the elliptically anisotropic velocity field described in Equation 6.25 constitute the 2-D equivalent acoustic model in conjunction with the full wave equation (Equation 6.22) or the eikonal equation (Equation 6.21). The full wave equation can be solved using FEM simulations while the eikonal equation can be solved using the methods discussed in Section 2.3; details of the FEM implementation is discussed next.

6.3.1 Finite element method

The elliptically anisotropic velocity field (Equation 6.25) is dispersive due to the frequency dependence of the phase velocity; therefore, also the terms c_1' and c_2' in the wave equation (Equation 6.22) are dispersive. As a result, the propagation of a broadband signal can be obtained by applying standard Fourier analysis to the

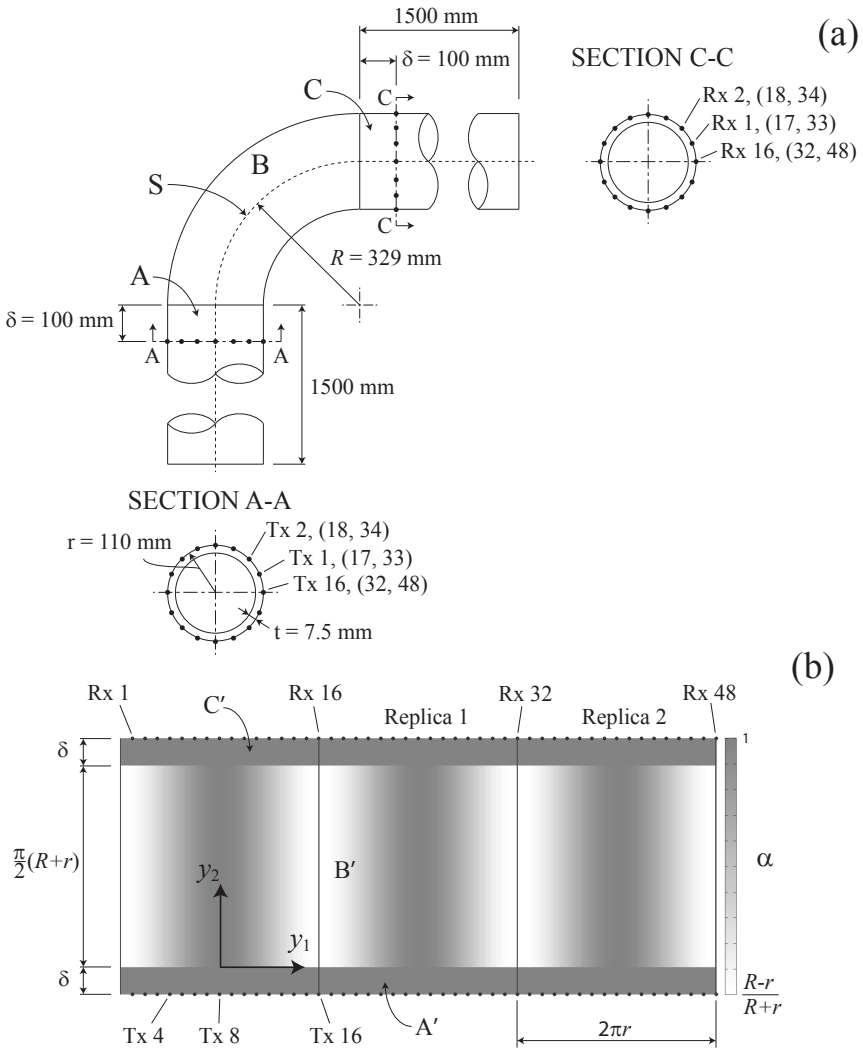

Figure 6-8: Geometrical characterization of the experimental configuration shown in Figure 6-1. (a) Schematic of the pipe, showing the straight sections A and C, and the bend B. The entire structure is a generalized cylinder with spine curve S; (b) Extended acoustic domain including two replicas. The background gray scale denotes the α parameter, with brighter regions on the inside of the bend corresponding to high sound speed.

solutions to Equation 6.22 corresponding to the frequencies contained within the signal bandwidth and letting $c[\mathbf{r}(\mathbf{p}')]$ equal to the mode phase velocity in the definition of the anisotropic group velocity. This requires the availability of *ad hoc* solvers for Equation 6.22 and can be time consuming due to the need for running multiple

frequencies.

COMSOL's Acoustics package [118] provides a time-domain solver for the acoustic equation

$$\frac{1}{c^2}\frac{\partial^2 p}{\partial t^2} - \nabla \cdot (\nabla p - \mathbf{q}) = Q, \tag{6.32}$$

where p is the pressure, $\mathbf{q}$, is a dipole source and Q is a monopole source. Letting, $Q = 0$, $q_1 = 0$ and $q_2 = \partial p/\partial y_2 - 1/\alpha^2 \cdot \partial p/\partial y_2$, Equation 6.32 reduces to

$$\frac{\partial^2 p}{\partial t^2} = c^2 \frac{\partial^2 p}{\partial y_1^2} + \frac{c^2}{\alpha^2}\frac{\partial^2 p}{\partial y_2^2}, \tag{6.33}$$

which is the time-domain wave equation for a non-dispersive elliptically anisotropic velocity field [117]. In order to use Equation 6.33, the frequency dependence of Equation 6.25 is suppressed by replacing the phase velocity term $c(fd)$ with the group velocity $c_g(f_0 d)$ at the center frequency of the propagated wave pulse. Therefore, while Equation 6.33 is not able to capture wave pulse dispersion it can provide accurate results for relatively narrowband signals.

Equation 6.33 was solved in the Ω domain to simulate propagation along the direct wave paths. The domain was discretized using a uniform mesh with square quadratic elements with size $\lambda/15$, λ being the wavelength of the A_0 mode at $f \cdot d$=1.31 MHz-mm. To avoid interference with the reflections from the boundaries of the domain the width of the domain was increased by 500 mm. The time step was 5.7 μs which is approximately the time required by the wave to travel across one mesh element. The source transducer was simulated by applying a 0.175 MHz center frequency, 5-cycle, Hann-windowed pressure wavelet to the node corresponding to the position of the selected transducer in the array.

The full-wave simulations required 10 GB of RAM, and took approximately 35 hours per source to complete on a Linux machine which has 128 GB of ram and runs 4 AMD Opteron 6134 8-core processors. Ray tracing calculations through the model shown in Figure 6-8 (b) were performed by discretizing the extended domain Ω_e with squared elements 10 mm size each containing eight equally spaced nodes around the

boundary of the element. As for the FEM simulation the velocity map Equation 6.25 was based on the group velocity of A_0 at $f \cdot d = 1.31$ MHz-mm to capture the arrival time of the wave packet center of gravity. Calculations were performed in under one second per source on a Windows machine running an Intel i7-3770k processor which is a dramatic reduction compared to the 35 hours required to simulate full wave propagation from a single source with COMSOL on a higher performance computer.

6.4 Numerical results

Figure 6-9 shows the first-arrival traveltime wave paths calculated with the SPR method for three different source positions. The gray scale represents the α-parameter distribution over the Ω_e domain with bright and dark regions corresponding to high and low sound speed, respectively. 3-D renderings of the wave paths are shown on the right for each case. Figure 6-9 (a) provides the ray paths emanating from Tx16 which, as shown in Figure 6-8 (a), is on the inner side of the bend at 3 o'clock. While in a uniform velocity domain the wave paths would be straight segments joining Tx16 to each transducer in the receive array, the region of high sound speed in front of Tx16 bends the rays which are initially forced to propagate within a confined region on the inner side of the bend and eventually spread out as the rays prepare to exit the bend (see rays Γ'_0 and Γ'_1). It should be observed that the rays joining the first replica of the receive array in Figure 6-8 (a) should be the mirror image of the rays joining the actual receive array around the line $y_1 = \pi r$. This is true for the rays shown in Figure 6-8 (a) with the exception of the ray on the far left of Figure 6-8 (a) which exhibits some distortion compared to its mirror counterpart. This effect is due to the rigid structure of the graphs and is a known limitation of SPR [119].

The Γ'_2 rays which perform from one to two full turns around the tube exhibit a similar behavior. However, since they have to cross the region of low sound speed on the outer side of the bend, their trajectories tend to align with the circumferential direction (y_1 in the Ω_e domain) when passing through the outer side of the bend so as to minimize the traveltime.

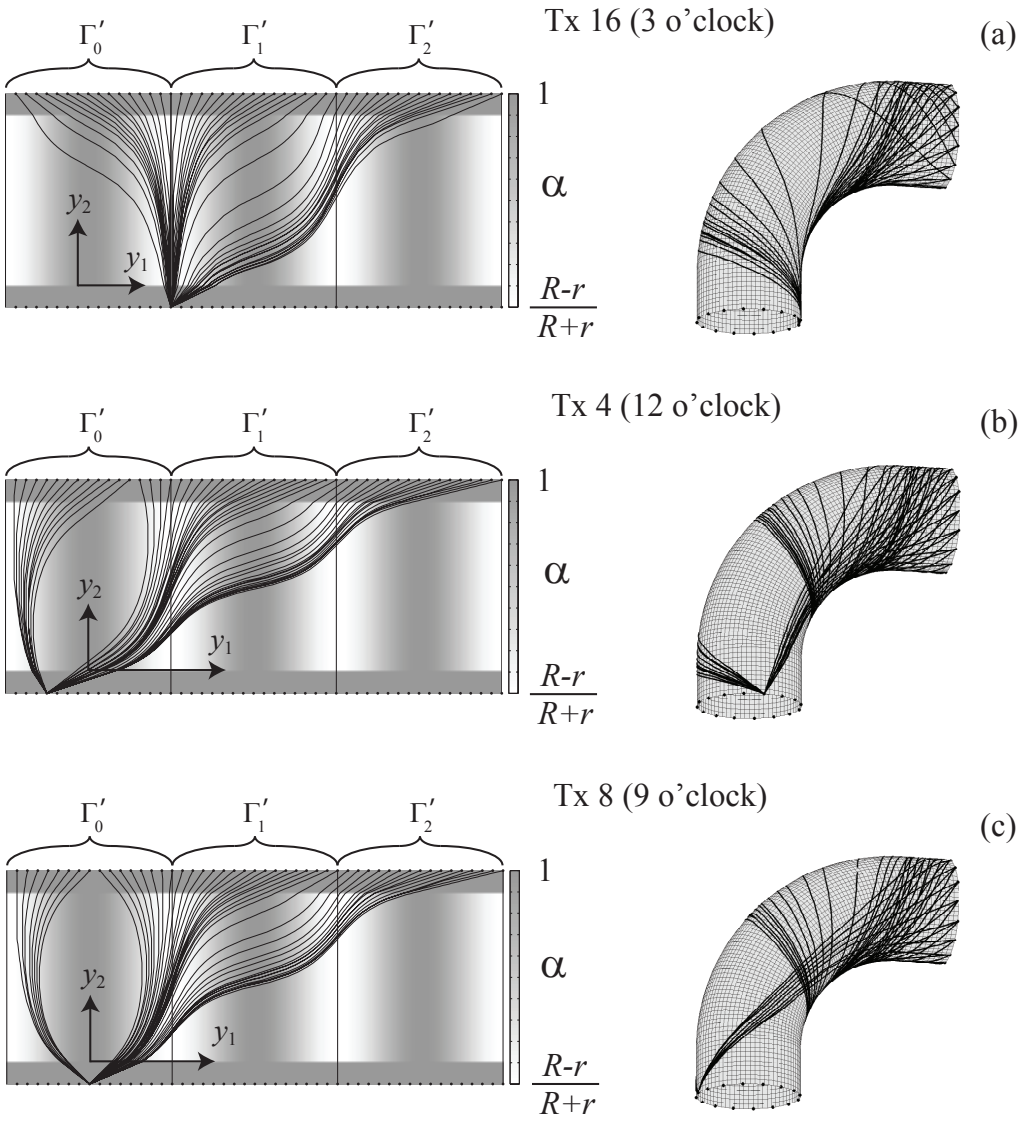

Figure 6-9: SPR predictions of A_0 first-arrival wave paths from one source to 16 equally spaced receivers. Paths performing up to two full turns around the pipe circumference are shown in the 2-D acoustic domain (left) and in the corresponding 3-D physical space (right). The rays are traced for three different source locations: (a) inner side of the bend at 3 o'clock; (b) top side of the bend at 12 o'clock; (c) outer side of the bend at 9 o'clock.

Similar trends are observed in Figure 6-9 (b) and (c) which correspond to source positions at 12 and 9 o'clock, respectively. Figure 6-9 (c) clearly shows that the region of low sound speed on the outer side of the bend tends to deflect the Γ_0' rays away towards the inner side of the bend. This implies that the first-arrival wave paths

do not contain information about potential defects located on the outer side of the bend. On the other hand, the Γ_1' rays provide a good coverage of the same region. These results suggest that attempting guided wave tomography of the bend without including wave paths which wrap around the bend multiple times would cause defects on the outer part of the bend to be under-represented or even undetected.

As observed in Section 2.3 SPR cannot predict intersecting rays. However, thanks to the replication process the distance between source and receive transducers is artificially increased so that later arrivals still correspond to the first -arrival traveltime. This is essential to obtain the modes that wrap around the pipe since they cause multiple intersections as shown in the 3-D renderings of Figure 6-9.

It should also be observed that the ray paths in Figure 6-9 coincide with the geodesics of the bend. Indeed, the SPR method in combination with the inhomogeneous anisotropic velocity model introduced in this chapter appears to provide an efficient numerical technique for solving the geodesic equation on generalized cylinders.

Figure 6-10 shows a comparison between SPR and FEM simulations of full wave propagation for the same source positions considered in Figure 6-9. Each cascade plot shows the 16 waveforms detected by the transducers of the receive array when a single transducer of the transmit array is excited. Overall there is good agreement between the first-arrival traveltime predictions of SPR and the FEM simulations for all the source positions thus demonstrating the consistency between the SPR and FEM models.

Analysis of Figure 6-10 (b) and (c) reveals the presence of a set of large wave pulses trailing behind the first-arrival pulses. The effect is most evident when the source is in the 9 o'clock position which corresponds to the outer side of the bend. The origin of the trailing pulses is revealed by Figure 6-11 (a) that shows selected screenshots of the FEM simulations when the source is at the 9 o'clock position. Here, only the Ω domain is shown and the solid lines delimit the beginning and end of the bend. As the wavefront propagates inside the bend it undergoes a spatial distortion due to the sound-speed *'valley'* at the center of the model that leads to the concave

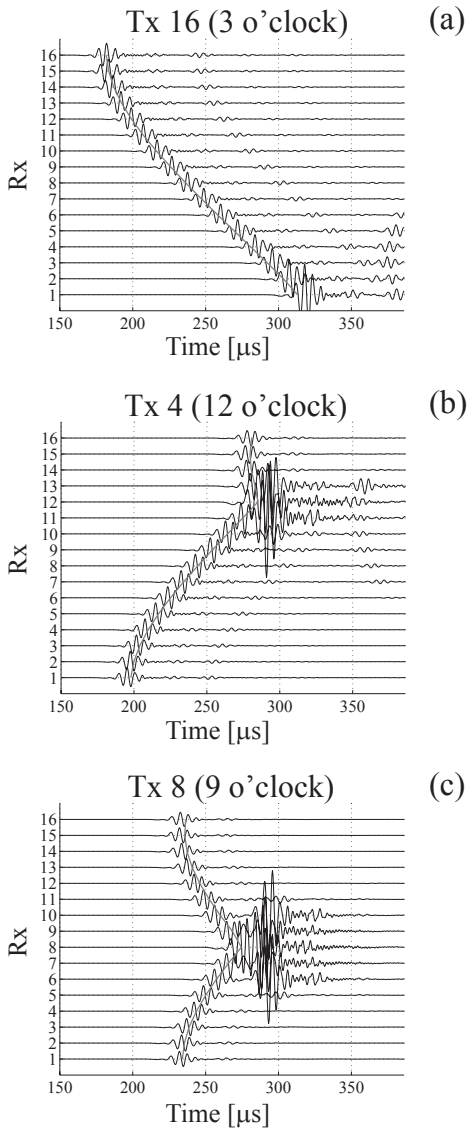

Figure 6-10: Full wave simulations obtained for the same source positions considered in Figure 6-9. The gray solid curves represent the first-arrival traveltimes obtained from ray theory. Large wave pulses trailing from the first arrivals are visible in (b) and (c) and are due to the self-focusing effect.

front seen at time t=240μs. The subsequent stages of the front propagation can be interpreted based on the theory of caustics proposed in [120] (p. 72) and with the aid of the diagram in Figure 6-11 (b). The diagram shows the concave front ABC and the caustic EDF obtained as the envelope of the rays emerging from the front; the caustic has a cusp singularity at point D. As the smooth front ABC transits

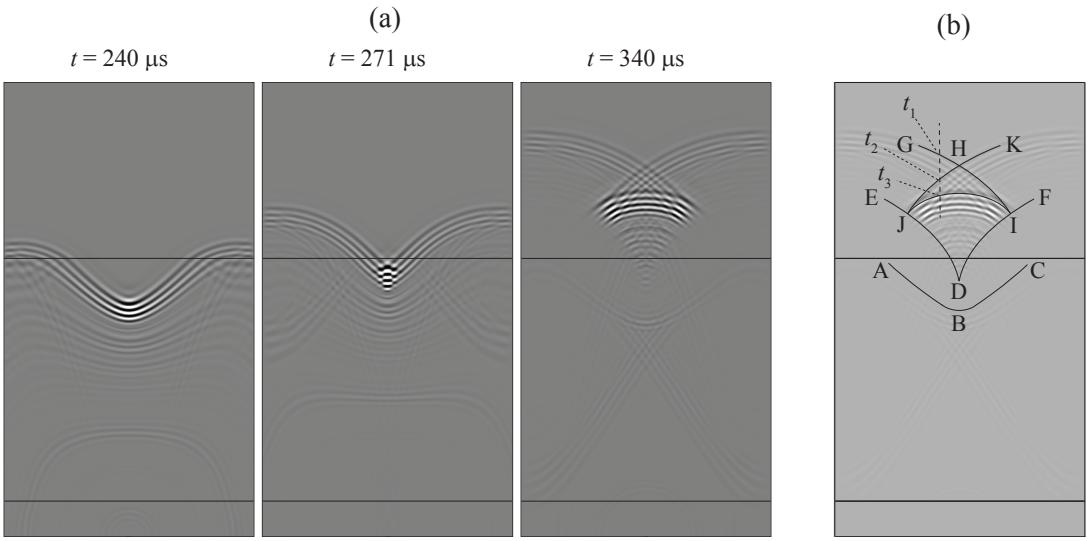

Figure 6-11: Illustration of the self-focusing phenomenon. (a) FEM snapshots capturing the evolution of the wavefront excited by a source transducer on the outer side of the pipe; (b) diagram showing the position of the caustic EDF associate with the concave wavefront shown in (a) at t=240 μs, the cusp in D, and the folded wavefront GHIJHK.

through the cusp D, it folds on itself leading to the new front $GHIJHK$ which has cusp singularities in I and J. The transition instant is captured by the snapshot at time t=271μs where the curvature of the front tends to infinity. The folded wavefront is clearly seen at time t=340μs where the two weak fast branches GHI and JHK are followed by the energized JI branch. JI is the result of self-focusing caused by the lensing effect determined by the sound-speed valley and corresponds to the trailing signals observed in Figure 6-10 (b) and (c). It can also be observed that the shape of the front $GHIJHK$ leads to three different traveltimes, a phenomenon known as triplication [121], when the receivers are located close to the center of the model. Therefore, a receiver located at the position indicated by the dashed line in Figure 6-11 (b) will see three arrival times, t_1, t_2, and t_3 corresponding to points, 1, 2, and 3 on the wavefront. However, SPR will only be able to predict the first-arrival traveltime, t_1, for the reasons outlined in Section 2.3.

6.5 Experimental results

Experimental validation was conducted on the bend pipe section shown in Figure 6-1 whose characteristics have been described in Section 6.3. Here, it is emphasized that the bend was welded to the pipe straight sections leading to weld caps approximately 2 mm thickness - these were not modeled in the numerical simulations. The ring arrays employed EMAT transducers specifically designed to maximize the A_0/S_0 ratio both in transmission and reception [122]. The arrays were driven by a custom-made, 32-channel control system with parallel architecture [122]. Each transducer of the transmit array was excited sequentially and each time the wavefield transmitted across the bend was sampled with all the transducers of the receive array leading to a total of $16 \times 16 = 256$ waveforms. The excitation signal was centered at 0.175 MHz and the waveforms were sampled at 3 MHz. To enhance the signal to noise ratio (SNR) 256 averages were taken for each channel.

Figure 6-12 compares the first-arrival traveltime predictions from ray theory with the experimental waveforms obtained for the same source locations considered in Section 6.4. When the source is on the inner side of the pipe at 3 o'clock, Figure 6-12 (a), ray theory correctly predicts the traveltimes of all the signals that have performed up to two full turns around the tube and in both directions. It can be noticed that channels #13-16 exhibit an additional wave pulse trailing behind the Γ_0 arrivals and pointed by the arrow. Similar groups of larger amplitude trailing signals are also visible for the 12 and 9 o'clock source positions and are due to the focusing effect that was observed in the FEM simulations of Section 6.4. The same effect also causes focusing of the spurious S_0 signal excited by the source leading to another group of signals pointed by the star arrow in Figure 6-12 (b) and (c). The spurious S_0 mode is also responsible for the other wave pulses which are not accounted for by ray tracing.

To further test the focusing hypothesis, measurements were repeated by changing the position of the receive array. Figure 6-13 shows the signals recorded when the source is on the outer side of the pipe (Tx 8, 9 o'clock position) and the receive array is 38.5, 100, and 200 mm away from the weld at the end of the bend. It can be

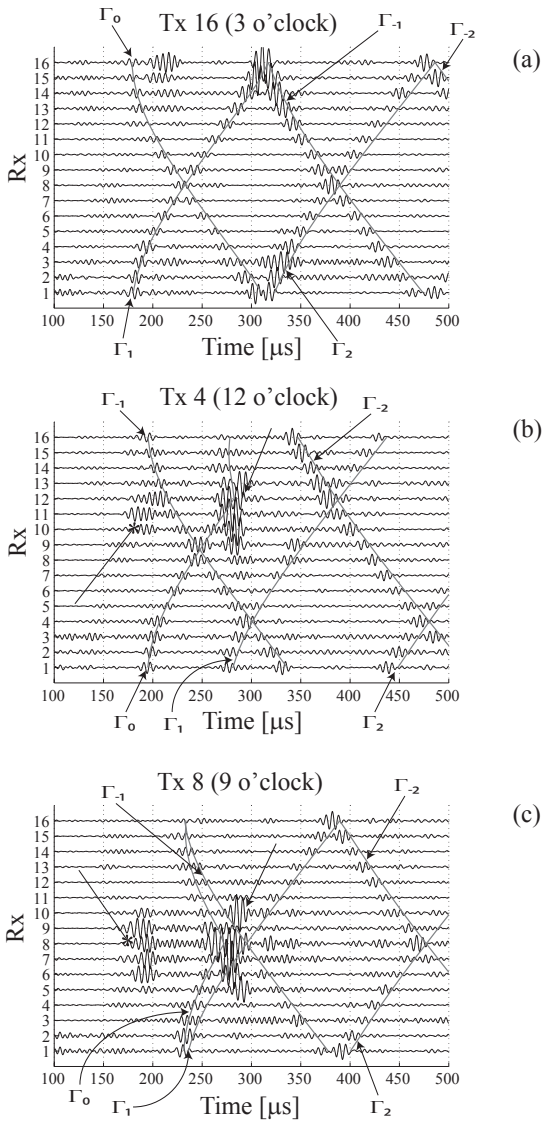

Figure 6-12: Experimental waveforms received for the same source positions considered in the simulations of Figure 6-9 and Figure 6-10. The solid curves indicate the first-arrival traveltime predictions from ray tracing. Ordinary arrows and star-arrows are used to indicate wave pulses originating from the self-focusing phenomenon of A_0 and S_0 modes, respectively.

clearly seen that as the array moves away from the weld the group of trailing signals grow wider affecting more and more receive channels. This is consistent with the FEM predictions and the fact that the caustic widens with distance from the cusp D, see Figure 6-11 (b). Additionally, the trailing signals have larger amplitude than the first-arrival signals according to the self-focusing mechanism observed in the FEM

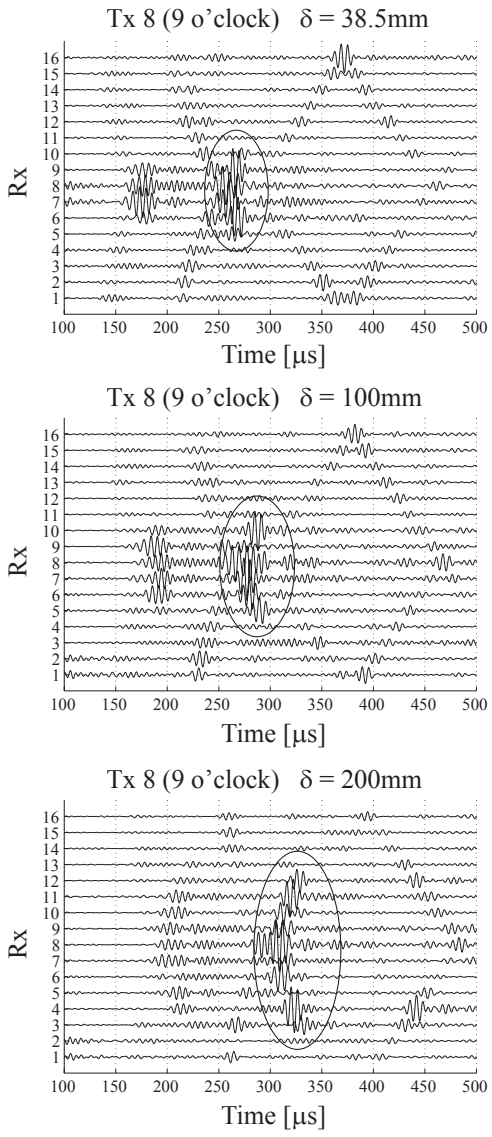

Figure 6-13: Experimental demonstration of the self-focusing phenomenon. Signals are recorded for a source located on the inner side of the bend at 3 o'clock and for three different distances of the receive array from the second weld of the bend: (a) δ=38.5 mm; (b) δ=100 mm; (c) δ=200 mm. As δ increases more receive channels are able to capture the energized wavefront that spreads from the cusp of the caustic which is located on the bend just before the second weld.

simulations.

6.6 Conclusions

This chapter has addressed theoretical, computational, and physical aspects of guided wave propagation and scattering in curved tubular structures which have led to predictions found to be in good agreement with experimental observations.

We have introduced a general theory to describe elastic guided wave propagation in tubular structures by means of an equivalent two-dimensional (2-D) inhomogeneous and anisotropic acoustic model. The equivalence is established based on the definition of orthogonal parametric representations of the structure that preserve traveltime. Under the orthogonality condition, the (2-D) acoustic model is elliptically anisotropic and can be described using differential equations introduced in geophysics to model transversely isotropic media with vertical symmetry. A method to obtain orthogonal parameterizations has been given for generalized cylinders with cross section orthogonal to the spine. Explicit formulas for the case of a torus have been presented.

Numerical implementations of the full-wave equation and ray tracing in elliptically anisotropic media have been introduced using commercially available finite element (FE) software for the full wave simulations and an in-house code based on the shortest path ray (SPR) method for ray tracing and traveltime estimations. Predictions from the two numerical methods have been found to be in good agreement, with SPR being faster than FE by five orders of magnitude. The 2-D equivalent model and the SPR method provide an ideal combination to implement advanced traveltime tomography algorithms in curved tubular structures.

Numerical and experimental results have given new insight into the propagation of guided waves in pipe bends. It has been discovered that wavefronts propagating on the outer side of a curved pipe undergo a concave distortion that eventually causes the front to fold onto itself forming three branches. A slow large amplitude branch trails behind two fast low amplitude branches and is the result of a self-focusing phenomenon. Importantly, the fast branches are deflected away from the outer side of the bend and therefore do not encode information about potential defects in this

region. This would represent a major drawback for detection methods based on first-arrival signal interpretation. However, higher order modes, wrapping around the bend multiple times, do cross the outer side of the bend in the circumferential direction and can therefore be used to detect and characterize defects that are elusive to first-arrival signals.

6.7 Appendix: Remarks on the INELAN model

In this section we provide additional clarifications about the use of group and phase velocities in the INELAN model. Different INELAN models are required to study the traveltime of signals that propagate at either the phase or group velocity of the selected Lamb mode in the physical space of the torus. This is apparent when considering the standard case of a straight pipe which can be unwrapped without any distortion. In this case the eikonal equation is dependent on a single velocity c and is given by

$$\left(\frac{\partial \tau}{\partial y_1}\right)^2 + \left(\frac{\partial \tau}{\partial y_2}\right)^2 = \frac{1}{c^2[\mathbf{r}(\mathbf{p}')]}, \tag{6.34}$$

which is obtained from Section 6.2.2 when $\alpha(\mathbf{p}') = 1$. To simulate the group traveltime, c is set equal to the group velocity of the selected guided mode at the frequency of interest, $c_{gr}(\mathbf{p})$. On the other hand, the traveltime of a signal traveling at the speed of the phase velocity (phase traveltime) is obtained by setting c equal to the phase velocity of the mode, $c_{ph}(\mathbf{p})$. Therefore, even in the conventional case of a straight pipe two different ray models are required to study the propagation of phase and group. In the case of a bend the two models are obtained by substituting the values of phase or group velocity in Equation 6.21. However, the physical interpretation of the INELAN velocity models is now more complex due to anisotropy. To illustrate some of the key aspects of the INELAN model we consider the simulation of phase and group traveltimes separately.

6.7.1 Phase traveltimes

Returning to the case of a straight pipe free from defects, it can be observed that the acoustic group velocity model is isotropic and homogeneous. Therefore at each point in the 2-D unwrapped domain the phase, v_{ph}, and group, v_{gr}, velocities are equal to the phase velocity of the selected Lamb mode, i. e. $v_{ph} = v_{gr} = c_{ph}$. For the torus instead, due to anisotropy the phase and group velocities in the 2-D domain are in general different, $v_{ph} \neq v_{gr}$, vary depending on propagation direction and position along the torus, and cause the phase fronts to propagate in a direction different from that of the energy (group) rays. As demonstrated in Chapter 6 traveltime equivalence between the physical space of the torus and the 2-D domain requires the introduction of elliptical anisotropy. In particular, the traveltime of a signal traveling at the speed of phase velocity on the torus is equivalent to the traveltime of a signal that in the INELAN 2-D model travels at the speed

$$v_{gr}(\mathbf{p}', \theta_g) = \frac{c_{ph}[\mathbf{r}(\mathbf{p}')]}{\sqrt{\cos^2\theta_g + \alpha^2(\mathbf{p}')\sin^2\theta_g}}, \tag{6.35}$$

in which θ_g is the propagation angle relative to the y_1 axis. It is then observed that Section 6.7.1 is the group velocity of a medium that is elliptically anisotropic. Therefore, there exists a formal equivalence between phase traveltime on the torus and group traveltime in the INELAN domain. The phase velocity corresponding to v_{gr} in the 2-D INELAN domain is

$$v_{ph}(\mathbf{p}', \theta) = \frac{c_{ph}[\mathbf{r}(\mathbf{p}')]}{\alpha(\mathbf{p}')}\sqrt{\sin^2\theta + \alpha^2(\mathbf{p}')\cos^2\theta}, \tag{6.36}$$

where θ is the propagation angle of the phase fronts and is related to the group angle, θ_g, through Section 6.2.3, repeated here as

$$\tan\theta = \frac{1}{\alpha^2(\mathbf{p}')}\tan\theta_g. \tag{6.37}$$

Because of the properties of elliptical anisotropy, the group traveltime in the 2-D INELAN model is the traveltime, τ, appearing in Equation 6.21 which for the case considered in this section is written using $c = c_{ph}$

$$\left(\frac{\partial \tau}{\partial y_1}\right)^2 + \frac{1}{\alpha^2(\mathbf{p}')}\left(\frac{\partial \tau}{\partial y_2}\right)^2 = \frac{1}{c_{ph}^2[\mathbf{r}(\mathbf{p}')]}. \tag{6.38}$$

6.7.2 Group traveltimes

Travel time preservation also implies that the group traveltime in the physical space of the torus is the same as the group traveltime of a wave traveling in the INELAN 2-D model where the group velocity field is obtained from Section 6.7.1 by replacing c_{ph} with c_{gr}, i.e.

$$v_{gr}(\mathbf{p}', \theta_g) \;=\; \frac{c_{gr}[\mathbf{r}(\mathbf{p}')]}{\sqrt{\cos^2\theta_g + \alpha^2(\mathbf{p}')\sin^2\theta_g}}. \tag{6.39}$$

Similarly, the expression of the 2-D phase velocity field and the group traveltimes are derived from Section 6.7.1 and Section 6.7.1 by replacing c_{ph} with c_{gr}.

In concluding this Appendix, we observe that the emergence of anisotropy and inhomogeneity in the 2-D model is linked to the distortion experienced by wavefronts as they propagate on the torus. The experiments reported in Chapter 6 have shown that the wavefront radiating from a point-like source does not expand as a circular wavefront but rather splits into multiple branches with some of them exhibiting a concave shape with non-uniform curvature. For such a complex wavefront geometry, the phase velocity is non-uniform along the front even when the front propagates in a homogeneous medium (see, for instance pp. 16-23 of Ref. [123]) and explains why the 2-D model must be inhomogeneous. The distortion of the wavefront also means that phase and energy do not necessarily propagate in the same direction leading to an anisotropic behavior.

Chapter 7

Experimental validation of a fast forward model for guided wave tomography of pipe elbows

7.1 Introduction

The aim of this chapter is to provide further validation of the model introduced in Chapter 6 by studying its accuracy in the presence of realistic corrosion defects. In addition, the sensitivity of traveltime measurements to the presence of damage is analyzed as a function of defect position around the pipe circumference. The experimental methods are discussed in Section 7.2 while validation of the model is provided in Section 7.3. Concluding remarks are given in Section 3.5.

7.2 Experimental methods

To validate the forward model in Section 6.2 multiple defects were introduced on the elbow of an 8" diameter (220 mm measured O.D.), schedule 40 (8.18 mm nominal wall thickness), carbon steel pipe bend consisting of two 1.5 m length straight sections welded to a 90° elbow with 1.5 D bend radius (R=305 nominal bend radius), shown in Figure 6-1 and described in Figure 6-8 (a). Due to the overall size of the pipe,

it was not possible to use controlled machining methods to introduce defects of a predetermined shape. Therefore, the approach used was to employ angle grinding and the method of impressed currents, which simulates accelerated corrosion, to introduce arbitrary defects and subsequently map their actual depth profile using 3-D laser scans. The maps obtained from the scans were then used to build the forward model and predict traveltimes to be compared with the measured ones. The different aspects of the experimental methods are further discussed in the subsections below.

7.2.1 Pipe bend specimen

Due to manufacturing tolerances the wall thickness of straight pipes undergoes variations along the pipe circumference that can be as high as $\pm 10\%$ of the nominal wall thickness. Pipe elbows are known to have greater variations [124] therefore the first step was to assess the extent of the wall thickness changes for the pipe bend considered in this study. For this purpose, wall thickness profiles were measured along five sections of the elbow and at one free end of one of the straight pipe sections as shown in Figure 7-1 - for each section the thickness was sampled at more than 50 locations. The thickness was measured with a 20 MHz, 1/8" diameter (3.2 mm) fingertip ultrasonic probe - the small diameter was necessary to improve the contact of the probe to the highly curved surface of the elbow. As it can be observed from Figure 7-1 the thickness exhibited quasi-periodic oscillation around the pipe circumference leading to peak-to-trough variations of 1.72 mm, i. e. 21% of the mean wall thickness estimated to be 8.25 mm. On the other hand, the thickness on the straight section was more uniform showing a mean value of 7.28 mm and a standard deviation of 70 μm.

7.2.2 Accelerated corrosion method

To introduce realistic corrosion defects an initial study was conducted on an 8.2 mm thickness, 76×146 mm, flat carbon steel coupon. The objective was to estimate the wall-thickness loss rate obtainable with the impressed current method which reproduces the electrochemistry of corrosion but with an accelerated kinetics. The method

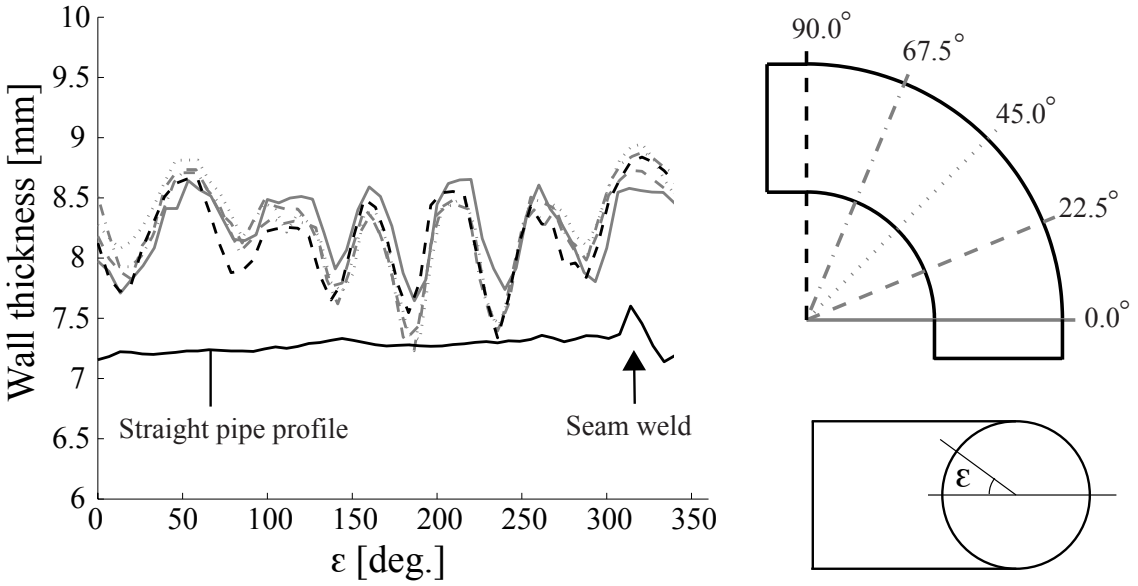

Figure 7-1: Wall-thickness profiles of a pristine 8", schedule 40, carbon steel pipe elbow with 1.5 D radius of curvature. The thickness is mapped along the circumference of the pipe at five different locations. The wall thickness is observed to have large cyclic variations with respect to the circumferential position. Wall thickness in the straight pipe section is included for comparison - the position of the pipe seam weld is indicated by the arrow.

has been used by other investigators in similar studies [125, 126] and employs an electrolytic cell in which the metal to be oxidized (corroded) is the anode (positive) with a second electrode acting as the cathode (negative) and using a water solution as the electrolyte. In the experiments, the anode was formed with an aluminum plate with the same dimensions as the steel coupon and oriented in the transversal direction so as to cover a 76×76 mm area over the coupon, Figure 7-2 (a). Spacers were used to maintain a constant 17.2 mm clearance between the two plates which was filled by a 3.5% (3.5g/100ml) saltwater solution. Electrical cables from the power supply were spot welded to the electrodes with the connection on the steel coupon protected by an insulator to avoid corrosion. A Kepco power supply was used to adjust the voltage between the electrodes and maintain a constant electrical current. The corrosion rate was monitored using a 10 MHz, 1/2" diameter (12.7 mm) ultrasonic probe operating in pulse-echo which estimated the wall thickness by monitoring the relative phase shifts between the first and second reflections from the top surface of the coupon.

The ultrasonic signal was digitized using a 250 MHz sampling rate after averaging the signal 1000 times. Ideally, the probe would have been attached to the back of the specimen, however due to the aggressive corroding environment it was instead glued to the outer surface of the wall of the Plexiglas box used to form the cell which therefore acted as a delay line. The temperature of the specimen and saltwater solution was kept constant at 25 °C by continuously circulating the solution in a temperature controlled 12 L bath. The circulation also allowed the partial removal of the oxide sludge from the sample surface. Six different levels of input current were tested over a period of 40 hours during which the wall thickness was sampled every 60 seconds.

Figure 7-2 (b) shows the measured wall-thickness loss as a function of time for the six current levels with the corresponding corrosion rates given in Figure 7-2 (c). The wall-thickness loss is measured with 5 nm precision which leads to the very straight lines seen in Figure 7-2 (b). The data exhibits the typical linear relationship between electrical current and corrosion rate according to Faraday's law. Linear regression of the data in Figure 7-2 (c) yields a corrosion rate of 18.4 μm/hr/A. However, this is the corrosion rate measured at the center of the specimen (this is the location of the ultrasonic probe) and cannot be used to predict the corrosion rate of neighboring points in the specimen. In spite of the highly controlled experimental conditions, wall-thickness loss varied significantly across the specimen as shown in the photograph of Figure 7-2 (d) thus meaning that it is not possible to rely on the measured current and corrosion time to estimate the true depth profile of the defect.

7.2.3 Defects

Defects were introduced at three different locations around the pipe circumference with each defect at an azimuthal location approximately 45° through the bend as shown in Figure 7-3. Defect I was introduced on the intrados by angle grinding, Defect II was produced on the side by the impressed current corrosion method, and Defect III was introduced on the extrados also by angle grinding. Defect depth was increased in consecutive steps according to the values given in Table 7.1 which also provides some of the statistical properties of the depth profile for each defect.

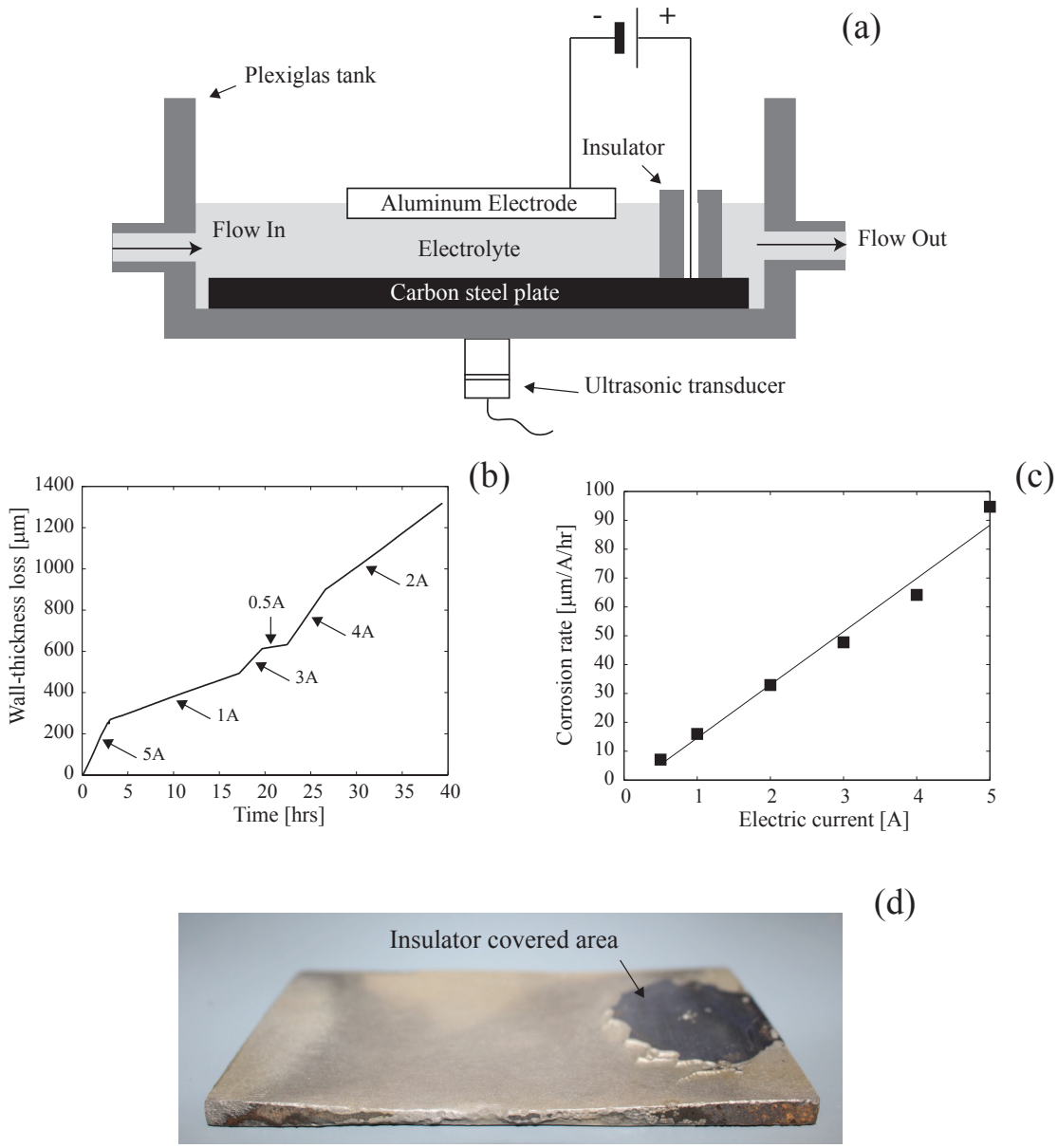

Figure 7-2: Measurement of corrosion rates obtainable with the impressed current method. (a) Diagram of the electrolytic cell used to corrode a flat steel coupon. (b) Continuously measured wall-thickness loss as a function of time and for six different electric current levels. (c) Corrosion rates as a function of electric current derived from (b). (d) Coupon at the end of the corrosion tests showing an uneven wall-thickness loss.

Application of the impressed current method to the pipe elbow was implemented using the setup shown in Figure 7-4. The cell was formed using a cylindrical container 100 mm diameter shaped on one side to conform to the complex surface of the elbow

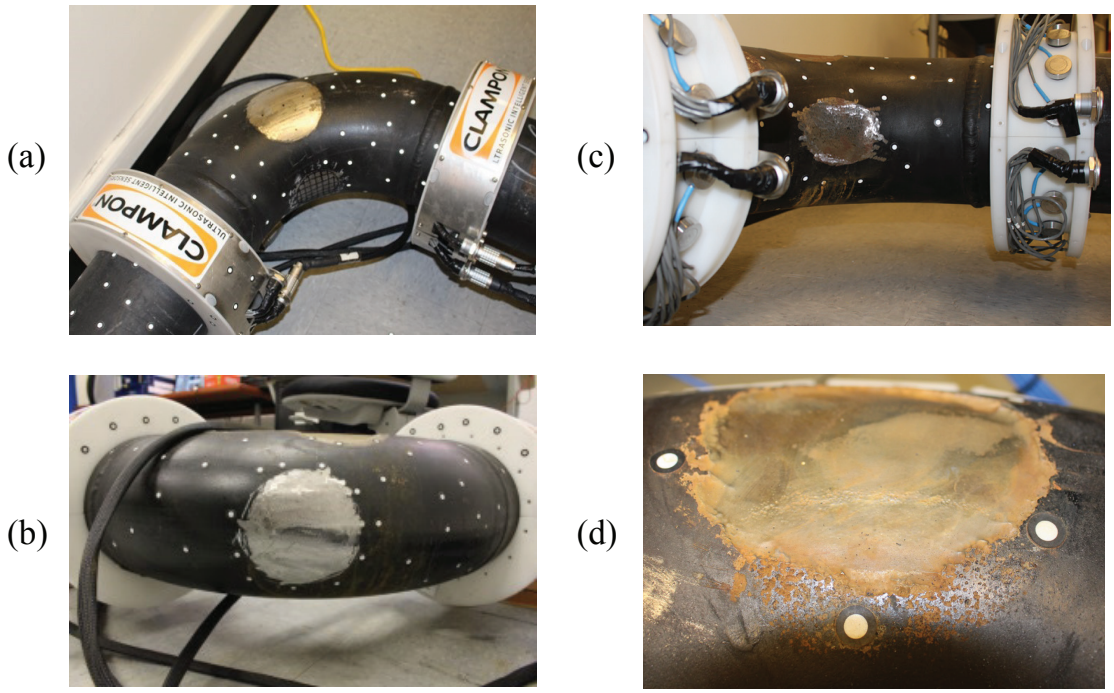

Figure 7-3: Photographs of the three defects considered in the experimental study. (a) Overview of pipe orientation and Defects I and II (b); Defect III, introduced via angle grinder, located on the extrados; (c) Defect I, introduced via angle grinder on the intrados; (d) Defect II, introduced via accelerated corrosion on the elbow side. The white stickers are reference markers used to map the wall-thickness loss with a 3-D laser scanner.

side. The defect was introduced from the outer surface of the pipe and the cell was held in position by elastic straps. To form the anode an electrode was spot welded to the pipe surface while the cathode was formed using a thin galvanized steel disk shaped as the surface of the elbow, Figure 7-4 (b). This shape was chosen so as to obtain a uniform thickness gap between the cathode and anode and hence a more uniform corrosion rate across the area of the defect. The current was kept constant at 6 A which was sufficient to produce large amounts of H_2 and led to vigorous bubbling of the electrolyte. The typical morphology of a defect obtained with the impressed current method is shown in Figure 7-3 (d). As in the case of the steel coupon, the defect had a nonuniform depth profile with a maximum depth typically 65% deeper than the defect mean depth as it can be deduced from the values of maximum and mean depth shown in Table 7.1. In this context, angle grinding led to more irregular

Table 7.1: Defect locations, methods of introduction, sizes and depths. All the defects are introduced in the same pipe specimen.

Defect ID	**Location**	**Type**	**Size (Azim. x Circ.)** [mm]
Defect I	Intrados	Grind	110 x 80
Defect II	Side	Impr. Curr.	100 x 100
Defect III	Extrados	Grind	120 x 120
Defect ID	**Maximum Depth** [μm]	**Mean Depth** [μm]	σ [μm]
Defect I 1	1238	555	242
Defect I 2	1462	795	411
Defect I 3	2292	1166	596
Defect I 4	2900	1404	857
Defect I 5	3739	1846	1141
Defect II 1	373	158	53
Defect II 2	559	329	100
Defect II 3	1329	843	308
Defect II 4	1720	1166	406
Defect II 5	2080	1475	541
Defect II 6	2603	1829	697
Defect III 1	729	339	122
Defect III 2	1121	558	255
Defect III 3	1627	756	386
Defect III 4	2036	914	511
Defect III 5	2887	1237	657

defects with a maximum depth typically more than 100% deeper than the defect mean depth. According to oil and gas industry standards, all the defects can be classified as localized corrosion since the maximum depth is more than 10% larger than the mean depth.

7.2.4 3-D laser scan

The Creaform EXAscan hand-held laser scanning system shown in Figure 7-5 (a) was used to map the wall-thickness loss at each stage of defect progression. The system has a function to map defect depth in straight pipe sections; however, this is not

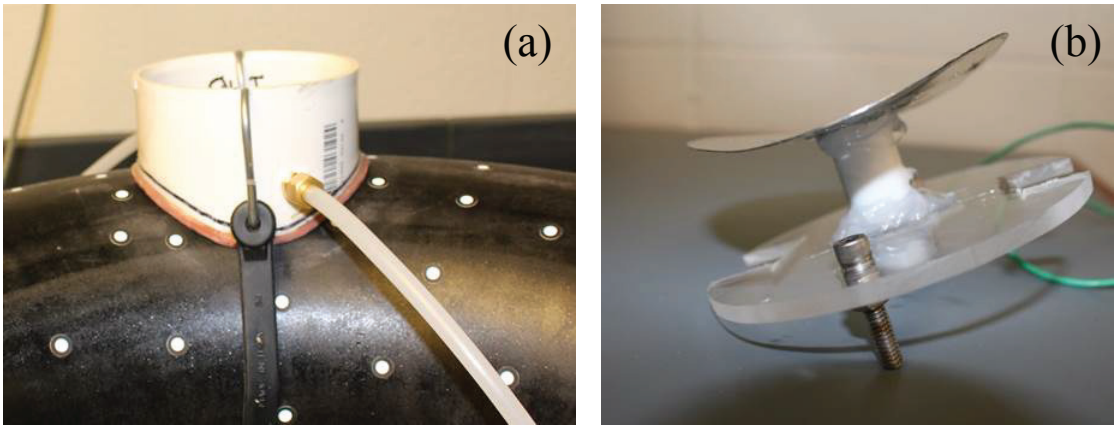

Figure 7-4: Electrolytic cells used to induce accelerated corrosion on the side of pipe elbows: (a) A cylindrical container conforming to the surface of the elbow is held in position by elastic straps; (b) A negative electrode is shaped to maintain a constant gap thickness between the electrode and the surface of the elbow.

applicable to the more complex surface of the elbow. Here, a method was developed that uses two scans performed before and after the introduction of a defect. For each scan, a set of points on the pipe surface is outputted as a cloud of points in the scan frame of reference $\{O'', x_1', x_2', x_3'\}$ which is arbitrarily oriented relative to the Cartesian system $\{O, x_1, x_2, x_3\}$ of Figure 6-4. Moreover, since the scan frame moves with each scan it is not possible to directly compare two scans to measure the wall loss. It is therefore necessary to transform the coordinates of each scan to the common coordinate system $\{O, x_1, x_2, x_3\}$. For this purpose, the three coordinates of the origin of the scan frame $\mathbf{r}_{O''} \equiv (x_{1O''}, x_{2O''}, x_{3O''})$ and the three Euler's angles $\mathbf{a} \equiv (\varphi, \vartheta, \psi)$ defining the 3×3 rotation matrix $M(\mathbf{a})$ from $\{O'', x_1', x_2', x_3'\}$ to $\{O, x_1, x_2, x_3\}$ need to be known so that the coordinate transformation can be written as

$$\begin{bmatrix} x_1 \\ x_2 \\ x_3 \end{bmatrix} = M(\mathbf{a}) \begin{bmatrix} x_1'' \\ x_2'' \\ x_3'' \end{bmatrix} + \mathbf{r}_{O''}. \tag{7.1}$$

The six unknown parameters of $\mathbf{a}$ and $\mathbf{r}_{O''}$ can be obtained by imposing that after the coordinate transformation (Equation 7.1) the cloud of points lies on the torus whose

analytical expression is given by the implicit form of Equation 6.23, i.e.

$$\left(R - \sqrt{x_1^2 + x_2^2}\right)^2 + x_3^2 - r^2 = 0, \tag{7.2}$$

where r and R are the pipe and bend radii defined earlier. This leads to the cost function $E(\mathbf{a}, \mathbf{r}_{O^{\prime\prime}})$ defined as

$$E(\mathbf{a}, \mathbf{r}_{O^{\prime\prime}}) = \sum_{i=1}^{N} \left[\left(R - \sqrt{x_{1i}^2 + x_{2i}^2}\right)^2 + x_{3i}^2 - r^2\right]^2, \tag{7.3}$$

where N is the total number of points in the cloud and (x_{1i}, x_{2i}, x_{3i}) is the set of coordinates corresponding to the measured coordinates $(x'_{1i}, x'_{2i}, x'_{3i})$ through Section 7.2.4. Parameters $\mathbf{a}$ and $\mathbf{r}_{O^{\prime\prime}}$ are obtained as

$$\mathbf{a}, \mathbf{r}_{O^{\prime\prime}} = \arg\min_{\mathbf{a}, \mathbf{r}_{O^{\prime\prime}}} E(\mathbf{a}, \mathbf{r}_{O^{\prime\prime}}), \tag{7.4}$$

where the minimization is implemented using MATLAB active-set algorithm [127]. In practice, the true bend radius is not known with sufficient accuracy and so the minimization is conducted by considering R in Equation 7.3 as an additional parameter to be optimized.

Once the coordinates of the baseline and defect scans are transformed into the same reference frame the wall-thickness loss is determined by measuring the distance between the intersections of each surface with the normal to the torus and for each point on its surface.

The method was validated by comparing the results of the laser scan with manual ultrasonic measurements performed on the defect on the intrados. Figure 7-5 (b) shows the three-dimensional rendering of the surface of the elbow obtained with the Creaform 3-D optical scan. The corresponding defect depth map produced with the method described above is shown in Figure 7-5 (c) - note that the circular shape of the defect is stretched in the horizontal direction due to the unwrapping of the torus onto a plane. The ultrasonic measurements were performed at 20 MHz with a 1/8" diameter finger tip probe over a grid of points with a ≈10 mm pitch and are plotted as

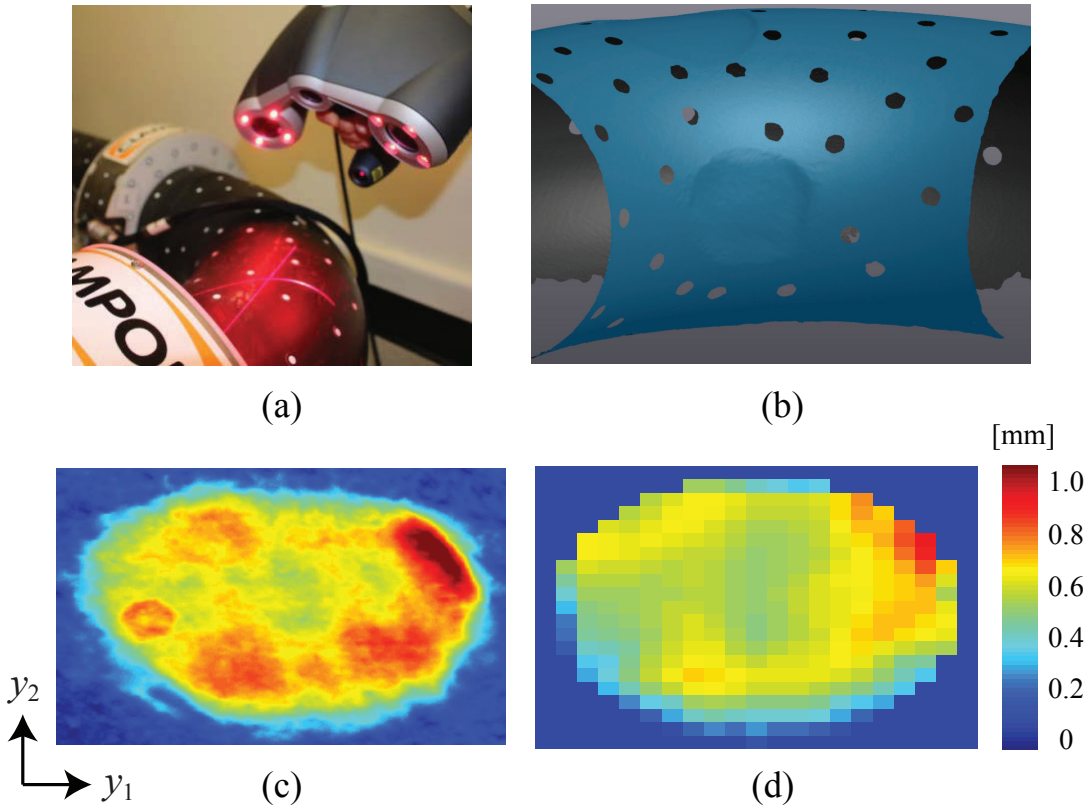

Figure 7-5: (Color online) 3-D laser mapping of wall-thickness loss. (a) Creaform hand-held laser scanning system being used on a pipe bend. (b) 3-D rendering of the cloud of points outputted by the scanner in an arbitrary reference frame. The indentation corresponds to the intrados defect, Defect I, while the holes are due to the reference markers. (c) Wall-thickness loss map of the intrados defect represented in the 2-D domain and obtained with the new differential approach - due to unwrapping the defect is stretched by a factor of two in the horizontal direction. (d) Ultrasonic wall thickness loss map for the same defect as in (c).

a wall-thickness loss map in Figure 7-5 (d). The laser scan, Figure 7-5 (c), reproduces the main features of the defect morphology observed in the manual ultrasonic scan, Figure 7-5 (d). However, it provides a larger maximum wall-thickness loss than the ultrasonic scan, 1.24 mm versus 1.00 mm. This is due to the higher spatial resolution of the laser which provides a pixel size of ≈ 0.5 mm while the ultrasonic measurements tend to underestimate depth when it varies over a spatial scale comparable or smaller than the probe diameter (3 mm).

The precision of the laser scan was estimated by mapping a defect free region multiple times and it was found that the measurements were reproducible within

$\pm 100\mu$m.

7.2.5 Experimental estimation of traveltimes

The purpose of this subsection is to describe how traveltimes are measured experimentally. To measure the guided wave signals the CEM system from ClampOn was used. The system consists of two ring arrays of 16 EMATs driven by a 32-channel controller as described in Section 6.5. The arrays were not moved as multiple defects were introduced. The transducers were excited by a two-cycle gaussian windowed toneburst centered at 140 kHz which corresponds to a wavelength of 18.6 mm. This frequency corresponds to $f \cdot d$=1.16 MHz-mm which is at the low end of the CVG spectrum where the dispersion of the group velocity of A_0 is negligible and was chosen because the EMATs employed in this study are designed to work on thicker pipe walls. Although the A_0 mode could be excited using piezoelectric transducers as in [128], EMATs provide higher mode selectivity at the relatively high $f \cdot d$ product considered in this study [129]. To suppress random electronic noise each signal was averaged 512 times. All the possible transmit-receive combinations, $16 \times 16 = 256$, were recorded in under 30 mins to form one dataset. Figure 7-6 shows a typical set of signals received by all the 16 receivers when transmitting with one of the EMATs closest to the intrados, the waveforms were digitized with a 3 MHz sampling frequency. Signals before and after the introduction of the intrados defect, Defect I 5, are shown. For most transmit-receive pairs, the signal perturbation caused by the defect is small and the two sets overlap almost exactly. The solid thick curves provide the traveltimes predicted by the INELAN model described in Section 6.2 - since here the group arrival is of interest $c[\mathbf{r}(\mathbf{p}')]$ in the numerator of Equation 6.25 is the group velocity. For each waveform the model predicts multiple traveltimes each corresponding to a wave path with a different number of turns around the pipe, i. e. to a particular transmit-receive pair of the virtual arrays in the 2-D domain. The theoretical traveltimes are used to position a window that extracts the wave pulse corresponding to a selected transmit-receive pair of the virtual arrays. Because the measurements are performed around the CGV point, only the phase of the pulse shifts due to damage while the

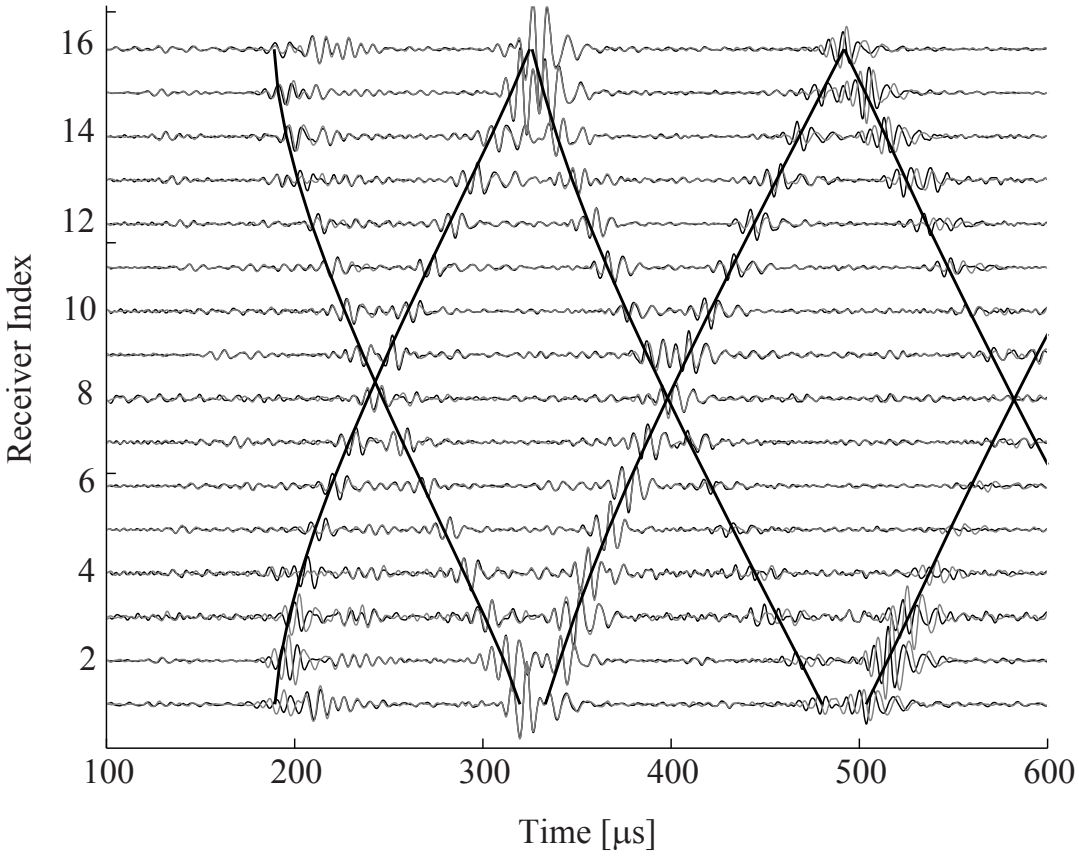

Figure 7-6: Ultrasonic signals measured when transmitting with Tx 16. (black) Baseline signals; (light gray) Signals measured after the introduction of the deepest intrados defect, Defect I 5; (thick black curves) Theoretical group traveltimes predicted by the INELAN model.

signal envelope does not move provided that temperature remains constant [129]. For each wave pulse the traveltime shift $\delta\tau$ is evaluated using the zero-crossing method applied to the baseline and current (before and after damage) signals as explained in Ref. [108].

7.3 Results

Figure 7-7 shows examples of the 2-D models obtained from the laser scans and used to predict the traveltime shifts for the three different defect positions. The maps refer to the isotropic phase velocity, $c[\mathbf{r}(\mathbf{p}')]$, at the numerator of the expression of the anisotropic velocity $c'(\mathbf{p}', \theta_g)$ in Equation 6.25. For each depth map measured by

the laser, $d_{\text{loss}}[\mathbf{r}(\mathbf{p}')]$, $c[\mathbf{r}(\mathbf{p}')]$ is the phase velocity of A_0 evaluated at the frequency-thickness product $f \cdot (d - d_{\text{loss}})$. These velocity maps together with the α-map in Figure 6-8 (b) provide the input for FMM traveltime calculations. For this purpose, the domain is discretized using 2×2 mm square elements leading to 332×518 nodes per replica. Moreover, since the domain has been replicated three times all the wave paths up to three full turns around the pipe circumference are considered.

Figure 7-8 compares the traveltime shifts predicted by the INELAN forward model and those measured experimentally for one depth profile of the defect on the intrados (a)-(b), side (c)-(d), and extrados (e)-(f). Each map corresponds to a matrix in which the ij-th entry is the traveltime shift measured when transmitting with the j-th source of the virtual transmit array and receiving with the i-th element of the virtual receive array. Different matrix blocks correspond to different combinations of the 16-element sub-apertures of the three sub-domains. Therefore, block $n = 0$ refers to the traveltimes from the 16 transmitters to the 16 receivers within the same replica. Block $n = 1$ refers to the traveltimes from the 16 transmitters in the first replica to the 16 receivers in the second replica and so on. Negative n values correspond to wave paths that wrap around the pipe in the opposite direction to the positive n values. A more detailed discussion about this convention can be found in Willey et al. [108].

For the intrados defect, Figure 7-8 (a), the direct paths from the transmitters to the receivers (n=0) encode little information about the defect and the traveltime shifts tend to vanish with exception of the rays traveling close to the intrados, (Tx 1, Rx 1) and (Tx 16, Rx 16). This is partially due to the relatively small circumferential size of the defect, 110×80 mm (azimuthal × circumferential) which means that only few direct rays intersect it. The ray coverage obtained when a source transducer is active close to the intrados is shown in Figure 7-9 (a) - the wave paths that go from the source to the receivers within the first rectangular domain on the left represent the direct paths. On the other hand, the rays that make at least one full turn ($n = \pm 1$) before reaching the receiver provide a denser ray coverage of the defect resulting in larger $\delta\tau$ in excess of 2.5μs for Defect I 3. This trend is confirmed by the experimental measurements in Figure 7-8 (b) which refer to the same defect. However, due to the

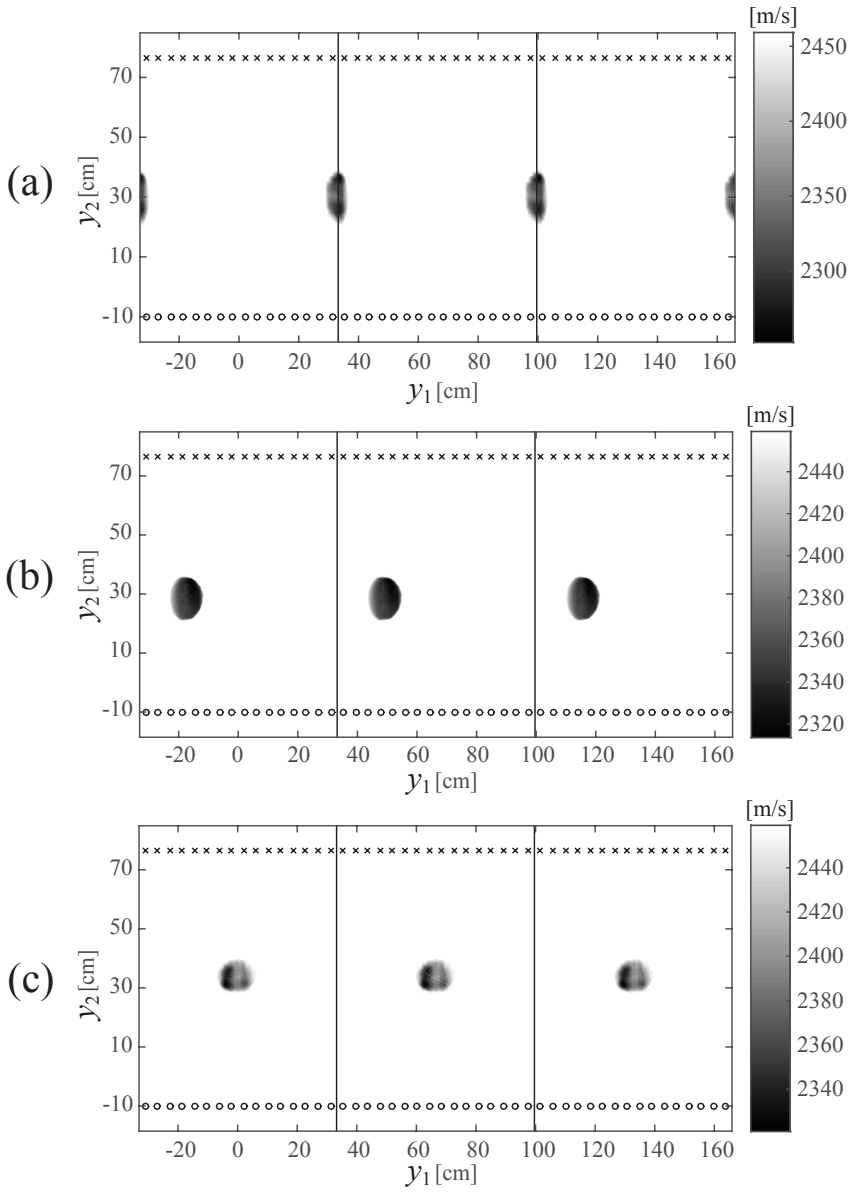

Figure 7-7: Isotropic phase velocity maps obtained from the wall-thickness loss maps measured with the 3-D laser scans. In order to model wave paths that perform up to three full turns around the pipe circumference, two replicas are added to each velocity model. (a) Intrados defect, Defect I 3; (b) Side defect, Defect II 4; (c) Extrados defect, Defect III 3.

presence of experimental noise and the loss of accuracy in the estimation of traveltimes when partial wave pulse overlapping occurs (see pulses close to the intersections of the theoretical arrivals in Figure 7-6) the map in Figure 7-8 (b) shows some degree of pixelation noise. The transmit-receive pairs for which pulse overlapping occurs are

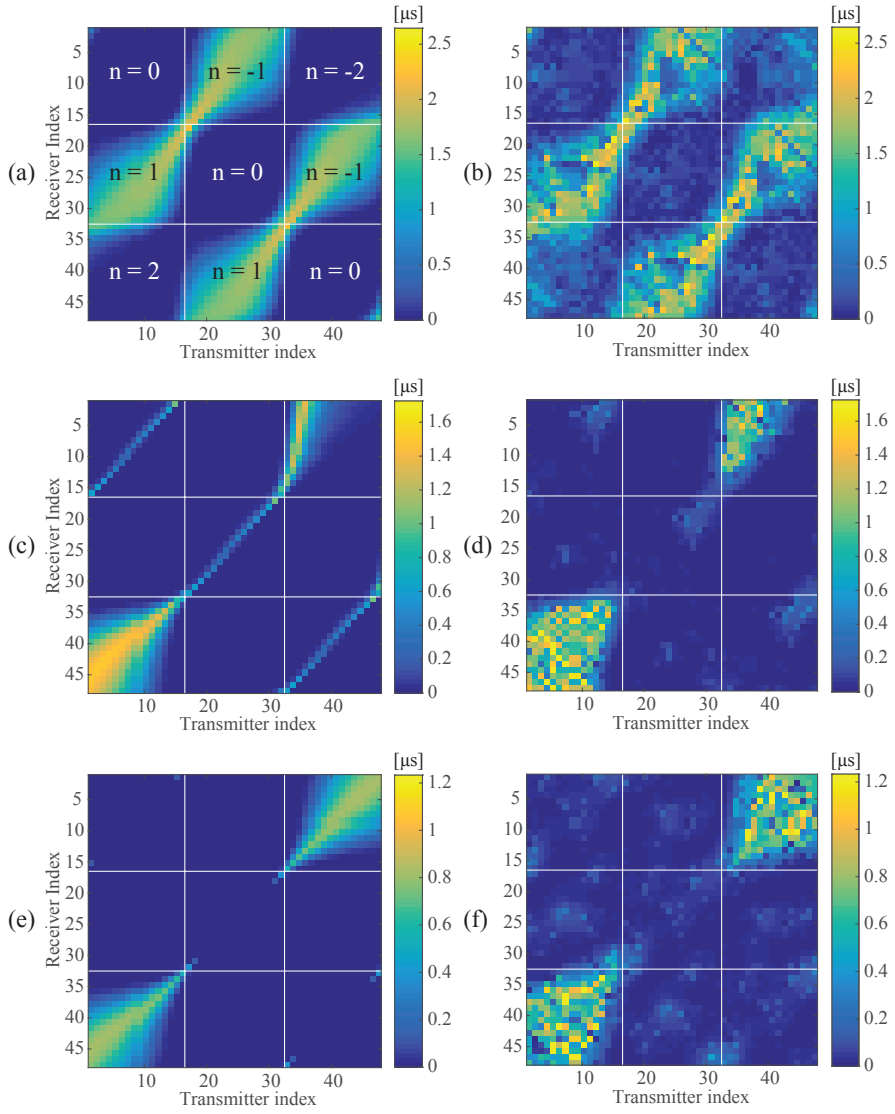

Figure 7-8: (Color online) Comparison between simulated (left) and experimental (right) traveltime shift matrices corresponding to the defects represented by the velocity models in Figure 7-7. (a) Intrados defect, Defect I 3; (c) Side defect, Defect II 4; (e) Extrados defect, Defect III 3. The white grid lines represent sub matrices associated with different groups of wave paths and are identified by the integers n. The n values are only shown for matrix (a) but it is understood that the same numbering applies to the other matrices.

marked on Figure 7-10 and are observed to correspond to the noisiest areas of the experimentally measured traveltime shifts for Defect I 3.

The defect on the elbow side, Figure 7-8 (c), whose lateral size is 100 × 100 mm (azimuthal × circumferential), produces two sets of patterns in the traveltime matrix.

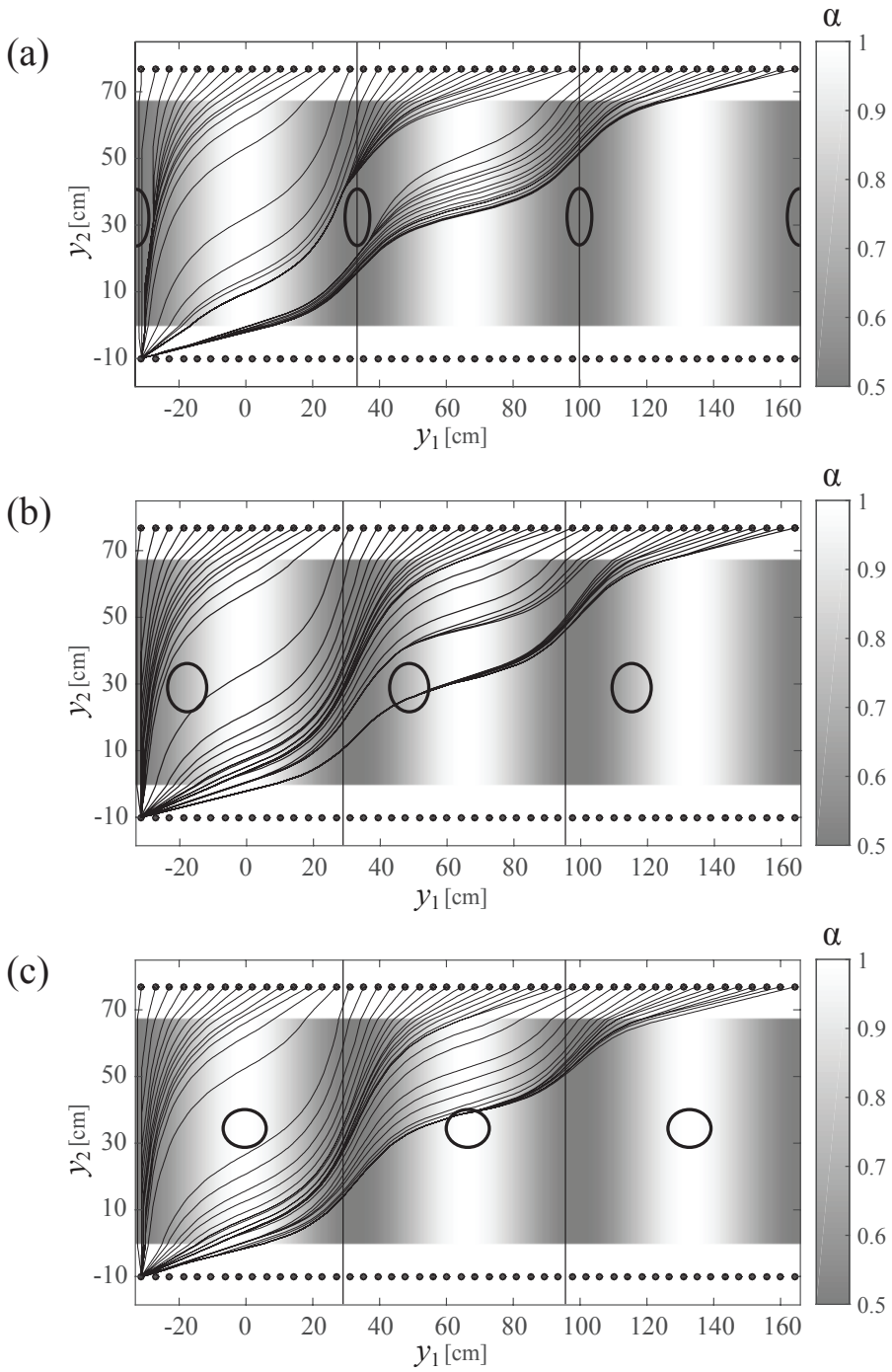

Figure 7-9: Examples of ray coverage obtained when the source transducer is close to the intrados for the: (a) intrados, (b) side, and (c) extrados defects considered in Figure 7-8. The ray paths are superimposed the α-map which is obtained by adding to replicas to the velocity model. The ellipses represent the location and shape of each defect.

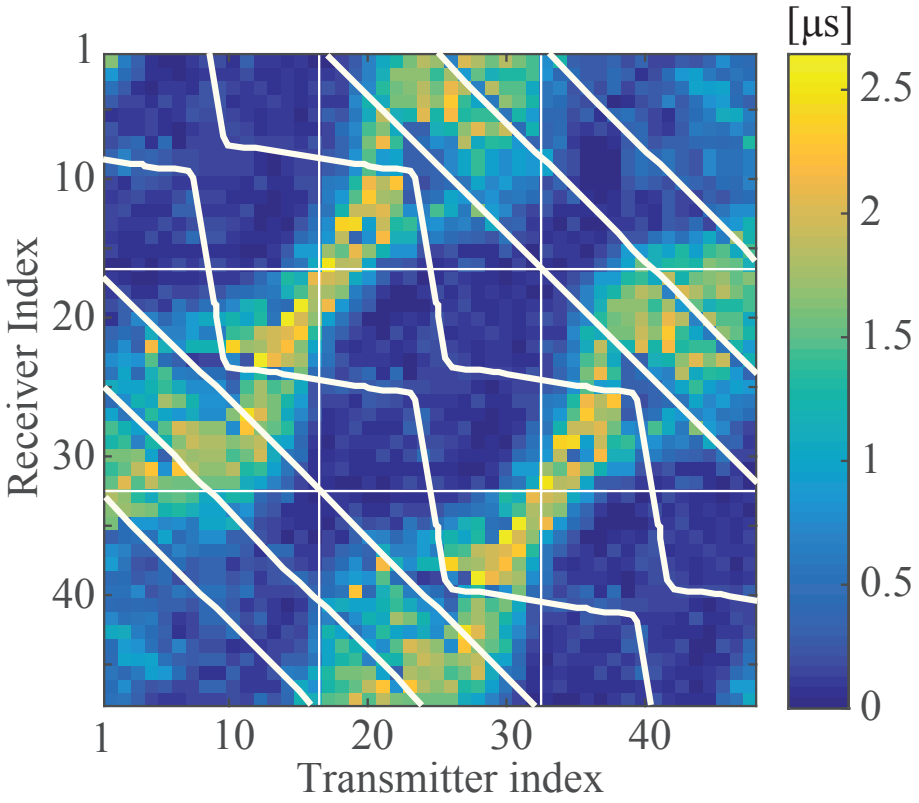

Figure 7-10: White lines signify transmit-receive pairs for which pulses corresponding to different wave paths arrive close to simultaneously, causing overlap. These overlaps are observed to correspond to regions where the experimental data appears noisy or incomplete.

Weaker traveltime shifts are seen along the secondary diagonal of the $n = 0$ block matrices and are the result of the rays bending around the extrados as shown in Figure 7-9 (b). These signatures are not visible in the corresponding experimental data, Figure 7-8 (d), as they probably fall below the noise level of the experiments. On the other hand, the larger traveltime shifts corresponding to the rays that have performed more than one full turn around the pipe ($n = \pm 2$) are reproduced in the experimental data. Finally, the matrices shown in Figure 7-8 (c), (d) are not symmetric because the defect is not exactly located at 45° through the bend but is instead closer to the transmit array as shown in Figure 7-7 (b).

The defect on the extrados, Figure 7-8 (e), whose lateral size is 120 × 120 mm (azimuthal × circumferential), experiences the lowest ray coverage since the rays tend to avoid the extrados, see Figure 7-9 (c). As a result, only the rays that perform

more than one full turn around the pipe circumference are sensitive to the defect and show nonzero traveltime shifts as also confirmed by the experiments, Figure 7-8 (f).

The results presented in Figure 7-8 prove that the INELAN model can reproduce the main signatures of the experimental traveltime matrices within the experimental error. To further investigate the agrement between the model and experiments it is necessary to introduce quantitative metrics. The definition of a single metric that can be used to compare matrices of data, such as the traveltime matrices, is challenging because the single number of the metric must embody the information contained in the multiple, independent entries of the matrix. Therefore, next we propose two independent metrics that can be applied to the traveltime matrices in an attempt to quantify the agreement between experiments and theory.

7.3.1 Sensitivity metric

Traveltimes are sensitive to damage if a change in wall thickness leads to a measurable traveltime change. Therefore, a sensitivity metric can be defined by considering the sum of the traveltime shifts for all possible transmit-receive pairs

$$\Delta\tau = \sum_{i=1}^{48}\sum_{j=1}^{48} |\delta\tau_{ij}|. \tag{7.5}$$

For a given defect, the more transmit-receive pairs are affected by the defect and the larger the traveltime shifts, the greater the value of the metric. This metric should not be confused with the more classic definition of sensitivity based on probability of detection.

Figure 7-11 (a) provides the metric $\Delta\tau$ for the simulated (dashed curves) and measured (solid curves) traveltime shift matrices corresponding to all the defect geometries listed in Table 7.1. From the simulated data it can be observed that as defect maximum depth grows, $\Delta\tau$ increases, whereas it decreases as the defect moves from the intrados to the extrados. Moreover, while for the defect on the intrados $\Delta\tau$ increases almost linearly with defect maximum depth, $\Delta\tau$ quickly reaches an asymptotic value when the defect is on the side or extrados. As a result, there is a loss of

sensitivity for defects outside the intrados region which is accentuated in the case of deeper defects. This trend can be explained by observing that the anisotropic velocity $c'(\mathbf{0}', \theta_g)$ is low around the extrados while it is largest at the intrados due to the structure of the α-map. Since rays follow the paths of least traveltime, only a few rays cover the extrados region. Due to the presence of a defect, $c'(\mathbf{p}', \theta_g)$ decreases even further causing the trajectories of those few rays that initially intersected the area of the defect to bend away from the defect once its depth reaches a critical level. Beyond this critical depth a further wall-thickness loss does not affect the traveltime measurements and leads to the asymptotes observed in Figure 7-11 (a). A detailed analysis of a similar phenomenon for slow inclusions in an acoustic medium can be found in [130].

The theoretical trends are confirmed by the experimental data also shown in Figure 7-11 (a) where the discrepancy between theory and experiments is primarily driven by the uncertainty associated with the traveltime shift measurements. This uncertainty is mainly caused by residual random electronic noise and the errors in traveltime estimations when two pulses partially overlap. The effect of uncertainty is greater when considering the defects on the side and extrados since the corresponding traveltimes tend to be significantly smaller than those associated with the intrados defect. For the same reason, the effects of diffraction become more apparent when considering defects outside the intrados region. For instance, comparison of Figure 7-8 (d) with (c) reveals that the area of the traveltime matrix occupied by the defect signature is greater when considering the experimental data (see block matrix $n = 2$). In fact, because of diffraction effects the interaction of the guided wave with the defect is not confined to a ray but rather to a volume around it as predicted by the sensitivity kernel theory [131]. As a result, the traveltime along rays that according to the eikonal equation do not intersect the defect, may still be affected by the presence of the defect thus leading to wider signatures. The widening of the signature also explains why the experimental $\Delta\tau$ values are larger than the simulated ones. On the other hand, for the defect on the intrados, the contribution from diffraction is lost in the dominant refraction effects thanks to the more ideal ray coverage.

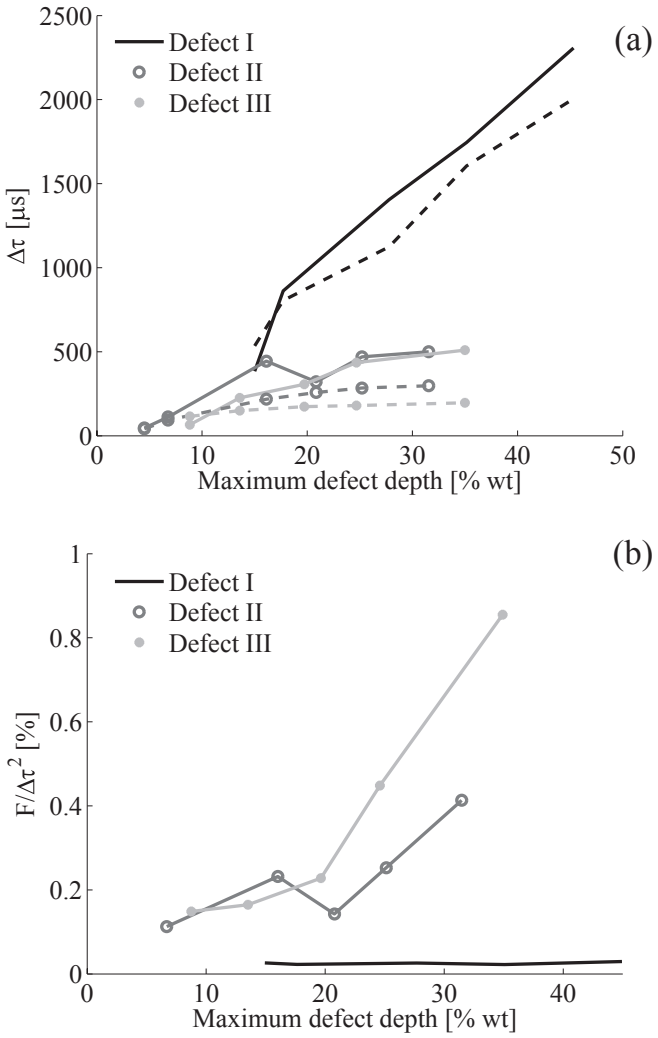

Figure 7-11: Evaluation of the INELAN model against experimental data for all the defects listed in Table 7.1. (a) Metric $\Delta\tau$ applied to simulated (dashed) and measured (solid) traveltime shift matrices - the metric provides a measure of sensitivity as a function of defect maximum depth and position around the circumference. (b) Normalized cost function capturing the residual between the simulated and measured traveltime matrices.

7.3.2 Cost function metric

Since the ultimate purpose of the INELAN forward model is to solve the inverse problem of GWT it is important to introduce a second metric that relates to the inversion. As observed in the introduction, GWT is based on a least-squares sense minimization of a cost function, F, that characterizes the residual between the measured traveltime

shifts, $\delta\tau^M$, and the simulated ones, $\delta\tau^S$. The cost function is typically defined as

$$F = \sum_{i=1}^{48}\sum_{j=1}^{48}(\delta\tau_{ij}^M - \delta\tau_{ij}^S)^2. \tag{7.6}$$

In GWT an iterative scheme is used to update the velocity model until the predicted $\delta\tau^S$ results in a global minimum for F. If the forward model provided a perfect representation of the experiments, the maps on the left of Figure 7-8 would be identical to those on the right and F would vanish. This would then imply that the inversion scheme would converge to the exact defect shape and provide unlimited accuracy. However, due to the factors discussed above the simulated maps differ from the measured ones even if the exact (within the accuracy of the laser scan) defect geometry is used to compute $\delta\tau^S$, leading to $F > 0$. Therefore, the cost function evaluated for the true defect shape provides a measure of the accuracy of the INELAN model, the smaller F the greater the accuracy of the model. The value of F evaluated for all the defects listed in Table 7.1 is shown in Figure 7-11 (b). The cost function is normalized relative to the square of the metric $\Delta\tau$ (defined based on the theoretical traveltimes) to compensate for the fact that traveltime shifts increase greatly as defect depth increases. The normalized F is typically below 1% and increases as defect position moves from the intrados to the extrados. The relatively larger values of F at the extrados imply that GWT will be less accurate on the extrados than in the intrados.

It can be observed that the error between the experimental and simulated values of $\Delta\tau$ in Figure 7-11 (a) can be as large as 100% of the simulated $\Delta\tau^S$ especially when considering Defects II and III. On the other hand, the upper bound in Figure 7-11 (b) is 1%. The percentage values between the two plots are not directly comparable because they refer to two independent metrics, in other words the data-points in Figure 7-11 (b) cannot be derived from the data-points in Figure 7-11 (a) and vice versa. However, the apparent discrepancy can be explained by considering how the metrics operate on the traveltime matrices. For this purpose, it is convenient to order the difference between the measured and simulated traveltimes $(\delta\tau_{ij}^M - \delta\tau_{ij}^S)$ in a

single super vector, $\mathbf{e}$, containing 48×48=2,304 components. The difference between the experimental and simulated values of $\Delta\tau$ in Figure 7-11 (a) is then

$$\Delta\tau^M - \Delta\tau^S = \sum_{i=1}^{48} |e_i|, \tag{7.7}$$

which means that all the pixel-to-pixel errors between the simulated and measured matrices in Figure 7-8 are added coherently, i. e. positive and negative errors do not cancel out. On the other hand, the value of the cost function F corresponds to the square of the length of vector $\mathbf{e}$. The length of a super vector is typically orders of magnitude smaller than the sum of its components. As a result, $F \ll (\Delta\tau^M - \Delta\tau^S)^2$ which leads to the 1% bound.

It is also important to stress that the larger values of F outside the intrados region are vastly due to the experimental uncertainty associated with the measurement of overall small traveltime shifts rather than a physical limitation of the INELAN model. Therefore, while using more accurate forward models based on the 3-D full-wave equations of elastodynamics can help capturing secondary phenomena such as the diffraction effects observed earlier, the improvement on the cost function would only be marginal and would come at a prohibitively high computational cost. As an example, the time required to compute one of the 48×48 matrices in Figure 7-8 is ≈ 7 seconds on a standard PC. For comparison, computation of the same matrix solving the 3-D full-wave equations of elastodynamics for a straight pipe section takes approximately 60 hours on an relatively powerful computer workstation (1 TB RAM, 48 threads, 4 GPUs). As it will be shown in the following Chapter 8, the accuracy limitation of GWT can be addressed by forcing the rays to travel on the pipe extrados through a suitable array design.

As a final remark, it is observed that the INELAN model was not affected by the morphology of the accelerated corrosion defect and yielded results that are in line with those obtained when the defects were introduced by angle grinding.

7.4 Conclusions

The development of guided wave tomography (GWT) methods for corrosion and erosion monitoring at pipe elbows requires the availability of robust and computationally efficient forward models that can describe the interaction of guided waves with regions of wall thinning. Moreover, the corrosion rates experienced by pipelines in the oil and gas industry are typically low - in some cases in the order of 1 mm/yr or less. In order to provide prompt feedback to asset operators it is therefore essential that GWT is sensitive to wall thickness changes in the order of a few tens of micrometers, thus posing demanding performance requirements on GWT and hence on the accuracy of the forward model.

Accurate forward models based on the three-dimensional equations of elastodynamics are available; however, their computational cost is too high for practical implementation in the iterative inversion schemes of GWT. On the other hand, rapid computation of guided wave traveltimes across the elbow of a pipe bend can be obtained using a two-dimensional acoustic model which is artificially inhomogeneous and elliptically anisotropic (INELAN). Such a model was previously shown to be effective in predicting the total traveltimes of guided waves traveling between the sources of a transmit array on one side of the elbow and the elements of a receive array on the opposite side. In this chapter it has been shown that the INELAN model is also effective in providing accurate predictions of traveltime shifts caused by shallow defects introduced on the pipe elbow by angle grinder and a more realistic accelerated corrosion method.

Experiments performed on an 8" diameter, schedule 40, carbon steel pipe with a 90°, 1.5 D elbow have shown that the traveltime shifts extracted from the measured guided wave signals using the zero-crossing method are consistent with the predictions from the INELAN model in which the defect is represented as a phase velocity perturbation. Moreover, matrices formed by considering the traveltime shifts for all possible transmit-receive pairs contained clear defect signatures which were observed in both the experimental and simulated data. Similarly, the metrics used to estimate the er-

rors between the measured and simulated matrices showed that the INELAN model provides good agreement with the measurements for different defect positions around the elbow and for a range of depths. Some discrepancies between the model and the measurements were primarily due to noise in the measured traveltime shifts caused by experimental uncertainties and difficulties with the application of the zero-crossing methods when different wave pulses are not well resolved in time. Therefore, it can be concluded that the INELAN model is accurate within the noise of the experimental measurements. Importantly, the computation time to predict a full dataset with the INEALN model on a standard PC is in the region of seven seconds while computation of the same dataset using the elastodynamic equations takes approximately 60 hours on a workstation.

Finally, the study has demonstrated that the sensitivity of traveltime measurements to the presence of a defect decreases as the defect moves from the intrados to the extrados of the elbow. This effect is due to the configuration of the transmit and receive arrays relative to the bend which causes the rays to avoid the extrados in order to minimize traveltime. As a result, ray coverage around the extrados is low leading to traveltimes shifts that are much smaller for a defect on the extrados than for the same defect on the intrados. Ultimately, this will cause GWT to underestimate the depth of defects on the extrados. In Chapter 8 we will show that the nonuniform ray coverage can be addressed using an array configuration that employs a line of transducers along the extrados.

Chapter 8

Guided wave tomography of pipe bends

8.1 Introduction

Although the benefits of extending the scope of GWT to the bend problem are apparent, no demonstration of the feasibility of such an approach has been reported in the literature, with the sole exception of a preliminary numerical study by Volker and van Zon [132]. Indeed, there are two main obstacles to the development of GWT for pipe bends: (a) the complexity of the forward model required to describe guided wave propagation along the bend, and (b) the presence of wave phenomena that occur at the extrados of the elbow which are not present in the case of straight pipes.

In straight pipes, the propagation of guided waves and their interaction with defects can be approximated by a two-dimensional (2-D) acoustic model in which defects are modeled as phase or group velocity perturbations. Moreover, the 2-D model is defined over a rectangular domain that corresponds to the pipe midsurface unwrapped onto a plane. Instead, for a bend the torus that defines the elbow midsurface cannot be unwrapped without introducing stretching and compression and therefore the guided wave problem cannot be formulated in terms of the standard acoustic model. In Chapter 6 we have shown that it is possible to model guided wave propagation in a bend using a 2-D rectangular domain in which the acoustic model is made artifi-

cially inhomogeneous and elliptically anisotropic (INELAN). The ability of INELAN to simulate traveltime shifts caused by shallow defects and small defect depth increments has been demonstrated experimentally in Chapter 7. Importantly, the INELAN model achieves fast computation of the forward model which is critical for the inverse problem that requires several forward simulations before convergence is achieved.

Around the extrados two important wave phenomena occur when guided wave signals are excited and detected by ring arrays placed at the two ends of the elbow. Since wave pulses follow Fermat's law of least traveltime, guided waves tend to avoid the extrados to travel closer to the inner side of the elbow (intrados) since here the wave paths are shorter. As a result, first-arrival traveltimes tend to encode little information about defects on the extrados and one must use later arrivals corresponding to wave paths that have wrapped around the pie circumference multiple times before reaching the receivers (Section 6.2.4). In addition, a self-focusing effect occurs at the extrados which results in a secondary source that radiates a strong wavefield trailing behind the first-arrival signals Section 6.4. The secondary field partially interferes with the first arrivals and complicates signal interpretation.

The objective of this chapter is to develop an inversion method based on the INELAN forward model and to integrate it with a new array configuration that can increase ray density on the extrados and therefore lead to more accurate wall-thickness map reconstructions.

Section 8.2 develops a new curved ray tomography algorithm based on the nonlinear conjugate gradient method. Numerical validation of the inversion scheme is provided in Section 8.3 where the performance of GWT is studied for the standard array configuration consisting of two ring arrays and a new configuration that includes a line of transducers along the extrados. Using the methods described in Section 8.4 the proposed approach is validated experimentally in Section 8.5 which is followed by concluding remarks in Section 8.6.

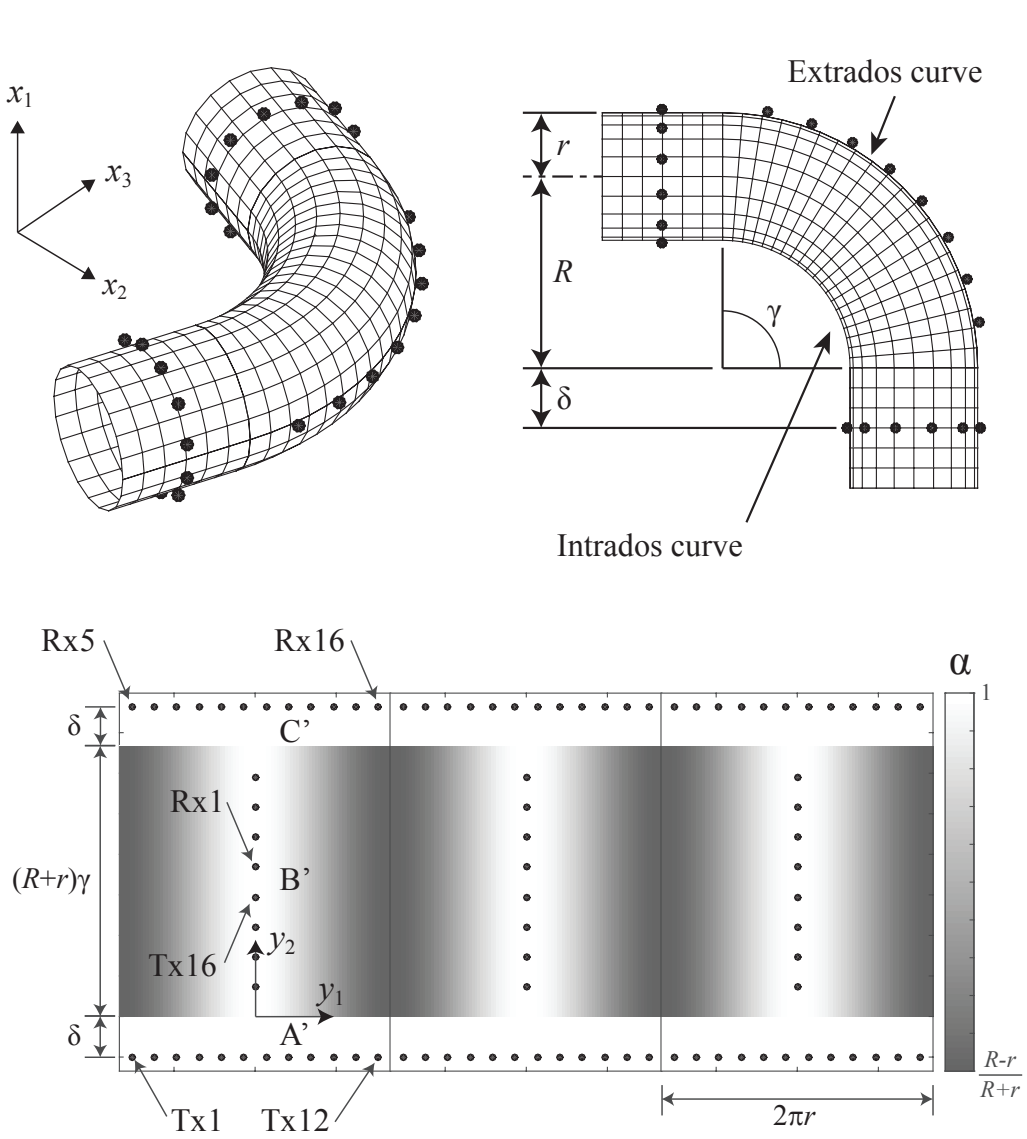

Figure 8-1: 2-D acoustic model associated with a 3-D pipe bend. (a) Diagram illustrating the position of two ring arrays encircling the pipe and a line array along the elbow extrados. (b) Extended acoustic domain including two replicas to simulate wave paths that perform up to three full turns around the pipe circumference and showing the convention for transducer numbering. The background gray scale denotes the α-map, with brighter regions corresponding to the bend extrados.

8.2 Curved ray tomography

The aim of the inversion is to reconstruct the slowness map, $s[\mathbf{r}(\mathbf{p}')]$, and hence $c[\mathbf{r}(\mathbf{p}')]$ from the set of $(N+M)\times(N+M)$ waveforms that are measured for all the possible

transmit-receive pairs. The velocity map is then converted into a wall-thickness map, $d(\mathbf{r})$, using the dispersion curve of A_0. Assuming that modes that have performed up to m full turns around the elbow are used, the input data to the inversion algorithm is the $\mathbb{U} \in \mathbb{R}^{m(N+M)\times m(N+M)}$ matrix of traveltimes arising from the virtual arrays [108].

The numerical formulation of the inverse problem starts from the discretization of the propagation domain into a grid of nodes where the traveltime, $\tau(\mathbf{p}')$, is defined. For a grid containing l nodes, $\tau(\mathbf{p}')$ can be represented by an $l \times 1$ vector, $\boldsymbol{\tau}$, so that the i-th entry defines the traveltime at the i-th node of the grid. Similarly, the slowness function $s(\mathbf{p}')$ can be represented by a $p \times 1$ vector of parameters, $\mathbf{s}$. The value of p depends on the number of nodes, l, and the order of the shape function used to represent the slowness distribution within each element of the grid. Here, it is assumed that $s(\mathbf{p}')$ is uniform inside each element and therefore the i-th entry of $\mathbf{s}$ corresponds to the average value of the slowness inside the i-th element. Rearranging the columns of the matrix $\mathbb{U}$ into a single vector $\mathbf{u}_m$, the inverse problem attempts to find the solution $\mathbf{s}$ to the set of nonlinear equations

$$\mathbf{u}_m = \mathbf{F}(\mathbf{s}), \tag{8.1}$$

where $\mathbf{F}$ represents the forward model described by the INELAM model of Section 6.2.2.

To illustrate the main aspects of the inversion it can be observed that the forward problem defined by Section 6.2.2 can be expressed as

$$\boldsymbol{\tau} = \mathbf{G}(\mathbf{s})\mathbf{s}, \tag{8.2}$$

where $\mathbf{G}$ contains the lengths of the ray paths to all the nodes of the grid from a single source position. In particular, the ij-th entry of $\mathbf{G}$ is the length of the ray segment intersecting the j-th element and reaching the i-th node. Finally, it should be emphasized that the dependence of $\mathbf{G}$ on $\mathbf{s}$ is included to account for ray bending caused by the inhomogeneity of the INELAN model.

The forward model provided by Section 8.2 can be used to predict traveltimes

measured by the arrays for a known **s**-map and leads to a synthetic data vector, $\mathbf{u}_s$. The objective of the inversion is to determine the vector **s** by minimizing the residual between the measured and predicted data

$$\delta\mathbf{u} = \mathbf{u}_m - \mathbf{u}_s. \tag{8.3}$$

This is achieved in a least-squares sense minimizing the cost function based on the L^2-norm of the residual

$$E(\mathbf{o}) = \frac{1}{2}\delta\mathbf{u}^T\delta\mathbf{u}, \tag{8.4}$$

where the superscript T refers to the matrix transpose. The minimization requires the use of iterative techniques such as gradient, Newton, or Gauss-Newton methods [133]. Among these, gradient methods are more computationally efficient due to the large size of vector **s**. Good convergence rates are obtained with the nonlinear conjugate gradient method which starts from an initial guess of the slowness map $\mathbf{s}_0$ and defines the slowness map at the $k+1$ iteration step as

$$\mathbf{s}_{k+1} = \mathbf{s}_k + \eta_k\boldsymbol{\delta}_k, \tag{8.5}$$

where η_k is the step size obtained from a line search that minimizes the cost function $E(\mathbf{s})$ along the descent direction $\boldsymbol{\delta}_k$ i.e.

$$\eta_k = \arg\min_{\eta}\{E(\mathbf{s}_k + \eta\boldsymbol{\delta}_k)\}. \tag{8.6}$$

With the steepest descent method, $\boldsymbol{\delta}_k$ is chosen to be opposite to the gradient of the cost function, i.e. $\boldsymbol{\delta}_k = -\nabla E(\mathbf{s}_k)$. On the other hand, more rapid convergence is obtained using a different descent direction given by

$$\boldsymbol{\delta}_{k+1} = -\nabla E(\mathbf{s}_{k+1}) + \xi_k\boldsymbol{\delta}_k, \tag{8.7}$$

where ξ_k is the conjugate gradient update parameter. Various formulas for ξ_k have

been proposed [134], in this work we adopt the Fletcher-Reeves formula

$$\xi_{k+1} = \frac{\|\nabla E(\mathbf{o}_{k+1})\|^2}{\|\nabla E(\mathbf{o}_k)\|^2}. \tag{8.8}$$

Each iteration step requires knowledge of the partial derivatives $\partial E/\partial s_i$ which form the gradient ∇E. Direct computation of the derivatives is highly inefficient since the large number of parameters in $\mathbf{s}$ would require the computation of a vast number of forward models. However, this is not necessary as the gradient can be calculated by back-projecting the residual $\delta\mathbf{u}$ along the rays that join the source to the receivers as in the filtered back-projection method [135] used in computerized tomography. As a result, calculation of the gradient can be achieved with the computation of a single forward model. It should be stressed that due to the anisotropy of the INELAN model, the phase front travels in a direction that is typically different from that of the group envelope. Since the phase shift measured experimentally corresponds to the delay in group traveltime of the INELAN model (Section 6.7), it is necessary to consider the rays tangent to the group velocity direction when back-projecting the residuals.

The block diagram shown in Fig. 8-2 summarizes the steps involved in the iterative solution to the inverse problem. The iteration begins with an initial guess for the slowness map, $\mathbf{s}_0$, which is assumed to be the slowness of the undamaged pipe. The slowness map is passed to a forward solver that predicts the synthetic dataset $\mathbf{u}_s$ using the FMM method. The synthetic and measured data are then used to compute the residual $\delta\mathbf{u}$ and evaluate the cost function E. If E does not meet the convergence criterion, the slowness map is updated computing its gradient ∇E and using the recursive expressions (8.5)-(8.8) until convergence is achieved. The convergence criterion is typically based on a threshold level applied to the cost function or its slope. Here, we stop the iteration at step k when $(G_{k+1} - G_k)/G_k \leq 0.001$.

To address the instability of the inverse problem and ensure the convergence of the iteration, the cost function in Equation 8.4 can be modified by adding a regularization

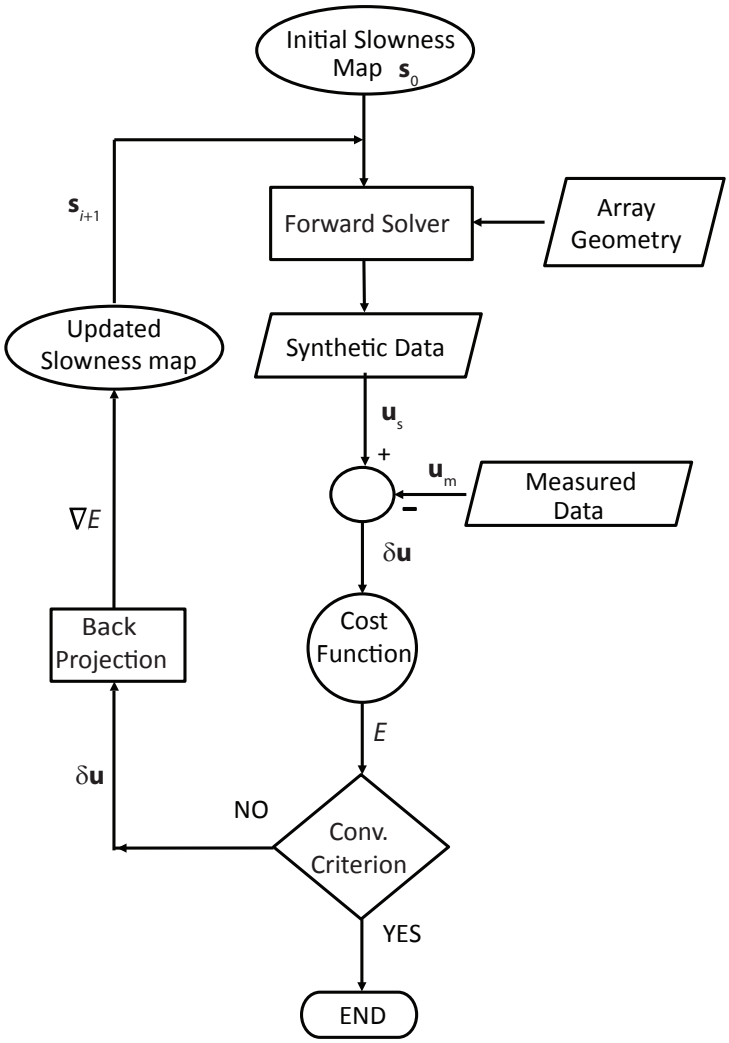

Figure 8-2: Block diagram of the iterative algorithm used to solve the inverse problem.

correction

$$E_{reg}(\mathbf{o}) = \frac{1}{2}\delta\mathbf{u}^T\delta\mathbf{u}^* + \frac{1}{2}\mu^2\|\mathcal{D}\mathbf{s}\|^2, \tag{8.9}$$

where μ is a regularization parameter and $\mathcal{D}$ is a weighting operator. If $\mathcal{D}$ coincides with the identity operator the minimization of Equation 8.9 is equivalent to the

damped least-squares minimization. In this work however the regularization parameter is set to zero and instead the solution is constrained based on the prior knowledge that corrosion and erosion damage can only cause the wall thickness to decrease and that the slowness map is replicated across the aperture of the virtual transmit and receive arrays. The first type of constraint is achieved by imposing phase velocity extrema. The phase velocity of A_0 increases monotonically with the frequency-thickness product $f \cdot d$ and therefore a wall-thickness loss can only cause a reduction in phase velocity. In this case the regularization condition is $c[\mathbf{r}(\mathbf{p}')] \leq c_0$ where c_0 is the phase velocity of A_0 corresponding to $f \cdot d_0$, with d_0 being the nominal wall thickness of the undamaged pipe.

The second type of constraint is dependent on the maximum order m used for the inversion. As discussed in Section 6.2.4 to account for modes that have performed up to m full turns around the pipe, the 2-D domain has to be expanded by adding $m-1$ replicas. If l is the number of nodes used to discretize a single sub domain, the total number of nodes of the extended domain is $l_e = ml$. Therefore, $\mathbf{s}$ has the cyclic structure

$$\mathbf{s}_i = \mathbf{s}_{i+kl}, \quad 1 \leq i \leq l \quad 0 \leq k \leq m. \tag{8.10}$$

Condition (8.10) is imposed when updating the slowness map in Equation 8.5.

The method introduced in this section provides a generalization of the curved ray tomography method, which is widely used in seismic exploration [136, 137], to the case of anisotropic media.

8.3 Numerical study

In this section, the performance of the inversion is studied using synthetic datasets as opposed to the experimental ones which will be considered later in Section 8.5. The synthetic datasets are obtained using the INELAN forward model given by Equation 6.21 and therefore are consistent with the forward model used by the inversion.

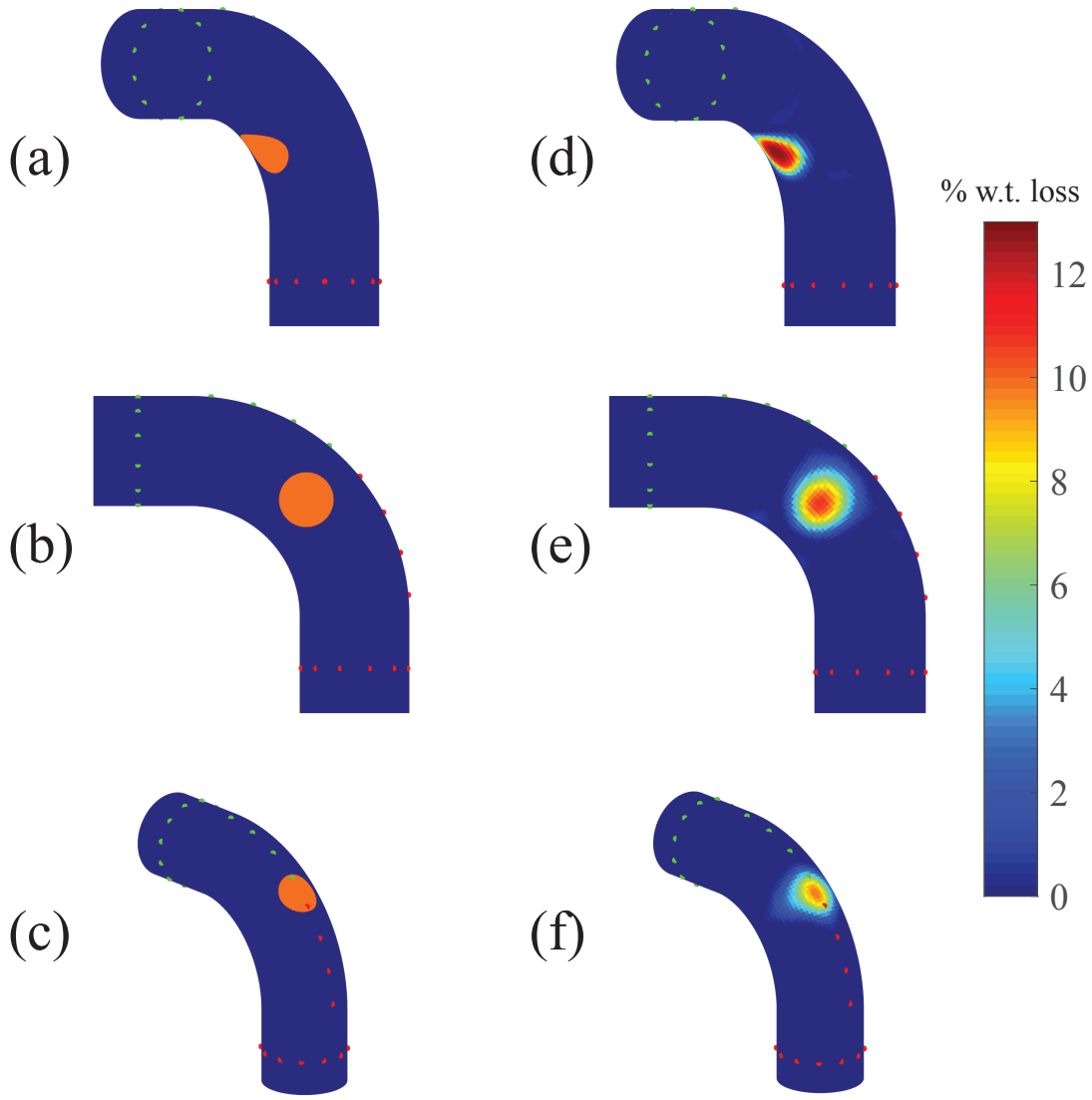

Figure 8-3: 3-D renderings of nominal (a)-(c) and reconstructed (d)-(f) wall-thickness loss maps for a uniform defect of diameter equal to the pipe radius and depth equal to 10% of the wall thickness.

The numerical models are based on the pipe bend geometry and guided wave frequency used in the experiments presented in Section 7.2. The reconstructions are obtained by considering all the modes that have performed up to three full turns around the circumference (m=3). Therefore, the 2-D domain contains two replicas as shown in Figure 8-1 (b) with each replica discretized using 5.5×5.5 mm squared elements with 120×187 nodes (circumferential×azimuthal).

Circular defects of diameter equal to the pipe mid-surface radius $r = 105.5$ mm and uniform depth are studied as a function of defect depth and position around the elbow as shown in Figure 8-3 (a)-(c). The defects are placed at the center of the elbow and are modeled as a phase velocity perturbation - for each depth, d_{loss}, the phase velocity $c(\mathbf{p})$ inside the defect is obtained from the A_0 dispersion curve at the frequency-thickness product $f \cdot (d_0 - d_{\text{loss}})$.

The two array configurations considered in Section 8.1 are simulated using: (a) two 16-element ring arrays (N=16) mounted on the straight pipe sections at distance δ=100 mm from the elbow, and (b) two 12-element ring arrays (N=12) at the same location as in case (a) and with a line array of $2M = 8$ transducers along the extrados.

Examples of the reconstructed wall-thickness loss maps for the array configuration that includes the line array on the extrados are shown in Figure 8-3 (d)-(e). The size and position of the reconstructed defect closely matches the defect in the model, while the sharp edges of the model defect are lost due to the limited spatial resolution of GWT.

Figure 8-4 provides the reconstructed maximum depth versus the nominal defect depth as a function of the defect position around the pipe circumference - depth is expressed as percentage of the nominal wall thickness. Figure 8-4 (a) refers to the array configuration without the transducers on the extrados. If the inversion achieved unlimited accuracy, all the curves would lie on the true depth line, instead it can be observed that accuracy varies with defect depth and most importantly with defect position. In particular, depth is significantly underestimated for defects close to the extrados. This is due to the low ray coverage around the extrados as shown in Figure 8-5 (a) which provides the ray paths radiating from the transmit ring array when the transducer closest to the extrados is excited. The direct wave paths do not intersect the extrados region and therefore GWT must rely on the wave paths that have performed at least one full turn around the circumference to reconstruct the defect. On the other hand, by adding source transducers on the extrados, guided waves are *forced* to propagate on the extrados leading to a denser ray coverage, Figure 8-5 (b). The same effect is obtained by adding receivers on the

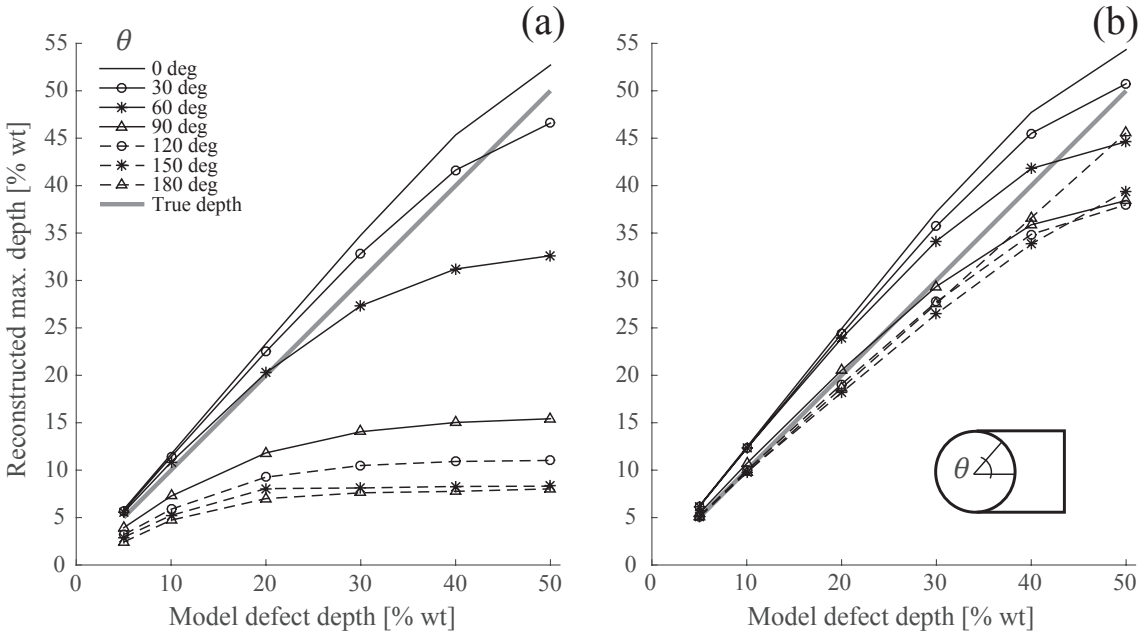

Figure 8-4: Reconstructed versus nominal defect maximum depth as a function of defect depth and position around the pipe circumference. (a) two-ring array configuration; (b) two-ring arrays and a line of transducers along the extrados. The reconstructions are obtained using $m = 3$ and the total number of transducers for both configurations is 32.

extrados by reciprocity. As a result, the accuracy of the reconstructions improves significantly as shown in Figure 8-4 (b). For defect depths up to 30% depth, the error in maximum depth estimation varies between -3 and +6% of wall thickness. The largest errors are over estimations (positive sign) that occur for defects around the intrados, $0 < \vartheta < 60°$, where ϑ is measured starting from the intrados.

To investigate the effect of the number of replicas used for the inversion, Figure 8-6 shows the reconstructed maximum depths for the same cases considered in Figure 8-4 but when only modes that have performed up to two full turns around the pipe ($m = 2$) are considered. It is clear that reducing m from 3 to 2 has a detrimental effect on accuracy when considering the two ring configuration, especially when defects are close to the extrados, compare Figure 8-4 (a) and Figure 8-6 (a). This is to be expected since the ray coverage offered by the direct wave paths is very limited on

the extrados and therefore there is significant benefit in adding higher order modes. This is also consistent with the trends observed with straight pipes [108]. On the other hand, the value of m is less critical for the array configuration that includes the transducers on the extrados, compare Figure 8-4 (b) and Figure 8-6 (b) since now the direct wave paths provide a more homogeneous coverage of the extrados. Indeed,

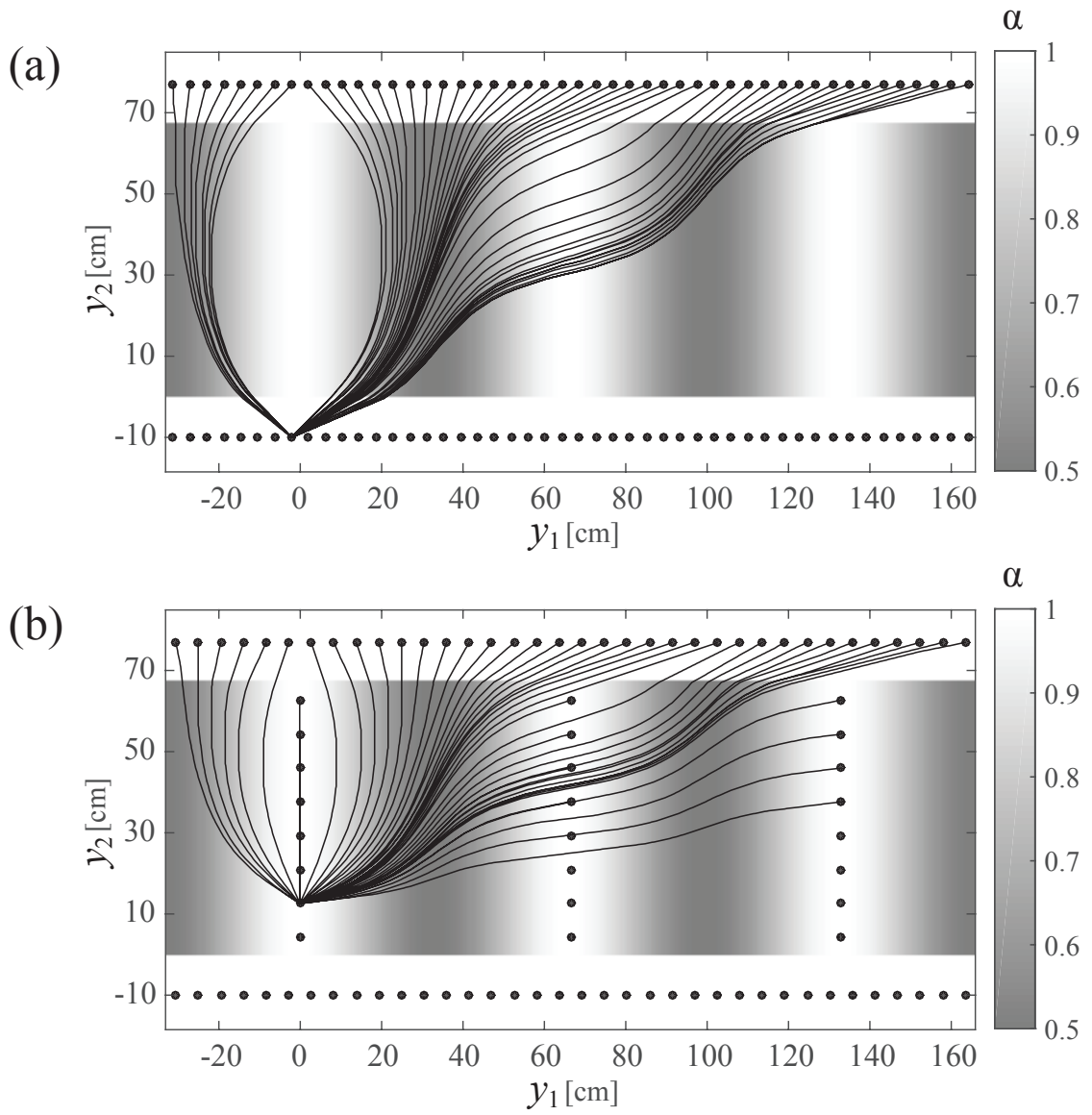

Figure 8-5: Ray paths radiating from (a) a source transducer on the transmit ring array, and (b) a transducer on the extrados. The background gray scale denotes the α-map as in Figure 8-1 (b).

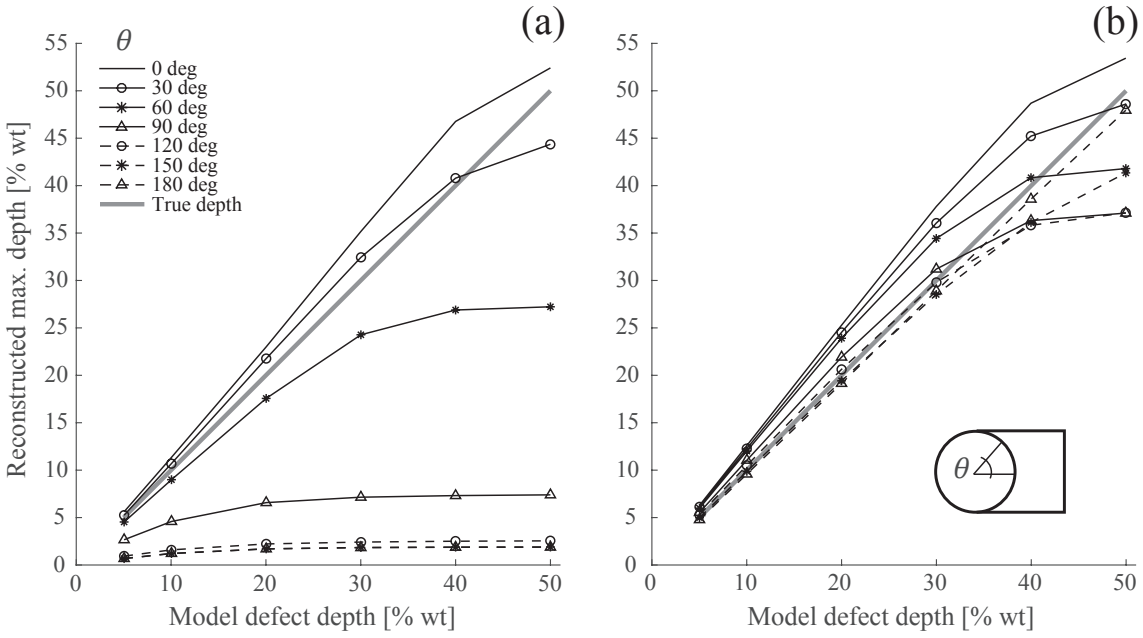

Figure 8-6: Same numerical simulations as in Figure 8-4 when only one replica is added, i. e. $m = 2$.

for some defect configurations the results for $m = 2$ are marginally more accurate than $m = 3$. This is due to the fact that the accuracy of ray tomography decreases as wave path length increases due to the widening of the so-called Fresnel zone, see for instance [130]. The length of the propagation path also poses an upper bound to the value of m which is dictated by experimental conditions. In fact, as the path length increases, the pulse amplitude decreases due to dispersion, possible energy leakage into surrounding media [56], and the continuous distortion of the wavefront with propagation distance which causes energy redistribution into multiple branches (Section 6.4). Since accurate traveltime estimations require the signal amplitude to be well above the noise floor, it is important that the wave path length is limited - experimentally we have found that there is no benefit in using $m > 3$.

For the case $m = 3$, the inversion is performed on a PC with an Intel(R) Core i7-3770k CPU and convergence is typically achieved after 60 iterations resulting in a total computation time under four minutes.

In concluding this section it should be emphasized that the reconstructed wall-thickness loss maps do not show streak artifacts which therefore implies that the total number of sensors used in the simulations provides adequate sampling of the wavefield. With wave-based inversion methods, such as diffraction tomography, the minimum number of sensor required to avoid aliasing artifacts is well defined [138]. For a straight pipe with the same diameter and schedule as the bend considered in the simulations it leads to around 70 sensors per array. On the other hand, the sampling requirements of ray tomography are much less stringent due to its lower resolution.

8.4 Experimental methods

Experimental validation of GWT was conducted on the two pipe bend specimens shown in Figure 8-7, hereafter identified as Pipe I and II. Pipe I was instrumented with two ring arrays according to configuration (a) in Section 8.3, while Pipe II also included the transducers on the extrados - configuration (b) of Section 8.3. In both cases, the transducers were left in position as multiple defects were added. Each specimen consisted of two 8" diameter (220 mm measured O.D.), schedule 40 (8.18 mm nominal wall thickness), 1.5 m length straight carbon steel pipes welded to a 90°, 1.5 D elbow (R=305 nominal bend radius). While the inversion scheme assumes that the wall thickness is uniform for the undamaged pipe, the actual thickness varied significantly due the presence of the weld caps, which were approximately 2 mm thickness, and manufacture tolerances that at the elbow of Pipe I led to peak-to-trough thickness variations of 1.72 mm, i. e. 21% of the mean wall thickness estimated to be 8.25 mm (Section 7.2). This information was not used in the inversion.

Each pipe contained three sets of defects labeled Defect I, II and III located at the intrados, side, and extrados, respectively. To simulate corrosion progression the depth of each defect was increased in consecutive steps using an angle grinder or the method of impressed currents to produce accelerated corrosion as described in Section 7.2.2. All the defects were introduced on the elbow outer surface with the exception of the extrados defect of Pipe II which was introduced on the inner surface. This defect

(a)

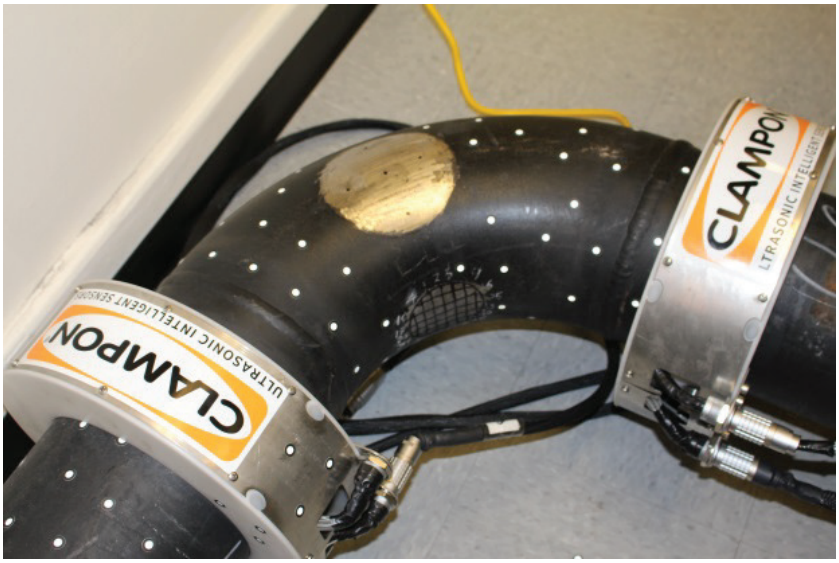

(b)

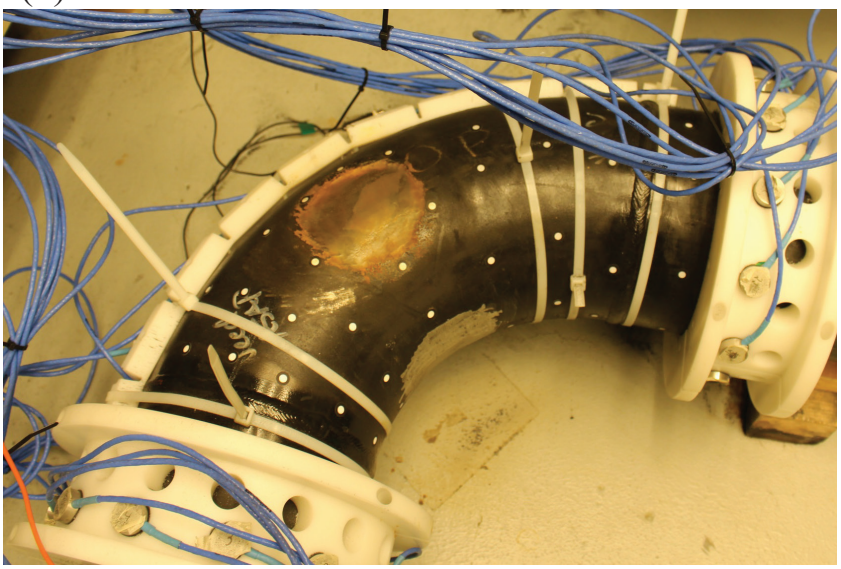

Figure 8-7: Experimental setup for GWT measurements: (a) Pipe I instrumented with two ring arrays each consisting of 16 EMATs; (b) Pipe II showing a line of eight EMATs along the extrados and two ring arrays each containing 12 EMATs.

Table 8.1: Pipe II defect locations, methods of introduction, and sizes and depths.

Defect ID	**Location**	**Type**	**Size (Azim. x Circ.)** [mm]
Defect I	Intrados	Grind	70 x 60
Defect II	Side	Impr. Curr.	100 x 100
Defect III	Extrados	Impr. Curr.	100 x 100
Defect ID	**Maximum Depth** [μm]	**Mean Depth** [μm]	σ [μm]
Defect I 1	1052	430	220
Defect I 2	1384	577-	297
Defect I 3	1861	833	394
Defect I 4	2629	1319	800
Defect I 5	3427	1735	1049
Defect II 1	519	265	58
Defect II 2	730	442	113
Defect II 3	1246	779	248
Defect II 4	2029	1368	477
Defect II 5	2271	1444	628
Defect II 6	2772	1657	942
Defect III 1	33	-	-
Defect III 2	59	-	-
Defect III 3	77	-	-
Defect III 4	96	-	-
Defect III 5	116	-	-
Defect III 6	136	-	-
Defect III 7	292	-	-
Defect III 8	516	-	-
Defect III 9	832	-	-
Defect III 10	945	-	-
Defect III 11	1695	-	-
Defect III 12	1593	-	-
Defect III 13	1691	-	-

was produced using the impressed current corrosion method with an electrolytic cell similar to that used in Section 7.2.2 mounted inside the pipe elbow before it was welded to the straight pipe sections. Defect depth was mapped by performing a 3-D laser scan using the system described in Section 7.2.4 which provides a spatial resolution in the order of 0.5 mm and depth estimation precision of ±100 μm. For

the interior defect of Pipe II it was not possible to map its depth with the laser and therefore the thickness was sampled at two points using two 15 MHz, 0.25" (6.4 mm) diameter probes permanently attached to the outer surface of the elbow.

The geometrical properties of all defects on Pipe I are summarized in Table 7.1 and the defects on Pipe II in Table 8.1. Defects exhibited an irregular depth profile leading to maximum depth that was typically more than 100% deeper than the defect mean depth when the angle griding method was used. For the accelerated corrosion defects, the maximum depth was more than 60% deeper than the mean depth for defects on the outer surface of the elbow. For the interior defect the maximum and mean depths could only be estimated from the thickness measurements at two locations. However, at the end of the corrosion tests the maximum depth was more than 500% deeper than the mean depth. As a result, all the defects can be classified as localized corrosion since for generalized corrosion the maximum depth is typically less than 10% deeper than the mean depth according to the oil and gas industry standards. Finally, defect size ranged from 70×60 mm (azimuthal×circumferential) to 120×120 mm.

Guided wave measurements were performed with 32 electromagnetic acoustic transducers (EMATs) driven by a 32 channel controller by ClampOn as described in Section 6.5. The transducers were excited by a two-cycle gaussian windowed tone burst centered at 140 kHz which corresponds to a wavelength λ=18.6 mm. This frequency corresponds to $f \cdot d$=1.16 MHz-mm which is at the low end of the CVG spectrum where the dispersion of the group velocity of A_0 is negligible and was chosen because the EMATs employed in this study are designed to work on thicker pipe walls. To suppress random electronic noise each signal was averaged 512 times. All the possible transmit-receive combinations, $16 \times 16 = 256$, were recorder in under 30 min to form one dataset.

To mitigate the effect of parametric uncertainties in the geometrical properties of the bend and the position of the transducers, the input matrix $\mathbb{U}$ to the inversion scheme contained the traveltime changes between two states of the pipe rather than the absolute traveltimes between transducers pairs. Therefore, a *baseline* dataset was measured at the time when the arrays were first installed on the pipe and then

current datasets were continuously acquired as the experiments progressed. The rationale is that the measured traveltime between two transducers is a function of the wall thickness, $\tau_m(d)$, that can be expressed as the sum of the traveltime that would be measured without uncertainties, $\tau(d)$, and a term $\Delta\tau_u(d)$ that incorporates the effect of uncertainty, i. e. $\tau_m(d) = \tau(d) + \Delta\tau_u(d)$. To a first order approximation, $\Delta\tau_u(d)$ is independent of defect depth and therefore it cancels out when considering the traveltime shift

$$\delta\tau = \tau_m^c - \tau_m^b, \tag{8.11}$$

between the measured current, τ_m^c, and baseline, τ_m^b, traveltimes, i. e. $\delta\tau$ is only dependent on defect depth. As a result, matrix $\mathbb{U}$ was populated by evaluating $\delta\tau$ for all the transmit-receive pairs using the zero crossing method applied to the baseline and current signals as explained in [108]. Examples of measured $\mathbb{U}$ matrices for the defects in Pipe I are given in Section 7.3 where it is shown that the INELAN model can predict the matrices with accuracy that is within the experimental error.

8.5 Results and discussions

We first discuss the results obtained with the two ring-array configuration of Pipe I. Figure 8-8 shows the GWT reconstruction of the intrados defect, Defect I1. In the 2-D map the vertical axis (labeled axial position) corresponds to the azimuthal direction along the elbow while the horizontal axis coincides with the circumferential direction around the pipe - the extrados lies on the two vertical edges of the map. In order to unwrap the complex 3-D surface of the elbow, the intrados length is stretched by a factor two to match the length on the extrados while the length along the circumferential direction is left unchanged. Both the 2-D image and the 3-D rendering are maps of wall-thickness loss in which the color of each pixel gives the local defect depth according to the color bar on the right.

The reconstruction provides the correct location of the defect. Its size is estimated

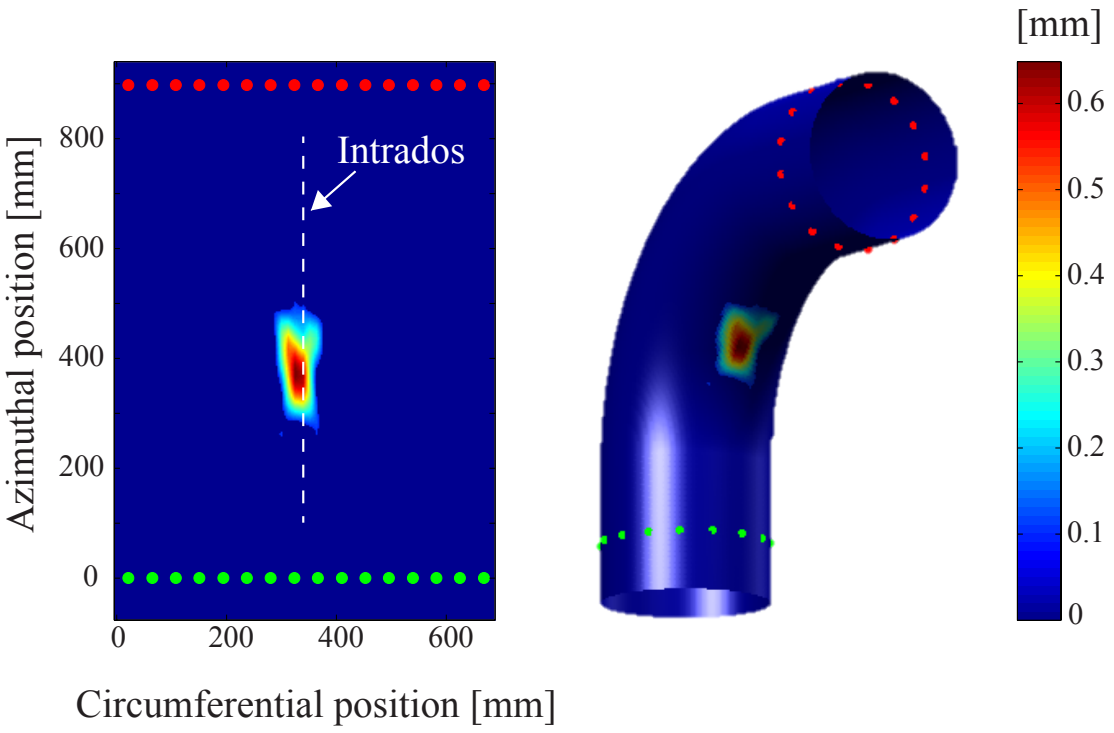

Figure 8-8: (Color online) Experimental wall-thickness loss reconstruction for the intrados defect of Pipe I, Defect I 1.

from the 2-D map setting a -15 dB threshold level and is found to be 100×90 mm (azimuthal×circumferential) which is in good agreement with the 110×80 mm measured with the 3-D laser scan (note that the length of the defect along the intrados appears doubled in the 2-D map due to stretching). On the other hand, the reconstruction underestimates the maximum depth giving 0.65 mm versus the 1.24 mm obtained with the laser scan. The underestimation is due to the highly irregular profile of the defect which causes the largest depth to occur in an area contained within a 5 × 10 mm rectangle. Thanks to its high resolution (0.5 mm), the laser scan can accurately map the depth profile within the rectangle. On the other hand, the size of the rectangle is smaller than the wavelength of A_0 (18.6 mm) thus meaning that the GWT reconstruction is a smoothed version of the true depth profile leading to an underestimation of the maximum depth. A rigorous characterization of the resolution scale of the GWT method introduced in this work and how it affects the accuracy of the reconstructions is made difficult by the highly nonlinear nature of the inver-

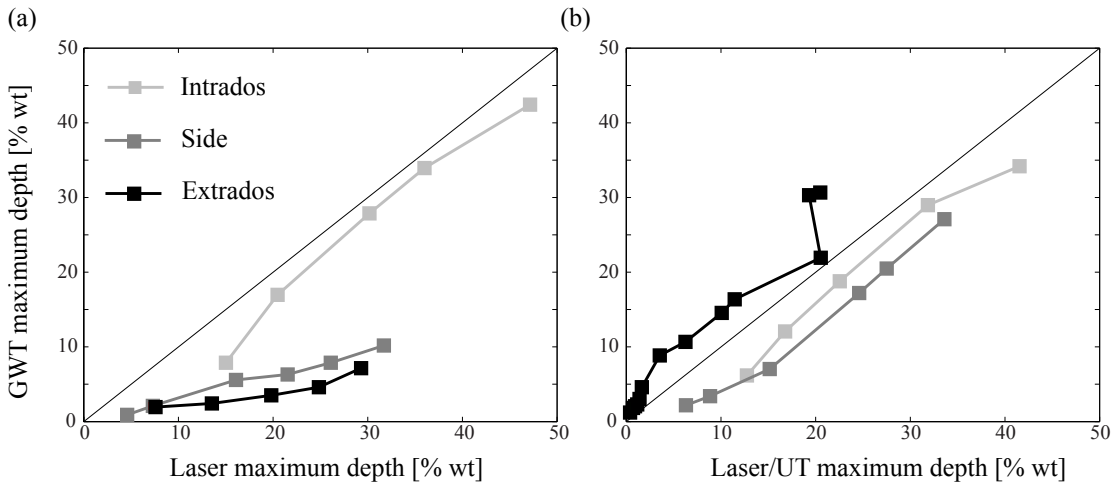

Figure 8-9: GWT maximum depth estimations versus 3-D laser scan maximum depths for (a) two-ring array configuration (Pipe I); (b) configuration with an additional line of transducers along the extrados (Pipe II). For the internal extrados defect in (b) depth is monitored at two points with permanently attached ultrasonic probes.

sion [139]. This implies that the reconstructed depth profile cannot be expressed as the convolution of the true profile with the so-called point spread function PSF, which is the reconstructed profile for an ideal wall-thickness loss which has vanishingly small lateral size but finite depth, see for instance Ref. [130]. Initial results suggest that reconstruction accuracy begins to degrade when the defect size is smaller than a length scale, Λ, that is greater than the wavelength, λ, but smaller than $\sqrt{\pi\lambda R/2}$ which corresponds to the resolution scale of straight ray tomography $\sqrt{\lambda L}$ [140], where L is the mean source-to-receiver distance that in the case of the bend pipe is about $\pi R/2$. A better characterization of the accuracy limit of GWT would require a large scale parametric study that is beyond the scope of this work.

Figure 8-9 (a) provides the reconstructed maximum depths for all the depth increments of Defect I, II and III of Pipe I against the corresponding maximum depths estimated from the laser scans - all the values are expressed as percentage of the mean wall thickness (8.25 mm). If the GWT reconstructions matched the laser measurements exactly, the data points would lie on the diagonal line. However, due to limited spatial resolution, GWT underestimates depth compared to the laser mea-

surements. Nevertheless, GWT achieves 100% sensitivity[1] by detecting three out of three defects and also correctly locating their position around the elbow. Moreover, it detects damage progression with 100% sensitivity by showing increased depth for 16 out of 16 depth increments.

For the intrados defect the differences between the laser and GWT maximum depth estimations are between 2 and 7% of wall thickness. The discrepancy between the two sets of measurements increases for the defects on the side and extrados causing underestimations between 4 and 22% of wall thickness. This is due to the non-ideal ray coverage afforded by the two ring array configuration and is in line with the results of the numerical simulations of Section 8.3.

We now consider the reconstructions for the defects introduced in Pipe II which was instrumented with two ring arrays and a line of transducers along the extrados. Figure 8-9 (b) again compares the GWT reconstructions against the maximum depth estimations from the laser scans for Defect I and II and the two permanently attached ultrasonic probes for Defect III. Three-dimensional renderings of the wall-thickness loss maps are shown in Figure 8-10 for the last four depth increments of each defect.

As in the case of the two ring array configuration, defects are reconstructed at the correct position and their presence and progression are detected with 100% sensitivity. The difference between the GWT and laser estimations is between 3 and 7% of wall thickness for the defect on the intrados which essentially reproduces the performance obtained with the two ring arrays. However, the addition of the line of transducers on the extrados significantly improves the depth estimation of the defect on the side narrowing the gap between the GWT and laser estimates from 4-22% to 4-8% of wall thickness.

For the defect on the extrados, GWT appears to overestimate the maximum depth. However, the true maximum depth is unknown since the defect was on the interior surface of the elbow and depth could only be sampled at the two locations of the ultrasonic sensors mounted on the outer surface of the pipe. Figure 8-11 (a) shows

[1]Sensitivity sometimes also referred to as true positive rate or probability of detection (POD), is defined as the ratio between the number of defects detected by the inspection system relative to the true number of defects and ranges between 0, no defect detected, to 100% all defects detected.

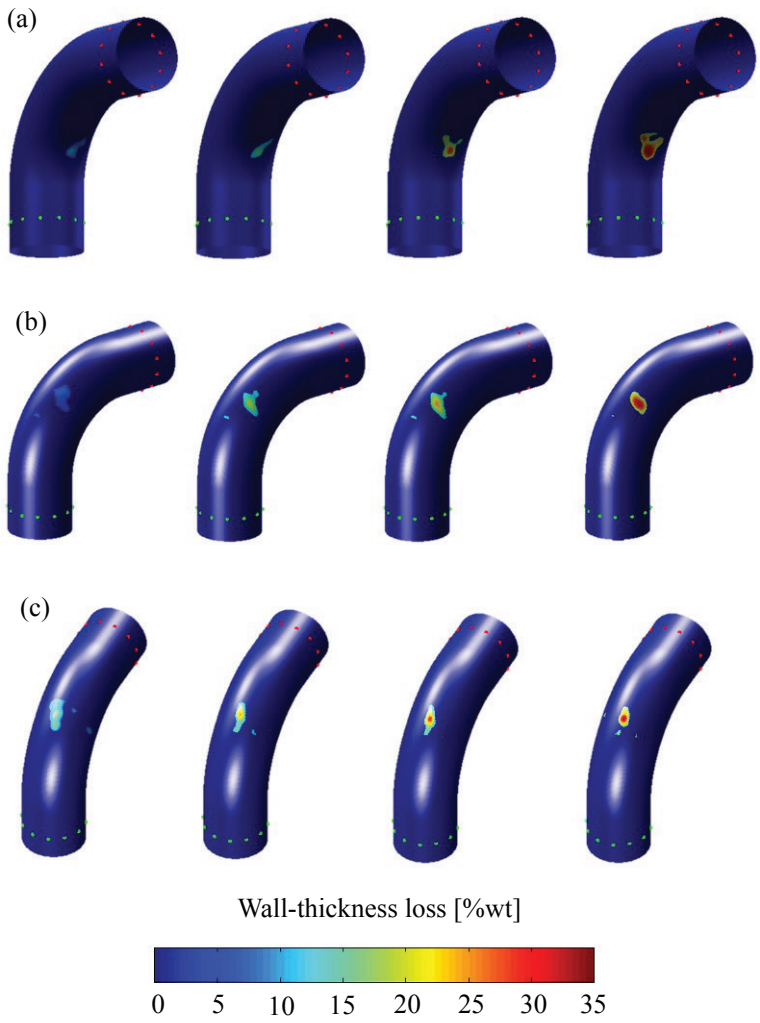

Figure 8-10: (Color online) Experimental 3-D renderings of wall-thickness loss maps reconstructed with GWT for the last four depth increments of the defects in Pipe II. (a) Defect I, (b) Defect II; (c) Defect III. The dots indicate the position of the transducers of the ring arrays while the transducers on the extrados are not shown for clarity.

the interior surface of a section of pipe wall removed from the elbow in correspondence of the area of Defect III - the circles indicate the position of the ultrasonic probes. The surface is covered in corrosion scale that at some locations spalls from the base metal. The wall thickness is highly irregular showing point-to-point variations exceeding 2

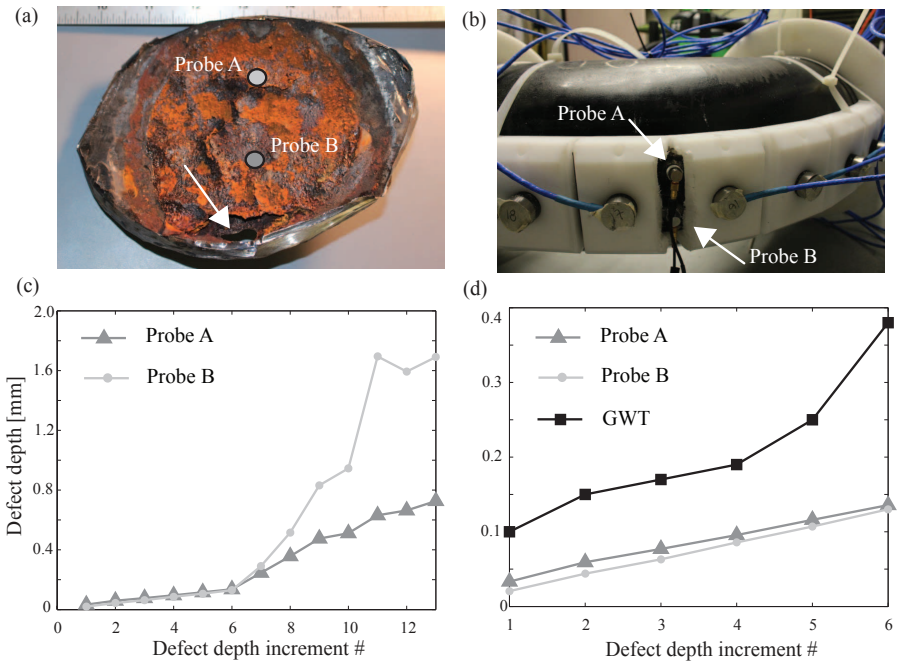

Figure 8-11: Ultrasonic measurements of the internal extrados defect of Pipe II. (a) Surface of the defect at the end of the accelerated corrosion tests showing a highly irregular depth profile and the presence of a through-thickness corrosion pit (pointed by the arrow). The circles indicate the areas inspected by the ultrasonic probes glued on the external surface as shown in (b); (c) Depth estimated by each probe for the 13 depth increments produced during the tests; (d) Comparison between GWT maximum depth and the depth readings from the ultrasonic probes for the first six depth increments.

mm. Most importantly, a through-thickness (100% wall thickness loss) corrosion pit with lateral size of approximately 8×12 mm is present. The contour of the pit is irregular and varies with depth. Defect depth was increased in 13 steps during which the two ultrasonic probes provided the wall-thickness loss readings shown in Figure 8-11 (c). It can be observed that initially, when the defect is shallow, the two probes yield similar results thus suggesting that the defect is relatively uniform. However, from defect increment #6 the readings start to diverge implying that the defect profile becomes more irregular and that the corrosion pit initiates. This hypothesis is corroborated by the fact that the corrosion times needed to produce the first six depth increments were consistent with the expected corrosion rate of the impressed current

method, while they increased significantly beyond depth increment #6. Therefore, while the ultrasonic probes may provide an accurate estimation of maximum depth for increments #1 to 6, they certainly underestimated maximum depth for defects #7 to 13 since they could only inspect the areas indicated by the circles in Figure 8-11 (a). For the shallow defects (#1 to 6), GWT follows the trend of the ultrasonic measurements but overestimates depth by about 100 μm as it can be seen in Figure 8-11 (d). Importantly, GWT is sensitive to maximum depth changes that could be as small as 20μm as it can be deduced from the first six depth steps of Defect III (see Table 8.1). For the largest depths #11-13, GWT provides a better indication of the severity of the corrosion pit by showing that defect depth continues to increase at a high rate, Figure 8-9 (b), while the ultrasonic measurements imply that the corrosion rate has slowed significantly [see Figure 8-11 (c)]. However, neither GWT nor the ultrasonic probes provide an indication of 100% wall-thickness loss for defect # 13 which corresponds to the through thickness hole caused by the corrosion pit.

8.6 Conclusions

This chapter has presented the experimental demonstration of guided wave tomography (GWT) of pipe bends based on a novel inversion algorithm and a new array configuration.

It has been shown that the inversion can be performed by extracting traveltimes from guided wave signals and interpreting the information they encode based on a two-dimensional acoustic model that is artificially inhomogeneous and elliptically anisotropic (INELAN). The numerical efficiency of the INELAN forward model means that rapid solution of the inverse problem can be achieved using an iterative scheme based on the conjugate gradient method, which leads to a generalization of the curved ray tomography method for anisotropic media. As a result, a wall-thickness loss map of the entire elbow can be formed in under four minutes on a standard PC.

The extrados' limited ray coverage offered by two ring arrays mounted at the ends of the elbow can cause severe underestimation of the depth of defects close to the

extrados. This limitation is addressed by introducing a line of transducers along the extrados which leads to a more uniform ray coverage of the elbow and hence significantly reduces the dependence of the accuracy of GWT on defect position around the pipe circumference.

Experimental validation has been conducted on two 8" diameter, schedule 40, carbon steel pipe bends with a 90° elbow, 1.5 D radius of curvature. It has been shown that detection of both the presence and progression of damage can be achieved with 100% sensitivity regardless of damage position around the bend and for defect sizes in the order of 100 mm. The shallowest detected defect could have been just under 40μm maximum depth while the smallest depth change was approximately 20μm. This is a remarkable result for a guided wave based method since 20μm is about 0.25% the nominal wall thickness and most importantly given that the pristine pipe shows point-to-point variations as large as 1.72 mm due to manufacturing tolerances. These unpredictable variations are not included in the forward model and are eliminated by using differential traveltime measurements between two states of the pipe.

For the defects considered in this study, GWT generally underestimated maximum depth relative to the values obtained from 3-D laser scans of the same defects leading in many cases to errors between 3 and 8% of wall thickness. All the defects simulated localized corrosion and had irregular depth profiles with the regions of maximum depth confined to narrow areas of a few millimeters in size. Several of these defects were introduced with the method of impressed currents which reproduces the electrochemistry of corrosion but with an accelerated kinetics. As a result, the morphology and length scale of damage around the deepest points should be representative of realistic defects. While the sharpness of the wall thickness minima did not cause significant loss of accuracy for the 3-D laser scans, which have a resolution scale $\approx$0.5 mm, they affected the accuracy of GWT since the wavelength of the A_0 mode used in the experiments was λ=18.6 mm. Therefore, GWT could only provide a smoothed reconstruction of the true depth profile that caused the maximum depth to be underestimated relative to the 3-D laser scans.

Chapter 9

Conclusions

9.1 Review

An investigation into the viability of ultrasonic testing using array configurations and advanced imaging techniques to tackle the challenges posed by complex specimen material and geometry was performed in this thesis. Chapter 1 reviewed the current state of the art in industrial NDT and explained the importance of developing better inspection and monitoring techniques for complex structures.

Chapter 2 has reviewed the theoretical background for the wavefront propagation in generally elastic materials. A simplified model of anisotropy known as elliptical anisotropy was introduced, and numerical methods for efficiently calculating wavefront traveltimes in inhomogeneous, elliptically anisotropic materials are described.

In Chapter 3 a phased array measurement technique which utilizes transmission as well as reflection measurements is applied to the problem of detecting ply waviness and porosity in composite laminate specimens with complex shapes. The applicability of the simplified elliptically anisotropic model to this problem was justified theoretically and experimentally. The ability of the technique to detect both porosity and waviness defects in composite laminate specimens was demonstrated.

Chapter 4 investigated the challenges of applying ultrasonic phased array imaging techniques to specimens with rich internal structure leading to multiple interfaces. Two main challenges with such parts were identified as the presence of refraction and

large reflection coefficients between water and high-grade steel alloys which limits the amount of energy transmitted inside the specimen. The challenge of refraction was answered by using the numerical methods discussed in Chapter 2 to develop focal laws that account for multiple interfaces, and a method of encasing the specimen in ice was presented as a means to increase the transmission coefficient between the coupling medium and the specimen, leading to better penetration.

Where Chapters 3 and 4 treated imaging as a 2-D problem, Chapter 5 performed an initial investigation into the use of matrix arrays and fully 3-D modeling of wavefront propagation into the specimen. Experiments were performed where cross-sectional images are formed with varying levels of out of plane curvature, and the ability of matrix arrays and 3-D focal law computation to correctly focus under such curvature was demonstrated.

Chapter 6 has introduced a theoretical description of elastic guided wave propagation in curved tubular structures by use of an equivalent 2-D inhomogeneous and elliptically anisotropic acoustic model. This model was the first step in the development of guided wave wall-thickness tomography (GWT) in pipe bends. Numerical simulations and experiments performed on a stainless steel pipe which contains a 90° bend were used to demonstrate the model's ability to accurately predict group arrival times.

The model introduced in Chapter 6 underwent more thorough experimental validation in Chapter 7. While Chapter 6 verified the model's ability to predict group arrival times, the presence of corrosion defects causes changes in the phase of the measured signal. In Chapter 7 several realistic corrosion defects were introduced into a stainless steel pipe bend using the method of impressed currents. A laser scanning system was used to measure the wall loss profiles. These profiles were used to theoretically predict the phase shift experienced by ultrasonic guided waves traveling through the bend. Experimental measurements were performed and the measured phase shifts in a set of signals were shown to be in good agreement with prediction.

The work done in Chapters 6 and 7 culminated in the development of a GWT algorithm in Chapter 8. An existing GWT algorithm for straight pipes was adapted to

pipes containing bends. This new GWT algorithm was used to reconstruct the defect topographies measured in Chapter 7 from recorded ultrasonic signals. Two transducer array configurations were considered, and a configuration containing transducers along the outside of the bend was demonstrated to have more uniform sensitivity with respect to defect location.

9.2 Discussion

This thesis has demonstrated that the use of ultrasonic sensors in array configurations and coupled with sophisticated imaging techniques have the potential to address the growing need of many industries to perform inspection and monitoring of complex systems.

Central to these applications is an efficient model of elliptically anisotropic elastic wavefront propagation described in Chapter 2. Although this model is simplified from the generally anisotropic case, it is shown in Chapter 3 to capture many key aspects of ultrasonic propagation in composite materials which are highly anisotropic. In Chapter 4 this model is shown to also be suitable to describe wavefront propagation in isotropic materials with multiple material interfaces. Furthermore, in Chapters 6 to 8 this same model of elliptical anisotropy is successfully applied to the description of guided elastic waves propagation through curved tubular structures.

Another important aspect of this work has been the use of novel measurement configurations. The use of two linear arrays capturing both transmission and reflection measurements in Chapter 3 is shown to provide good sensitivity to a wide range of defects. The reflection measurements are shown to be sensitive to porosity damage, while defects which consist of wrinkles in the composite laminate plies cause very little back-scattering and therefore are not consistently represented in the reflection images. However, the wrinkles do cause subtle changes in the propagating wavefronts' amplitudes and arrival times which are clearly present in the transmitted signals. Chapter 4 demonstrates a novel use of ice encapsulation in conjunction with phased array measurements to overcome the limitations of immersion testing imposed by the

large water-metal impedance mismatch. Chapter 6 shows that matrix arrays are more effective than linear arrays in imaging objects which exhibit complex 3-D curvature. Another novel array configuration consisting of electromagnetic acoustic transducers (EMAT) permanently installed on a pipe is presented in Chapter 8. Previous work in GWT applications have focused on measuring the wall-thickness in a region of straight pipeline bounded by two ring-arrays of transducers. In Chapters 6 and 7 we have shown that when a bend is present in such a configuration, the measured signals will have extremely low sensitivity to defects on the outside of a bend. A new configuration utilizing two ring-arrays plus a belt of transducers along the outside of a bend is introduced in Chapter 8 and is shown to provide sensitivity in this region, along with relatively uniform sensitivity to defect growth with respect to circumferential position.

The third key contribution of this thesis is the introduction of imaging methods which utilize the previously mentioned model of wavefront propagation and novel array configurations. In Chapter 3 the Total Focusing Method (TFM) algorithm modified to use the model of elliptical anisotropy is applied to the task of interpreting both back-scattered and through-transmitted signals. The images formed are shown to provide consistent indications of porosity damage and wrinkle defects over a range of specimen orientations. Moreover, it was shown that the use of adaptive apertures is required to account for the high attenuation and dispersion experienced by waves traveling in a direction parallel to the plies of a composite material. In Chapter 4 it is shown that this modified TFM algorithm is equivalent to an imaging technique known as Diffraction Migration (DM) in the context of geophysics, and the suitability of this algorithm to form images of complex layered media is demonstrated. Chapter 8 builds on the work of Chapters 6 and 7 to introduce a GWT algorithm which is valid on curved tubular structures. Key theoretical challenges involving the subtle distinction between group and phase velocity are navigated during this formulation, and the algorithm is validated on numerical as well as experimental measurements and the resulting images of wall-thickness loss are shown to have good agreement with laser-scan measurements of the defect profiles.

9.3 Future work

The work done in this thesis has opened the door to future industrial inspection and monitoring applications which overcome material and geometrical complexities.

The combined reflection and transmission beamforming measurement of composite materials presented in Chapter 3 is valid for specimens which have approximately 2-D curvature, but could be made more robust by incorporating known models of specimen geometry and ply orientation. Incorporating such a known model would require either very precise positioning of the arrays relative the specimen, or an optimization routine to determine this positioning from the recorded signals.

The work done in Chapter 4 has opened many avenues of future research. The use of colloidal suspensions to alter the mechanical properties of the coupling medium once it is frozen may allow for better matching of the specimen impedance and or compressional wave velocity. Advanced migration algorithms which incorporate the information encoded in multiple internal reflections have been developed in the context of geophysics and could potentially be applied to improve image quality.

Extending the beamforming techniques presented in Chapters 3 and 4 from 2-D to fully 3-D imaging remains an open problem due to the significant computational burden. Progress has been made in the development of algorithms which utilize parallel processing to speed up wavefront traveltime computations in isotropic media, but parallel computation of 3-D anisotropic traveltimes is an open challenge. On the other hand, massively parallel algorithms for computing beamforming images are well established, but how to incorporate traveltime information for complicated wavefronts with these algorithms is not straight-forward.

The GWT application developed in Chapters 6 to 8 is currently being tested in situ on an oil drilling platform in the Gulf of Mexico. Future avenues of research may include investigation of forward models which account for diffraction as well as refraction effects. As demonstrated in Chapter 6 there is a strong focusing effect in the presence of a bend which leads to very large signals that trail behind the wavefront. As the current model only accounts for the arrival time of the wavefront, the information

which is encoded in these signals remains unaccounted for and could serve to increase sensitivity and accuracy if properly integrated in the inversion scheme.

List of publications

Published journal papers

(P1) A. Brath, F. Simonetti, P. Nagy and G. Instanes. "Acoustic formulation of elastic guided wave propagation and scattering in curved tubular structures". In: *IEEE transactions on ultrasonics, ferroelectrics, and frequency control* 61.5 (2014), pp. 815-829.

(P2) A. Brath, F. Simonetti, P. Nagy and G. Instanes. "Experimental validation of a fast forward model for guided wave tomography of pipe elbows". In: *IEEE transactions on ultrasonics, ferroelectrics, and frequency control* 64.5 (2017), pp. 859-871.

(P3) A. Brath, F. Simonetti, P. Nagy and G. Instanes. "Guided wave tomography of pipe bends". In: *IEEE transactions on ultrasonics, ferroelectrics, and frequency control* 64.5 (2017), pp. 847-858.

(P4) A. Brath and F. Simonetti. "Phased array imaging of complex-geometry composite components". In: *IEEE transactions on ultrasonics, ferroelectrics, and frequency control* 64.10 (2017), pp. 1573-1582.

Journal papers currently under review

(P5) F. Simonetti, I. Satov, A. Brath, K. Wells, J. Porter, B. Hayes, T. Hall and K. Davis. "Cryoultrasonic NDE: Ice-cold ultrasonic waves for the detection of damage in complex-shape engineering components". In: *IEEE transactions on ultrasonics, ferroelectrics, and frequency control* (2017), submitted.

Bibliography

[1] M. Fellet and W. Rossner. "Ceramic-matrix composites take the heat". English. In: *MRS BULLETIN* 40.11 (2015), pp. 916–917.

[2] L. Jyothish Kumar and C. G. Krishnadas Nair. "Current trends of additive manufacturing in the aerospace industry". English. In: 2016. ISBN: 9789811008122.

[3] A. Scott. *Printed titanium parts expected to save millions in Boeing Dreamliner costs*. Ed. by reuters.com. Apr. 2017. URL: http://www.reuters.com/article/us-norsk-boeing-idUSKBN17C264.

[4] D. Brackett, I. Ashcroft, and R. Hague. "Topology optimization for additive manufacturing". In: *Proceedings of the solid freeform fabrication symposium, Austin, TX*. Vol. 1. S. 2011, pp. 348–362.

[5] S. Galjaard et al. "Optimizing structural building elements in metal by using additive manufacturing". In: *of the International Association forShell and Spatial Structures (IASS) Symposium 2015*. 2015.

[6] S. Cheong and D. Murtaugh. *Now there's another source of oil that's starting to get cheap*. Ed. by Bloomberg. https://www.bloomberg.com/news/articles/2017-05-30/trouble-brewing-for-opec-as-once-costly-deep-sea-oil-turns-cheap. Accessed: 2017-09-12. May 2017.

[7] The University of Stavanger. *Norway's oil industry working in extreme conditions*. Ed. by ScienceDaily. www.sciencedaily.com/releases/2012/11/121123092134.htm. Accessed: 2017-09-12. Nov. 2012.

[8] L. A. S Rocha and J. L. Junqueira P. andRoque. "Overcoming deep and ultra deepwater drilling challenges". In: *Offshore Technology Conference*. Offshore Technology Conference. 2003.

[9] J. B. Curtis. "Fractured shale-gas systems". In: *AAPG bulletin* 86.11 (2002), pp. 1921–1938.

[10] T. Fitzgerald. "Frackonomics: some economics of hydraulic fracturing". In: *Case W. Res. L. Rev.* 63 (2012), p. 1337.

[11] C. Summerhayes. "Deep Water–The Gulf Oil Disaster and the Future of Offshore Drilling". In: *Underwater Technology* 30.2 (2011), pp. 113–115.

[12] A. F. Grandt. *Fundamentals of structural integrity: damage tolerant design and nondestructive evaluation*. English. Hoboken, N.J: John Wiley, 2004. ISBN: 9780471214595;0471214590;

[13] C. Boller, F .K. Chang, and Y. Fujino. *Encyclopedia of structural health monitoring*. English. Vol. 1. Hoboken, NJ USA;Chichester, West Sussex U.K: Wiley, 2009. ISBN: 9780470058220;0470058226;0470061626;9780470061626;

[14] R. Di Sante. "Fibre Optic Sensors for Structural Health Monitoring of Aircraft Composite Structures: Recent Advances and Applications". English. In: *SENSORS* 15.8 (2015), pp. 18666–18713.

[15] C. Boller, F. K. Chang, and Y. Fujino. *Encyclopedia of structural health monitoring*. English. Vol. 4. Hoboken, NJ USA;Chichester, West Sussex U.K: Wiley, 2009. ISBN: 9780470058220;0470058226;0470061626;9780470061626;

[16] C. Boller, F. K. Chang, and Y. Fujino. *Encyclopedia of structural health monitoring*. English. Vol. 5. Hoboken, NJ USA;Chichester, West Sussex U.K: Wiley, 2009. ISBN: 9780470058220;0470058226;0470061626;9780470061626;

[17] *Permasense: experts in remove monitoring solutions*. http://www.permasense.com/home.php. Accessed: 2017-08-30.

[18] B. Raj, T. Jayakumar, and M. Thavasimuthu. *Practical non-destructive testing*. 3rd. Oxford, U.K: Alpha Science International, 2007. ISBN: 9781842653753.

[19] G. N. Hounsfield. "Computerized transverse axial scanning (tomography): Part 1. Description of system". In: *The British journal of radiology* 46.552 (1973), pp. 1016–1022.

[20] T. Kundu. *Ultrasonic nondestructive evaluation: engineering and biological material characterization*. CRC press, 2003. Chap. 3.

[21] W. W. Hansen and J. R. Woodyard. "A new principle in directional antenna design". In: *Proceedings of the Institute of Radio Engineers* 26.3 (1938), pp. 333–345.

[22] L. W. Gardner. "An areal plan of mapping subsurface structure by refraction shooting". In: *Geophysics* 4.4 (1939), pp. 247–259.

[23] J. C. Somer. "Electronic sector scanning for ultrasonic diagnosis". In: *Ultrasonics* 6.3 (1968), pp. 153–159.

[24] F. Gassmann. "Introduction to seismic travel time methods in anisotropic media". English. In: *Pure and Applied Geophysics PAGEOPH* 58.1 (1964), pp. 63–112.

[25] V. Cerveny. *Seismic ray theory*. English. New York;Cambridge, U.K; Cambridge University Press, 2001. ISBN: 9780521366717.

[26] L. Thomsen. *Understanding Seismic Anisotropy in Exploration and Exploitation*. Society of Exploration Geophysicists, 2014. Chap. 1. ISBN: 978-1-56080-327-0. DOI: 10.1190/1.9781560803270. URL: http://geoscienceworld.org/content/9781560803270/9781560803270.

[27] "First-Order Nonlinear Equations and Their Applications". In: *Nonlinear Partial Differential Equations for Scientists and Engineers*. Boston, MA: Birkhäuser Boston, 2005, pp. 221–250. ISBN: 978-0-8176-4418-5. DOI: 10.1007/0-8176-4418-0_4. URL: https://doi.org/10.1007/0-8176-4418-0_4.

[28] T. J. Moser. "Shortest path calculation of seismic rays". In: *Geophysics* 56.1 (1991), pp. 59–67.

[29] J. Vidale. "Finite-difference calculation of travel times". In: *Bulletin of the Seismological Society of America* 78.6 (1988), pp. 2062–2076.

[30] J. A. Sethian. "A Fast Marching Level Set Method for Monotonically Advancing Fronts". In: *Proceedings of the National Academy of Sciences of the United States of America* 93.4 (1996), pp. 1591–1595.

[31] F. Qin et al. "Finite-difference solution of the eikonal equation along expanding wave-fronts". In: *GEOPHYSICS* 57.3 (1992), pp. 478–487.

[32] T. Watanabe, T. Hirai, and K. Sassa. "Seismic traveltime tomography in anisotropic heterogeneous media". In: *Journal of Applied Geophysics* 35.2 (1996), pp. 133–143.

[33] R. Fischer and J. M. Lees. "Shortest path ray tracing with sparse graphs". In: *Geophysics* 58.7 (1993), pp. 987–996.

[34] E. W. Dijkstra. "A note on two problems in connexion with graphs". English. In: *Numerische Mathematik* 1.1 (1959), pp. 269–271.

[35] M. Fredman and R. Tarjan. "Fibonacci heaps and their uses in improved network optimization algorithms". English. In: *Journal of the ACM (JACM)* 34.3 (1987), pp. 596–615.

[36] J. M. Mirebeau. "Anisotropic fast-marching on cartesian grids using lattice basis reduction". In: *SIAM Journal on Numerical Analysis* 52.4 (2014;2012;), pp. 1573–1599.

[37] P. Petersen, Ohio Library, and Information Network. *Riemannian geometry.* English. Third;3rd 2016; vol. 171. Cham: Springer, 2016. Chap. 1. ISBN: 9783319266541;33192665

[38] F. Bornemann and C. Rasch. "Finite-element Discretization of Static Hamilton-Jacobi Equations based on a Local Variational Principle". In: *Computing and Visualization in Science* 9.2 (2006;2004;), pp. 57–69.

[39] K. W. Ferrara et al. "Ultrasound". In: *Biomedical imaging.* Ed. by Karen M . Mudry, Robert Plonsey, and Joseph D . Bronzino. Boca Raton, FL: CRC Press, 2003. Chap. 12, pp. 12–1–12–41.

[40] C. Holmes, B. Drinkwater, and P. Wilcox. "The post-processing of ultrasonic array data using the total focusing method". In: *Insight-Non-Destructive Testing and Condition Monitoring* 46.11 (2004), pp. 677–680.

[41] L. Le Jeune et al. "Adaptive ultrasonic imaging with the total focusing method for inspection of complex components immersed in water". In: *AIP Conference Proceedings*. Vol. 1650. 1. AIP. 2015, pp. 1037–1046.

[42] M. Weston et al. "Time efficient auto-focussing algorithms for ultrasonic inspection of dual-layered media using Full Matrix Capture". In: *NDT & E International* 47 (2012), pp. 43 –50. ISSN: 0963-8695. DOI: http://dx.doi.org/10.1016/j.ndteint.2011.10.006. URL: http://www.sciencedirect.com/science/article/pii/S0963869511001526.

[43] D. L. Hopkins et al. "Surface-Adaptive Ultrasound (SAUL) for phased-array inspection of composite specimens with curved edges and complex geometry". In: *AIP Conference Proceedings*. Vol. 1511. 1. AIP. 2013, pp. 809–816.

[44] J. Camacho et al. "Automatic dynamic depth focusing for NDT". In: *IEEE Transactions on Ultrasonics, Ferroelectrics, and Frequency Control* 61.4 (2014), pp. 673–684.

[45] J. Camacho and J. F. Cruza. "Auto-focused virtual source imaging with arbitrarily shaped interfaces". In: *IEEE transactions on ultrasonics, ferroelectrics, and frequency control* 62.11 (2015), pp. 1944–1956.

[46] G. D. Connolly et al. "The application of Fermat's principle for imaging anisotropic and inhomogeneous media with application to austenitic steel weld inspection". In: *Proceedings of the Royal Society of London A: Mathematical, Physical and Engineering Sciences*. Vol. 465. 2111. The Royal Society. 2009, pp. 3401–3423.

[47] C. Höhne et al. "SAFT imaging of transverse cracks in austenitic and dissimilar welds". In: *Journal of Nondestructive Evaluation* 32.1 (2013), pp. 51–66.

[48] C. Li et al. "Imaging composite material using ultrasonic arrays". In: *Ndt & E International* 53 (2013), pp. 8–17.

[49] D. Yan, B. Wright, and I. Cooper. "Inspection of anisotropic composites using ultrasonic phased arrays". In: *World Journal of Engineering* 10.2 (2013), pp. 101–106.

[50] D. Pain and B. W. Drinkwater. "Detection of fibre waviness using ultrasonic array scattering data". In: *Journal of Nondestructive Evaluation* 32.3 (2013), pp. 215–227.

[51] I. Tsvankin. "Anisotropic parameters and P-wave velocity for orthorhombic media". In: *Geophysics* 62.4 (1997), pp. 1292–1309.

[52] "Department of Defense Handbook: Composite Materials Handbook; Volume 3. Polymer Matrix Composites Materials Usage, Design, and Analysis". English. In: vol. 3. 2002, pp. 10–26–10–27.

[53] MATLAB and Curve Fitting Toolbox Release 2012b. Natick, Massachusetts: The MathWorks Inc., 2012.

[54] O. Roy et al. "Robust array calibration using time delays with application to ultrasound tomography". English. In: vol. 7968. 2011. Chap. 1. ISBN: 0277-786X;1605-7422;

[55] A. J. Hunter, B. W. Drinkwater, and P. D. Wilcox. "Autofocusing ultrasonic imagery for non-destructive testing and evaluation of specimens with complicated geometries". In: *NDT & E International* 43.2 (2010), pp. 78–85.

[56] J. L. Rose. *Ultrasonic Waves in Solid Media*. Cambridge, UK: Cambridge University Press, 1999.

[57] P. B. Nagy and L. Adler. "Surface roughness induced attenuation of reflected and transmitted ultrasonic waves". In: *J. Acoust. Soc. Am.* 82.1 (1987), pp. 193–197.

[58] E. G. Williams. *Fourier acoustics: sound radiation and nearfield acoustical holography*. Academic press, 1999.

[59] J. Achenbach. *Wave propagation in elastic solids*. Vol. 16. Elsevier, 2012.

[60] R. E. Gagnon et al. "Acoustic velocities and densities of polycrystalline ice Ih, II, III, V, and VI by Brillouin spectroscopy". In: *The Journal of Chemical Physics* 92.3 (1990), pp. 1909–1914.

[61] C. Vogt, K. Laihem, and C. Wiebusch. "Speed of sound in bubble-free ice". In: *The Journal of the Acoustical Society of America* 124.6 (2008), pp. 3613–3618.

[62] L. E. Raraty and D. Tabor. "The adhesion and strength properties of ice". In: *Proceedings of the Royal Society of London. Series A, Mathematical and Physical Sciences* (1958), pp. 184–201.

[63] P. Archer and V. Gupta. "Measurement and control of ice adhesion to aluminum 6061 alloy". In: *Journal of the Mechanics and Physics of Solids* 46.10 (1998), pp. 1745–1771.

[64] K. Matsumoto and T. Kobayashi. "Fundamental study on adhesion of ice to cooling solid surface". In: *International Journal of Refrigeration* 30.5 (2007), pp. 851–860.

[65] M. Zou et al. "Effects of surface roughness and energy on ice adhesion strength". In: *Applied Surface Science* 257.8 (2011), pp. 3786–3792.

[66] F. Audebert et al. "Imaging complex geologic structure with single-arrival Kirchhoff prestack depth migration". In: *Geophysics* 62.5 (1997), pp. 1533–1543.

[67] R. H. Stolt. "Migration by Fourier transform". In: *Geophysics* 43.1 (1978), pp. 23–48.

[68] E. Baysal, D. D. Kosloff, and J. W. C. Sherwood. "Reverse time migration". In: *Geophysics* 48.11 (1983), pp. 1514–1524.

[69] J. F. Claerbout and S. M. Doherty. "Downward continuation of moveout-corrected seismograms". In: *Geophysics* 37.5 (1972), pp. 741–768.

[70] J. Gazdag. "Wave equation migration with the phase-shift method". In: *Geophysics* 43.7 (1978), pp. 1342–1351.

[71] T. J. Moser and C. B. Howard. "Diffraction imaging in depth". In: *Geophysical Prospecting* 56.5 (2008), pp. 627–641.

[72] R. Abbasi et al. "IceTop: The surface component of IceCube". In: *Nuclear Instruments and Methods in Physics Research Section A: Accelerators, Spectrometers, Detectors and Associated Equipment* 700 (2013), pp. 188–220.

[73] D. M. Otten et al. "Ice-front propagation monitoring in tissue by the use of visible-light spectroscopy". In: *Applied optics* 37.25 (1998), pp. 6006–6010.

[74] Ch. Körber et al. "Interaction of particles and a moving ice-liquid interface". In: *Journal of Crystal Growth* 72.3 (1985), pp. 649–662.

[75] B. W. Drinkwater, R. S. Dwyer-Joyce, and P. Cawley. "A Study of the Interaction between Ultrasound and a Partially Contacting Solid–Solid Interface". In: *Proceedings of the Royal Society of London A: Mathematical, Physical and Engineering Sciences*. Vol. 452. 1955. The Royal Society. 1996, pp. 2613–2628.

[76] J. J. Petrovic. "Review mechanical properties of ice and snow". In: *Journal of materials science* 38.1 (2003), pp. 1–6.

[77] T. M. Tharp. "Conditions for crack propagation by frost wedging". In: *Geological Society of America Bulletin* 99.1 (1987), pp. 94–102.

[78] G. P. Davidson and J. F. Nye. "A photoelastic study of ice pressure in rock cracks". In: *Cold Regions Science and Technology* 11.2 (1985), pp. 141–153.

[79] F. V. Araújo et al. "Inverse scattering series for multiple attenuation: An example with surface and internal multiples". In: *SEG Technical Program Expanded Abstracts 1994*. Society of Exploration Geophysicists, 1994, pp. 1039–1041.

[80] A. B. Weglein et al. "An inverse-scattering series method for attenuating multiples in seismic reflection data". In: *Geophysics* 62.6 (1997), pp. 1975–1989.

[81] A. B. Weglein. "Multiple attenuation: an overview of recent advances and the road ahead (1999)". In: *The Leading Edge* 18.1 (1999), pp. 40–44.

[82] H. Jakubowicz. "Wave equation prediction and removal of interbed multiples". In: *SEG Technical Program Expanded Abstracts 1998*. Society of Exploration Geophysicists, 1998, pp. 1527–1530.

[83] A.J. Berkhout and D.J. Verschuur. "Removal of internal multiples with the common-focus-point (CFP) approach: Part 1ï£¡Explanation of the theory". In: *Geophysics* 70.3 (2005), pp. V45–V60.

[84] M. Davydenko and D. J. Verschuur. "Full-wavefield migration: Using surface and internal multiples in imaging". In: *Geophys. Prospect.* (2016).

[85] A. Aldawood et al. "The possibilities of least-squares migration of internally scattered seismic energy". In: *Geophysics* 80.4 (2015), S93–S101.

[86] Y. Liu et al. "Reverse time migration of internal multiples for subsalt imaging". In: *Geophysics* 80.5 (2015), S175–S185.

[87] S. Singh et al. "Marchenko imaging: Imaging with primaries, internal multiples, and free-surface multiples". In: *Geophysics* 80.5 (2015), S165–S174.

[88] S. W. Smith, H. G. Pavy, and O. T. von Ramm. "High-speed ultrasound volumetric imaging system. I. Transducer design and beam steering". In: *IEEE transactions on ultrasonics, ferroelectrics, and frequency control* 38.2 (1991), pp. 100–108.

[89] L. Sugeng et al. "Live 3-dimensional transesophageal echocardiography: initial experience using the fully-sampled matrix array probe". In: *Journal of the American College of Cardiology* 52.6 (2008), pp. 446–449.

[90] W. K. Jeong and R. T. Whitaker. "A fast iterative method for eikonal equations". In: *SIAM Journal on Scientific Computing* 30.5 (2008), pp. 2512–2534.

[91] M. Sutcliffe et al. "Real-time full matrix capture for ultrasonic non-destructive testing with acceleration of post-processing through graphic hardware". In: *Ndt & E International* 51 (2012), pp. 16–23.

[92] R. N. Tuttle. "Corrosion in oil and gas production". In: *J. Petrol. Technol.* 39.7 (1987), pp. 756–762.

[93] K. G. Boving. "NDE methods used in optimum maintenance programs for oil and gas-pipelines". In: *Insight* 37.6 (1995), pp. 444–446.

[94] D. N. Alleyne et al. "Rapid, Long Range Inspection of Chemical Plant Pipework Using Guided Waves". In: *Insight* 43 (2001), pp. 93–96,101.

[95] P. Mudge. "Field application of the teletest long range ultrasonic testing technique". In: *Insight* 43 (2001), pp. 74–77.

[96] P. Cawley et al. "Practical long range guided wave testing: application to pipes and rail". In: *Mater. Eval.* 61.1 (2003), pp. 66–74.

[97] R. Carandente and P. Cawley. "The effect of complex defects profiles on the reflection of the fundamental torsional mode in pipes". In: *NDT&E Int.* 46 (2012), pp. 41–47.

[98] K. R. Leonard and M. K. Hinders. "Lamb wave tomography of pipe-like structures". In: *Ultrasonics* 43.7 (2005), pp. 574 –583. ISSN: 0041-624X. DOI: http://dx.doi.org/10.1016/j.ultras.2004.12.006. URL: http://www.sciencedirect.com/science/article/pii/S0041624X04003154.

[99] F. Yan, jr Roger L. Royer, and J. L. Rose. "Ultrasonic Guided Wave Imaging Techniques in Structural Health Monitoring". In: *Journal of Intelligent Material Systems and Structures* 21.3 (2010), pp. 377–384. DOI: 10.1177/1045389X09356026. eprint: http://dx.doi.org/10.1177/1045389X09356026. URL: http://dx.doi.org/10.1177/1045389X09356026.

[100] A. Volker and J. Bloom. "Experimental results of guided wave tomography". In: *Rev. Prog. Quant. NDE*. Ed. by D. O. Thompson and D. E. Chimenti. Vol. 30B. 2011, pp. 215–222.

[101] P. Huthwaite and F. Simonetti. "High-resolution guided wave tomography". In: *Wave Motion* 50.5 (2013), pp. 979–993. ISSN: 0165-2125. DOI: 10.1016/J.WAVEMOTI.2013.04.004. URL: http://rave.ohiolink.edu/ejournals/article/332909501.

[102] R. G. Pratt. "Seismic waveform inversion in the frequency domain, Part 1: Theory and verification in a physical scale model". In: *Geophysics* 64.3 (1999), pp. 888–901.

[103] D. P. Jansen and D. A. Hutchins. "Lamb wave tomography". In: *Ultrasonics Symposium, 1990. Proceedings., IEEE 1990*. IEEE. 1990, pp. 1017–1020.

[104] J. Pei et al. "Lamb wave tomography and its application in pipe erosion/corrosion monitoring". In: *Res. Nondestruct. Eval.* 8 (4 1996), pp. 189–197. ISSN: 0934-9847.

[105] E. V. Malyarenko and M. K. Hinders. "Fan beam and double crosshole Lamb wave tomography for mapping flaws in aging aircraft structures". In: *J. Acoust. Soc. Am.* 108 (2000), p. 1631.

[106] P. Belanger, P. Cawley, and F. Simonetti. "Guided wave diffraction tomography within the Born approximation". In: *IEEE Trans. Ultrason. Ferroelectr. Freq. Contr.* 57 (2010), pp. 1405–1418.

[107] K. R. Leonard and M. K. Hinders. "Guided wave helical ultrasonic tomography of pipes". In: *J. Acoust. Soc. Am.* 114.2 (2003), pp. 767–774.

[108] C. L. Willey et al. "Guided wave tomography of pipes with high-order helical modes". In: *NDT & E International* 65 (2014), pp. 8–21.

[109] H. Lamb. "On waves in an elastic plate". In: *P. Roy. Soc.* 93 (1916-1917), pp. 114–128.

[110] Lord Rayleigh. "On the free vibrations of an infinite plate of homogeneous isotropic elastic matter". In: *P. Lond. Math. Soc.* 20.357 (1888-1889), pp. 225–237.

[111] A. N. Norris and C. Vemula. "Scattering of flexural waves on thin plates". In: *J. Sound Vib.* 181.1 (1995), pp. 115–125.

[112] L. R. Rose and C. H. Wang. "Mindlin plate theory for damage detection: imaging of flexural inhomogeneities". In: *J. Acoust. Soc. Am.* 127 (2010), pp. 754–763.

[113] D. J. Struik. *Lectures on classical differential geometry*. Mineola N. Y.: Dover Publications, 1988.

[114] G. Liu and J. Qu. "Guided circumferential waves in a circular annulus". In: *J. Appl. Mech.* 65.2 (1998), pp. 424–430.

[115] P. M. Morse and H. Feshbach. *Methods of Theoretical Physics*. New York, London: McGraw-Hill Book Company, 1953.

[116] W. S. Phillips and M. C. Fehler. "Traveltime tomography: A comparison of popular methods". In: *Geophysics* 56.10 (1991), pp. 1639–1649.

[117] T. Alkhalifah. "An acoustic wave equation for anisotropic media". In: *Geophysics* 65.4 (2000), pp. 1239–1250.

[118] *Acoustic Module User's Guide*. COMSOL, 2012.

[119] T. J. Moser. "Shortest path calculation of seismic rays". In: *Geophysics* 56.1 (1991), pp. 59–67.

[120] V. A. Borovikov and B. Y. Kinber. *Geometrical theory of diffraction*. Vol. 37. Iet, 1994.

[121] S. H. Hung, F. A. Dahlen, and G. Nolet. "Wavefront healing: a banana–doughnut perspective". In: *Geophys. J. Int.* 146.2 (2001), pp. 289–312.

[122] G. Instanes et al. "Measuring wall thickness loss for a structure". Patent US 61758433 (US). Jan. 2013.

[123] M. Born and E. Wolf. "Principles of Optics, seventh expanded edition". In: *Cambridge, England* (1999).

[124] R. M. Sanderson et al. "The investigation of guided wave propagation around a pipe bend using an analytical modeling approach". In: *The journal of the acoustical society of america* 133.3 (2013), pp. 1404–1414.

[125] F. B. Cegla et al. "High-temperature (>500 C) wall thickness monitoring using dry-coupled ultrasonic waveguide transducers". In: *IEEE Transactions on Ultrasonics, Ferroelectrics, and Frequency Control* 58.1 (Jan. 2011), pp. 156–167. ISSN: 0885-3010. DOI: 10.1109/TUFFC.2011.1782.

[126] D. Chew and P. Fromme. "Monitoring of corrosion damage using high-frequency guided ultrasonic waves". In: *AIP Conference Proceedings*. Vol. 1650. 1. AIP. 2015, pp. 777–784.

[127] MATLAB version 8.4.0 (R2014b). Natick, Massachusetts: The MathWorks Inc., 2014.

[128] T. Clarke et al. "Development of a low-frequency high purity A 0 mode transducer for SHM applications". In: *IEEE transactions on ultrasonics, ferroelectrics, and frequency control* 56.7 (2009).

[129] P. B. Nagy, F. Simonetti, and G. Instanes. "Corrosion and erosion monitoring in plates and pipes using constant group velocity Lamb wave inspection". English. In: *ULTRASONICS* 54.7 (2014), pp. 1832–1841.

[130] C. L. Willey and F. Simonetti. "A two-dimensional analysis of the sensitivity of a pulse first break to wave speed contrast on a scale below the resolution length of ray tomography". In: *The Journal of the Acoustical Society of America* 139.6 (2016), pp. 3145–3158.

[131] F. A. Dahlen, S. H. Hung, and G. Nolet. "Fréchet kernels for finite-frequency traveltimesâĂŤI. Theory". In: *Geophysical Journal International* 141.1 (2000), pp. 157–174.

[132] A. Volker and T. van Zon. "Guided wave travel time tomography for bends". In: *AIP Conference Proceedings*. Vol. 1511. 1. AIP. 2013, pp. 737–744.

[133] R. Potthast. *Point sources and multipoles in inverse scattering theory*. CRC Press, 2001.

[134] W. W. Hager and H. Zhang. "A survey of nonlinear conjugate gradient methods". In: *Pacific journal of Optimization* 2.1 (2006), pp. 35–58.

[135] A. C. Kak and M. Slaney. "Principles of computerized tomographic reconstruction". In: *IEEE, New York* (1998).

[136] Ö. Yilmaz. *Seismic data analysis*. Vol. 1. Society of Exploration Geophysicists Tulsa, 2001.

[137] G. Nolet et al. “A breviary of seismic tomography”. In: *Imaging the Interior* (2008).

[138] T. Clarke et al. “Development of a low-frequency high purity A 0 mode transducer for SHM applications”. In: *IEEE transactions on ultrasonics, ferroelectrics, and frequency control* 56.7 (2009).

[139] D. Colton and R. Kress. *Inverse acoustic and electromagnetic scattering theory*. Vol. 93. Springer Science & Business Media, 2012.

[140] P. R. Williamson and M. H. Worthington. “Resolution limits in ray tomography due to wave behavior: Numerical experiments”. In: *Geophysics* 58.5 (1993), pp. 727–735.